Microseismic Monitoring As a Site Investigation Tool: A Feasibility Study

By

Chiara Mary Hooper

A thesis submitted for the degree of Doctor of Philosophy

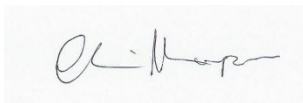**Department of Civil and Environmental Engineering**

University of Strathclyde

DECLARATION

This thesis is the result of the author's original research. It has been composed by the author and has not been previously submitted for examination which has led to the award of a degree.

The copyright of this thesis belongs to the author under the terms of the United Kingdom Copyright Acts as qualified by University of Strathclyde Regulation 3.50. Due acknowledgement must always be made of the use of any material contained in, or derived from, this thesis.

Signed:

Date: 12th September 2016

SUMMARY

A proof of concept for using microseismics as a site investigation tool has been developed and presented as a feasibility study utilising changes in the seismic wave Peak Particle Velocity (PPV) (m/s) and dominant frequency (Hz). The key significance of this thesis is the enhancement of near surface seismic imaging applications using a novel concept.

Researchers have observed low frequencies when detecting geological features at depths greater than 100m. Mitchell, Derzhi et al. (1997) and Dilay and Eastwood (1995) have shown previously that the dominant frequency observed moved towards the low frequency range (<100Hz). Marfurt (1984), investigated how the dominant frequency varies with geological feature thickness and Marfurt and Kirlin (2001) used this concept to resolve geological features with a thickness of <20m.

This thesis identified the following gaps in knowledge and identified that there is:

- No study to demonstrate if the relationship between dominant frequency and geological feature thickness is observed in the near surface (i.e. depths less than 100m) at metre scale accuracy (i.e. <10m);
- No study has used micro seismometers to apply this technique for near surface applications; and
- No study which has considered if the dominant frequency and PPV characteristics can be used to develop a concept for a near surface site investigation tool deployed in the near surface.

Considering the effect of medium properties there was significant effect on seismic wave characteristics such as PPV and frequency when utilising low frequency seismic sources in the range of 1-100Hz. The changes in the seismic wave characteristics during wave propagation through geological features characterised by different central feature widths and low Pressure (P) wave velocity zones were investigated. COMSOL Multiphysics Finite Element software modelled seismic excitations using the linear elastic equations that govern mechanical wave

propagation. Dominant frequency was more responsive than PPV to material property changes.

Considering the presence of a material property boundary, there was a significant effect on the PPV and dominant frequency characteristics, allowing a novel prediction methodology to be developed. The presence and width of a geological feature was detected at sub metre scale accuracy.

Considering the presence of a geological feature surrounded by a low P wave velocity zone, the differentiation between the material zones can be detected numerically at sub metre scale accuracy, and this was validated in "blind" tests and pilot field trials with a systematic error of +0.4m and a random uncertainty of ±0.39m.

Plotting PPV as a horizontal profile across the monitoring cross section allowed the visualisation of geological feature width, which inferred that geological feature location can be visualised with good accuracy.

This research has confirmed that we can use the seismic wave characteristics i.e. PPV and frequency, to effectively map and locate near surface geological and manmade structures using a novel concept which can be deployed in the near surface. The range of validity of this novel concept is the detection and location of geological structures of a known type (i.e. a vertical dyke formation) for a range of different geological parameters such as, width and material properties in a low ambient noise environment.

The effect of noise is important in terms of resolution and applicability of the method, and was investigated by adding noise to the sensitivity analysis. This research intentionally selected a field site that was characterised by a low ambient noise environment removing the requirement to utilise signal processing filtration methods as the impact from ambient noise was deemed insignificant.

Consideration was given to sites that may be characterised by high ambient noise. When noise was increased to 2 x source PPV the "worst case" systematic error was -

2m and the random uncertainty was ± 1.6m. Both of which are greater than systematic error of +0.4m observed in the field trial.

In high noise environment it would be advantageous prior to the experiment to establish if the PPV of the seismic source is powerful enough to overcome the effect of ambient noise. Future work could consider the application of filtration via various signal processing methods to minimise the effect of ambient noise.

Preliminary simulations were conducted to consider the feasibility of future applications. There is potential to utilise the changes in the dominant frequency and PPV of the seismic signal as it propagates to locate voids and other subsurface features at depth. Future work will have to be conducted to determine subsurface feature location capabilities.

Numerical simulations and pilot field trials demonstrate that this novel concept can be applied effectively achieving sub metre scale accuracy for a site with specific material properties and metre scale accuracy for site characterised by high ambient noise. These results are significant in forming the theoretical basis for the development of a novel microseismic site investigation tool.

ACKNOWLEDGEMENTS

Firstly, I would like to thank Dr Stella Pytharouli and Professor Becky Lunn for providing me with opportunity to do this PhD. Thank you both for all your advice, support and encouragement throughout my research. Both of you have been tremendous mentors for me. I would like to thank you for encouraging my research and for allowing me to grow as a research scientist and engineer. Your advice on research as well as my career has been invaluable.

I appreciate your contributions of time and ideas to make my Ph.D. experience productive and stimulating. The joy and enthusiasm you both have for your research was contagious and motivational for me, even during tough times in the Ph.D. pursuit. I am also thankful for the excellent example you both have provided as successful women engineers and researchers.

Thank you to EPSRC for funding this PhD project. Thank you also to the American Associate of Petroleum Geologists (AAPG), Scottish International Education Trust (SIET), Institution of Civil Engineers (ICE), American Geophysical Union (AGU) and European Geosciences Union (EGU) for providing funding for field work and conference attendance.

This thesis has would not have been possible without valuable and stimulating conversations with members of the Engineering Geosciences & Geomechanics (EGG) research group.

A special thanks to James Minto for going out of his way to help me with my "blind" tests. A special thank you to my field assistants Giulia and Megan for standing by me and withstanding the wonderful Scottish weather.

I would like to thank Neil, Sandra, Chris, Erica and Ian for being fantastic office mates.

Sincere thanks to my parents Carol and Phil for their unreserved love and encouragement throughout my life. Thank you to my sister Giuliana for her love, support and assisting with printing and all things grammatical. A special thanks to my uncle Gianfranco for your support and encouragement throughout my academic studies both as an undergraduate and as a research student.

My heartfelt thanks to my husband Brian for always encouraging me and supporting me in whatever I do, this PhD would not have been possible without your unconditional love, help and encouragement to "get on with it" and succeed in everything I do to the best of my ability.

LIST OF FIGURES

LIST OF TABLES

Abbreviation/ Symbol	Description	Units
A	Amplitude of Prescribed Velocity	-
CFL	Courant–Friedrichs–Lewy (CFL) condition is a necessary condition for convergence while solving certain partial differential equations	-
CFW	Central Feature Width	M
D	Elasticity Matrix	-
E	Youngs Modulus	Pascal
ε	Strain	-
f	Frequency	Hz
f Max	Maximum frequency present in the model that requires detection	Hz
FFT	Fast Fourier Transform	-
Fv	Sinusoidal Force (Prescribed Velocity)	m/s
G	Rigidity Modulus	Pascal
GPR	Ground Penetrating Radar	-
i	Time Increment number	-
K	Bulk Modulus	Pascal
L	Length	m
LNP	Lomb Normalised Perdiogram	-
N	Length of the time series	-
PPV	Peak Particle Velocity	m/s
s	Stress	N/m^2
t	Time	s
T	Period	s
$t_{critical}$	Critical Time Step	s
u	Displacement	m
ù	Velocity	m/s
ü	Acceleration	m/s^2
v	Poisson's Ratio	-
V_p	P wave velocity	m/s
V_p Max	Maximum P wave velocity defined in the model	m
V_s	S wave velocity	m/s
Δh	Height of Smallest Mesh Element	m
Δt	Time Increment	s
λ	Wavelength	m
λ and μ	Lame Parameters	-
Λu	Gradient of displacement	-
ρ	Density	kg/m^3
t_r	Record time length	-

THIS PAGE IS INTENTIONALLY LEFT BLANK

1   Introduction

The locations and properties of small fault zones, geological intrusions, voids, fractures and manmade subsurface infrastructure are of interest to industries involving:

- Radioactive Waste Disposal;
- Underground Mining;
- Carbon Capture and Storage; and
- Site Investigation.

They can act as barriers and conduits to fluid flow, contributing to loss of integrity in the subsurface rock mass e.g. sinkhole formation.

Imaging methods are limited by site conditions e.g. the resolution of Ground Penetrating Radar (GPR) is limited by the material properties of the subsurface. A near surface imaging concept that could overcome such limitations and at the same time be quick and simple to implement and analyse is desirable.

Minimal or no exposure of geological features in the field can result in difficulty in effectively detecting their presence and predicting their dimensions and locations. Existing near surface geophysical methods commonly used today for imaging the near surface are:

- ground-penetrating radar (GPR);
- electrical resistivity;
- high-frequency seismology, and
- magnetics.

This thesis focuses on the development of a novel approach to image the near surface based on finite element analysis and verifying the feasibility of the results with a pilot field trial.

In the last 25-30 years, near surface geophysics and the demand for novel geophysical tool concepts has grown rapidly. To highlight this point the number of publications in the Science Citation Index (www.isiknowledge.com) published between 1980–2014 containing the keyword "ground penetrating radar" in the title or abstract is detailed in Figure 1-1. GPR was chosen as the example variable as certain aspects of the GPR technology are comparable to the approach for near surface imaging developed in this thesis.
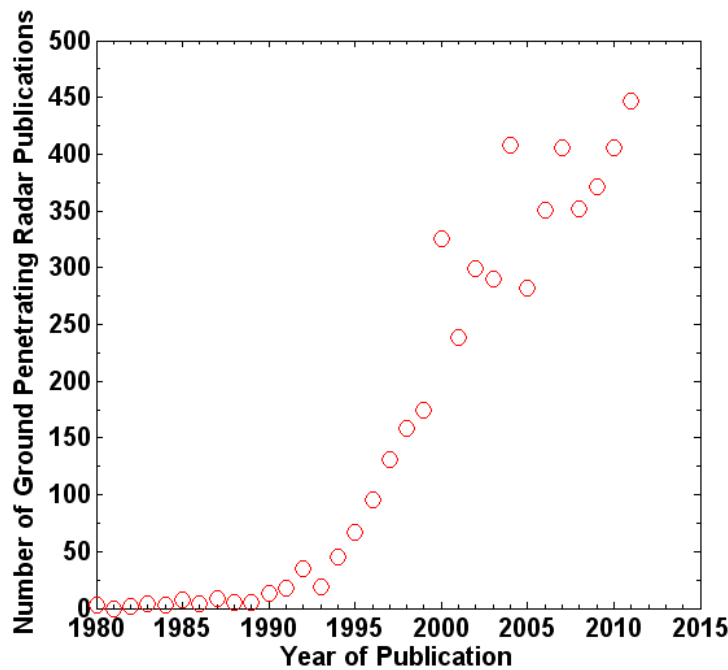
Figure 1-1: Numbers of papers in Science Citation Index between 1980 and 2010 with "ground penetrating radar" as keyword created from the Science Citation Index Database (www.isiknowledge.com).

Researchers have observed low frequencies when detecting geological features at depths greater than 100m. Sinha, Routh et al. (2005), show that the reduction in the frequency observations are probably caused by the attenuation of high frequency energy as a result of the signal passing through the geological feature at depth. Mitchell, Derzhi et al. (1997) and Dilay and Eastwood (1995) have shown previously that the dominant frequency observed moved towards the low frequency range (<100Hz), further demonstrating that the low frequencies are observed after the seismic signal has travelled through the geological feature. Ebrom (2004) suggested

that that low frequencies observed are probably not caused by inelastic attenuation but due to the medium being characterised by low characteristic attenuation factor (<5.0) and is therefore caused by the multiple reflections that take place as a result of geological feature presence. Marfurt (1984), investigated how the dominant frequency varies with geological feature thickness and Marfurt and Kirlin (2001) used this concept to resolve geological features with a thickness of <20m.

The gaps in knowledge in the low frequency observations identified above are outlined below:

- No study to demonstrate if the reduction in dominant frequency with geological feature thickness is observed in the near surface (i.e. depths less than 100m) at metre scale accuracy (i.e. <10m);
- No study has used micro seismometers to apply this technique for near surface applications; and
- No study which has considered if the dominant frequency and PPV characteristics can be used to develop a concept for a near surface site investigation tool deployed in the near surface.

The gaps in knowledge outlined above influence the researched questions which were developed for this thesis.

Therefore, the research presented in this thesis offers a novel approach for predicting the width and location of near surface features by mathematically modelling the propagation of seismic waves induced by a known source. There are two main categories of parameters considered that affect seismic wave propagation:

- Material properties of the sub-surface ; and
- Characteristics of the seismic source

The methodology followed for this thesis focuses on the generation, propagation and reception of mechanical waves and vibrations as they propagate through the

near subsurface. Specifically, the focus is the change in the seismic wave characteristics in terms of frequency and peak particle velocity (PPV) and using this change to create a useful relationship between these parameters and geological feature width which is a novel approach which further develops the research by Marfurt and Kirlin (2001) which shows that internal geological structures exhibit themselves as subtle variations in PPV rather than changes in seismic wave arrival times at depth. The originality of this work is the:

- creation of a useful relationship between the two seismic wave characteristics (dominant frequency and PPV) and geological feature width and location;
- application at the near surface using low frequency induced seismic sources; and
- monitoring of the seismic signals using short period seismometers.

The main argument of this thesis is by modelling these two seismic wave characteristics and mapping their changes as the seismic signal propagates, the novel concept for accurate subsurface feature detection and location tool can be developed. The conditions of the subsurface structure are varied. Computationally generated scenarios are developed and subsequently validated using "blind" simulations. Finally, with additional knowledge of the mechanical properties of a field site, a pilot field trial was used to test the feasibility of microseismics as a novel concept for a site investigation tool.

The aim of this work is not to fully develop a site investigation tool, but to provide a proof of concept for a novel approach. Further research could incorporate more complex subsurface features to characterise field sites with different material properties to those examined here.

1.1   Research Questions

The main question of this thesis is: Can we use seismic wave characteristics i.e. PPV and frequency, to effectively map and locate near surface geological and manmade structures?

Specifically the objectives to be investigated are:

1. Considering the effect of medium properties, is there a significant effect on seismic wave characteristics such as PPV and frequency when utilising low frequency seismic sources?

2. Considering the presence of a material property boundary, is there a significant effect on seismic wave characteristics and subsequently can that effect potentially be used to detect the presence and location of a subsurface feature?

3. Can the presence of a subsurface feature surrounded by a low velocity zone be detected numerically at metre scale accuracy and if so, can this concept be validated in pilot field trials?

1.2   Research Approach

Figure 1-2 shows the research approach consisting of six phases, on which this thesis structure is based. A brief outline of each of the six phases is presented below.

Phase 1: Established the theoretical foundations of this thesis. The research questions, approach and outline were defined. The current geophysical technologies used in near surface site investigations and associated theories were explored. As short period seismometers were the focal equipment available for this thesis, the basic concepts and theory are defined laying down the foundations for subsequently exploring and presenting the numerical modelling and spectral analysis theory.

Phase 2: Mechanical model development using finite element software COMSOL Multiphysics, describing the propagation of a mechanical wave from a point source in a single medium, based on seismic wave propagation theory. Mat Lab was used for spectral analysis. The model was compared against benchmark parameters which govern wave propagation models and then refined based on adequate convergence being achieved in the sensitivity analysis. The consideration of different material properties prompted further research in Phase 3.

Phase 3: Model was used to answer questions 1 and 2 outlined in Section 1.1, page 5. The model was initially applied to simulate the effect of medium properties on seismic wave propagation considering a single material medium followed by the presence of a single geological boundary. This led on to Phase 4 and the simulation of a subsurface structure surrounded by a low velocity zone.

Phase 4: Imaging concept for a new near surface site investigation tool was developed considering target geological features. A code was developed in order to create a concept for a near surface geophysical tool that can predict the presence

and location of a subsurface feature. This imaging concept was applied to numerical results and the feasibility of the concept was verified via "blind" tests.

Phase 5: Imaging concept applied and validated in a pilot field trial and used to answer question 3 outlined in Section 1.1, page 5. The results in Phase 5 implied that this concept could be applied to different subsurface scenarios. Preliminary subsurface features simulated in Phase 6 further evidenced this idea.

Phase 6: Explores the effect of noise which is important in terms of resolution and applicability of the method. This was investigated by adding noise to the sensitivity analysis. Phase 6 also considers potential future applications for this imaging concept, supported with preliminary simulations. The key findings, and conclusions identified in this thesis are presented.
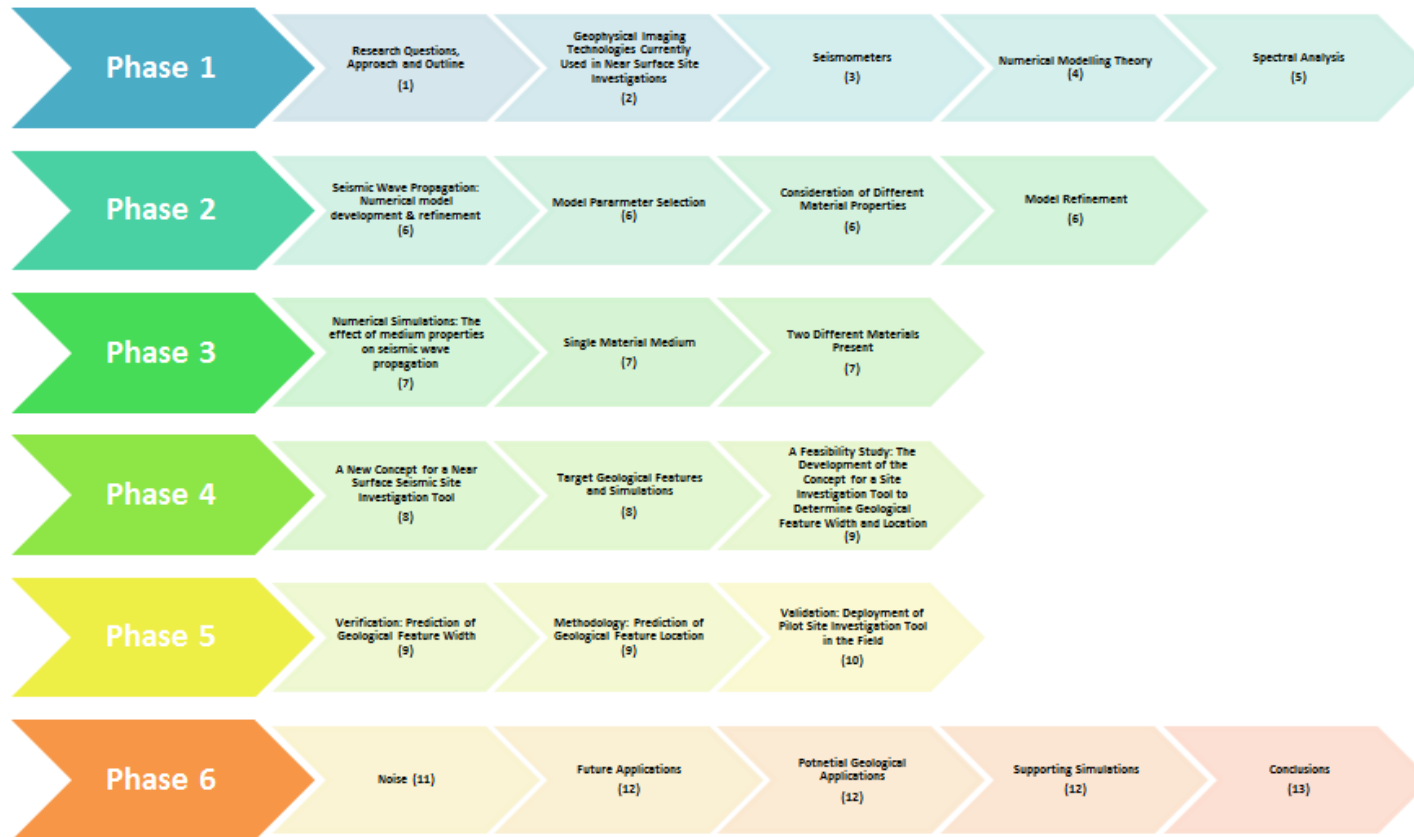
Figure 1-2: Symbolic representation of the route taken in completing the research for this PhD. The number in brackets denotes the thesis chapter that each phase is described in.

2   Geophysical Imaging Technologies Currently Used in Near Surface Site Investigations

Geophysical technologies are used for many different applications. The specific problem that this thesis addresses is the use of geophysical methods to detect and locate small geological features in the shallow subsurface at a scale of a few tens of meters. This field of study is closely linked to applied geophysics and exploration geophysics. There are several different conventional methods currently used today to image the subsurface including seismic refraction and reflection, gravity, magnetic, electric, and electromagnetic methods. In recent years, the energy industry required the development of seismic reflection methods for oil and gas exploration but many of the near surface geophysical methods can also be applied to a wide variety of industries including, environmental science, forensic science, military intelligence, geotechnical investigation, and hydrogeology (Desai 2011).

In this review the following is discussed:

1. The methods used for the detection of fault zones and underground voids, subsurface features which are a challenge in the mining industry, and in the construction of geological storage repositories;

2. A selection of the surface geophysical technologies, briefly outlining their fundamental concepts, advantages and limitations; and

3. Summarise explicitly the merits and drawbacks of the surface geophysical technologies presented comparing them to the specific problem focal to this thesis.

2.1 Near surface Geology – The Characterisation of Fault Zones and Underground Voids

2.1.1 Fault Zones

The detection of underground fault zones has been subject to extensive research particularly large scale faults in the region of hundreds of meters. At the Tournmire experimental platform (France), electrical resistivity has been applied effectively detecting low-resistivity discontinuities corresponding to a fault zone. The researchers tested the efficiency of electrical resistivity to detect secondary faults (in the region of hundreds of meters) in clay–rock intersected by a tunnel. Seismic methods were unsuccessful due to the weak contrast in material properties between the clay and rock layers and the small vertical offset of sub-vertical fault zones (Gautschi 2001). Seismic methods have been shown to be successful in detecting profiles up to 100m but are very limited in the shallow subsurface as is the electrical resistivity method (Wust-Bloch 2010). Magnetics have not been used for detecting subsurface fault zones due to a lack of magnetic minerals in such geological features. GPR has been successfully used in the detection of active fault zones (approximately 23m with detection of 2-3m damaged zones) in the shallow subsurface (Wust-Bloch 2010), but the method can be subject to precision, interference, or depth limitations in non-optimal conditions.

Small fault zones (4m) are generally considered to be too small to be detected by geophysical imaging (Pine, Coggan et al. 2006). This kind of faulting can play a tremendous role in loss of integrity of reservoir and cap rock systems in the cases of geological radioactive waste disposal and CO_2 storage. The need for a method that can detect geological features at such scales without limitations due to site conditions is necessary.

2.1.2   **Underground Voids**

The detection of underground voids such as sink holes or old mine workings is a concern, particularly in recent years in the UK due to increased rainfall making the occurrence of these undetected voids more common (Kumar 2015, Muchan, Lewis et al. 2015). There are many geophysical methods that are considered applicable to detecting underground voids, but they do have associated limitations. Gravity methods have been successful in detecting cavities at depths up to 15m. Cavities result in relative gravitational lows, however resolution is limited by topographical variations (Joswig 2008). Seismic measurements delineate reflections and refractions of pressure (P) or shear (S) waves off subsurface layers with contrasting material properties resulting in a strong reflection off of a cavity boundary (Lowrie and Swiss Federal Institute of Technology 2007, McLaskey and Glaser 2009). Electromagnetic and electrical methods measure changes in resistivity, successfully detecting sinkholes (Joswig 2008). Cavities alter the electrical resistivity of the subsurface. Voids in coal mines are usually encountered as resistivity lows because they are filled with acidic mine water (Lowrie and Technology 2007), therefore if mine water is not present within the void, detection is limited. Other methods, such as magnetics and GPR have been used for detecting subsurface cavities (Elmo and Stead 2010), but can be subject to precision, interference, or depth limitations which limit their use in mining applications and sink hole detection. The electrical resistivity method offers the greatest potential for the rapid mapping of mine workings at a depth of 30m or less. For cavities at a depth of 30m or greater, the seismic reflection method, especially with the use of S waves, has the greatest potential for success (Musset and Khan 2007).

2.2 Geophysical Imaging Technologies: Fundamental Concepts, Advantages and Limitations

2.2.1 Ground Penetrating Radar

2.2.1.1 Fundamentals

The GPR technique has been applied to a variety of near surface civil engineering, ground water analysis and contaminated land problems (Grandjean, Gourry et al. (2000), Takeshita, Kobayashi et al. (2004), and .Cassidy (2007)).

The GPR method uses a transmitter that emits a pulse of high frequency electromagnetic waves into the subsurface. The transmitter is either moved at fixed intervals or moved slowly at a constant pace across the ground surface. The electromagnetic waves penetrate into the subsurface and are scattered when changes in the complex dielectric permittivity of subsurface are located. The dielectric permittivity of the subsurface is primarily dependent upon the bulk density, clay content and the water content (Benson 1995). The electromagnetic energy is reflected back to the receiver at the ground surface where the antenna records the transient signal.

The depth penetration of the GPR method is limited by the attenuation and absorption of the transmitted electromagnetic signal in the subsurface and the wavelength of the propagating electromagnetic wave (Olhoeft 1999). Depth of investigations are less than 1 meter in mineralogical clay soils (montmorillonite) (Benson 1995). The depth achieved in the investigation increases with decreasing frequency however, the resolution decreases. Typical depths of investigation in fresh-water saturated, clay-free sands are about 30 meters. The optimum conditions for near surface GPR is dry sandy soil where the water table is located at depth (Benson, Glaccum et al. 1984).

Depths of investigation (and resolution) are controlled by electrical properties through conduction losses, dielectric relaxation in water, electrochemical reactions at the mineralogical clay-water interface, scattering losses, and magnetic relaxation losses (iron bearing minerals) Olhoeft (1999).

The output produced by the GPR method is comparable to a seismic reflection profile i.e. the horizontal axis represents distance along the GPR cross section and the vertical axis represents time. The GPR plot should not be mistaken for a geological cross section which represents data as horizontal distance versus depth.

Under optimum conditions GPR can detect changes in the soil profile, fractures in bedrock, water insoluble contamination, geological features, buried objects, voids, and hydrological features in the near surface.

2.2.1.2 Advantages

The majority of GPR systems permit a continuous display of data along the cross section which can be interpreted on site. GPR is capable of producing high resolution data, approximately 0.1m under optimal conditions Bradford, Ramaswami et al. (1996).

2.2.1.3 Limitations

GPR is resolution limited by the material properties of the site. Another limitation is the cost of site preparation which can cost an average of £1200 per day SANDBERG_GPR (2014) . The majority of GPR systems are towed across the surface in order to achieve the constant movement across the site. To increase the accuracy of the data collection the site has to be flat, dry and clear of any debris which could affect signal penetration. The quality of the data collection can be reduced by several factors such as an uneven ground surface and various noise sources such as the presence of a strong electromagnetic field.

There is limited knowledge of the link between the subsurface dielectric properties (GPR data) and the material properties (porosity and permeability). This is an essential component when imaging the spatial variation in the material properties of the subsurface (Romig 2000).

2.2.2 Magnetics (Potential Field Method)

2.2.2.1 Fundamentals

A magnetometer measures the magnetic field strength in the units of gammas or nanoteslas. Changes or irregularities of the earth's magnetic field are the result of turbulence caused by changes in concentrations of ferromagnetic material within the detection range of the magnetometer. Studies by Barrows and Rocchio (1990), Marchetti, Chiappini et al. (1998) and Rezos, Schultz et al. (2011) have shown that buried ferrous objects e.g. metallic objects, steel drums and firearms in the vicinity of the magnetometer change the earth's magnetic field causing a magnetic irregularity. A magnetic survey aims to map these irregularities and define the location of the buried object. Both magnetic and gravity (Section 2.2.3) methods are based on potential field theory and the fundamentals are explained in detail by Blakely (1996) and Hinze, von Frese et al. (2013).

The analysis of magnetic data can estimate the location of buried ferrous objects such as a steel tank, drum or pipe. An estimation of the depth of the buried object can be produced from the data. These estimates are based on graphical techniques (Nettleton 1971). The accuracy of these approximations is dependent on the quality of the data and the experience of the analyst.

The magnetic method can also be applied in order to map geological features (Kane, Harwood et al. 1971) e.g. igneous intrusions and geological structure which play an important role in the hydrogeology of a site (Romig 2000).

2.2.2.2   Advantages

The magnetic method is associated with a relatively low cost when compared to other geophysical techniques and the survey time is short. There is very little site preparation required. The surveying requirements are not as prescribed as other methods and it can be an efficient way of characterising a site suspected to contain buried steel objects such, as pipes. The magnetic method has been optimal in laterally detecting objects in the region of 20m to 100m (Oldenburg and Pratt 2007).

2.2.2.3   Limitations

Noise is one of the main limitations. Man-made structures which contain ferrous material for example steel have an unfavourable effect on data quality. There are several features that should be avoided, such as steel structures, power lines, metal fences, steel reinforced concrete, surface metal and underground utility pipelines.

The magnetic method has an inability to detect the difference between various steel objects. For example, it is not possible to detect if an irregularity is the consequence of a group of steel tanks or old tumble dryers, therefore the contents of a buried object cannot be defined. If the objects are not located along the surveying line they will not be detected, profiles are only produced along the surveying line and not over an area.   In order to gain adequate resolution sophisticated post processing techniques are required (Telford and Sheriff 1990, Burger 1992).

2.2.3   Gravity Method (Potential Field Method)

2.2.3.1   Fundamentals

The gravity method involves measuring the acceleration due to the earth's gravitational field. A gravity meter measures variations in the earth's true

gravitational field at the specified field site. These variations are directly dependent on variations in subsurface density at the specified field site which are generally small and uniform. Gravity meters have to be extremely sensitive, the unit of measurement is the milligal, and the acceleration caused by the earth's gravitational field is 900,000 milligal. The average sensitivity of a gravity meter is 0.01 milligal, allowing a detection of 1 part per 100million of the earth's gravitational field (Reynolds 2011). The fundamentals are explained by Blakely (1996) and Hinze, von Frese et al. (2013). The gravity method has been shown to be useful in the detection of buried valleys, bedrock topography, geological features and voids in the subsurface (Carmichael and Henry Jr 1977, Butler 1984). A study by Roberts, Hinze et al. (1990) detected density changes within a landfill site in the United States.

2.2.3.2   **Advantages**

An advantage of using the gravity method for site characterisation is that the gravity signals are not prone to noise contamination. The system can be deployed and data can be acquired in urban environments. The main sources of noise contamination that can negatively affect gravity studies are vibrations from traffic, mechanical equipment such as generators, low flying planes (Hinze, von Frese et al. 2013). Natural noise from the sea and wind can cause reduced data quality. Gravity surveys can acquire data in many locations including indoors.

2.2.3.3   **Limitations**

A disadvantage of gravity studies is that each receiver requires an accurate elevation and latitude survey. This can be time consuming and costly particularly for large survey areas. The accuracy of the survey data directly affects the quality and resolution of the gravity survey.

The method is computationally demanding due to the reduction and interpretation of the acquired data. The density contrasts of the subsurface are required prior to

conducting the survey and this is one of the main error contributors. The determination of density is based on rocks that are accessible at the surface where the rocks may be dehydrated, weathered, or from boreholes which can cause the rock to be susceptible to stress relaxation and cracking which would not be present in-situ (Reynolds 2011).

Due to the sensitivity of gravity meters the effect of uncompensated temperature, seasonal variations in the earth's gravitational field and tidal effects cause irregularities in gravity meter readings over time. These temporal variations must be accounted for in post processing (Hinze, von Frese et al. 2013). Certain frequencies of mechanical vibrations can affect the quality and resolution (Romig 2000). For engineering and environmental applications, the scale of the problem is generally small. Targets are often from 1 to 10m in size (Wightman, Jalinoos et al. 2004).

2.2.4   Electrical Resistivity

2.2.4.1   Fundamentals

The electrical resistivity technique is used to map the subsurface electrical resistivity structure. The data is interpreted by geophysicists to analyse the geological structure and the physical properties of the subsurface. The unit of measurement is ohmmeters, which is derived from the porosity, permeability, water content and concentration of dissolved solids in the pore fluids of the subsurface.

Electrical resistivity methods measure the bulk resistivity of the subsurface, similar to electromagnetic methods (Section 2.2.5). The difference between these two techniques is the method in which the electrical currents propagate into the subsurface. In the electrical resistivity method, the current is injected into the subsurface through electrodes, unlike electromagnetic methods where the current is induced by time varying electromagnetic fields. The potential detection depth of electrical resistivity investigations increases with electrode separation.

Mapping small fluid flows associated with cracks in contaminant containment barriers are too small to be observed, however significant fluid flow has been successfully monitored and modelled using electrical resistivity (Romig 2000).

2.2.4.2 Advantages

An advantage of electrical resistivity is that quantitative modelling can be carried out using post processing software, providing accurate depth, thickness and resistivity characteristics of the near surface. It has a relatively low cost.

2.2.4.3 Limitations

Electrical resistivity can be limited by the site characteristics, rather than limitations of the technique itself. Carpenter, Calkin et al. (1991) demonstrated the limitations of variable site characteristics, which resulted in the inadequate assessment of a fractured landfill cover using electrical resistivity.

When sites are located in urban or industrial areas, there is electrical noise which reduces quality and resolution of the measured voltage. Mineral grains found in crystalline rocks are essentially nonconductive, except in some materials such as metallic ores. The resistivity of soils and rocks is governed primarily by the amount of pore water and the arrangement of the pores. Therefore, applying electrical resistivity on crystalline rock can be challenging due to the lack of conductivity. Borehole methods can be used to increase conductivity but this is invasive and costly (Section 2.2.7). Conditions must be favourable for underground anomalies to be detected i.e. large differences in chemical concentration (Romig 2000).

Electrical resistivity surveys require a relatively large area which is situated a considerable distance from power cables and metal structures e.g. railway tracks, pipelines and electric fences to be conducted successfully which can limit the application of electrical resistivity in industrial environments. It is a labour intensive technique, with a minimum of 3 people required to conduct the survey. Research

has shown that resistivity method has demonstrated good resolution in resolving bed thickness greater than approximately 3m. Bed thickness less than 2m has a resolution accuracy of between 0.3m-2.7m depending on the material properties of the subsurface (Yin 2011).

2.2.5 Electromagnetic Method

2.2.5.1 Fundamentals

The electromagnetic method is based on the physical principles of inducing and detecting electrical current within the geological structure of the subsurface.

This method should not be confused with electrical resistivity or magnetics as explained in (Section 2.2.4). Electromagnetic readings are displayed using conductivity units of millimhos/meter. A mho is the inverse of an ohm. Electromagnetic methods can be used to detect pipes, utility cables, buried metal objects and contaminant plumes. The method can also detect shallow geological features such as clay layers and fault zones (Romig 2000).

2.2.5.2 Advantages

This electromagnetic equipment is light and portable and the readings can be obtained quickly with very few people required. This method is a commonly applied technique in ground water contamination surveys.

2.2.5.3 Limitations

Noise contamination caused by the presence of large metal objects, buried cables, buried pipes, buildings and metal enclosures will disguise the faint response generated by the presence of geological features. A review of noise contamination sources is presented by Munkholm and Auken (1996). Lateral changes in the structural geology can result in irregularities in the conductivity which can lead to misidentification e.g. a contaminant plume. The resolution of the method is low in

comparison to GPR and seismic methods. Techniques are generally limited in penetration depth of approximately 200m. The method has been shown to detect a 55-gallon drum at a depth of over 3m beneath the instrument. The resolution attainable is normally considered as a percentage of penetration depth, such that absolute resolution decreases with depth (Nekut and Spies 1989).

2.2.6   Seismic Imaging Methods

Seismic imaging methods are traditionally restricted to active seismics (seismic refraction and reflection methods) and passive seismics (seismic interferometry and microseismic imaging). The equipment that is deployed for both methods is basically the same and both these techniques measure the travel time of acoustic waves propagating through the earths subsurface. In refraction, the travel time of the waves refracted along an interface is measured. In reflection, the travel time of the wave which reflects off of an interface (geological boundary) is measured.

2.2.6.1   Seismic refraction

Seismic refraction is commonly applied when the depth to bedrock is less than approximately 150m below the ground surface. Seismic refraction is defined as the travel path of an acoustic wave produced from an active source through an upper medium and along an interface then back to the surface. A detailed presentation of seismic refraction can be found in (Dobrin and Savit 1960, Knox, Musgrave et al. 1967, Telford and Sheriff 1990).

2.2.6.1.1 Advantages

The P and S wave velocity of the subsurface can be determined using seismic refraction. Accurate depth to geological boundaries can also be determined.

Seismic refraction surveys produce depth information at locations that are between boreholes. Subsurface information can be gained in an economic way without the

requirement to drill. Data can be used to calculate the depth to bedrock, thickness of overburden and water table location (Ewing, Woollard et al. 1939).

The velocity information obtained can be related to the bedrock physical properties. Rock types are characterised by a range of seismic velocities and these are not specific and unique to certain rocks. For example dolomites and granites have similar seismic velocities (Carmichael 1988). Where there is a material property contrast the method can differentiate between the materials e.g. a clay and granite.

2.2.6.1.2 Limitations

To image the subsurface using the refraction method the geological environment must adopt the following assumptions:

1. the seismic velocities of the geological layers increase with depth;
2. the seismic velocity contrast between the layers is large enough to resolve the layers;
3. the geometry of the seismic array with relation to refracting layers will allow the detection of thin geological beds; and
4. the dip of the layers is less than 10-15 degrees (Romig 2000).

If these conditions are not fulfilled then accurate depth information cannot be obtained. Seismic refraction produces simplified topography models. A resolution of approximately 1m has been achieved at approximately 20m depth (Watanabe, Matsuoka et al. 1999) .

The collection processes can be resource intensive. Large cable lengths are required to fulfil the refraction criteria: distance from the seismic source to the seismic sensors must be at least 3 times the target depth of the seismic survey.

2.2.6.2   Seismic Reflection

In seismic reflection the sound wave produced from an active source travels down to a geological boundary and reflects back to the sensors at the ground surface. Reflections take place when there is a contrast in the acoustic properties within the subsurface.

2.2.6.2.1 Advantages

The seismic reflection technique allows geophysicists to detect discrete geological boundaries. The reflection method has been successfully applied in stratigraphy mapping. The reflection data is generally presented as a reflection profile of the subsurface and the depths to geological boundaries are presented as a function of time (Griffiths and King 1981).

Depth information can be achieved by converting time sections into depth from seismic velocities that are obtained using seismic refraction methods outlined in Section 2.2.6.1, sonic logs or velocity logs (Koppe, Gambin et al. 2005).

The reflection surveys do not require as much physical space as refraction surveys. The long offset of the seismic source from the sensors is not required in reflection surveys. In optimum conditions reflection surveys can produce acceptable depth estimates. The method is not dependent on the assumption that the velocity structure of the subsurface increases with depth. Seismic reflection methods have been successfully applied detecting buried objects and concrete pipes at depths ranging from approximately 0.5m up to 1m (Nye 1985, Knight 2008).

2.2.6.2.2 Limitations

The main limitation is that precise depth location cannot be determined. Velocities which are produced from most reflection data are 10 − 20% of the true seismic subsurface velocity (Koppe, Gambin et al. 2005). The post processing of reflection

data requires a qualitative approach. The acquisition of reflection data is more complex than refraction data.

Resolution is dependent on the capabilities of the seismic equipment. Reflection data has been used in many surveys for petroleum exploration in the oil and gas industry and requires long survey times and lengthy data acquisition methods, it is resource intensive. Data has to be converted into a digital format to carry out analysis. There is a high demand on computational resources for data acquisition and post processing in order to achieve a seismic resolution that is acceptable. The resolution of the data is dependent on the skill of the interpreter and the site being characterised by optimum conditions (Koppe, Gambin et al. 2005). In site investigations water-filled cavities responsible for sinkholes in a 0.6 m thick coal seam at 7 m depth have been effectively detected (Miller and Steeples 1991).

2.2.6.3   Seismic Interferometry

Seismic interferometry utilises the seismic wave produced from passive sources, more commonly known in the geophysics industry as noise. Interferometry examines the general interference between pairs of signals in order to gain useful information about the subsurface. Seismic interferometry utilises the cross-correlation of signal pairs to reconstruct the impulse response of the subsurface. The cross-correlation of passive noise measured at the surface reproduces the subsurface impulse response. It is possible to obtain information about the subsurface with no need for an active seismic source.

In the early of 2000s, the field of seismic interferometry was beginning to change the way geophysicists view noise. Seismic interferometry uses this previously ignored noise in models of the shallow subsurface and the fundamental theory is explained in detail by Schuster (2008). Potential applications for seismic interferometry include both research and industry.

2.2.6.3.1 Advantages

Since passive seismic interferometry relies on the geometry of seismic receiver locations only, and requires no impulsive sources like earthquakes in order to obtain useful seismograms, the technique is useful in areas which are virtually seismically inactive, for example within the British Isles. The first surface wave group velocity maps of the Scottish Highlands from ambient seismic noise produced by Nicolson, Curtis et al. (2012) shows useful information about the crust and upper mantle that is consistent with geological features of the region.

2.2.6.3.2 Limitations

Seismic interferometry is currently limited by a number of factors. Real world operations and noise contaminating the signal represent limitations for current theoretical development. In addition, attenuation and geometrical spreading are largely neglected and need to be incorporated into more robust models. Velocity analysis and filtering can reduce but not eliminate the occurrence of interference from other noise sources.

One of the biggest remaining challenges is extending the theory to account for real world media and noise sources in the subsurface. Natural sources typically do not comply with mathematical models. Additional problems must be addressed before applications of seismic interferometry can become more widespread (Wapenaar, Draganov et al. 2008).

In the exploration for hydrocarbons the maximum imaging depth using seismic interferometry is approximately 4km to 5km, the horizontal dimensions are approximately 20km by 20km and the vertical resolution is in the order of 40 m. A major limitation of this method is logistics and cost (ASTRON 2015).

2.2.6.4   **Microseismics**

Microseismic monitoring is the passive observation of very small-scale earthquakes which occur in the ground as a result of human activities or industrial processes such as mining, hydraulic fracturing, enhanced oil recovery, geothermal operations or underground gas storage. Microseismic monitoring grew out of earthquake seismology and focuses on micro-earthquakes (i.e. magnitude less than 3) (Kamei, Nakata et al. 2015). Some micro-earthquakes can be too small to be felt on the surface, but they can be detected by sensitive equipment such as geophones and accelerometers.

Currently, microseismic monitoring is performed to monitor hydraulic fracturing in unconventional reservoirs (Warpinski, Wolhart et al. 2001, Zoback, Kohli et al. 2012, Hakso, Zoback et al. 2015). It is also used for monitoring CO_2 sequestration (Kühn, Albaric et al. 2014, Kaven, Hickman et al. 2015), active fault mapping (Jeanne, Rutqvist et al. 2014) and the stability of mineshafts and boreholes (Abdellah, Mitri et al. 2014), as well as being evaluated as a tool for monitoring the dewatering of coal bed methane reservoirs (Ren, Zhang et al. 2014).

Researchers have observed low frequencies when detecting geological features at depths greater than 100m. Sinha, Routh et al. (2005), show that the low frequency observations are probably caused by the attenuation of high frequency energy as a result of the signal passing through the geological feature at depth. Mitchell, Derzhi et al. (1997) and Dilay and Eastwood (1995) have shown previously that the dominant frequency observed moved towards the low frequency range (<100Hz), further demonstrating that the low frequencies are observed after the seismic signal has travelled through the geological feature. Ebrom (2004) suggested that that low frequencies observed are probably not caused by inelastic attenuation but due to the medium being characterised by low characteristic attenuation factor (<5.0) and is therefore caused by the multiple reflections that take place as a result of geological feature presence. Marfurt (1984), investigated how the dominant

frequency varies with geological feature thickness and Marfurt and Kirlin (2001) used this concept to resolve geological features with a thickness of <20m.

The gaps in knowledge in the low frequency observations identified above are outlined in Section 1 and influence the research questions explored in this thesis.

2.2.6.5   **Advantages**

Microseismic monitoring allows real-time monitoring of the fracture processes in subsurface rock allowing effective geological feature location at depth (Pytharouli, Lunn et al. 2011). Interpreted microseismic data is also used to calibrate and validate geomechanical models and to provide a more detailed understanding of the stress and fracture characteristics associated with the mechanics of hydrocarbon flow in reservoirs. The advantage of surface arrays over downhole arrays is that surveys can be acquired where there is no well available for downhole deployment. In comparison to other methods the deployment costs are relatively low.

2.2.6.5.1 **Limitations**

Microseismic monitoring resolution is limited by the material properties of the site being surveyed (Hardy 2005). To increase the accuracy of the data collection the sensors have to be levelled on a surface that is dry and clear of any debris as this could affect signal detection. The level surface would ideally be hard rock to enhance sensor coupling with the ground surface. The quality of the data collection can be reduced by various noise sources e.g. the presence of a strong ambient noise such as vibration from water flowing through pipes.

The resolution of microseismics depends on the wavelength of the seismic signal i.e. smaller wavelength/higher frequency signals are more easily detected but are greatly affected by attenuation. Detection is better when the signal propagates

through rock characterised by a high P wave velocity, where the effects of attenuation are less (Stein and Wysession 2009).

Pytharouli, Lunn et al. (2011), have shown that microseismic monitoring can resolve the three-dimensional structure and hydraulic characteristics of flowing fractures at 2 to 3 km depth.

2.2.7   Borehole Geophysical Methods

2.2.7.1   Fundamentals

There are various borehole probes and tools that can be used to obtain information. Most borehole methods are derived from the same principles as surface geophysical methods. Two most commonly deployed methods are natural gamma ray logs and resistivity logs (Ellis and Singer 2007).

2.2.7.2   Advantages

Borehole logs provide a wealth of information on the earth's subsurface (Schürch and Buckley 2002). Information on the stratigraphy, hydrogeology and contamination of a site can be obtained.

2.2.7.3   Limitations

The main limitation is cost. In addition, borehole information is only descriptive of the subsurface for a limited radius surrounding the borehole well approximately 0.3 – 0.9m (Romig 2000). If there is a variation in the subsurface conditions between boreholes, irregularities may have to be qualitatively evaluated. Some tools may have to be used in unlined or saline filled boreholes i.e. certain borehole tools require specific logging conditions for accurate results.

2.2.8 **Summary**

Table 2-1 presents a summary of all the considered methodologies.

Table 2-1: Different surface geophysical methods considered and the potential applications.

Indication of Geophysical Method Effectiveness P = Extremely Effective S = Very Effective O = Effective N= Potentially Effective Grey Box = NOT APPLICABLE	Dependant Material Property	Engineering Site Investigations	Hydrogeological Site Investigations	Detection of Subsurface Voids	Mapping Contamination Plumes	Buried Metal Objects	Buried Objects	Soil Profile Changes	Geological Features in Near Surface Crystalline Rock	Fractures in Bedrock	Resolution in Optimal Conditions
Geophysical Surface Method											
GPR	Permittivity, Conductivity	P	P	P	S	P	P	P	S	P	0.1m
Magnetics	Susceptibility	S		O		P	P		S		20m
Gravity	Density	S	S	S			S		S	S	1.0m
ERT	Resistivity	P	P	P	P	S	P	P		P	3.0m
Seismic Refraction	Elastic Moduli, Density	P	S	S						P	1.0m
Seismic Reflection	Elastic Moduli, Density	S	S	O			O			S	0.6m
Seismic Interferometry	Elastic Moduli, Density	S	S				O		O	S	40m
Microseismic Monitoring	Elastic Moduli, Density	S	S	S			O		O	P	Tens of meters. Dependant on the wavelength of seismic signal. Potentially between 3-10m

3   Seismometers

3.1   Introduction

This Chapter describes how seismometers work. A seismograph detects, amplifies, and records earthquakes as well as other ground motions. The word seismograph is often used synonymously with seismometer, but there is a distinction. The seismometer is the ground-motion detector which detects the seismic signal which is then post processed to create a seismograph or seismogram. In this Chapter the main points of the theory is presented. Textbooks by Grotzinger, Jordan et al. (2009) and Stein and Wysession (2009) present this theory in detail.

3.2   How Seismometers Work

A good way to describe how seismometers work is to start by understanding the seismograph. A seismograph is a geophysical representation which allows us to visualise the movement of the earth by means of a graph. A form of seismograph is a plot of PPV (ground velocity) vs time in a specific direction. A ground motion sensor (seismometer) which measures the velocity of the ground is combined with a recording system known as a data logger. The analogue signal produced by the seismometer and recorded by the data logger is converted into a digital format (post processed) and thus allows the seismograph to be produced (Figure 3-1).
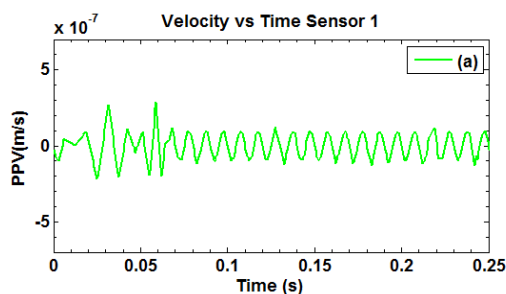
Figure 3-1: A seismograph as a plot of PPV (ground velocity) vs time

A seismometer which records the vertical motion of the earth is known as a 1D seismometer. This type of seismometer can be understood by visualising a weight hanging on a spring (Figure 3-2). The spring and the weight are suspended from a frame that moves in conjunction with the earth's surface. As the earth moves the relative motion between the weight and the frame gives a measure of the vertical motion of the earth. This motion is recorded as an analogue signal on the data logger. The data logger records the relative motion of the earth allowing history of the earth's ground motion to be recorded for a finite period of time thus producing a seismograph. The signal visualised on the seismograph must be converted into meaningful units e.g. ground velocity/PPV in meters per second (Alterman and Karal 1968).
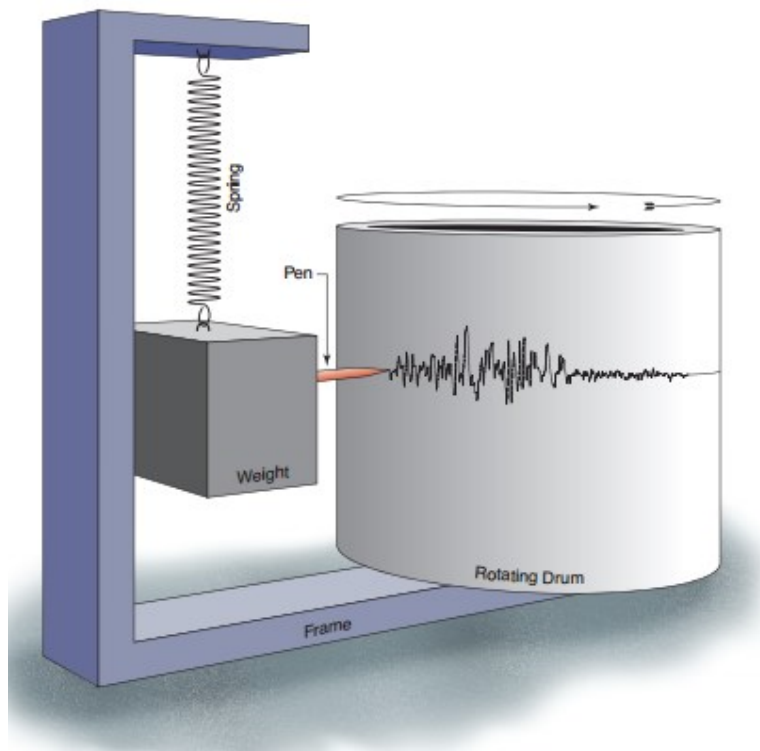
Figure 3-2 - Schematic detailing the basic scientific concepts of a seismometer. (Alterman and Karal 1968)

Seismographs are operationally based on the principle of inertia, in other words stationary objects such as a weight will remain stationary unless a force is applied to it.

The seismometers used in this thesis are electronic and are made up of a sensing coil suspended by a spring in an axial magnetic field provided by a small permanent magnet (Figure 3-3). Thus when shaken due to relative motion caused by an induced source such as the vibrations from a generator, the coil moves and interacts with the magnetic field producing an electric voltage that is recorded by the data logger and then converted into PPV (m/s) resulting from the vibrations. The arrangement of the coil, inertia mass, springs and magnet can be changed allowing the seismometer to record ground motion and thus PPV in all directions. This type of seismometer is known as a 3D seismometer (Bolt and Smith 1976).
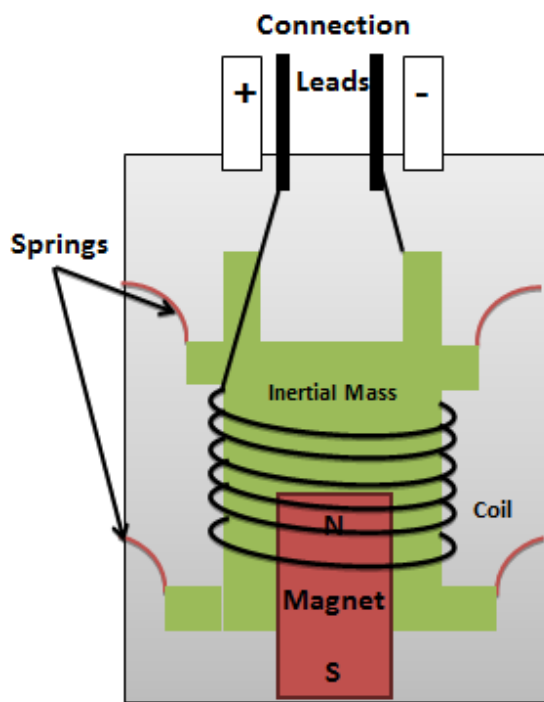
Figure 3-3: Schematic of the inside of a modern seismometer similar to the seismometers available for use in this thesis as detailed in Section 4.2.1. Adapted from (Dupuis, Butler et al. 2007)

3.3   Seismic Field Equipment

In this section the specifications of the equipment available for use in this thesis are presented: 1) seismometers used (Table 3-1), 2) data logger (Figure 3-4) and 3) seismic source/generator (Figure 3-5).

3.3.1   Seismometers

Two 1D seismometers were available for use as the PPV of interest was the vertical component. This has some advantages in that 1D seismometers are considerably cheaper than 3D seismometer which detects PPV in all directions (Lennartz_Electronic 2015).

The ground motion/PPV (velocity) detected by the seismometers presented in Table 3-1 is not proportional to the recorded signal when frequencies out with the range of 1-100Hz are present in the signal (Lennartz_Electronic 2015). Therefore, the frequencies out with the range of 1-100Hz can be detected by the seismometers but the corresponding amplitude of the ground motion (velocity) is not a true representation of the recorded signal.

Table 3-1: Lennartz Electronic GmbH Seismometer Technical Specification. (Lennartz_Electronic 2015)

1D Sensor	
Sensitivity	400V/m/s
Natural Frequency	1Hz
Upper Corner Frequency	Approx. 100Hz
Full Scale Output Voltage	± 5V
Damping	0.707 critical
Weight	0.9kg
Temperature Range	-15 …. +65°C
Supply Current @ 12V DC	3mA
Warm-up Time	30seconds

3.3.2   **Datalogger**

The datalogger used was a REFTEK RT130 (Figure 3-4). The data logger records the vibrations caused by the seismic signal in counts per volt. Therefore an analogue to digital conversion factor must be applied to convert the signal into PPV. The A/D conversion factor is 629,327 counts/volt, or 1.58997 µV/count. Equation 3-1 describes the A/D conversion to ground velocity:

Equation 3-1: IRIS and PASSCAL (2013)

$$\text{Ground Velocity } m/s = \frac{\text{Amplitude (counts)} * \text{A/D Conversion Factor (V/counts)}}{\text{Gain} * \text{Sensitivity } V/m/s}$$

Where:

Amplitude is the detected signal (counts)

A/D Conversion Factors is 1.58997µV/count

Gain is 1 or 32 and changes the sensitivity of the device. When the seismometer is set to high gain (32) it can detect much lower particle velocities than when set to low gain (1).

Sensitivity is 400 V/m/s (Lennartz_Electronic 2015)

Figure 3-4: REFTEK model RT130 Datalogger

3.3.3   **Seismic Source**

The seismic source available for use in this thesis was a Honda EU10i generator (Figure 3-5). The generator had a predefined operating frequency of 100Hz which was suitable for use with the seismometers (Honda 2002).

Figure 3-5: Seismic Source: Honda EU10i Generator (Honda 2002).

4   Numerical Modelling Theory

4.1   Introduction

This Chapter presents the numerical modelling theory applied in this thesis outlining the theory of wave propagation in elastic materials, subsequently demonstrating how the theory is applied in a numerical modelling context.

The aim is to use the theory of wave propagation in elastic materials to solve the forward modelling problem i.e. the estimation of seismic signals recorded at control points as the signal travels through a medium of known material properties. The inverse problem will then be considered i.e. the estimation and approximation of geological properties of the medium through which known recorded seismic signals travel.

There are several methods that can be implemented for modelling seismic wave propagation numerically which are capable of approximating the seismic signal considering elasticity, isotropy, anisotropy, and attenuation. The finite element method is a common approach, where the partial differential equations that govern the model are asked to be defined inside the elements present in the medium. The capabilities of the finite element method will be presented in the context of this thesis.

The Governing Equations and the COMSOL Multiphysics procedure will be benchmarked against the analytical solution for an elastic half space and is introduced formally within Section 6.2.2.

4.1.1   Governing Equations

4.1.1.1   Wave propagation in elastic materials

Linear elasticity is the theory that describes how solid objects such as rock deform and become internally stressed due to prescribed loading conditions (Jaeger and

Cook 1976, Pyrak-Nolte, Myer et al. 1990). Linear elasticity models materials as a continuous medium. To generate analytical solutions for rock mechanics problems, it is usually necessary to simplify the stress-strain behaviour. The fundamental "linearizing" assumptions of linear elasticity are: infinitesimal strains or "small" deformations (or strains) are exhibited as a linear relationship between the components of stress and strain. This assumption allows many complex engineering problems to be solved, such as the stresses around:

- tunnels;
- boreholes; and
- faults and fractures.

Although no rocks are linearly elastic over a wide range of stresses this approximation is often valuable and accurate since many rocks behave linearly for incremental changes in stress. The changes in stress that are caused by a tunnel excavation for example, are small throughout the majority of the region of the rock except in the immediate area of the excavation. Therefore, the theory of linearity is a sound approximation throughout the bulk of the rock mass (Jaeger and Cook 1976).

Three types of wave are generated by an impulse applied to a linear elastic material e.g. a solid rock mass:

1. Surface waves have an elliptical particle displacement and are the slowest travelling waves (Equation 4-3);

2. S waves are characterised by a particle displacement that is perpendicular to the wave propagation direction (Equation 4-2); and

3. P waves are characterised by a particle displacement in the direction of travel and travel the fastest (Equation 4-1).

The equations describing the P and S wave velocities are:

Equation 4-1

$$V_p == = \sqrt{\frac{K + \frac{4}{3}G}{\rho}}$$

Equation 4-2

$$V_s = \sqrt{\frac{G}{\rho}}$$

Equation 4-3

$$V_R/V_s = \frac{0.862 + 1.14v}{1 + v}$$

The wavelengths of these waves are defined as:

Equation 4-4

$$\lambda_P = \frac{V_P}{f} \ and \ \lambda_s = \frac{V_s}{f}$$

Where:

K is the Bulk Modulus

G is the Rigidity Modulus

λ is the wavelength of the wave

ρ is the density of the medium

v is the Poisson Ratio

f is the frequency of the wave.

P waves have a higher frequency on arrival than S waves and travel further (Jaeger and Cook 1976). As a result they can be detected at longer source to receiver distances and attenuate less compared to S waves. Equation 4-1 and Equation 4-2 show that the velocity of the wave depends on the elastic properties of the medium or rock mass.

The elastic properties of a medium often change with depth, due to the changing properties of the material. This means that the velocity of the wave becomes

dependent on the wavelength (and therefore frequency), a phenomenon referred to as dispersion (Stein and Wysession 2009).

In seismology P and S waves are termed as body waves. Rayleigh waves are generated by the interaction of P and S waves at the surface of the earth, and travel with a velocity that is lower than the P and S waves (Stein and Wysession 2009).

Rayleigh waves propagating in an ideal, homogeneous and flat elastic solids show no dispersion unless numerically, a dispersion coefficient is added (Multiphysics 2014). In the Earths subsurface density and P wave velocity increase with depth and therefore the Rayleigh waves become dispersive, which is what is observed in field observations (Stein. and Wysession 2003). Therefore, in order to effectively simulate Rayleigh waves in the field numerically the model must account for dispersion (Multiphysics 2014).

4.1.2   **COMSOL Multiphysics Procedure**

To model wave propagation problems in the time domain, the COMSOL Structural Mechanics Module and Solid Mechanics interface was used. This module was used to conduct a time dependent (transient) analysis in a linear elastic isotropic material domain. The transient analysis simulated a mechanical wave propagating as a result of a seismic source applied at the free surface. The seismic sources used in the numerical simulations in this thesis are comparable to the seismic source frequencies observed on an operational engineering site, e.g. a generator.

Explicit dynamic analysis in COMSOL Multiphysics is a direct time stepping method where a direct computation of the dependent variables can be made in terms of known quantities (e.g. PPV and time). It is based on the excitation of a point at the near surface due to the application of a sinusoidal force.

The numerical equations describe the motion and deformation of solid objects in 3-dimensional space. For the purpose of this thesis only the 2-dimensional components were simulated. The Solid Mechanics user interface has the equations

and functionality for stress analysis and general linear and nonlinear solid mechanics already built in for solving the resulting displacements. The linear elastic material is the default material, which adds a linear elastic equation for the displacements. The elastic material properties are defined by the user (COMSOLMultiphysics 2013).

The formulation used for structural analysis in COMSOL Multiphysics for both small and finite deformations is total Lagrangian. This means that the computed stress and deformation state is always referred to the material configuration i.e. the changes in material properties rather than the geometrical changes (COMSOLMultiphysics 2013).

The gradient of the displacement is always computed with respect to the material configuration, X, Y and Z:

Equation 4-5

$$\nabla \mathbf{u} = \begin{bmatrix} \dfrac{\partial u}{\partial X} & \dfrac{\partial u}{\partial Y} & \dfrac{\partial u}{\partial Z} \\[2mm] \dfrac{\partial v}{\partial X} & \dfrac{\partial v}{\partial Y} & \dfrac{\partial v}{\partial Z} \\[2mm] \dfrac{\partial w}{\partial X} & \dfrac{\partial w}{\partial Y} & \dfrac{\partial w}{\partial Z} \end{bmatrix}$$

In order to solve the model in COMSOL different pairs of elastic moduli can be defined, and as long as two moduli are defined, the others can be computed as defined in Table 4-1 . For the purpose of this thesis the P wave and S wave velocity values were defined.

Table 4-1: Expressions and Corresponding Variables Defining the Elastic Moduli in COMSOL (COMSOLMultiphysics 2013)

DESCRIPTION	VARIABLE	$D(E,v)$	$D(K,G)$	$D(\lambda,\mu)$
Young's modulus	E		$\dfrac{9KG}{3K+G}$	$\mu\dfrac{3\lambda+2\mu}{\lambda+\mu}$
Poisson's ratio	v		$\dfrac{1}{2}\left(1-\dfrac{3G}{3K+G}\right)$	$\dfrac{\lambda}{2(\lambda+\mu)}$
Bulk modulus	K	$\dfrac{E}{3(1-2v)}$		$\lambda+\dfrac{2\mu}{3}$
Shear modulus	G	$\dfrac{E}{2(1+v)}$		μ
Lamé parameter λ	λ	$\dfrac{Ev}{(1+v)(1-2v)}$	$K-\dfrac{2G}{3}$	
Lamé parameter μ	μ	$\dfrac{E}{2(1+v)}$	G	
Pressure-wave speed	c_p		$\sqrt{\dfrac{K+4G/3}{\rho}}$	
Shear-wave speed	c_s		$\sqrt{G/\rho}$	

Equation 4-1 and Equation 4-2

Using the equations presented in Table 4-1, for this thesis the elasticity matrix D for isotropic materials is written in terms of the bulk modulus K and shear modulus G:

Equation 4-6

$$D = \begin{bmatrix} K+\dfrac{4G}{3} & K-\dfrac{2G}{3} & K-\dfrac{2G}{3} & 0 & 0 & 0 \\ K-\dfrac{2G}{3} & K+\dfrac{4G}{3} & K-\dfrac{2G}{3} & 0 & 0 & 0 \\ K-\dfrac{2G}{3} & K-\dfrac{2G}{3} & K+\dfrac{4G}{3} & 0 & 0 & 0 \\ 0 & 0 & 0 & G & 0 & 0 \\ 0 & 0 & 0 & 0 & G & 0 \\ 0 & 0 & 0 & 0 & 0 & G \end{bmatrix}$$

The strain conditions at a point are completely defined by the deformation components (*u, v, and w*) and their derivatives (Equation 4-5).

The precise relationship between strain and deformation depends on the relative magnitude of the displacement. The normal strain components $\varepsilon_x, \varepsilon_y, \varepsilon_z$ and the shear strain components $\varepsilon_{xy}, \varepsilon_{yz}, \varepsilon_{xz}$ are related to the deformation components as follows:

Equation 4-7

$$\varepsilon_x = \frac{\partial u}{\partial x} \qquad \varepsilon_{xy} = \frac{\gamma_{xy}}{2} = \frac{1}{2}\left(\frac{\partial u}{\partial y} + \frac{\partial v}{\partial x}\right)$$

$$\varepsilon_y = \frac{\partial v}{\partial y} \qquad \varepsilon_{yz} = \frac{\gamma_{yz}}{2} = \frac{1}{2}\left(\frac{\partial v}{\partial z} + \frac{\partial w}{\partial y}\right)$$

$$\varepsilon_z = \frac{\partial w}{\partial z} \qquad \varepsilon_{xz} = \frac{\gamma_{xz}}{2} = \frac{1}{2}\left(\frac{\partial u}{\partial z} + \frac{\partial w}{\partial x}\right).$$

The symmetric strain tensor ε consists of both normal and shear strain components:

Equation 4-8

$$\varepsilon = \begin{bmatrix} \varepsilon_x & \varepsilon_{xy} & \varepsilon_{xz} \\ \varepsilon_{xy} & \varepsilon_y & \varepsilon_{yz} \\ \varepsilon_{xz} & \varepsilon_{yz} & \varepsilon_z \end{bmatrix}$$

The total strain tensor is written in terms of the displacement gradient ∇u:

Equation 4-9

$$\varepsilon = \frac{1}{2}(\nabla \mathbf{u} + \nabla \mathbf{u}^T)$$

Or in components:

Equation 4-10

$$\varepsilon_{mn} = \frac{1}{2}\left(\frac{\partial u_m}{\partial x_n} + \frac{\partial u_n}{\partial x_m}\right)$$

The Duhamel-Hooke's law relates the stress tensor to the strain tensor and temperature:

Equation 4-11

$$s = s_0 + C : (\varepsilon - \varepsilon_0 - \alpha\theta)$$

Where C is the 4th order elasticity tensor derived by Hooke's law for elastic media, ":" stands for the double-dot tensor product, s_0 and ε_0 are initial stresses and strains, $\theta = T - T_{ref}$, and α is the thermal expansion tensor (COMSOLMultiphysics

2013). For the purpose of thesis $\theta = 0$ and $\alpha = 0$, as temperature was not defined as an input parameter.

The following equation derived from the above theory is the governing equation for the time dependant model simulation:

Equation 4-12
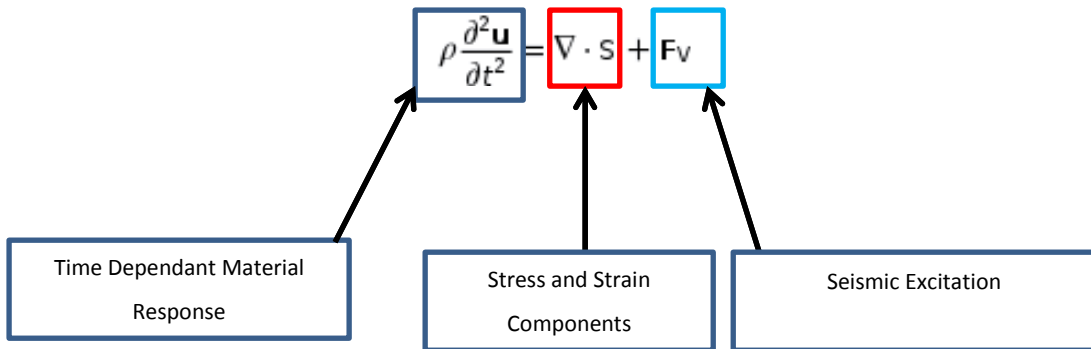
Wave propagation is initiated when the initial equilibrium is excited by the application of a sinusoidal force F_v. This force applied at a defined point (Section 4.2.2 pg. 47) in the model as a prescribed velocity (Figure 4-1), in other words the material particles within the model are excited at a velocity of 2 x 10^{-7} m/s (PPV), at a frequency of 100Hz for 2 seconds. Equation 4-13 is solved as a function of time.

Equation 4-13

$$Prescribed\ velocity = A * (sin2\pi ft)$$
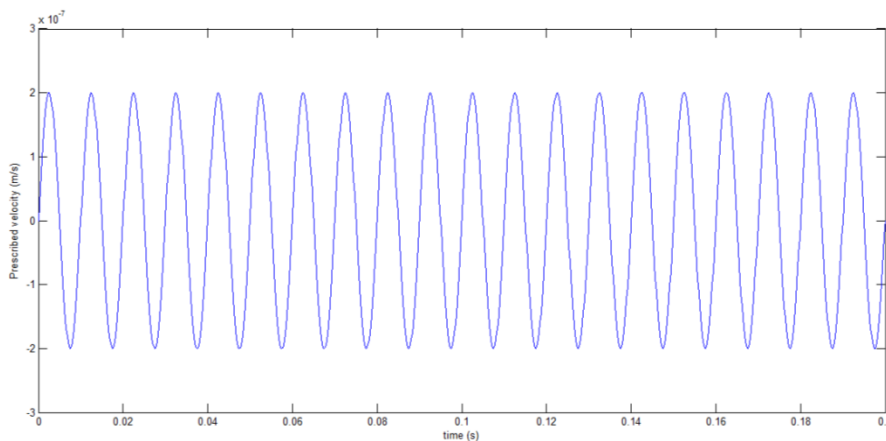
Figure 4-1: Prescribed velocity data extract from COMSOL. The sinusoidal force i.e. the seismic excitation which initiates wave propagation in the model

The displacement, velocity and acceleration of the material particles in the model are linked as follows:

Equation 4-14

$$\dot{u}^{(i+0.5)} = \dot{u}^{(i-0.5)} + \frac{\Delta t^{(i+1)} + \Delta t^{(i)}}{2} \ddot{u}^{(i)}$$

Equation 4-15

$$u^{(i+1)} = u^{(i)} + \Delta t^{(i+1)} \dot{u}^{(i+0.5)}$$

With, Δt the time increment and i, the time increment number demonstrating, that the simulation is computed using known values from the previous time step.

4.1.3   Time Step and Mesh

The numerical model is explicit because the simulation progresses using known values from the previous time step. This numerical method is stable providing certain conditions are met. These conditions are produced from the Courant–Friedrichs–Lewy (CFL) condition derived by Courant, Friedrichs et al. (1928) which is explained below.   The time step Δt defined in the model has to be less than a critical time step, $t_{critical}$ which depends on the largest frequency that requires detection within the model. In wave propagation simulations, as small deformations in the elements are assumed to take place, an approximation commonly adopted is that the critical time step is the travel time of a P wave through the smallest element in the numerical model:

Equation 4-16

$$\Delta t \leq t_{critical} = \frac{\Delta h}{V_{p\,MAX}} = \frac{2}{f_{max}}$$

Where, $fmax$ (Hz) is the maximum frequency that requires detection, Δh (m) is the height of the smallest element and $V_{p\,MAX}$ (m/s) is the maximum P wave velocity defined in the model domain. Where the model comprises more than one domain with different P wave velocities, the maximum value is used. Figure 4-2 describes the value Δh for a) linear square element, b) linear triangular element and c) quadratic triangle element (Multiphysics 2014). The distance represents the

shortest distance between 2 nodes for a square element, but this is not the case for triangular elements.
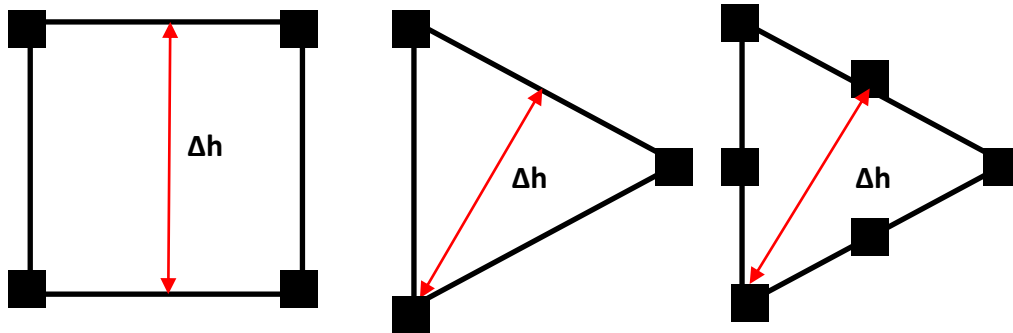
Figure 4-2: Schematic of Δh for a) linear square element, b) linear triangle element and c) quadratic triangle element.

The condition defined in Equation 4-16 is referred to as the CFL condition derived by Courant, Friedrichs et al. (1928). The actual time step defined in a simulation can be expressed in terms of its ratio with the critical time step. This ratio is known as the Courant (CFL) Number:

Equation 4-17

$$CFL = \frac{\Delta t}{\Delta t_{critical}}$$

Therefore the resulting time increment is defined as:

Equation 4-18

$$\Delta t = CFL.\Delta t_{critical} = CFL.\frac{\Delta h}{V_{p\ MAX}}$$

COMSOL recommends to achieve optimum numerical solutions the CFL ratio should be defined as 0.2 (Multiphysics 2014). This is analysed in Section 6.2.4.

The model domain needs to be meshed in a way that the shortest wavelength in the model is adequately resolved i.e. a minimum of 5 mesh elements per wavelength (Multiphysics 2014).

The number of time increments in an explicit scheme (time domain) is larger than one required with an implicit scheme (frequency domain) as the computation must store the incident signal/numerical solution at each time step/iteration. As a result, the storage requirements when using the time domain approach can be a constraint. An advantage of using the time domain approach is that attenuation effects are simulated accurately (Jaeger and Cook 1976, Multiphysics 2012).

4.1.4   **Explicit Direct Solvers**

Transient waves are to be investigated with minimal numerical damping to ensure that the wave propagation can be accurately followed. This situation is best treated with the explicit method available in COMSOL Multiphysics.

Explicit direct solvers require a time-step size that limits the advance of the P wave. This restriction is related to accuracy because the equations are solved using quantities from neighbouring elements i.e. the previous time step. A wave that propagates further than one element in one time step would then be moving into regions that have no defined influence on the wave. Not only is this physically unrealistic, it also leads to numerical instability. As time accuracy is important, and the direct solver has been shown to provide greater accuracy in numerical methods for wave propagation by FlowScience (2015), it was used in this thesis.

Solving the systems of equations can be performed via breaking down or decomposing the matrix. MUMPS, PARDISO, and SPOOLES are all COMSOL direct solvers and each takes advantage of all of the processor cores on a single machine.

The direct solver MUMPS was initially used in this thesis. There is no difference in the solution obtained if the other available direct solvers in COMSOL are used. PARADISO tends to be the fastest when using a single machine (Frey 2013).

Generally, matrices will have thousands to millions of degrees of freedom (DOF's), and finding the solution to the equations is usually the most computationally demanding part of solving the model. All direct solvers are RAM intensive however

both MUMPS and PARADISO can store the solution out-of-core which means that they can offload some of the computational requirements onto the hard disk.

An advantage of using a direct solver is that once the LU decomposition of the domain has been performed i.e. the domain has been broken down, the equations can be efficiently solved using backward and forward substitutions (Marfurt 1984). This approach has been shown to be very efficient for 2D forward modelling problems (Harari and Hughes 1992, Jo, Shin et al. 1996, Hustedt, Operto et al. 2004). However, the time and memory constraints of the LU decomposition and its limited scalability on large memory platforms, constrains the application of the direct solver approach for large 3D models i.e. models which consist of more than ten million unknowns (Operto, Virieux et al. 2007).

4.2   Boundary Conditions

A problem in solid mechanics is not adequately defined numerically unless the appropriate boundary conditions are applied and defined. In seismic subsurface explorations, two boundary conditions are required in order to model wave propagation in an efficient manner. An advantage of using the finite element method is that only the geometric boundary conditions need to be defined (Bleistein, Cohen et al. 2001). Free surface conditions are required, on the top of the computational domain (ground surface) to represent the air to solid interface which is characterised by the largest impedance contrast. For internal boundaries i.e. geological feature contained within the host rock, the effects are well represented by the changes in the material properties of the medium (Kelly, Ward et al. 1976).

4.2.1   The Free Surface

The free surface boundary condition is naturally implemented by applying zeroing functions on these boundaries, which follow the edges of the mesh elements (Chopra, Castagna et al. 2006). The interface between a gas and solid or liquid is often referred to as a free surface, hence why the top layer is characterised by a

free surface boundary condition. The reason for the "free" entitled term comes from the large difference in the densities of the air (gas) and solid (rock mass).

4.2.2   Source Application

The application of a prescribed velocity using Equation 4-13 (pg. 42) produces a transient response to a known excitation (Figure 4-1, pg. 42) in one or more directions. In this thesis the direction is vertical. The force is applied across 5 elements (body force) rather than applied to a single element (point force) as this offers a better representation of the source. In real life a point force would not be applied to a single particle. This generates an almost pure pressure wave. The size of the source is only a fraction of the wavelength of the resulting seismic wave therefore it is a close representation of a point source (Figure 4-3).
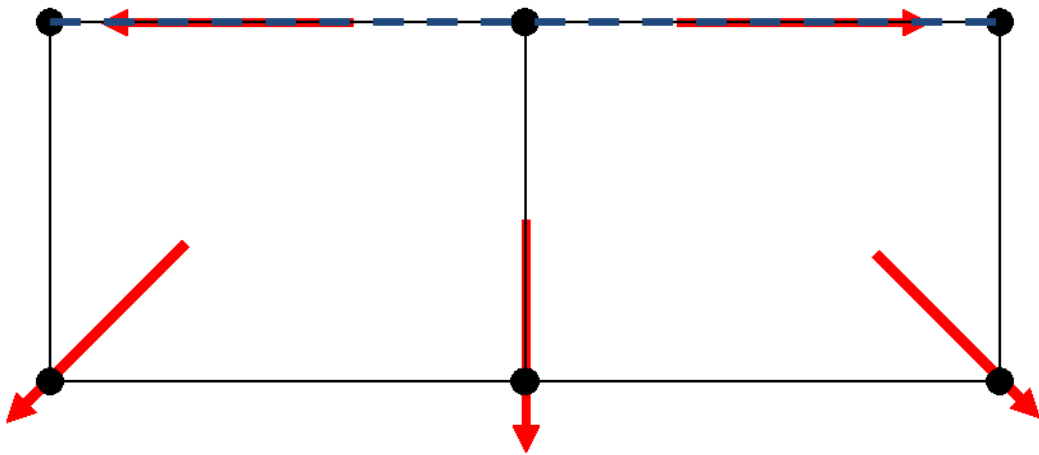
Figure 4-3: Schematic representation of the pressure wave excitation applied in the vertical direction for square mesh elements. Blue dashed line represents the source being applied as a body force. Red arrows represent the radial wave propagation. Black lines represent the mesh elements.

Figure 4-4 demonstrates the application of a source and the corresponding seismograms recorded at 2 monitoring points. The seismogram at the monitoring point located at 350m from the source demonstrates a reduction in PPV and a time delay which corresponds to the expected arrival time: L/V_p. Where L is 350m and V_p is 5000m/s giving an arrival time of 0.08s. This is in good agreement with the arrival time presented in Figure 4-4. This demonstrates the effective simulation of

mechanical waves in COMSOL. The latter 0.2s window of the signal is not affected by the delay in arrival time at the monitoring point 350m from the source, and the non-steady state nature of the signal on arrival is used as explained in detail in Chapter 6, Section 6.2.1, pg. 58.
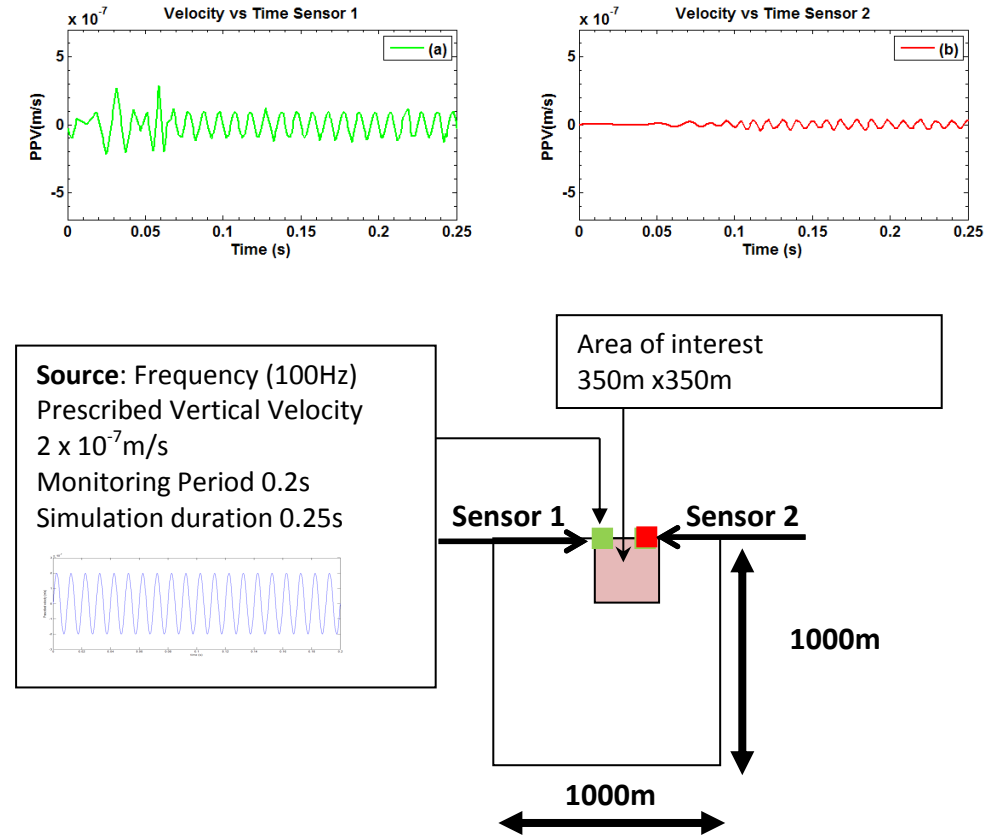
Figure 4-4: Schematic representation of model to highlight the simulation theory and method. Not to scale. The model dimensions (white area) are much larger than the area of interest (pink area) allowing the effects of unwanted reflections to be minimised. Green square: monitoring point located at the source and corresponds to seismogram (a). The source is applied over several mesh elements. Red square: monitoring point located 350m from the source and corresponds to seismogram (b). Material property of the domain is characterised as a granite Vp = 5000 m/s.

4.2.3 **Low Reflecting Boundary Conditions**

To minimise signal reflections on external boundaries a low reflecting boundary can be applied to the model.

A Low Reflecting Boundary also known as an absorbing boundary condition is applied in order to let waves pass out from the model without reflection in

transient simulations. As a default it takes material data from domain that is it applied to and creates a perfect impedance match for both P and S waves with the external boundaries allowing wave to pass through the external boundary without reflecting off of the surface.

Detailed descriptions of low reflecting boundaries and their applications can be found in Cohen and Jennings (1983) and Marfurt and Kirlin (2001).

5   Spectral Analysis

Spectral analysis techniques are used in many scientific and engineering applications for analysing periodic signals. Periodic signals are signals which complete a pattern within a measurable time frame, referred to as a period. The pattern is repeated over identical subsequent periods. The completion of a full pattern is defined as a cycle. A period is defined as the amount of time (seconds), required to complete one full cycle. The duration of a period may be different for each signal but it is constant for any given periodic signal.

Spectral analysis is required for this thesis as the frequency spectra of the seismic signals is of interest. Spectral analysis produces a power spectrum with frequency (x-axis) and spectral amplitude (y-axis).

The Fast Fourier Transform commonly known as FFT is the most common spectral analysis technique. The FFT technique can be used for continuous and discrete signals. One of the constraints associated with the FFT is that the sampling rate used to obtain the signal is constant. For data which is detected using equipment (short period seismometers used in this thesis) that automates the collection process, this is generally not a concern.

Another method is the Lomb Normalised Periodogram (LNP) developed by Lomb and is described in (Press, Flannery et al. 1986). This method can analyse short and long duration seismic signals in the time domain to post process the data. This method was selected as an estimation of the significance of the peaks in the LNP is required. The LNP provides this significance and the spectrum is the same as from the FFT method for equidistant data sets. The algorithm used to implement the method was the "normperiod" by Pytharouli and Stiros (2008) and is explained in more detail in Section 5.1.1.

5.1.1 **Lomb Periodogram**

The Lomb periodogram is a spectral analysis algorithm which was initially developed by Lomb (Lomb 1976) and further developed by Scargle (Scargle 1982). It allows the analysis of both evenly and unevenly spaced data (Pytharouli and Stiros 2008), as it corresponds to the fitting of a sine curve to the data time series (velocity and time vectors of the seismic signal) using the least square method:

Equation 5-1

$$h(t) = a.\cos(\frac{2\pi}{T}(t-\tau)) + b.\sin(\frac{2\pi}{T}(t-\tau))$$

The full analytical derivation can be found in Lomb (1976). The Lomb normalised periodogram LNP P (T) for a signal with period T is defined by the following equation:

Equation 5-2

$$P(T) = \frac{1}{2\sigma^2} \left\{ \frac{\left[\sum_{j=1}^{N}(x_j - \overline{x)\cos\frac{2\pi(t_1 - \tau)}{T}}\right]^2}{\sum_{j=1}^{N}\overline{\cos^2\frac{2\pi(t_1 - \tau)}{T}}} + \frac{\left[\sum_{j=1}^{N}(x_j - \overline{x)\sin\frac{2\pi(t_1 - \tau)}{T}}\right]^2}{\sum_{j=1}^{N}\overline{\sin^2\frac{2\pi(t_1 - \tau)}{T}}} \right\}$$

Where the parameter τ is defined:

Equation 5-3

$$\tan\left(\frac{4\pi\tau}{T}\right) = \frac{\sum_{j=1}^{N}\overline{\sin\frac{4t_i}{T}}}{\sum_{j=1}^{N}\overline{\cos\frac{4t_i}{T}}}$$

Where:

N is the number of data points in the dataset

t_i is the time at which the variable i was measured (in this case PPV)

$\bar{x}$ is the means of the data values $\bar{x} = \frac{1}{N}\sum_{i=1}^{N} x_i$ **(Equation 5-4)**

σ^2 is the variance of the data values $\sigma^2 = \frac{1}{N-1}\sum_{i=1}^{N}(x_i - \bar{x})^2$ **(Equation 5-5)**

The values produced by the equation P(T) are dimensionless, as P(T) is normalised when multiplied the term $\frac{1}{2\sigma^2}$. This value of P(T) gives an indication of periodicity with period T in the signal. Dominant peaks in the spectrum correspond to frequencies that are present in the signal. A high peak within the power spectrum indicates a good fit of Equation 5-2 to the data set for that specific frequency (Scargle 1982). The significance level of any peak within the spectrum is given by P:

Equation 5-6

$$p = 1 - (1 - e^{-P(T)})^N$$

This equation assumes that the values of x_i are independent random noise and that P(T) has an exponential probability distribution with unit mean (Scargle 1982, Leroy, Revil et al. 2007).

The significance level of any peak p is used to produce the power level z_0. This is the P(T) value above which the presence of a peak in the periodogram or power spectrum is statistically significant. The power level z_0 calculated by Equation 5-6 when solved for P(T):

Equation 5-7

$$z_0 = = \ln\left[1 - (1 - p)^{\frac{1}{N}}\right]$$

Where

z_0 is the LNP amplitude above which frequency peaks are regarded as statistically significant. The confidence level can be expressed as a percentage: $(1 - p) * 100\%$

p is the significance level, with the value of 95% being most commonly used and the value used in this thesis

N is the number of data points in the signal

5.1.2 Range of Frequencies in the Lomb Periodogram

The range of frequencies for which the LNP can be calculated is the same as that of the Fast Fourier Transform (FFT) spectrum in the case of equidistant data such as those used in this thesis. The following equation governs the range of frequencies that can be detected:

Equation 5-8

$$\frac{1}{2t_r} \le f \le \frac{N}{2t_r}$$

Where t_r is the record length (time) and N is the length of the time series (number of data points) (Günther, Rücker et al. 2006). The upper bound limit of the frequency range $\frac{N}{2t_r}$ represents the Nyquist Frequency f_c, which is the maximum frequency that can be observed in the spectrum. Computation of the spectrum for frequencies which are greater than $\frac{N}{2t_r}$ can cause a phenomen called aliasing (Leroy, Revil et al. 2007).

Aliasing is a threat for data sampled at nearly perfect intervals like for example data obtained using short period seismometers. Aliasing is an effect that causes different signals to become indistinguishable (or aliases of one another) when sampled. It also refers to the distortion that occurs when the signal is reconstructed from samples that are different from the original continuous signal (Press, Flannery et al. 1986).

5.1.3 The Normperiod

Four parameters and one input file are required in order to run "Normperiod". A two column data file is required containing the values of the time series and the corresponding PPV values to be analysed. The format for the input files is a simple text file as described in detail in Pytharouli and Stiros (2008).

The frequencies f_i at which the code can successfully compute:

Equation 5-9

$$\frac{1}{4t_r} \leq f_i \leq \text{fratio} * \frac{N}{2t_r}$$

For the purpose of this thesis the value of $fratio$ is defined as one due to the Nyquist Theorem and the fact that the data is equidistant, therefore Equation 5-9 becomes:

Equation 5-10

$$\frac{1}{4t_r} \leq f_i \leq \frac{N}{2t_r}$$

This is the same frequency range as that of the FFT (Equation 5-8). The total number of frequencies f_i is determined by the formula:

Equation 5-11

$$N_p = \frac{4N}{2}$$

Where N is the length of the time series.

The code calculates the difference between the upper and lower bounds of Equation 5-10 and the interval specified is then divided by the total number of frequencies N_p in order to compute the frequency step for the x-axis of the LNP.

The frequency step $fstep$, calculates the distance between two successive frequencies in the LNP spectrum:

Equation 5-12

$$fstep = \frac{\frac{N}{2t_r} - \frac{1}{4t_r}}{N_p}$$

The output files for of the code contain the values of the power spectrum i.e. the frequency values (x-axis) and the corresponding spectral amplitude or LNP Power (y-axis).

6 Wave Propagation: Numerical Model Development & Refinement

6.1 Introduction

The work carried out in this chapter has a focus on the setup of the numerical model to be used for the simulation of the propagation of a seismic wave through a single medium (up to 350m). A 1000m x 1000m domain model was used. This ensured that no unwanted reflections existed. However, simulating such a large domain was computationally demanding. The model simulated the excitation (in terms of the PPV vertical component) of the medium as a result of a periodic seismic source with a single specified frequency in the range (1-100Hz).The dominant frequency as computed by Lomb Normalised Peridogram (LNP) described in Chapter 5 was used to derive any conclusions.

Within this chapter the model is bench marked against the analytical solution for an elastic half space allowing a systematic error to be quoted for the numerical simulation.

The results which highlight the downscaling of the geometrical domain size which reduced the computational demands of the simulations are also presented. This geometrical reduction allowed the exploration of more than one material property in a single domain. The dominant frequency as computed by the LNP and the PPV were used to derive any conclusions and potential for further investigation.

6.2 Model Development

The governing equations are the same as those outlined in Chapter 4 and are applied throughout all simulations. There are four parameters which had to be defined in each COMSOL simulation:

1. mechanical properties of the domain;

2. frequency of the source;

3. initial PPV generated by the source; and

4. domain size.

1) **Mechanical properties of the domain:** Initially, the focus was hard rock, therefore the material properties set in initial simulations were comparable to that of a granitic rock (Carmichael 1988). The P wave velocity, S wave velocity, density and Poisson's Ratio are defined in Table 6-1.

2) **Frequency of the source:** The frequency range of interest was defined as 1-100Hz. This was decided based on published frequency spectra produced by civil engineering equipment commonly found in-situ (Carnevale M, Young G et al. 2000, Shuting, Zhaofeng et al. 2003). The consideration of potential field trials and the available equipment also influenced the definition as outlined in Chapter 3, Section 3.3, pg.32. It was likely that a generator would be the most viable option as a seismic source for field application. Research by Shuting, Zhaofeng et al. (2003) highlighted that the chosen frequency range would be adequate.

3) **Peak Particle Velocity (PPV) of the Source:** The PPV chosen was based on research conducted in monitoring tunnelling construction vibrations. A value of 2 x 10^{-7} m/s was defined (Figure 4-1 pg. 42), which corresponded to an average of those presented in Carnevale M, Young G et al. (2000).

4) **Domain Size:** Initially a conservative approach was adopted defining a geometrical domain size that would be large enough to ensure that no unwanted boundary reflections would take place (Figure 6-1). If the P wave velocity is defined as 4000 m/s and a monitoring area of 350m is used, then a domain size of 1000m x 1000m was deemed sufficient.

The modelled area was much larger than the area of interest in order to minimise the effect of unwanted reflections off of the external domain boundaries. The travel time L/V_p from A to B for the P wave (fastest travelling wave) is 0.0875s (Figure 6-1). The travel time from A to C and back to A (external boundary) is 0.25s (Figure

6-1). The same travel time applies to the external boundary opposite C and the travel times to all other boundaries are greater than this. Therefore simulation time of 0.25s is adequate to fulfil this criterion. The source is applied at S which is 500m from the external boundary. The source is applied over 5 mesh elements. There are 8 monitoring points located every 50m over the 350m area of interest. Each monitoring point is located on the first mesh element from the surface to ensure that there are minimal boundary effects on the detected signal.

Source Frequency (100Hz)
Prescribed Vertical Velocity 2 x 10^{-7}m/s
Monitoring Period 0.2s
Simulation duration 0.25s

Area of interest

350m x350m

S

C

A

B

Monitoring Points Located Every 50m. Monitoring Vertical Component Only

1000m
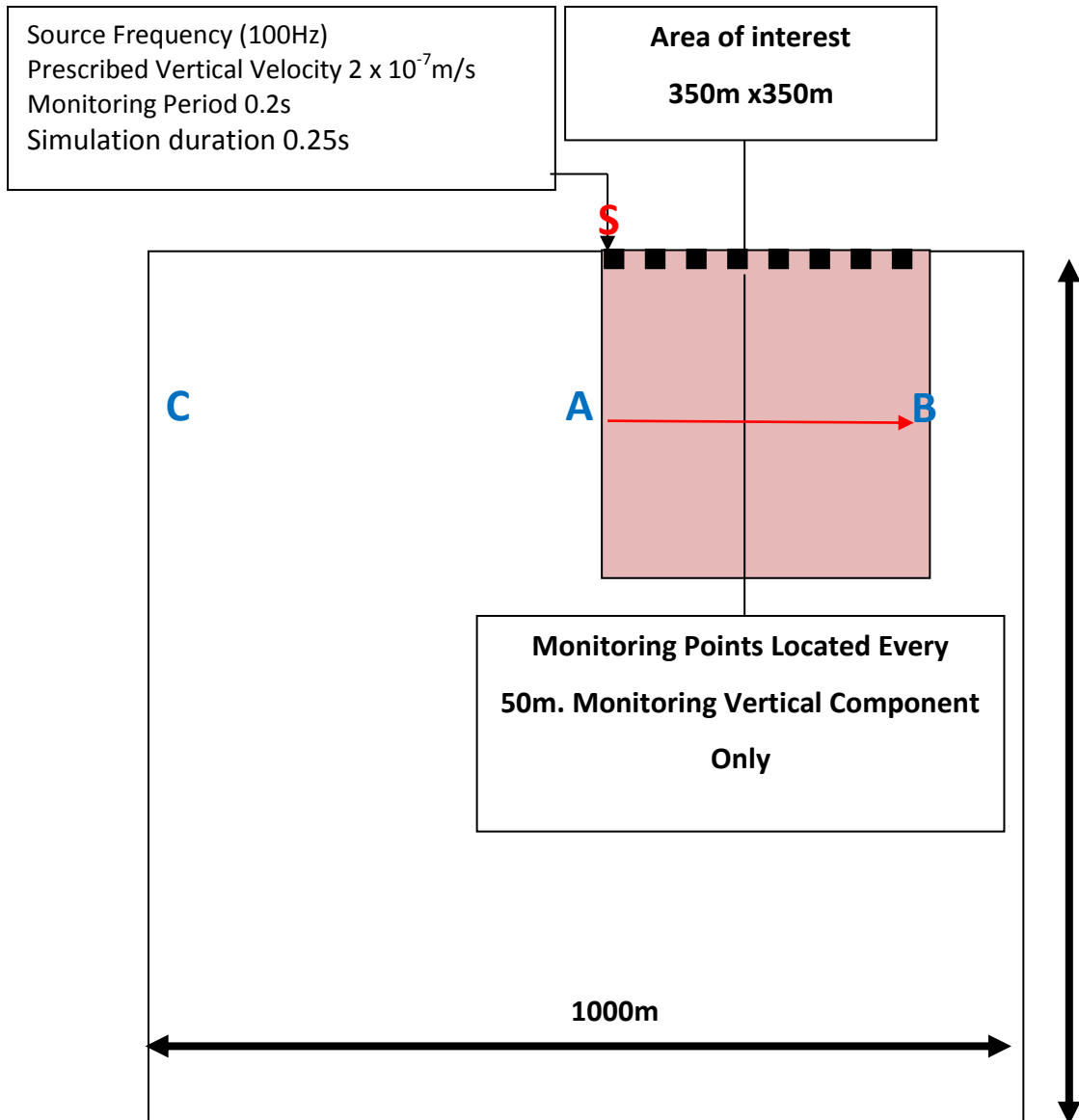
Figure 6-1: Schematic presentation of initial model. The model dimensions (white area) are much larger than the area of interest (red area) allowing for the minimisation of the effect of unwanted reflections. Black squares represent the monitoring point locations. The red arrow shows the incident wave.

Table 6-1: Details of the mechanical properties for each material used in the simulations throughout Chapter 6. Values are given for P wave and S wave velocity, density and Poisson's Ratio. Values were taken from Carmichael (1988).

Mechanical Property	Value
P Wave Velocity Granite	4000 m/s
S Wave Velocity Granite	3000 m/s
Density Granite	2000 kg/m^3
Poisson's Ratio Granite	0.2
P Wave Velocity Clay	500m/s
S Wave Velocity Clay	400 m/s
Density Clay	1500 kg/m^3
Poisson's Ratio Clay	0.3

6.2.1   Determination of the output signal length used in spectral analysis

Not the whole length of the output signal as recorded at the monitoring points was suitable for spectral analysis. For example, Figure 6-2 (a)(b) shows the PPV over time output at the two different monitoring points of the domain (Sensor 1 and Sensor 2) for a 0.25s long simulation. Figure 6-2 (c)(d) shows the LNP for the whole signal (0-0.25 seconds). Figure 6-2 (e)(f) shows the LNP for part of the signal (0.05-0.25 seconds) represented by the purple box in Figure 6-2 (a)(b).

The power spectrum over the entire duration of the simulation is affected by the non-steady state nature of the wave on arrival highlighted by the formation of additional peaks in the spectra. The power spectrum over the later 0.2s of the simulation is more representative of the signal that would be obtained in practice. It is the frequency response of the steady state harmonic vibration that this thesis is interested in, not the arrival time of the wave.

The amplitude of the power spectra over the 0.25s is exactly 1.25 times that of the latter 0.2s power spectra. This is expected as there is exactly 1.25 times the number of data points 5010 and 4008, respectively.

A conscious decision was made to select the latter 0.2s of each simulation to post process the data throughout the research as the focus is the characteristics of the steady state vibration of the seismic wave as it propagates, not the arrival time of the wave.
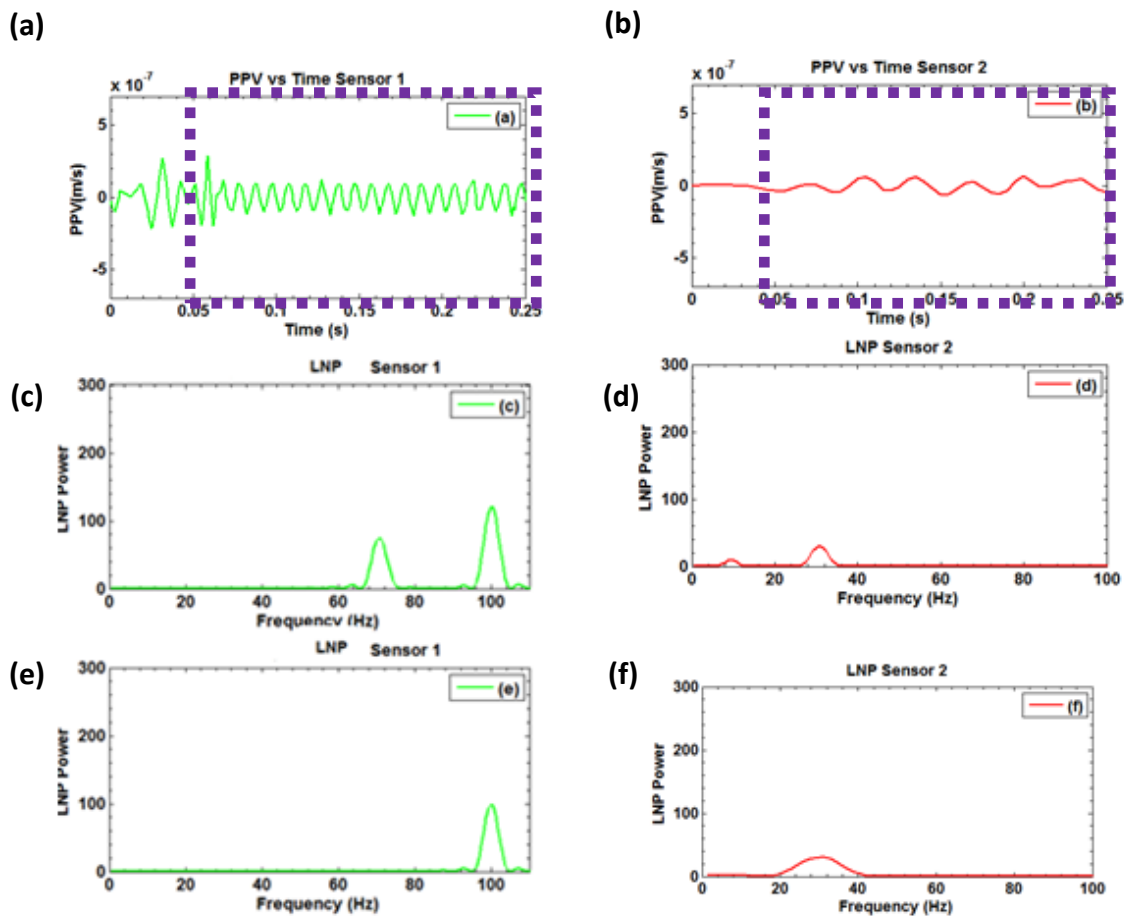
Figure 6-2: Numerical simulation for granite domain. Left: sensor 1 Right: sensor 2. Each line of the figure corresponds to 1) PPV over time data (a,b), 2) Power Spectrum of entire 0.25s simulation (c,d) and 3) Power Spectrum over later 0.2s (e,f) of the simulation highlighted by purple dashed box.

The reduction in frequency observed in Figure 6-2 aligns with findings described by Ebrom (2004) who suggested that reduction in the frequencies observed are probably not solely caused by inelastic attenuation due to the medium being characterised by very low characteristic attenuation factor (k<5.0) and is therefore caused by the multiple reflections that take place as a result of the free surface boundary condition. Finally, Buckingham (1997) demonstrates that the seismic wave characteristics of PPV and dominant frequency detected and thus the reduction in the observed characteristics are related to the mechanical properties of the medium i.e. Bulk Modulus, Rigidity Modulus, density and porosity.

Key Point: There is a dispersion coefficient automatically applied to the wavenumber k within COMSOL (Multiphysics 2014) for an induced seismic wave. This is a known parameter as presented in Suharsono (2014) and reflects the material properties of the medium such as Bulk Modulus, P wave velocity etc. The reduction in frequency and PPV observed is a result of the dispersion coefficient added to the model to effectively simulate wave propagation comparable to that observed in the field.

6.2.2   Analytical Solution

Lord Rayleigh was the first to study the propagation of seismic waves localised near the free surface of an isotropic elastic half-space. When surface waves propagate along the free surface of infinite homogeneous isotropic elastic solid the resulting displacement is confined to the near surface region. This is similar to the behaviour exhibited by deep water waves only that the potential energy of surface waves in this region depends on the elastic properties of the medium (Raleigh and Strutt 1885).

In order to bench mark the solution in COMSOL against the analytical solution for seismic wave localised near the free surface in an elastic half space the following points are derived:

- Potentials;
- Free surface boundary conditions; and

- Solutions propagating along the surface, decay with depth.

This is based on the method detailed in Romanelli (2004) which is developed from the theory presented in Raleigh and Strutt (1885).

6.2.2.1 Solution to the wave equation for an elastic half space, which travel along the interface

Firstly the potentials are defined which form the basis of the solution to the surface wave equation:

Equation 6-1

$$u_i = \nabla \Phi + \nabla \times \Psi \qquad\qquad \partial_t^2 \Phi = \alpha^2 \nabla^2 \Phi$$
$$\nabla = (\partial_x, \partial_y, \partial_z) \qquad\qquad \partial_t^2 \Psi_i = \beta^2 \nabla^2 \Psi_i$$

$\quad u_i$ Particle displacement $\qquad\qquad \alpha$ P-wave speed

$\quad \Phi$ scalar potential $\qquad\qquad\qquad \beta$ Shear wave speed

$\quad \Psi_i$ vector potential

An evanescent P-wave propagates along the free surface and decays exponentially with depth. The reflected post-critically reflected SV wave is totally reflected and phase-shifted. These two wave types can only exist together. They both satisfy the free surface boundary condition as detailed in Figure 6-3.
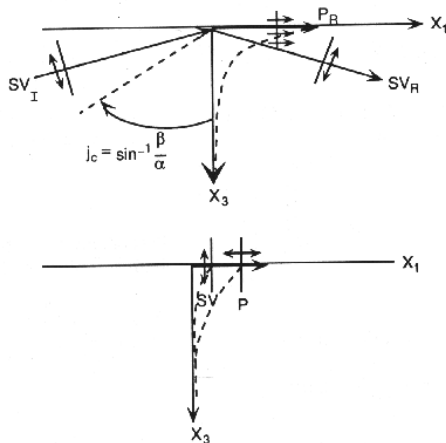
Figure 6-3: Schematic giving an overview of wave propagation of seismic waves localised near the free surface of an isotropic elastic half-space.

The aim is to find the solution for plane surface waves traveling along one horizontal coordinate axis, so we can set:

Equation 6-2

$$\partial_y(.) = 0$$

Therefore, only motion in the x ,z plane is considered as detailed in Figure 6-4:
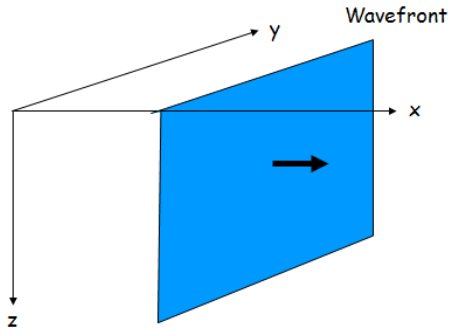
Figure 6-4: Schematic detailing propagation of the wave from in the x,z plane

Then using the potential defined earlier the following equations for particle displacement can be obtained:

Equation 6-3

$$u_x = \partial_x \Phi - \partial_z \Psi_y$$
$$u_z = \partial_z \Phi + \partial_x \Psi_y$$

As we only require Ψ_y we set $\Psi_y = \Psi$ from now on. The potential now becomes:

Equation 6-4

$$\Phi = A\exp[ik(ct \pm az - x)]$$

With this solution the coefficient *a* for which travelling wave solution exists can be obtained:

Equation 6-5

$$a = \pm\sqrt{\frac{c^2}{\alpha^2} - 1}$$

In order for a plane surface wave of that form to decay with depth *a* has to be imaginary, in other words:

Equation 6-6

$$c < \alpha$$

Together the following equations for the potentials can be obtained:

Equation 6-7

$$\Phi = A\exp[ik(ct \pm \sqrt{c^2/\alpha^2 - 1}z - x)]$$
$$\Psi = B\exp[ik(ct \pm \sqrt{c^2/\beta^2 - 1}z - x)]$$

So that:

$$c < \beta < \alpha$$

Analogous to the problem of finding the reflection-transmission coefficients we now have to satisfy the boundary conditions at the free surface (stress free):

Equation 6-8

$$\sigma_{xz} = \sigma_{zz} = 0$$

In isotropic media the following equations describe stress and strain:

Equation 6-9

$$\sigma_{zz} = \lambda(\partial_x u_x + \partial_z u_z) + 2\mu\partial_z u_z$$
$$\sigma_{xz} = 2\mu\partial_x u_z$$

Where the particle displacement is defined by:

Equation 6-10

$$u_x = \partial_x\Phi - \partial_z\Psi_y$$
$$u_z = \partial_z\Phi + \partial_x\Psi_y$$

And the solution for potentials now becomes:

Equation 6-11

$$\Phi = A\exp[ik(ct \pm \sqrt{c^2/\alpha^2 - 1}z - x)]$$
$$\Psi = B\exp[ik(ct \pm \sqrt{c^2/\beta^2 - 1}z - x)]$$

This leads to the following relationship for c, the phase velocity:

Equation 6-12

$$(2 - c^2/\beta^2)^2 = 4(1 - c^2/\alpha^2)^{1/2}(1 - c^2/\beta^2)^{1/2}$$

The phase velocity of the wave is independent of k: **there is no dispersion** for a homogeneous half space.

For simplicity a fixed relationship between P and S wave velocity is assumed:

Equation 6-13

$$\alpha = \sqrt{3}\beta$$

To obtain the following equation:

Equation 6-14

$$c^6/\beta^6 - 8c^4/\beta^4 + 56/3c^2/\beta^2 - 32/2 = 0$$

The only root which fulfills this condition is:

Equation 6-15

$$c = 0.9194\beta$$

Putting this value back into the solutions we obtain the displacement in the x-z plane for a plane harmonic surface wave propagating along direction x in a half space:

Equation 6-16

$$u_x = C(e^{-0.8475kz} - 0.5773e^{-0.3933kz})\sin k(ct - x)$$

Equation 6-17

$$u_z = C(-0.8475e^{-0.8475kz} + 1.4679e^{-0.3933kz})\cos k(ct - x)$$

Where:

k = is the wavenumber

Equation 6-18

$$k = 2\pi f/V_p$$

z = the depth of the initial source application

x = the monitoring cross section distance

t = simulation time

C= initial particle displacement

This development was first made by Lord Rayleigh in 1885. It demonstrates that there are solutions to the wave equation propagating along a **free surface.**

Rayleigh waves travel in the vertical (z) and radial (x) plane and exhibit a combination of SV and P wave energy. For the purpose of this analytical solution the radial (x) component is the component of interest as can be seen from Figure 6-5. Therefore, the displacement of the z component will not be considered further.
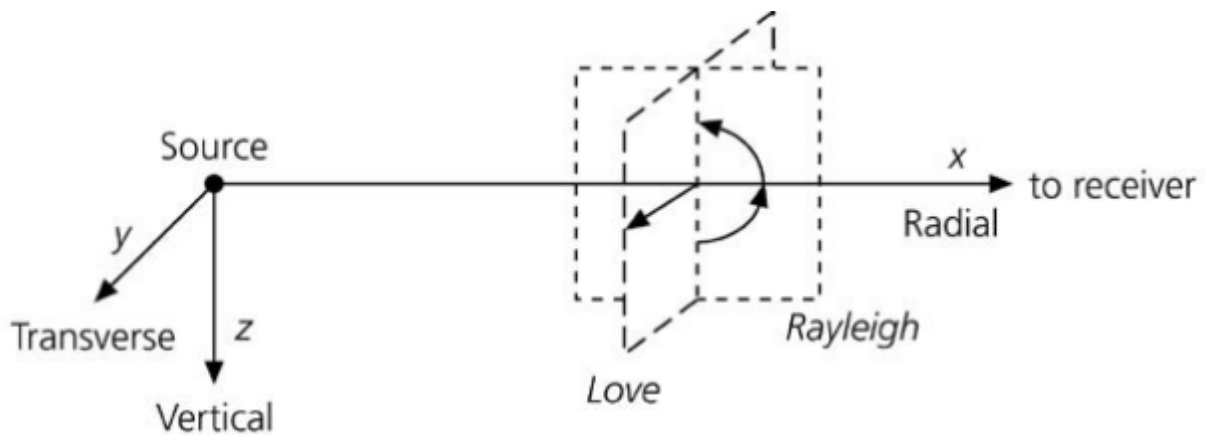
Figure 6-5: Schematic detailing that Rayleigh waves travel in the vertical (z) and radial (x) plane and exhibit a combination of SV and P energy.

6.2.2.2   Fitting the analytical solution to COMSOL solution

Using the following model parameters the analytical equations presented above were fitted to the COMSOL model:

k = 0.5

NOTE: In COMSOL the wavenumber is calculated with a wave dispersion coefficient automatically applied within COMSOL (Multiphysics 2014) for an induced seismic wave. This is a known parameter as presented in Suharsono (2014) to reflect the propagation surface waves in the field.

The utilization of the dispersion coefficient is essential to ensure that the simulation has taken into account that as the seismic wave propagates through the medium, the elastic energy associated with the wave is gradually absorbed by the medium, eventually ending up as heat energy. This is known as absorption (or anelastic attenuation) and will eventually cause the total disappearance of the seismic wave (Multiphysics 2014).

Note from Equation 6-19 that the wavenumber k is dependent on the material properties of the domain. The dispersion coefficient automatically applied with COMSOL equals 3.0 which aligns with values presented in Johnston, Toksöz et al. (1979).

Equation 6-19

$$k = \left(\frac{2\pi f}{V_p}\right) * dispersion\ coefficient$$

z = the sensor location in the z direction (0.1m)

x = the sensor location in the x direction (350m)

t = simulation time (0.25s)

C= initial PPV ($2\text{x}10^{-7}$ m/s) corresponding to an initial displacement of $3.2\text{x}10^{-7}$mm

Solving Equation 6-16 the following value was re obtained for PPV in the radial (x) direction:

U_x = $1.093\text{x}10^{-7}$ mm which corresponds to a PPV of $2\text{x}10^{-8}$ m/s
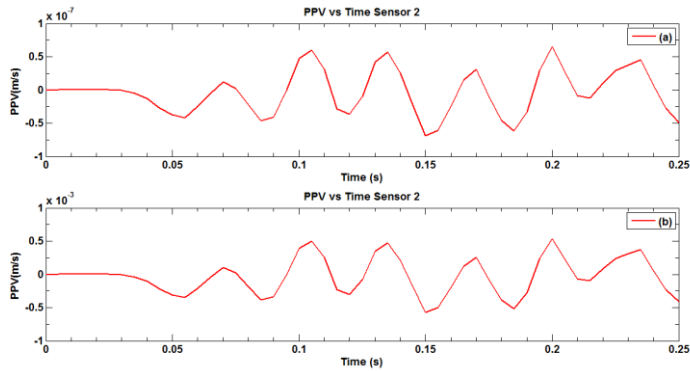
Figure 6-6: Numerical simulation for granite domain. Each line of the figure corresponds to PPV over time data (a,b), Top: X direction with a maximum PPV of 6.5x10^{-8} m/s Bottom: Z direction with a maximum PPV of 5.4x10^{-4}m/s. This is in good agreement with the analytical solution. There is no change in the frequency of the signal. There only a difference in the value of PPV observed.

The numerical solution of 2.35x10^{-8} m/s obtained from COMSOL was found to be in good agreement with the analytical solution allowing systematic error of +0.35x10^{-8} m/s to be quoted.

There was a slight variation in the PPV values obtained, however the model is not an exact representation of the analytical solution and can be subject to small errors.

6.2.3 Selection of PPV and Dominant Frequency

PPV: The PPV within the later 0.2s of the 0.25s monitoring window which has the largest value/amplitude.

Dominant frequency: The frequency within the LNP spectra which has the greatest amplitude i.e. the most significant peak.

Selection: These maximum values of PPV and dominant frequency were obtained using a "max" function in Mat lab. This was a conscious decision to minimise error and ensure consistency when selecting the maximum PPV and dominant frequency values for all simulation data.

6.2.4 Model development: mesh and time step selection

To ensure that the seismic waves are modelled accurately, a mesh validation was conducted to investigate the effect of the mesh element size on results, and to ensure that the observed results are not just a model artefact.

Then, a time step analysis was conducted. This analysis aimed to determine the optimum time step for the simulations i.e. a time step that does not bias the results of the simulation.

The optimal mesh size $h\,max$ and time step Δt recommended by the CFL condition as presented in Chapter 4, Section 4.1.3, pg. 43 was initially used and then reduced to ensure that the model solution was robust. In accordance with COMSOL recommendations a CFL number of 0.2 was used. However, other researchers recommended using a CFL number of <0.2 (Polívka 2008), which prompted this validation.

6.2.4.1 Mesh Selection

Mesh aspect ratio: The maximum allowable value of the mesh aspect ratio was calculated using Equation 6-20. The theory associated with $h\,max$ is presented in Section 4.1.3. Using a P wave speed of 5000 m/s as an upper limit gives a maximum element size (*h_max*) of 10m. The P wave velocity of 5000m/s was used to calculate *h_max* as this value sufficiently greater than the P wave velocity of 4000m/s which was used in the domain simulated. Using a value of 5000m/s is conservative and takes into account that calculating *the h_max using* a P wave velocity that is exactly the same as the simulated domain may not have produced accurate results.

Equation 6-20

$$h\_max = 5000/(f*N))$$

Where f = 100Hz and N =5 mesh elements per wavelength

There is a requirement to have a minimum of 5 mesh elements per wavelength (Multiphysics 2014). The frequency of 100Hz was chosen to calculate h_max as this

is the upper limit of the frequency range (1-100Hz) that was considered. The larger the frequency that has to be detected the smaller the mesh required. If the upper limit is used to calculate h_max (100Hz) all frequencies less than this value can be adequately simulated.

The model was simulated for 4 different mesh sizes. All monitoring points were placed directly on mesh elements, to ensure that interpolation effects were minimized. The time step of 4×10^{-5}s was used based on the COMSOL recommended CFL = 0.2 condition for a domain characterised by a P wave velocity of 5000m/s. For this series of simulations a frequency of 55Hz was chosen as the source frequency as it was roughly in middle of the frequency range of interest (1-100Hz).

Spectral analysis was performed on the data outputs from the different models and the results were plotted in Figure 6-7 to determine the optimal mesh refinement solution.
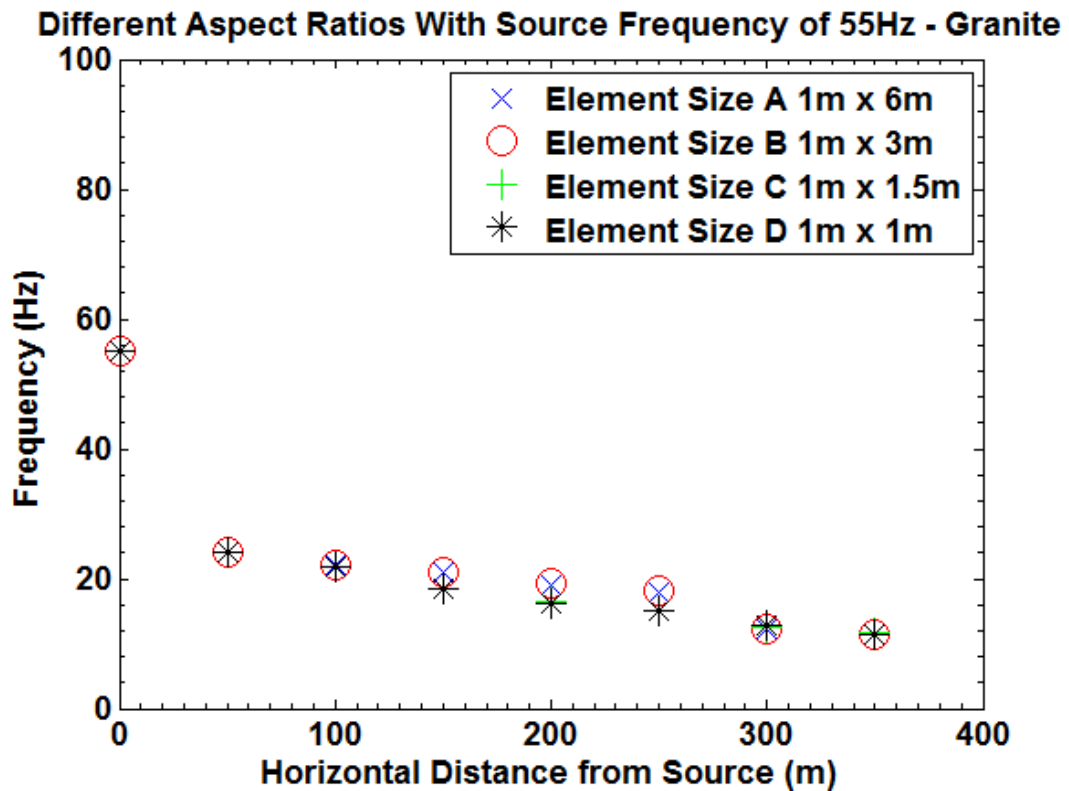
Figure 6-7 Frequency of seismic wave as a function of horizontal distance from the source for different mesh element sizes (A, B, C and D). Computed frequencies were the same for Element Size C and D. This resulted in the choice of Element D (1m x 1m) as the element size to be used in all subsequent simulations in this chapter.

Results: For conservativeness the maximum element size utilised was 1m x 6m, as dimensions greater than this did not exhibit an acceptable difference (<1Hz) between the data points. Figure 6-7 demonstrates consistency between resulting frequencies at the same distance from the source using Element Size C and D.

Element Size A and B demonstrated a difference. Element sizes A, B, C and D are consistent within ± 0.26Hz at all distances except 150, 200 and 250m. This consistency is acceptable as it is below the detectable frequency (1Hz) in real life.

When the element becomes almost square i.e. C the difference in frequency values observed between 150m and 250m for Element size A and B no longer exists and the decline in frequency becomes gradual. This implies the observed difference for A and B could have been the result of a numerical effect, caused by an inadequate element size and shape.

An additional model was run for a perfect square element i.e. Element D. These results demonstrate an acceptable difference (<1Hz) and corresponding frequency values of ± 0.31Hz with Element size C. The gradual reduction in frequency is maintained.

Results for Element Size C and D demonstrate that the monitoring points are at an adequate distance from the boundary to eliminate unwanted boundary reflections as there is an adequate consistency in the results. The mesh size was reduced until no significantly detectable difference in frequency was observed.

Conclusion: For conservativeness a uniform mesh was selected. Using a uniform square mesh minimises any numerical errors and produces a solution as close to reality as possible. Therefore for the remainder of this Chapter Element Size D (1m x 1m) was used. A concern with these solutions although accurate was the run time and memory constraints (Table 6-12, Page 96).

6.2.4.2 Time Step Selection

Time Step Variation: A model was run for 3 different time steps (Table 6-2), the material properties were kept the same as the previous simulations i.e. Granite (Section 6.2.4.1). The frequency of the source was defined as 55Hz as in Section 6.2.4.1. Spectral analysis was performed on the data outputs from the different models and the results were plotted in Figure 6-8 to determine the optimal time step refinement solution i.e. when there is an acceptable difference (<1Hz) between the data sets.

The initial time step of 4×10^{-5}s was calculated based on the COMSOL recommended CFL = 0.2 condition for a domain characterised by a P wave velocity of 5000m/s. No model was run for 5000m/s domain. This P wave value was only used to calculate the time step and mesh size limits ensuring that the model parameters were adequate to simulate a domain characterised by a P wave velocity of 4000m/s. This also gave the opportunity to explore material properties with a higher P wave velocity than 4000m/s in future simulations. The mesh element size (h) was defined

as a uniform 1m x 1m square element as concluded in Section 6.2.4.1. The time step was initially calculated using Equation 4-18.

The Nyquist frequency must be higher than the highest frequency in the signal that is required to be detected. The smaller the sampling interval Δt the higher the Nyquist frequency, therefore the maximum frequency that can accurately be detected without the effect of aliasing increases as described in Chapter 5, page 50.

Although not a requirement for the LNP spectral analysis, in numerical simulation practice it is generally desirable to sample densely. Generally 8 or more times greater than the Nyquist criteria for a given sample. When the sampling is dense, the sampled signal becomes a better representation of the true signal and the spectrum becomes a better representation of the true spectrum (Stein and Wysession 2009). The different time steps (s) used in the investigation and corresponding Nyquist Frequency (Hz) and CFL Number are presented in Table 6-2. The Nyquist Frequency is calculated using:

Equation 6-21

$$Nyquist\ Frequency = \frac{1}{\Delta t}$$

Where Δt is the sampling rate defined in the numerical simulation.

Table 6-2: Table detailing the different time steps (s) considered, the corresponding Nyquist Frequency (Hz) and CFL Number.

Time Step (s)	Nyquist Frequency (Hz)	CFL Number
4×10^{-5} (A)	25000	0.2
2×10^{-5} (B)	50000	0.1
1×10^{-5} (C)	100000	0.1

Spectral analysis performed on the data outputs from the different models were plotted in Figure 6-8 to determine the optimal time step refinement solution.
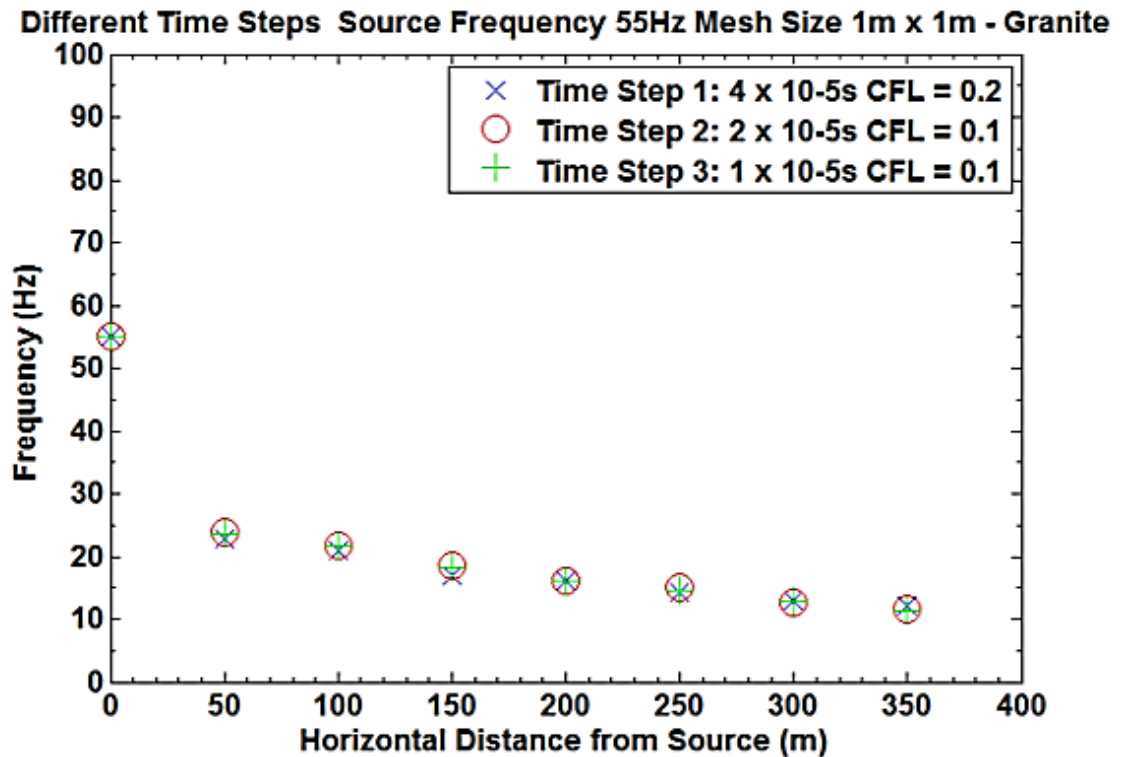
Figure 6-8: Frequency of seismic wave as a function of horizontal distance from the source for 3 different time steps (1, 2 and 3). The medium was characterised by a P-Wave velocity of 4000m/s comparable to that of granite. Resulting frequency values were the same for Time Step 2 and 3, Time Step 2 was concluded to be adequate.

Results: Time steps 2 and 3 are consistent within a range of ± 0.50Hz, which is below the detectable range using seismometers. Time step 1 demonstrates a bigger difference with the corresponding time step 2 and 3 values at 150m. The smooth reduction in frequency is maintained.

Reducing the CFL Number (Equation 4-18) to 0.1 resulted in more consistent results. The time steps 2 and 3 were in good agreement within ± 0.5Hz which again is below the detectable range using seismometer. The maximum detectable frequency in the numerical simulations is > 25000Hz for all datasets considered (Table 6-2), this is adequate as the frequency range of interest is 1-100Hz and there is potential to explore frequencies greater than this range, if required.

Conclusion: Due to the good agreement between time step 2 and 3, time step 2 was selected as it requires less computation and memory compared to that of time step 3.

Further investigation: The results in Section 6.2 demonstrate a tendency for the signal frequency to reduce to a certain value after a certain distance from the source. This prompted further investigation to:

1. Identify if this reduction toward a certain value occurs for different sources characterised by different frequencies;
2. Identify if this reduction depends on the medium properties; and
3. Establish if the variation in the seismic wave dominant frequency values can potentially be used in the development of a new concept for a site investigation tool. Dominant frequency refers to the frequency within the LNP spectra which has the greatest amplitude i.e. the most significant peak.

Point 3 is investigated further in Chapter 8.

6.2.5   Selection of the frequency of the seismic source

The frequencies examined were:

- 100Hz;
- 55Hz;
- 25Hz; and
- 10Hz.

The rationale was that none of frequency values when divided or multiplied by two is a harmonic of each other. This would ensure that a potential reduction in frequency observed was a result of a real change in the frequency of the seismic signal and not the representation of a harmonic of the original source frequency.

The effect of seismic sources characterised by different frequencies were investigated using a model with characteristics:

- **Medium:** granite only (P wave velocity, S wave velocity, density and Poisson's Ratio: 4000m/s, 3000m/s, 2000 kg/m^3 and 0.2, respectively);

- **Mesh element size**: – uniform mesh 1m x 1m (as defined in Section 6.2.4.1); and

- **Time step:** 2 x 10^{-5} seconds (as defined in Section 6.2.4.2).

The only parameter varied among the simulations was the frequency of the source. The geometry of the domain is the same as that in Figure 6-1.

The most notable reduction in frequency took place when the frequency of the source used was 100Hz (Figure 6-9 and Table 6-3).

Granite Only Analysis
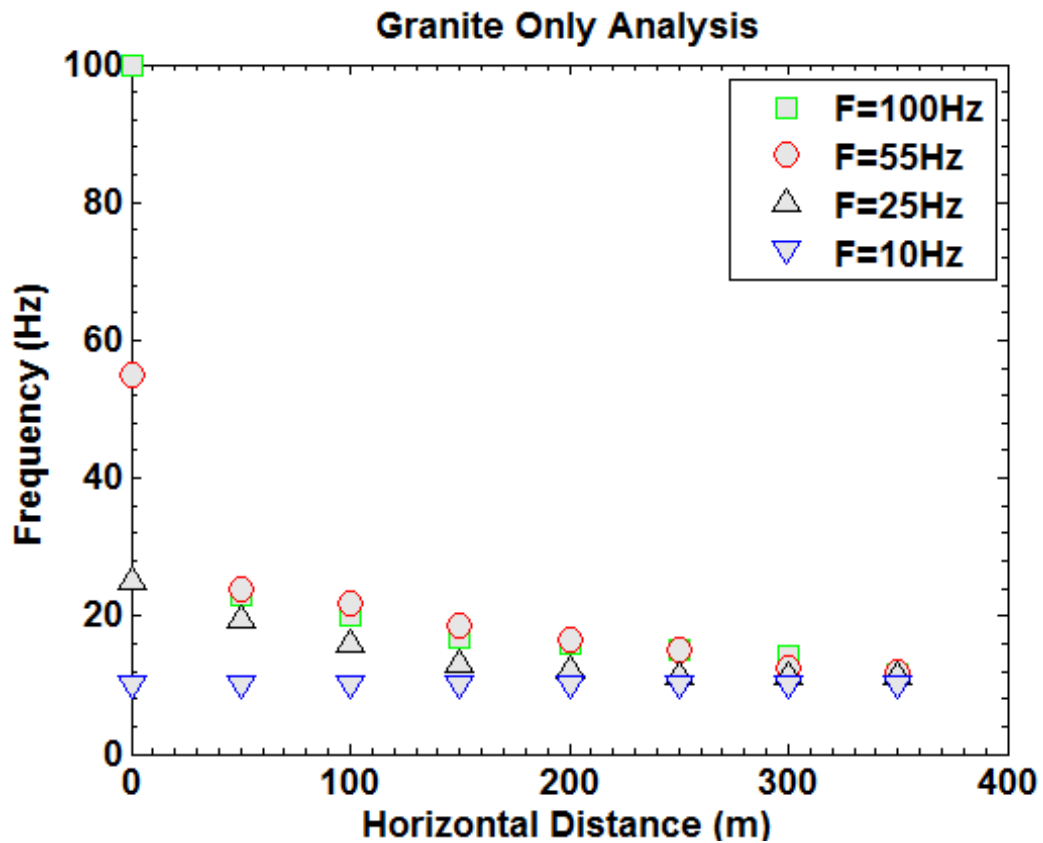
Figure 6-9: Granite: Frequency of seismic wave as a function of horizontal distance from the source for different source frequencies (100Hz, 55Hz, 25Hz and 10Hz). The frequency of the seismic signal gradually reduces to an average convergence value (10.17Hz) at approximately 350m. For a source with a frequency of 10Hz or less there is no change in frequency over the 350m. The 100Hz source demonstrates a larger percentage difference when compared to the source frequency over the 350m.

Table 6-3: Granite: Frequency of seismic wave as a function of horizontal distance from the source for different source frequencies (100Hz, 55Hz, 25Hz and 10Hz)

Distance from source x	Frequency Values: Granite			
	Input Frequency: 10Hz	Input Frequency: 25Hz	Input Frequency: 55Hz	Input Frequency: 100Hz
0	10.0	25.0	55.0	100.0
50	10.0	19.4	24.0	22.9
100	10.0	16.1	21.7	20.0
150	10.0	13.0	18.6	16.9
200	10.0	12.2	16.6	16.1
250	10.0	11.2	15.2	15.2
300	10.0	11.2	12.5	14.2
350	10.0	11.2	11.8	10.2

The percentage difference between the frequency values detected and the frequency of the source are presented in Table 6-4. The percentage difference between the frequency values detected and the frequency detected at the previous monitoring point are presented in Table 6-5.

Table 6-4: Granite: Percentage difference from source frequencies (100Hz, 55Hz, 25Hz and 10Hz) with horizontal distance from the source

Distance from source	Difference in Percentage from Input Frequency Values: Granite			
(m)	Input Frequency: 10Hz	Input Frequency: 25Hz	Input Frequency: 55Hz	Input Frequency: 100Hz
0	0	0	0	0
50	0	23	56	77
100	0	36	60	80
150	0	48	66	83
200	0	51	70	84
250	0	55	72	85
300	0	55	77	86
350	0	55	79	90

Table 6-5: Granite: Percentage difference from previous monitoring point

Distance from source	Difference in Percentage from Previous Monitoring Point : Granite			
	Input Frequency: 10Hz	Input Frequency: 25Hz	Input Frequency: 55Hz	Input Frequency: 100Hz
(m)	10	25	55	100
0	-	-	-	-
50	0	23	56	77
100	0	17	9	13
150	0	19	14	15
200	0	6	11	5
250	0	8	9	6
300	0	0	17	6
350	0	0	6	28

Results: In the first 50m the frequency reduced from 100Hz to approximately 23Hz a percentage difference of 77%. The reduction in the subsequent 50m intervals was more gradual creating a smooth curve. At 350m there was a percentage difference

of 90% when compared to 100Hz of source, this was the largest percentage difference observed for all frequencies.

A reduction in frequency can also be clearly seen when the induced source is 55Hz. In the first 50m the frequency reduced from 55Hz to approximately 24Hz, a percentage difference of 56%. When the induced source is 25Hz the reduction in frequency is not as notable reducing to approximately 19Hz in the first 50m, a percentage difference of 23%. The reduction is again gradual but the frequency of the signal was slightly lower than the previous two simulations. Interestingly the frequency of the signal tends toward the same value at 350m for these 3 simulations with an average of 10.17Hz, slightly greater than the induced source frequency of the fourth simulation, 10Hz. When the induced source is 10Hz there is no obvious variation in frequency with a percentage difference of 0%.

For a source with a frequency of 10Hz or less there is no change in frequency over the 350m as evidenced by Table 6-5 where the percentage difference is consistently 0% for between all monitoring locations. The 100Hz source demonstrates a larger percentage difference when compared to the source frequency over the 350m as highlighted in Table 6-4.

Table 6-5 demonstrates that convergence has not been reached when the source frequency is 100Hz, as the percentage difference between the frequency value at 350m and the value of the previous monitoring point is 28%.

6.2.5.1 Simulation of Common Conventional Seismic Exploration Frequencies

For comparison, also tested here was a simulation of sources commonly utilised in conventional seismic exploration studies using different instrumentation such as the seismic survey conducted in Lake Turkana and Lake Victoria in Kenya (Johnson, Halfman et al. 1987, Stager and Johnson 2008). The rationale was to establish if the largest reduction in frequency of the seismic signal and tendency towards a specific frequency value still took place in the first 100m of propagation as observed in the simulations so far.

From reviewing research papers (Johnson, Halfman et al. 1987, Stager and Johnson 2008) which utilised 28-kHz echo sounding over 900km and 1kHz echo sounding over 700km, it was decided to simulate with sources with frequencies of 1KHz, 0.5KHz and 0.4KHz. Then evaluate this over a shorter distance of 100m due to computational capability constraints.

The model geometry, time step and mesh size used in the previous simulations was adequate and fulfilled the CFL criterion. The PPV of the source 2 x 10^{-7}m/s remained the same. The only variable to change was the source frequency.

Again, the most notable reduction in frequency took place within the first 50m of propagation (Figure 6-10 and Table 6-6).
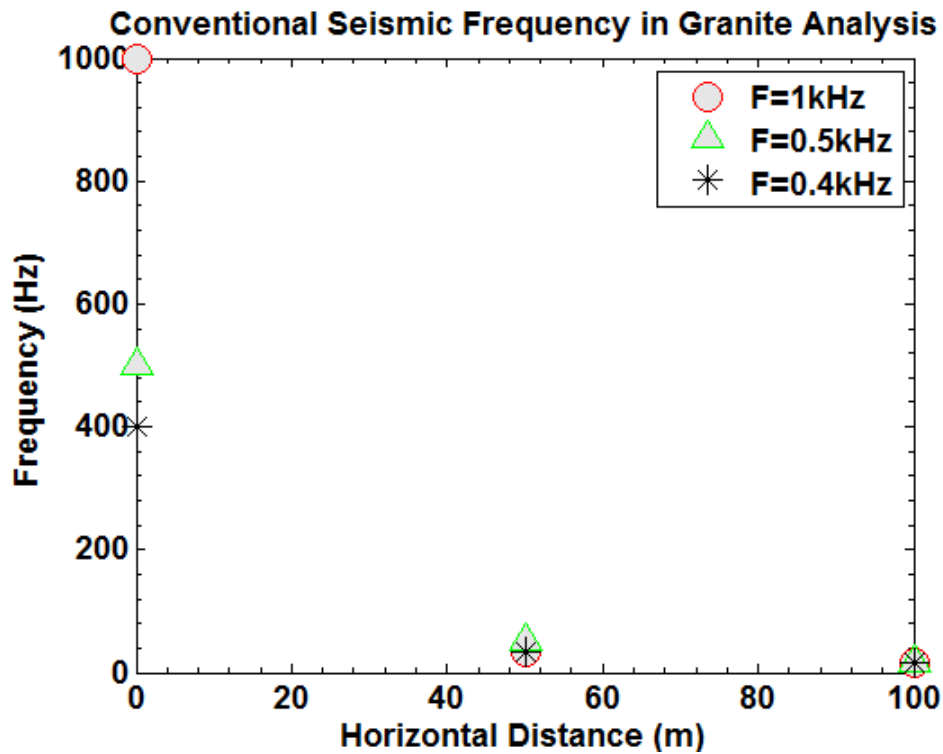
Figure 6-10: Granite: Frequency of seismic wave as a function the horizontal distance from the source for different source frequencies (1 KHz, 0.5 KHz, and 0.4 KHz). These results show that for conventional seismic exploration frequency the most notable reduction in the dominant frequency of the seismic signal also occurs within the first 100m of propagation agreeing with previous simulations.

Table 6-6: Granite Frequency of seismic wave as a function of horizontal distance from the source for different source frequencies (1kHz, 0.5 kHz, and 0.4 kHz)

Distance from source x	Frequency Values: Granite		
	Input Frequency:0.4kHz	Input Frequency: 0.5kHz	Input Frequency: 1kHz
0	400.0	500.0	1000.0
50	35.0	52.6	33.3
100	16.0	16.6	16.6

The percentage difference between the frequency values detected and the frequency of the source are presented in Table 6-7. The percentage difference between the frequency values detected and the frequency detected at the previous monitoring point are presented in Table 6-8.

Table 6-7: Granite - Percentage difference from source frequencies (1kHz, 0.5 kHz, and 0.4 kHz) with horizontal distance from the source

Distance from source x	Percentage Difference from Input Frequency Values: Granite		
	Input Frequency: 0.4kHz	Input Frequency: 0.5kHz	Input Frequency: 1kHz
0	0	0	0
50	91	89	97
100	96	97	98

Table 6-8: Granite - Percentage difference from previous monitoring point

Distance from source x	Percentage Difference from Previous Monitoring Point		
	Input Frequency: 0.4kHz	Input Frequency: 0.5kHz	Input Frequency: 1kHz
	400	500	1000
0	-	-	-
50	91	89	97
100	54	68	50

Results: In the first 50m the frequency reduced from 1 KHz to approximately 33Hz, a percentage difference of 97% (Table 6-7). This is two orders of magnitude less than the initial frequency of 1 kHz. The reduction in the subsequent 50m interval is more gradual, with a percentage difference of 98% (Table 6-7) when compared to the source frequency.

A reduction in frequency can also be clearly seen when the induced source is 0.5kHz. In the first 50m the frequency reduces from 0.5 KHz to approximately 53Hz, a percentage difference of 89% when compared to the source value of 0.5 kHz (Table 6-7). The subsequent reduction in the next 50m is gradual with a percentage difference of 97% when compared to the frequency of the source (Table 6-7). The

frequency values are the same order of magnitude as those produced from the 100Hz, 55Hz and 25Hz simulations. When the induced source is 0.4 KHz the reduction in frequency is notable reducing to approximately 35Hz in the first 50m, a percentage difference of 91% (Table 6-7). The reduction is again subsequently gradual but the frequency of the signal at the monitoring points was slightly lower than the previous two simulations.

The reduction in frequency was greater in the first 50m when the induced source was 1kHz, when compared to the 0.5kHz and 0.4kHz results.

Table 6-7 demonstrates that the largest percentage difference compared to the source occurs when the source is 1kHz. This indicates that the greater the frequency the larger the variation with distance.

Table 6-8 demonstrates that convergence has not been reached as the percentage difference between the frequency value and the value of the previous monitoring point is not less than 50% on any occasion.

Conclusion: The numerical simulations demonstrate that the most responsive frequency in the first 50m of propagation was 100Hz. This will be further clarified and confirmed in Section 6.2.6.

6.2.6 Consideration of different material properties

6.2.6.1 Clay: Various Source Frequencies

To investigate if the reduction in frequency also occurred for a medium with different material properties numerical models with various source frequencies were simulated:

- 100Hz;
- 55Hz;
- 25Hz;
- 10Hz; and

- 5Hz were considered.

Clay was chosen as the P wave velocity of the domain as it is an order of magnitude lower (500m/s) than granite (4000m/s).

The material properties used in this simulation were based on a dry unsaturated clay characterised by a P wave velocity, S wave velocity and Poisson Ratio of 500m/s, 400m/s and 0.2, respectively (Carmichael 1988).

There were no other changes to the model set up used for the granite medium (Section 6.2.5) to ensure comparability, focusing on the effect of material properties on the dominant frequency of the seismic signal.

An additional simulation for a source frequency of 5Hz, was ran for clay, the rationale for this was that after the simulation for 10Hz demonstrated a continued reduction in frequency towards a specific value, further investigation was required (Figure 6-11 and Table 6-9).

Clay Only Analysis
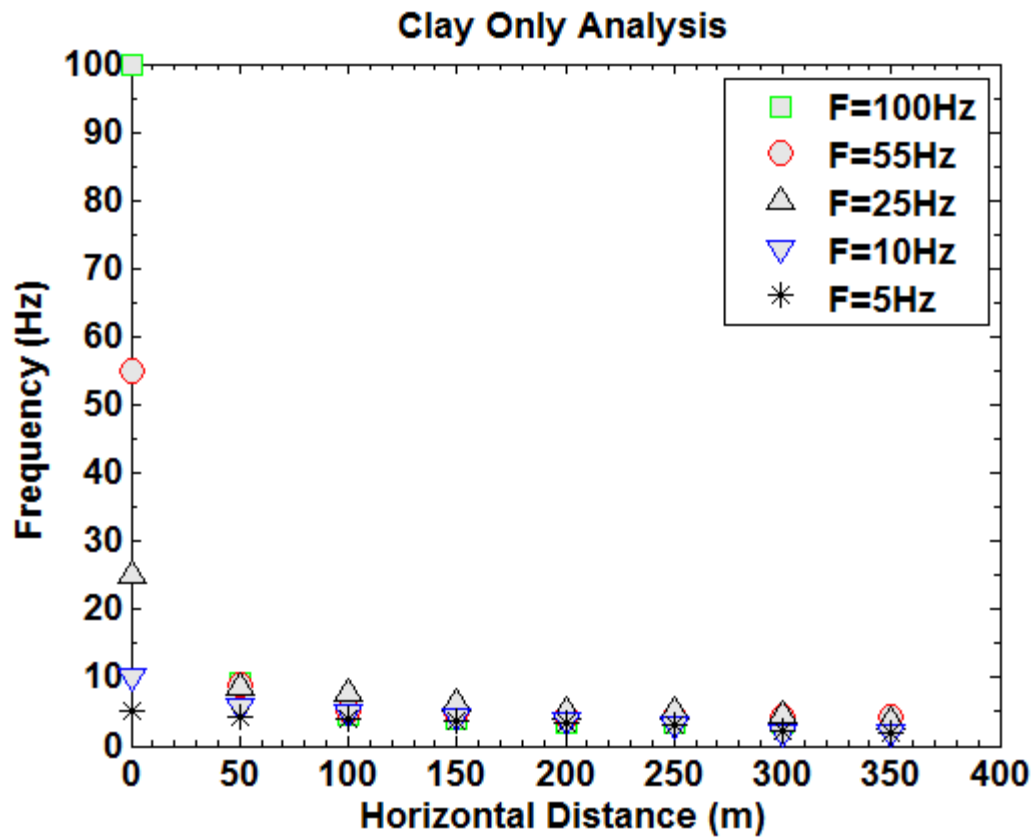
Figure 6-11: Clay: Frequency of seismic wave as a function of horizontal distance from the source for different source frequencies (100Hz, 55Hz, 25Hz, 10Hz and 5Hz). The frequency of the seismic signal gradually reduces to a similar value (4Hz) at approximately 200m with no further reduction thereafter.

Table 6-9: Clay - Frequency of seismic wave as a function of horizontal distance from the source for different source frequencies (100Hz, 55Hz, 25Hz, 10Hz and 5Hz)

Distance from source x	Frequency Values: Clay				
	Input Frequency: 5Hz	Input Frequency: 10Hz	Input Frequency:25Hz	Input Frequency: 55Hz	Input Frequency: 100Hz
0	5.0	10.0	25.0	55.0	100.0
50	4.3	5.6	8.5	9.1	9.3
100	4.0	4.7	7.8	5.3	4.5
150	4.0	4.1	6.3	4.8	3.3
200	4.0	4.0	5.2	4.4	3.3
250	4.0	4.0	5.2	4.4	3.3
300	4.0	4.0	4.6	4.3	3.3
350	4.0	4.0	4.0	4.3	3.3

The choice of material properties for this investigation was based on the rationale that the resolution of a seismic survey increases when there is a large material property contrast. A granite rock has significantly different material properties when compared to clay i.e. the P wave velocity in granite is an order of magnitude greater than in clay. Clay was an appropriate choice in order to establish if the gradual reduction in frequency observed in the initial granite model also occurred in a clay medium.

The percentage difference between the frequency values detected and the frequency of the source are presented in Table 6-10. The percentage difference between the frequency values detected and the frequency detected at the previous monitoring point are presented in Table 6-11.

Table 6-10: Clay - Percentage difference from source frequencies (100Hz, 55Hz, 25Hz, 10Hz and 5Hz) with horizontal distance from the source

Distance from source x	Percentage Difference from Input Frequency Values: Clay				
	Input Frequency: 5Hz	Input Frequency: 10Hz	Input Frequency: 25Hz	Input Frequency: 55Hz	Input Frequency: 100Hz
0	0	0	0	0	0
50	14	44	66	83	91
100	20	53	69	90	95
150	20	59	75	91	97
200	20	60	79	92	97
250	20	60	79	92	97
300	20	60	82	92	97
350	20	60	84	92	97

Table 6-11: Clay- Percentage difference from previous monitoring point

Distance from source x	Percentage Difference from Input Frequency Values: Clay				
	Input Frequency: 5Hz	Input Frequency: 10Hz	Input Frequency: 25Hz	Input Frequency: 55Hz	Input Frequency: 100Hz
	5	10	25	55	100
0	-	-	-	-	-
50	14	44	66	83	91
100	7	16	8	42	51
150	0	12	20	9	27
200	0	3	17	10	0
250	0	0	0	0	0
300	0	0	13	0	0
350	0	0	12	0	0

Results: Figure 6-11 and Table 6-9 show that the most notable reduction in frequency took place when the induced source used was 100Hz. In the first 50m the frequency reduced from 100Hz to approximately 9Hz, a percentage difference of 91%. The value of 9Hz is an order of magnitude less than the comparable reduction in Granite. The reduction in the subsequent 50m intervals is more gradual.

A reduction in frequency can also be clearly seen when the induced source is 55Hz. In the first 50m the frequency reduces from 55Hz to approximately 9Hz, a percentage difference of 83%. The subsequent reduction every 50m is gradual and the values are comparable to those produced from the 100Hz simulation. When the induced source is 25Hz the reduction in frequency is not as notable reducing to approximately 8.5Hz in the first 50m, a percentage difference of 66%. The reduction is again subsequently gradual, but the frequency of the signal at the monitoring points was slightly lower than the previous two simulations.

Interestingly when the induced source is 10Hz and 5Hz respectively, it appears that convergence occurs at approximately 200m from the source with a frequency value of 4Hz. No further reduction frequency was detected at 350m.

Table 6-10 demonstrates that the largest percentage difference from source values takes place when the source is 100Hz, further indicating that 100Hz is the ideal source frequency to use.

Table 6-11 further highlights this apparent convergence when the induced source is 10Hz and 5Hz as the percentage difference at 250m when compared to the previous monitoring point value is 0%.

Interestingly, for all source frequencies considered except the 25Hz source the percentage difference in frequency compared to the previous monitoring point dramatically reduces to 0%. This indicates that for mediums characterised by a lower P wave velocity an apparent convergence in frequency occurs closer to the source.

Conclusion: The numerical models (Section 6.2.5 and 6.2.6) demonstrate that the most responsive dominant frequency in the first 50m of propagation was 100Hz. Dominant frequency refers to the frequency within the LNP spectra which has the greatest amplitude i.e. the most significant peak. Therefore, the source frequency used throughout the remainder of this thesis was 100Hz and the source PPV was defined as 2×10^{-7} m/s, unless otherwise stated.

6.2.6.2   Effect different media have on the reduction of the frequency of an induced seismic source

To further investigate the effect that different media have on the reduction of the frequency of an induced seismic source an additional 4 simulations were ran, with different P wave velocities to account for a range of different materials.

All parameters remained the same as those in the model Section 6.2.5, except the geometric area of interest was then extended from 350m (Figure 6-1) to 450m to ensure that no further reductions in frequency took place after this initial area of interest (350m) was considered. No further reduction or convergence in frequency

is when the percentage difference between that frequency value and the frequency value at the previous monitoring point was less than 1%.

Figure 6-12 and Figure 6-13 show results from the different simulations. From each simulation the dominant frequency value was obtained from spectral analysis performed on the data outputs. The selected frequency corresponds to the y axis value in Figure 6-12. The corresponding distance from the source at which the frequency value was observed was defined as the y-axis value in Figure 6-13. These parameters were then related to the P wave velocity of the domain (x-axis) in Figure 6-12 and Figure 6-13.
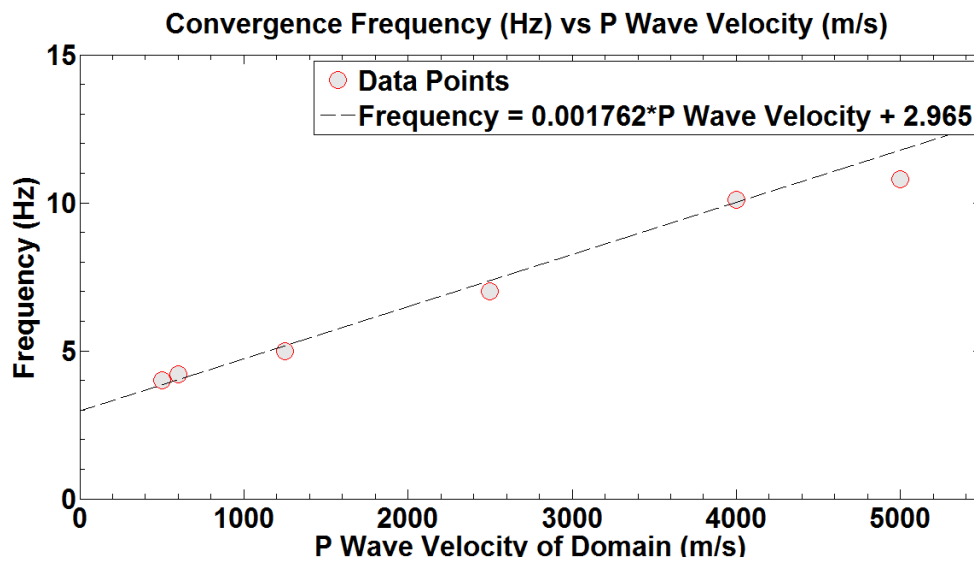
Figure 6-12: Data from 6 numerical simulations. There is a strong linear relationship (Adjusted R-Squared 0.9944) observed implying that the convergence frequency value observed increases linearly with the P wave velocity of the medium
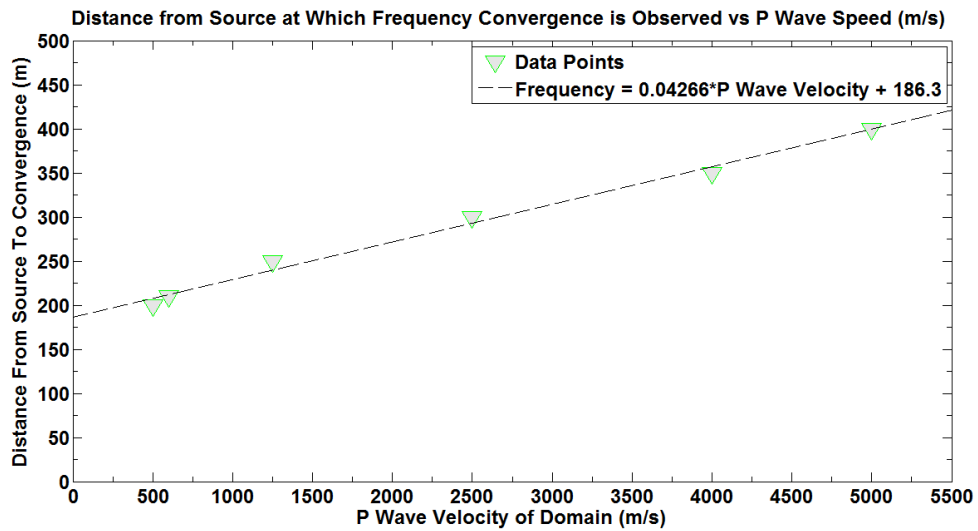
Figure 6-13: Data from 6 numerical simulations. There is a strong linear relationship (Adjusted R-Squared 0.9932) observed implying that distance from the source where the frequency of the seismic signal converges on a specific value increases linearly with the P wave velocity of the medium.

The x-axis in Figure 6-12 and Figure 6-13 is defined as the corresponding P wave velocity of the domain in the simulation. For example, the convergence frequency of 10.2Hz and corresponding distance of 350m obtained from the granite domain (Figure 6-9) corresponds to the P wave velocity of 4000 m/s in Figure 6-12 and Figure 6-13.

The frequency of value 4Hz and the corresponding distance of 200m obtained from the clay domain (Figure 6-11) corresponds to the P wave velocity of 500 m/s in Figure 6-12 and Figure 6-13.

MATLAB Curve Fitting Toolbox was used to create the line of best fit for both graphs. It is an application that can perform linear regression using its library of algorithms. The algorithm Linear model Poly1 was applied:

Equation 6-22

$$F(x) = p1*x + p2$$

The coefficients were within 95% confidence bounds.

The adjusted r-square was chosen to analyse the goodness of the fit of the line to the data. It is more conservative than r-squared and ensures that there is enough

data points to great an accurate regression calculation. Adjusted R square calculates the proportion of the variation in the dependent variable accounted for by the explanatory variables (Field 2009). The adjusted R-squared increases only if the term improves the model more than would be expected by chance and is explained by the following equation:

Equation 6-23

$$1 - (1 - R^2)\frac{n-1}{n-m-1}$$

Where n is the number of data points, and m is the number of independent variables.

Figure 6-12 reveals a strong linear relationship between the P wave velocity of the domain and the frequency which the induced source reduces or convergences to. The adjusted r-square is 0.9944, described by the dashed line on the graph which shows a line of best fit created using the MATLAB Curve Fitting Toolbox.

Figure 6-13 shows a strong linear relationship between the P wave velocity of the domain and the distance from the induced source where no further reductions or convergence in frequency takes place. The adjusted r-square is 0.9932, described by the dashed line on the graph which shows a line of best fit created using the MATLAB Curve Fitting Toolbox.

6.3   Model Refinement

Modelling with a domain that is sufficiently large enough ensures that no unwanted reflections would contaminate the seismic signal. This has an extremely high computational demand in terms of storage and solver time as outlined in Table 6-12, page 96. This section focuses on using a model with a geometrical scale that is representative of relevant near surface site investigations e.g. 25m x 25m.

The choice of source frequency was based on the frequency of the source available for field experiments (approximately 100Hz) and the frequency range that the micro

seismic equipment can detect (0-100Hz) which gives an accurate representation of the signals PPV (Chapter 3, Section 3.3, pg. 28). PPV of the source was $2x10^{-7}$m/s. The material properties of the domain were comparable to that of a granite rock (Table 6-1, page 58).

Key Point: A smaller domain simulation was run without and then with the low reflecting boundaries applied. A more refined mesh giving solutions with an accuracy of 0.1m instead of 1m was applied. This is a better representation of the detection scales at which new geophysical methods are being pushed.

The rationale was to:

1. establish if the external boundaries cause unwanted frequency peaks in the power spectrum;
2. check that the low reflecting boundaries were effective; and
3. consider the effect of material boundaries on the power spectrum.

Point 3 is particularly interesting as the results have the potential to infer what effects a significant material property contrast between adjacent zones may have on the seismic signal e.g. a cavity such as a sink hole.

6.3.1   Smaller domain with no low reflecting boundary

The granite domain (Table 6-1) was reduced to 25m x 25m to establish the effect of unwanted reflections on the frequency power spectrum of the seismic signal. Figure 6-14 presents the model set up used. Figure 6-15 (a) presents the frequency power spectrum obtained from Sensor 1 in the 25m x 25m domain the using LNP spectral analysis method presented in Chapter 5.
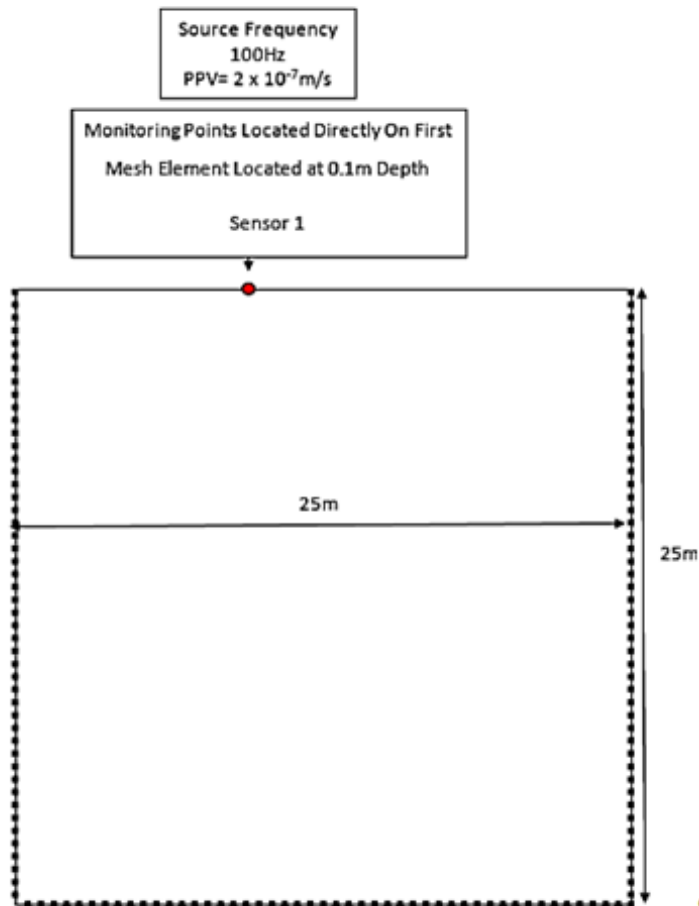
Figure 6-14: Schematic presentation of smaller granite domain model
The model dimensions are 25m x 25m. The source is applied vertically downwards at the surface at Sensor 1 (red dot). The black squares surrounding the base and sides of the domain highlight the external boundaries that will cause unwanted reflections.

(a)

(b)
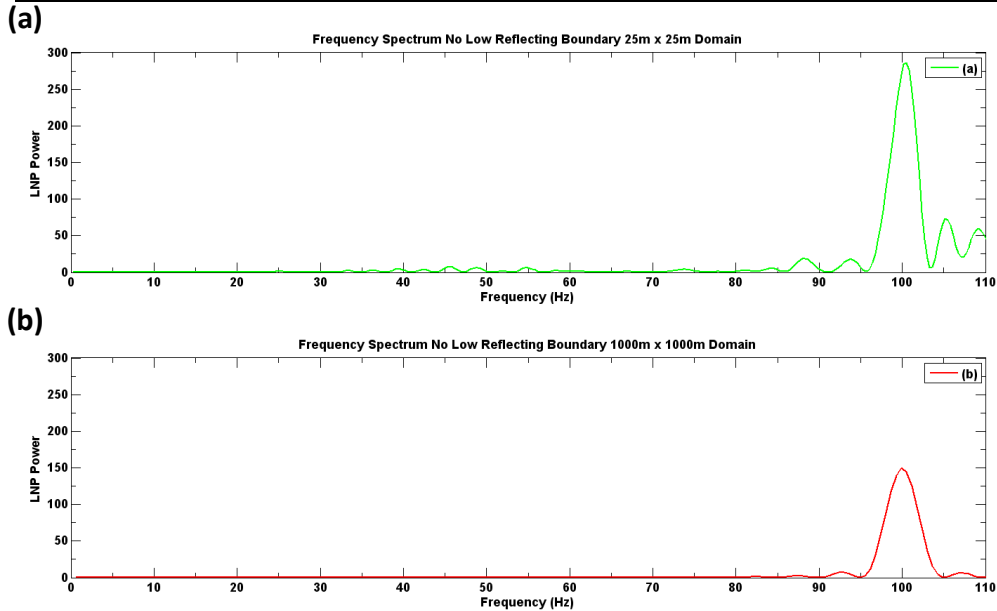
Figure 6-15: Frequency Power Spectrum from seismic signal (velocity vs time) detected at Sensor 1 when (a) no low reflecting boundary is applied to the base and side external boundaries of the 25m x 25m domain. There is a dominant peak at 100Hz as expected, however unwanted peaks as result of reflections can also be seen in the spectrum. (b) Frequency Power Spectrum from seismic signal detected at Sensor 1 no low reflecting boundary is applied to the base and side external boundaries of the 1000m x 1000m domain. There is a dominant peak at 100Hz as expected with no unwanted peaks. Significant peaks are peaks with greater than 95% statistical significance.

There is a notable dominant peak at 100Hz. However, there are several unwanted peaks in the spectrum caused by the seismic wave reflecting off of the external boundaries of the domain particularly between 30-60Hz, 80-95Hz and 105-110Hz. All peaks regarded as significant are defined as 95% statistically significant by the "normperiod".

Figure 6-15 (b) demonstrates the power spectrum obtained from Sensor 1 when the domain was 1000m x 1000m as presented in Section 6.2. As in Figure 6-15 (a) there is a dominant peak at 100Hz, however the amplitude of the signal is less and there is no unwanted peaks present in the spectrum (greater than 95% statistical significance). This implies that the reflections off of the external boundaries in the smaller domain model are contaminating the power spectrum of the signal as presented in Figure 6-15 (a).

These results prompted the utilisation of COMSOL's built in low reflecting boundary feature to establish if it is possible to reduce the domain without the problem of signal reflections at the boundaries.

6.3.2   Smaller domain with application of the low reflecting boundary

Basic theory associated with low reflecting boundaries is discussed in Chapter 4, Section 4.2.3, pg. 48.

In order to validate the effectiveness of the low reflecting boundaries further simulations were ran with granite as medium reducing the domain size to 75m to 75m (Figure 6-16) and then 25m x 25m (Figure 6-14) allowing a direct comparison with Figure 6-15 (a).
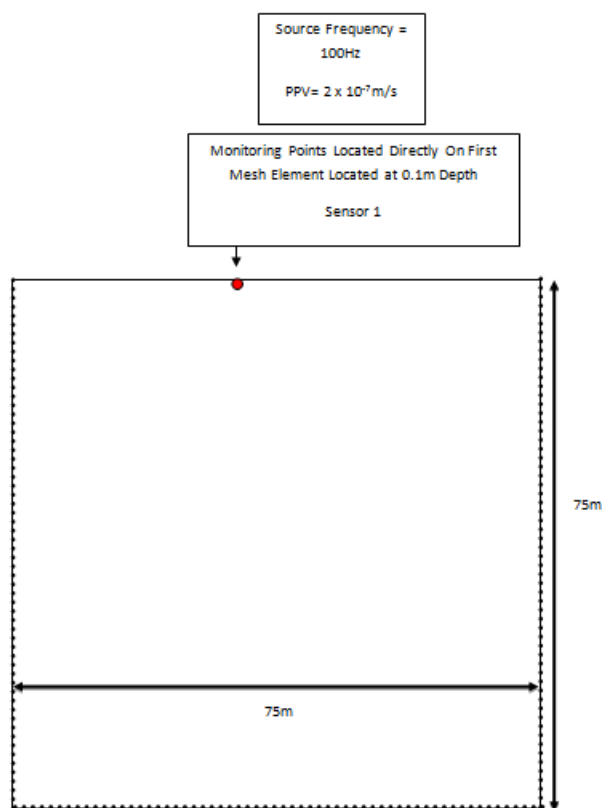
Figure 6-16: Schematic presentation of smaller granite domain model
The model dimensions are 75m x 75m. The source is applied vertically downwards at the surface at Sensor 1 (red dot). The black squares surrounding the base and sides of the domain highlight the low reflecting boundaries.

The low reflecting boundaries were applied to the base and side external boundaries highlighted in Figure 6-14 and Figure 6-16. The monitoring point is Sensor 1 as defined in Figure 6-14 and Figure 6-16, allowing a comparison between the 3 different domain sizes, ensuring that:

- the LNP spectra in Figure 6-17 (a), (b) and (c) could be evaluated/compared; and

- the LNP power and frequency had a percentage difference of less than 1%.
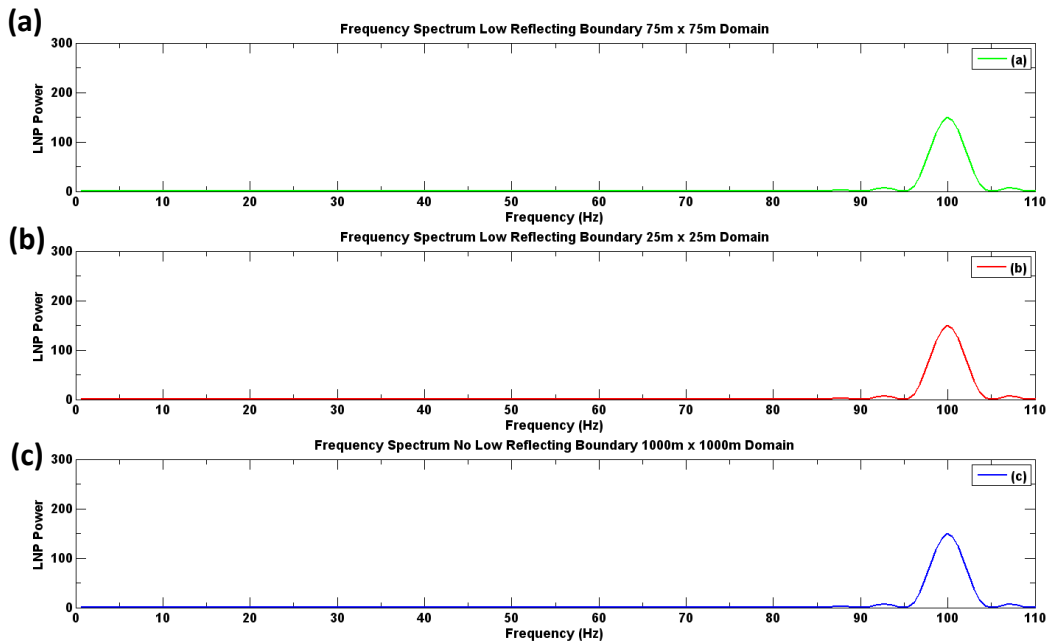
Figure 6-17: Comparison of power spectra for 3 domain sizes (a), (b) and (c): (a) 75m x 75m, (b) 25m x 25m and (c) 1000m x 1000m domain. Results in all cases are almost identical with a percentage difference of less than 1%. This means that the 25m x 25m domain is adequate for simulations instead of a large 1000m x 1000m domain. The data values used are the signal values at the location Sensor 1.

Using COMSOLs low reflecting boundary condition, the domain size was reduced from hundreds of meters to tens of meters, considerably reducing the number of computational elements and the solve time by a factor of 16 and 16.3 respectively. The memory storage requirements were reduced by a factor of 10.8 (Table 6-12).

Table 6-12: Table presenting the domain size, element size, number of elements and simulation solve time for each of the simulations presented in Figure 6-18.

Domain Size (m)	Element Size (m)	Number of Elements	Solve Time approx. (hours)	Memory Storage (Gigabytes)
1000 x 1000	1 x 1	1000000	61	61.04
1000 x 1000	0.1 x 0.1	100000000	Did not process as not enough RAM on PC	N/A
75 x 75	0.1 x 0.1	562500	34	17.76
25 x 25	0.1 x 0.1	62500	3.75	5.72

Figure 6-18 summarises the results obtained from the use of different domain sizes and the effective use of low reflecting boundary conditions to enable the reduction of the domain size.

There are three data sets considered:

1. **1000m x 1000m Domain (Green Squares):** Data set corresponds to Figure 6-9, pg. 76. The area of interest is 350m to ensure that there are no external boundary effects;

2. **75m x 75 Domain (Red Squares):** The area of interest is evaluated over 50m to ensure that there are no external boundary effects; and

3. **25m x 25m domain (Blue Crosses):** The area of interest is evaluated over 20m to ensure that there are no external boundary effects.
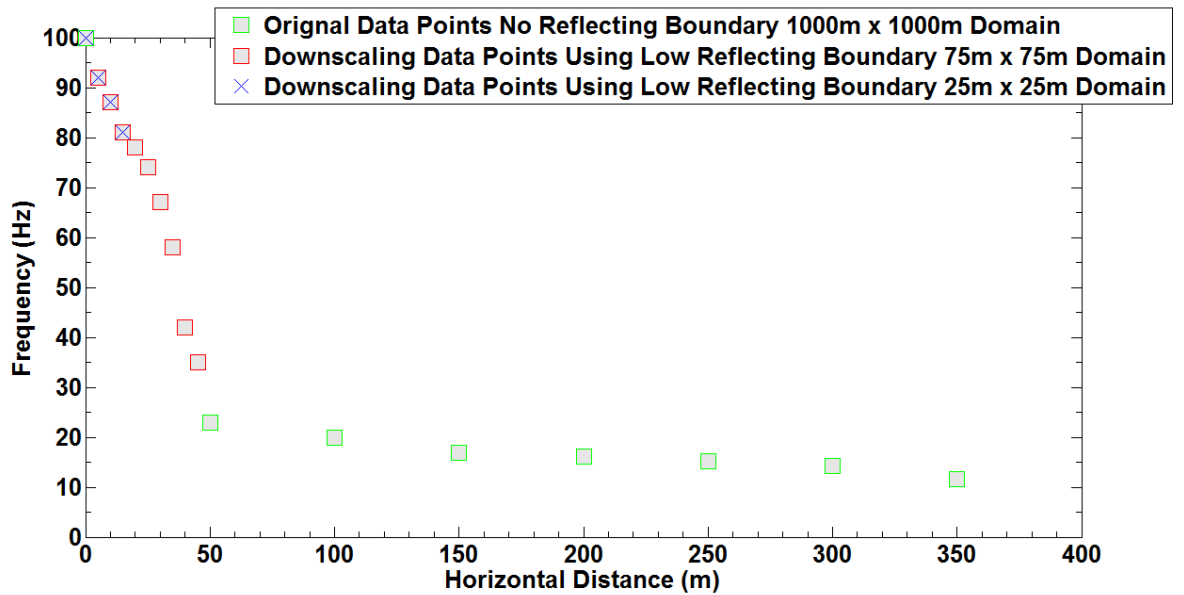
Figure 6-18: Frequency of seismic wave as a function of the horizontal distance from the source for 3 domain sizes: 1000m x 1000m (red squares), 75m x 75m (green squares) and 25m x 25m (blue crosses). The material properties are comparable with a granite rock. The data points are identical allowing the conclusion that the low reflecting boundaries are effective. The 25m x 25m was deemed suitable for future simulations effectively reducing simulation time.

The choice not to evaluate the signal over the full horizontal domain is a recommended numerical approach (Multiphysics 2014). Below is a summary of the key findings for each domain considered:

1000m x 1000m Domain (Green Squares): The green square represents results produced from a 1000m x 1000m domain, with no low reflecting boundary condition in place. These results are the same as those presented in Figure 6-9, pg. 76 when the induced source frequency is 100Hz. As detailed in Section 6.2.5, pg. 74 the largest reduction in frequency occurs in the first 50m of propagation.

75m x 75 Domain (Red Squares): It was decided to reduce the domain size to 75m x 75m utilising the low reflecting boundary condition which minimises unwanted reflections from the external boundaries while at the same time reduced simulation times. These results are represented by the red square with the aim of reducing the simulation time, memory constraints thus increasing simulation efficiency without having a negative impact on the robustness of the simulation.

The 75m x 75m simulation has monitoring points located every 5m, allowing the frequency reduction in the first 50m to be considered in more detail. The results in Figure 6-18 (red square) present a gradual reduction in the first 50m.

25m x 25m domain (Blue Crosses): The blue cross (Figure 6-18) represents results from a 25m x 25m domain utilising the low reflecting boundary condition. The smaller domain was chosen as this would most likely be the size of the seismic survey in the field. Good convergence takes place between all 3 simulations, demonstrating the effectiveness of using the low reflecting boundary condition for this domain size.

Conclusion: The low reflecting boundaries are effective in minimising reflection effects and in reducing the computational demands of the simulation. Over the first 50m of propagation in a granite domain there is a gradual reduction in the frequency of the seismic signal as expected.

The unwanted frequency peaks appear in the power spectrum produced in Section 6.3.1, Figure 6-15 (a), pg.93 when no low reflecting boundary is applied to the 25m x 25m domain. The unwanted reflections of the seismic wave off of the external boundaries imply that a material property boundary may have an effect on the frequency of the seismic signal as it propagates prompting further investigation.

In the subsequent Chapters a 25m x 25m domain will be used. A more refined mesh giving solutions with an accuracy of 0.1m instead of 1m is used giving a better representation of the detection scales at which new geophysical methods are being pushed

7 Numerical Simulations: The Effect of Medium Properties on Seismic Wave Propagation

7.1 Introduction

After the refinement of the numerical model, this Chapter focuses on the use of the refined model for the numerical simulation of:

1. the propagation of a seismic wave through one or more media; and
2. the spectral analysis of the signal (seismic wave) values at various distances from the source.

The aim of the analysis is to identify any potential changes in the spectral characteristics of the signal that are a result of the media through which the signal propagates. A number of different scenarios were considered, as outlined in Table 7-1. The response spectra observed is similar to those produced from construction vibrations, yielding response spectra similar to a harmonic motion rather than an earthquake (Tirado 2004).

For all scenarios the same basic model geometry was used: Figure 7-1 is a schematic of the model geometry used detailing:

- the application of the low reflecting boundary condition;
- induced source location and characteristics; and
- the monitoring point locations.

The domain is a 25m x 25m domain. The total length of the monitoring area is 15m. Sensor 1 is the base point where the source is located; sensor 2 is 5m from the source, sensor 3 is 10m from the source and sensor 4 is 15m from the source.
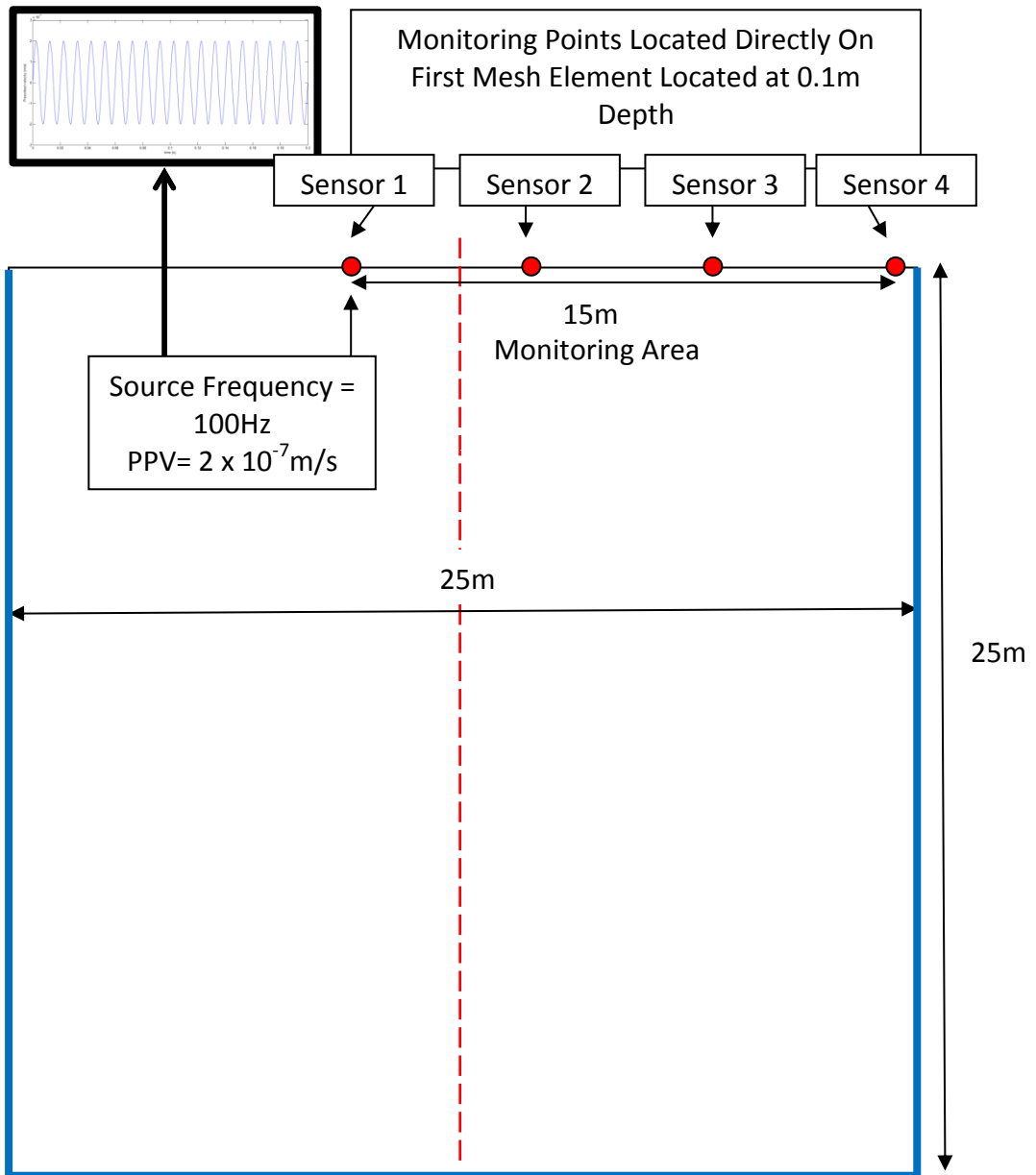
Figure 7-1: Schematic of model used in this Chapter. The low reflecting boundaries are highlighted in blue. The sensor locations (monitoring points) are also highlighted in red dots. The red dashed line represents the boundary between different materials when present.

Table 7-1: Different model scenarios considered in this Chapter, corresponding schematic representation and brief description

Scenario No.	Model Schematic Representation	Brief Description
1) Single Material Medium: Modelled area is defined with by one material property, i.e. there is no material change. **Aim:** Consider the effects of a single material property on the: 1) PPV (m/s); and 2) dominant frequency of the signal.		
1a) Granite		The material property modelled is granite. Granite is characterised by a high P wave velocity.
1b) Sandstone		The material property modelled is sandstone. Sandstone is characterised by a low P wave velocity.

Scenario No.	Model Schematic Representation	Brief Description
2) Two Different Materials Present Model is characterised by two different materials, to establish the effect of a material change on the seismic signal. The model domain consists of two vertical zones each of a different material. The boundary between the two materials is located 3m from the source. **Aim:** Consider the effects a material change on the: 1) PPV (m/s); and 2) dominant frequency of the signal. Establish if there is a notable difference between all scenarios and if a material property change can be detected.		
2a) Granite & Sandstone		The material properties modelled are granite (blue) and sandstone (orange). The red dashed line represents the boundary of the material change. Wave propagation from a high velocity to a low velocity zone
2b) Sandstone & Granite		The material properties modelled are sandstone (orange) and granite blue). The red dashed line represents the boundary of the material change. Wave propagation from a low velocity zone to a high velocity zone

Scenario No.	Model Schematic Representation	Brief Description
2c) Sandstone & Fracture Zone	Monitoring Points Located Directly On First Mesh Element Located at 0.1m Depth Sensor 1 Sensor 2 Sensor 3 Sensor 4 15m Monitoring Area Source Frequency = 100Hz PPV= 2 x 10⁻⁷m/s 25m 25m	The material properties modelled are sandstone (orange) and fracture zone (red). The red dashed line represents the boundary of the material change. Wave propagation from a low velocity zone to a slightly lower velocity zone

Table 7-2 presents the mechanical properties used in this Chapter. The material property boundary (material change) when present (Section 7.1.2) is located 3m from the source (Figure 7-1).

Table 7-2: Details of the mechanical properties for each material used in the simulations in Sections 7.1.1 and 7.1.2. Values are given for P wave and S wave velocity, density and Poisson's Ratio. Values were taken from Carmichael (1988).

Mechanical Property	Value
P Wave Velocity Sandstone	2000 m/s
S Wave Velocity Sandstone	1500 m/s
Density Sandstone	1000 kg/m^3
Poisson's Ratio Sandstone	0.2
P Wave Velocity Granite	4000 m/s
S Wave Velocity Granite	3000 m/s
Density Granite	2000 kg/m^3
Poisson's Ratio Granite	0.3
P Wave Velocity Fracture Zone	1000 m/s
S Wave Velocity Fracture Zone	500 m/s
Density Host Fracture Zone	1000 kg/m^3
Poisson's Ratio	0.2

7.1.1　Scenario 1: Single material medium

The domain consists of a single material:　1) a granite only domain was considered followed by 2) a sandstone only domain as detailed in Table 7-1. The rationale behind simulating one material only is to:

1. verify the previous simulations for a granite domain;
2. consider the effects of the material property on PPV)(m/s); and
3. consider the effects of the material property on the dominant frequency of the signal.

7.1.1.1　Scenario 1a: Granite

Figure 7-2 presents the effects of granite as the sole material in the domain on the PPV and frequency of the signal. Results are summarised in Table 7-3.
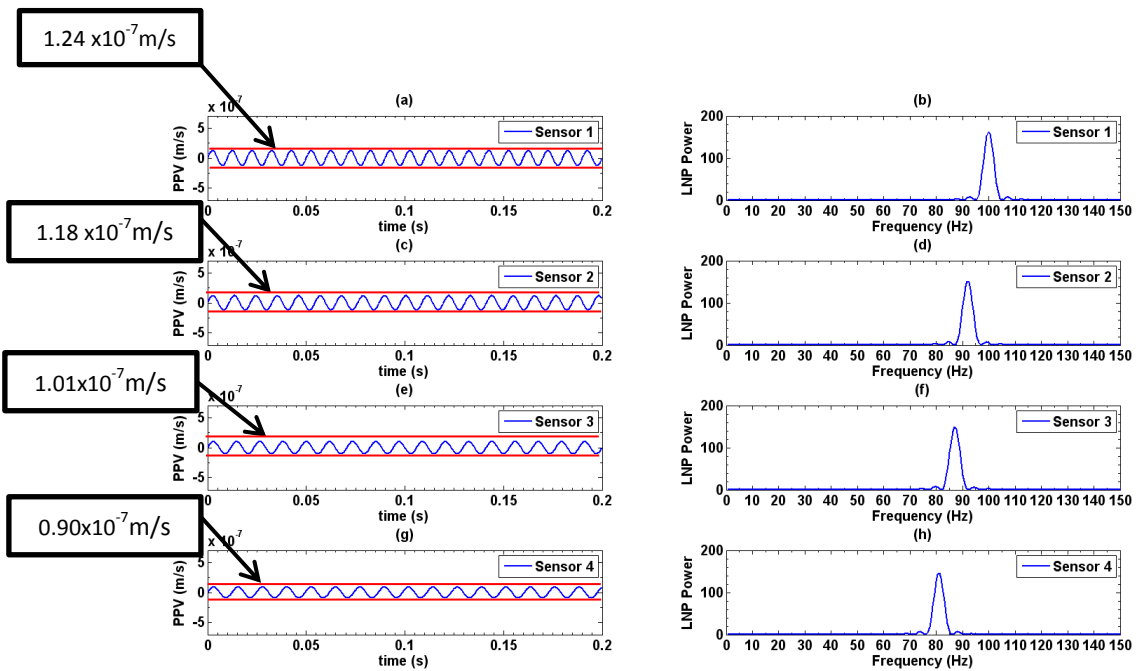
Figure 7-2: Scenario 1a – Granite only: PPV (left) and Dominant Frequency (right) changes over distance from the source for granite as the sole material property in the domain. Each line of the graph from top corresponds to a sensor located at distances 0m, 5m, 10m and 15m from the source, respectively. As the distance from the source increases a reduction in PPV, dominant frequency amplitude and dominant frequency value is observed. The PPV amplitude remains constant over the whole 0.2s monitoring interval for each sensor location.

Table 7-3: Scenario 1a: Granite Results. Column 1: Distance of monitoring point from source, Column 2: PPV observed Column 3: The change in PPV observed from the previous monitoring point, Column 4: Amplitude of dominant frequency from LNP spectrum, Column 5: Dominant frequency of LNP spectrum, Column 6: Change in amplitude observed from the previous monitoring point Column 7: Change in dominant frequency observed from the previous monitoring point

$*$ **This denotes the change from the source location**

		Change from previous sensor			Change from previous sensor	
Column 1: Distance from Source	Column 2: PPV (m/s)	Column 3: PPV (m/s)	Column 4: Amplitude	Column 5: Frequency (Hz)	Column 6: Amplitude	Column 7: Frequency (Hz)
0m (base point)	1.24×10^{-7}	0.76×10^{-7} *	162.5	100	-	0
5m	1.18×10^{-7}	0.06×10^{-7}	150.9	92	11.6	8
10m	1.01×10^{-7}	0.17×10^{-7}	148.9	87	2.0	5
15m	0.9×10^{-7}	0.11×10^{-7}	145.8	81	3.1	6

Dominant Frequency: The reduction in dominant frequency is in agreement with previous simulations in a granite domain Chapter 6, Section 6.3, Figure 6-18, pg. 97. The amplitude of the PPV over the 0.2s monitoring duration at each sensor remains the same, which can be explained by:

1. source is steady state;
2. no material property boundary; and
3. low reflecting boundary conditions ensure that there are no reflections.

PPV: Interestingly, the PPV at the base point demonstrates a reduction of 0.76×10^{-7} m/s when compared to the PPV of the source, a significant reduction compared to the reduction in PPV that takes place at 5m, 10m and 15m from the source. This can be explained by the fact the monitoring point is located 0.1m from the source on the first mesh element, therefore the exact PPV of the source would not be an expected value. Also, the surface boundary is modelled as a free surface thus the rock to air interface will affect the PPV value observed.

Key Observation: For PPV, dominant frequency amplitude and dominant frequency there is a gradual reduction in the detected value.

7.1.1.2 Scenario 1b: Sandstone

Figure 7-3 presents the effects of sandstone as the sole material in the domain on PPV and frequency of the signal, results are summarised in Table 7-4.
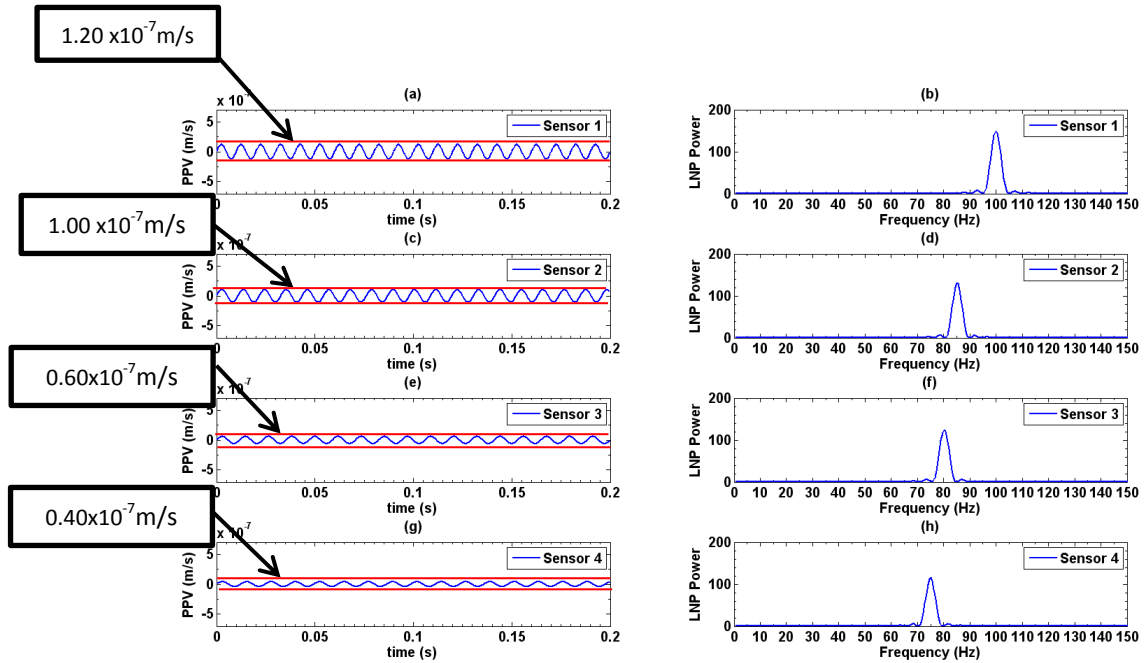
Figure 7-3: Scenario 1b – Sandstone only: PPV (left) and Dominant Frequency (right) changes over distance from the source for sandstone as the sole material property in the domain. Each line of the graph from top corresponds to a sensor located at distances 0m, 5m, 10m and 15m from the source, respectively. As the distance from the source increases a reduction in PPV, dominant frequency amplitude and dominant frequency value is observed. The PPV amplitude remains constant over the whole 0.2s monitoring interval for each sensor location.

Table 7-4: Scenario 1b: Sandstone Results. Data in blue brackets represents the difference from the corresponding Scenario 1a value. Column 1: Distance of monitoring point from source, Column 2: PPV observed Column 3: The change in PPV observed from the previous monitoring point, Column 4: Amplitude of dominant frequency from LNP spectrum, Column 5: Dominant frequency of LNP spectrum, Column 6: Change in amplitude observed from the previous monitoring point Column 7: Change in dominant frequency observed from the previous monitoring point

* **This denotes the change from the source location**

		Change from previous sensor			Change from previous sensor	
Column 1: Distance from Source	**Column 2: PPV (m/s)**	**Column 3: PPV (m/s)**	**Column 4: Amplitude**	**Column 5: Frequency (Hz)**	**Column 6: Amplitude**	**Column 7: Frequency (Hz)**
0m (base point)	1.20×10^{-7}	0.80×10^{-7}* (0.04×10^{-7})	149.6	100	- (12.9)	0
5m	1.00×10^{-7}	0.20×10^{-7} (0.18×10^{-7})	130.8	85	18.8 (20.1)	15 (7)
10m	0.6×10^{-7}	0.4×10^{-7} (0.41×10^{-7})	124.8	80	6.0 (24.1)	5 (7)
15m	0.4×10^{-7}	0.20×10^{-7} (0.5×10^{-7})	115.7	75	9.1 (30.1)	5 (6)

Dominant Frequency: The reduction in dominant frequency is greater that the reduction observed in Scenario 1a.

PPV: The amplitude of the PPV over the 0.2s monitoring duration at each sensor remains the same as observed in Scenario 1a.

Key Observation: PPV, dominant frequency amplitude and dominant frequency a gradual reduction in the detected value is observed which is greater that the reduction observed for Scenario 1a at all monitoring points. There is a clear detectable difference between the parameter values observed for Scenario 1a and Scenario 1b.

This is expected as Scenario 1b has a lower P wave velocity, causing the seismic signal to attenuate quickly resulting in a reduced particle displacement (PPV) within in the medium.

7.1.2   **Scenario 2: Two different materials present**

For this scenario the domain consists of two vertical zones each of a different material. The boundary between the two materials is located 3m from the source (See Table 7-1).

Firstly, granite zone followed by a sandstone zone is considered. Secondly, a sandstone zone followed by a granite zone is considered as detailed in Table 7-1, pg. 101. The rationale behind considering these two numerical simulations is to establish:

1. if there is any change in the PPV and dominant frequency when the seismic signal propagates from a high velocity zone (granite) to a low velocity zone (sandstone);

2. if the difference in material properties can be detected using the PPV and dominant frequency values over time; and

3. if the difference between the two scenarios can be detected using the parameters above.

Lastly, a sandstone zone followed by a fracture zone is considered, with the material property boundary located 3m from the source. The rationale behind considering this numerical scenario is to establish if:

1. a material property boundary can be detected when the difference between P wave velocities of the different zones is relatively small; and

2. there is a notable difference in the PPV and dominant frequency between all of the scenarios considered.

7.1.2.1 Scenario 2a: Granite and Sandstone: Wave propagation from a high velocity to a low velocity zone

Figure 7-4 presents results for the granite zone and sandstone zone contained within the same domain, results are summarised in Table 7-5.
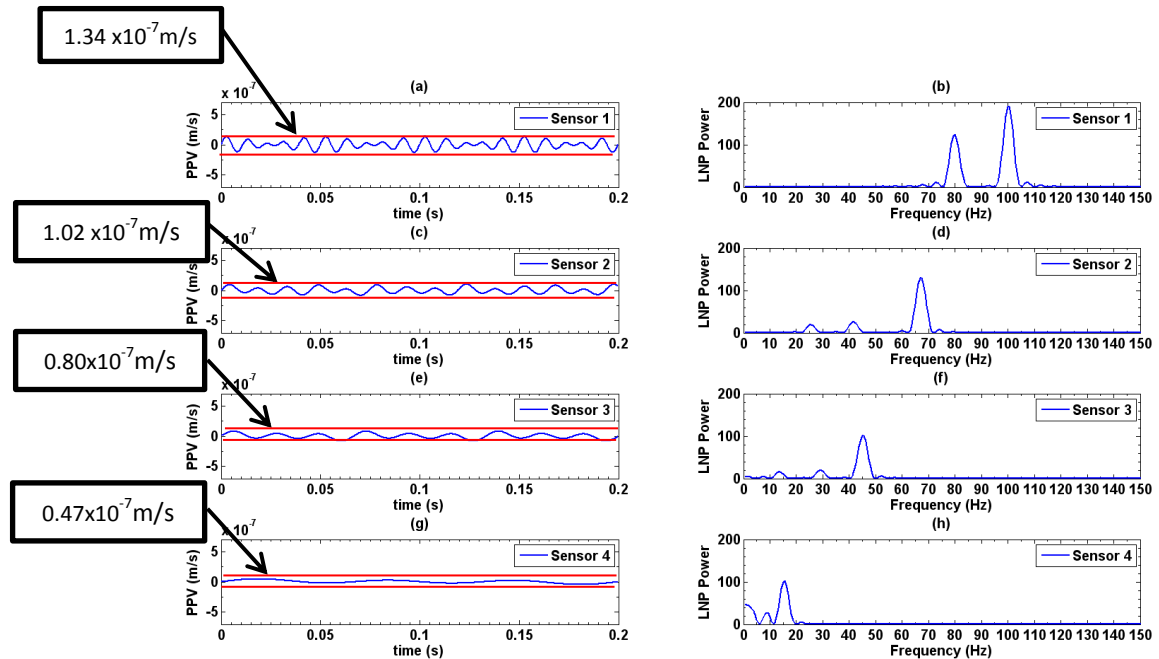
Figure 7-4: Scenario 2a Granite and Sandstone: PPV (left) and Dominant Frequency (right) for a granite zone followed by a sandstone zone .with the material boundary located 3m from the source Each line of the graph from top corresponds to distances: 0m, 5m, 10m and 15m from the source, respectively.As the distance from the source increases when see a reduction in PPV, amplitude and dominant frequency values. The formation of secondary peak in frequency spectra is observed at each sensor location.

Table 7-5: Scenario 2a: Granite and sandstone results. Data in blue brackets represents the difference from the corresponding Scenario 1a value. Data in orange represents the difference from the corresponding Scenario 1b value. Column 1: Distance of monitoring point from source, Column 2: PPV observed Column 3: The change in PPV observed from the previous monitoring point, Column 4: Amplitude of dominant frequency from LNP spectrum, Column 5: Dominant frequency of LNP spectrum, Column 6: Change in amplitude observed from the previous monitoring point Column 7: Change in dominant frequency observed from the previous monitoring point

* **This denotes the change from the source location**

The + represents when there has been an increase in the value of the corresponding parameter i.e. a value of 1.34 x10^{-7}m/s is observed, a reduction of 0.66x10^{-7} m/s, when compared to the PPV of the source and a (+0.1 x10^{-7}m/s) increase and a (+0.14 x10^{-7}m/s) increase when compared to a Scenario 1a and 1b respectively.

| Column 1: Distance from Source | Column 2: PPV (m/s) | Change from previous sensor | | Column 5: Frequency (Hz) | Change from previous sensor | |
		Column 3: PPV (m/s)	Column 4: Amplitude		Column 6: Amplitude	Column 7: Frequency (Hz)
0m (base point)	1.34 x10^{-7}	0.66x10^{-7} * (+0.1 x10^{-7}) (+0.14 x10^{-7})	190.1	100	- (+27.6) (+40.5)	0
5m	1.02 x10^{-7}	0.32x10^{-7} (0.16 x10^{-7}) (+0.02 x10^{-7})	130	67	60.1 (20.9) (0.8)	33 (25) (18)
10m	0.8x10^{-7}	0.22x10^{-7} (0.21 x10^{-7}) (+0.20 x10^{-7})	101	45	29 (47.9) (23.8)	22 (42) (35)
15m	0.47 x10^{-7}	0.33x10^{-7} (0.44 x10^{-7}) (+0.65 x10^{-7})	103.3	15	+2.3 (42.5) 12.4	30 (66) (60)

Dominant Frequency: The reduction in dominant frequency is greater than the reduction observed in Scenario 1 (Section 7.1.1).

PPV: The amplitude of the PPV over the 0.2s monitoring duration at each sensor does not remain the same, implying that the interaction of the wave with the material boundary results in a change in PPV amplitude. The PPV observed at the source is greater than the PPV observed in Scenario 1, indicating that the material boundary causes some of the wave's energy to be reflected back toward the source causing an increased PPV.

The PPV after the wave passes through material boundary is consistently less than Scenario 1a and consistently greater than the value for Scenario 1b. As the wave

hits a domain with a lower P wave velocity (Scenario 2a) less energy is reflected off of the material boundary and the wave continues to propagate into the domain.

Additional Frequency Peaks: In the power spectrum additional frequency peaks (Table 7-6), which appear to be the result of a material property boundary being present. As the signal interacts with the material boundary, the energy of the signal is dispersed or attenuated. The dominant frequency of the signal also disperses, forming additional frequency peaks.

Table 7-6: Scenario 2a: Granite zone followed by a sandstone zone. Additional peak data (peaks in addition to the dominant frequency peaks) Column 1: Distance from the source, Column 2: Amplitude of frequency peaks observed in the LNP spectra Column 3: Frequency of peaks observed in the LNP spectra

Distance from Source	Amplitude	Frequency (Hz)
0m (base point)	123.5	80
5m	25	41
	19.4	26
10m	20	29
	16	14
15m	28.1	9
	45.3	1

Key Observation: The reduction in dominant frequency amplitude and dominant frequency is greater than in the domain where there is one material property. This implies that the dominant frequency amplitude and frequency characteristics vary differently for different material properties and when there is a material change.

7.1.2.2 Scenario 2b: Sandstone and Granite: Wave propagation from a low velocity to a high velocity zone

Figure 7-5 presents results for the sandstone zone and granite zone contained within the same domain, results are summarised in Table 7-7.
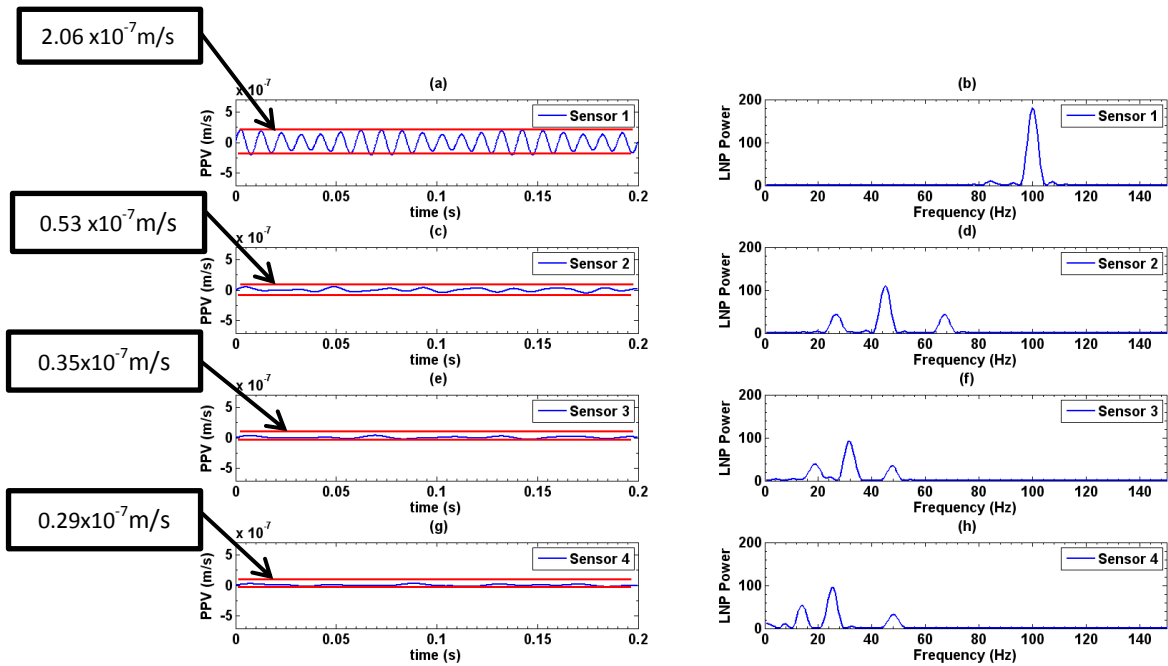
Figure 7-5: Scenario 2b – Sandstone and granite: PPV (left) and Dominant Frequency (right) for sandstone zone followed by a granite zone with the material property boundary located 3m from the source. Each line of the graph from top corresponds to distances: 0m, 5m, 10m and 15m from the source, respectively. As the distance from the source increases when see a reduction in PPV, amplitude and dominant frequency values. The formation of secondary peak in the frequency spectra is observed. There is a notable change in values compared to the Scenario 2a.

Table 7-7: Scenario 2b: Sandstone and granite results. Data in blue brackets represents the difference from the corresponding Scenario 1a. Data in orange represents the difference from the corresponding Scenario 1b. Data in green represents the difference from Scenario 2a. Column 1: Distance of monitoring point from source, Column 2: PPV observed Column 3: The change in PPV observed from the previous monitoring point, Column 4: Amplitude of dominant frequency from LNP spectrum, Column 5: Dominant frequency of LNP spectrum, Column 6: Change in amplitude observed from the previous monitoring point Column 7: Change in dominant frequency observed from the previous monitoring point

* **This denotes the change from the source location**

The + represents when there has been an increase in the value of the corresponding parameter i.e. a value of 1.34 $\times 10^{-7}$m/s is observed, a reduction of 0.66$\times 10^{-7}$ m/s, when compared to the PPV of the source and a (+0.1 $\times 10^{-7}$m/s) increase and a (+0.14 $\times 10^{-7}$m/s) increase when compared to a Scenario 1a and 1b respectively.

Column 1: Distance from Source	Column 2: PPV (m/s)	Change from previous sensor — Column 3: PPV (m/s)	Column 4: Amplitude	Column 5: Frequency (Hz)	Change from previous sensor — Column 6: Amplitude	Column 7: Frequency (Hz)
0m (base point)	2.06 $\times 10^{-7}$	+0.06$\times 10^{-7}$ * (+0.83 $\times 10^{-7}$) (+0.86 $\times 10^{-7}$) (+0.72 $\times 10^{-7}$)	176.3	100	- (+13.8) (+26.7) (13.8)	0
5m	0.53 $\times 10^{-7}$	1.53$\times 10^{-7}$ (0.65 $\times 10^{-7}$) (0.47 $\times 10^{-7}$) (0.49 $\times 10^{-7}$)	110	45	66.3 (40.9) (20.8) (20)	55 (47) (40) (22)
10m	0.35$\times 10^{-7}$	0.18$\times 10^{-7}$ (0.66 $\times 10^{-7}$) (0.25 $\times 10^{-7}$) (+0.45 $\times 10^{-7}$)	91	31	19 (57.9) (33.8) (10)	14 (56) (49) (14)
15m	0.29 $\times 10^{-7}$	0.06 $\times 10^{-7}$ (0.61$\times 10^{-7}$) (0.11$\times 10^{-7}$) (0.18 $\times 10^{-7}$)	92	26	+1 (53.8) (23.7) (11.3)	5 (55) (49) (+11)

Dominant Frequency: The reduction in dominant frequency is greater than the reduction observed in Scenario 1 (Section 7.1.1).

The dominant frequency observed at the source, 5m and 10m from the source is less than the comparable dominant frequency in scenario 2a. As sandstone causes the wave to slow down quicker than the granite, more energy is initially lost and a quicker reduction in dominant frequency is observed. At 15m from the source the dominant frequency observed is greater than scenario 2a as the wave is propagating in granite (high P wave velocity).

PPV: The amplitude of the PPV over the 0.2s monitoring duration at each sensor does not remain the same as observed in Scenario 2a. The PPV observed at the source is greater than the PPV observed in Scenario 1 and Scenario 2a.

The time for the wave to attenuate is less when it hits a zone with a higher P wave velocity (Scenario 2b), therefore the force exerted on the wave is more i.e. more of the waves energy is reflected off of the material boundary causing an increase in PPV.

The PPV after the wave passes through material boundary is consistently less than the value for Scenario 1a and consistently greater than the value for Scenario 1b. The sandstone zone attenuates the signal more than Scenario 1a domain, and the granite zone attenuates the signal less than Scenario 1b.

Additional Frequency Peaks: Additional frequency peaks are observed in the power spectrum (Table 7-8) as in Scenario 2a.

Table 7-8: Scenario 2b: Sandstone zone followed by a granite zone. Additional peak data (peaks in addition to the dominant frequency peaks). Column 1: Distance from the source, Column 2: Amplitude of frequency peaks observed in the LNP spectra Column 3: Frequency of peaks observed in the LNP spectra Additional peak data

Distance from Source	Amplitude	Frequency (Hz)
0m (base point)	10.33	84
5m	43.4	67
	43.7	27
10m	33.6	48
	37.3	19
15m	32.4	48
	54	14

Key Observation: The data implies that the dominant frequency amplitude and frequency characteristics vary differently for different material properties and when there is a material change. There is a clear difference in dominant frequency and PPV when a signal propagates from high velocity zone to a low velocity zone and from a low velocity zone to a high velocity zone.

7.1.2.3   Scenario 2c: Sandstone and Fracture Zone: Wave propagation from a low velocity to a slightly lower velocity zone

Figure 7-6 presents results for the sandstone zone and fracture zone contained within the same domain, results are summarised in Table 7-9.
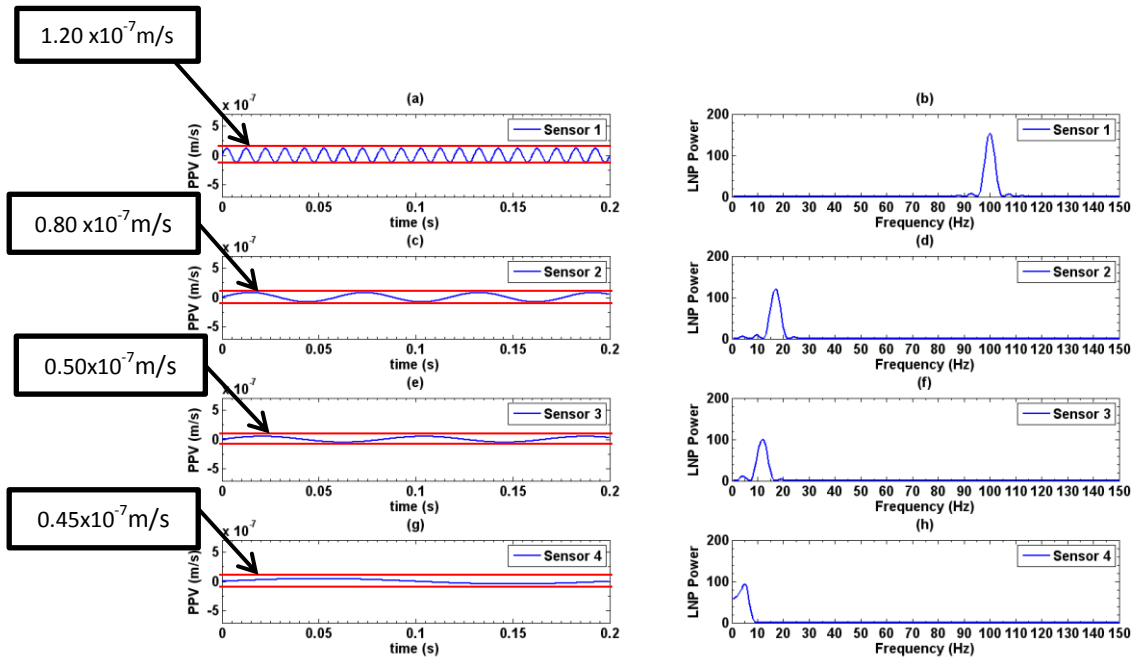

Figure 7-6: Scenario 2c – Sandstone and Fracture Zone: PPV (left) and Dominant Frequency (right) for sandstone zone followed by a fracture zone contained within one domain with the material property boundary located 3m from the source. Each line of the graph from top corresponds to distances: 0m, 5m, 10m and 15m from the source, respectively. As the distance from the source increases when see a reduction in PPV, amplitude and dominant frequency values for all monitoring point locations. The formation of secondary peak in frequency spectra is not clearly observed. There is a notable change in values compared to all other scenarios.

Table 7-9: Scenario 2c: Sandstone and fracture zone results. Data in blue brackets represents the difference from Scenario 1a. Data in orange represents the difference from Scenario 1b. Data in green represents the difference from Scenario 2a. Data in red represents the difference from Scenario 2b. Column 1: Distance of monitoring point from source, Column 2: PPV observed Column 3: The change in PPV observed from the previous monitoring point, Column 4: Amplitude of dominant frequency from LNP spectrum, Column 5: Dominant frequency of LNP spectrum, Column 6: Change in amplitude observed from the previous monitoring point Column 7: Change in dominant frequency observed from the previous monitoring point

* **This denotes the change from the source location**

The + represents when there has been an increase in the value of the corresponding parameter i.e. a value of 1.34 $\times10^{-7}$ m/s is observed, a reduction of 0.66$\times10^{-7}$ m/s, when compared to the PPV of the source and a (+0.1 $\times10^{-7}$ m/s) increase and a (+0.14 $\times10^{-7}$ m/s) increase when compared to Scenario 1a and 1b respectively.

		Change from previous sensor			Change from previous sensor	
Column 1: Distance from Source	Column 2: PPV (m/s)	Column 3: PPV (m/s)	Column 4: Amplitude	Column 5: Frequency (Hz)	Column 6: Amplitude	Column 7: Frequency (Hz)
0m (base point)	1.20×10^{-7}	0.80×10^{-7} * (0.04$\times10^{-7}$) (0) (0.14$\times10^{-7}$) (0.86 $\times10^{-7}$)	154.5	99	- (8) (+4.9) (35.6) (21.8)	1 (1) (1) (1) (1)
5m	0.80×10^{-7}	0.40×10^{-7} (0.38 $\times10^{-7}$) (0.20$\times10^{-7}$) (0.22 $\times10^{-7}$) (+0.27 $\times10^{-7}$)	120.2	17	34.3 (30.7) (10.6) (9.8) (+10.2)	82 (75) (68) (50) (28)
10m	0.50×10^{-7}	0.30×10^{-7} (0.51$\times10^{-7}$) (0.10 $\times10^{-7}$) (0.3 $\times10^{-7}$) (+0.15 $\times10^{-7}$)	100	12	20.2 (48.9) (24.8) (1) (+9)	5 (75) (68) (33) (19)
15m	0.45×10^{-7}	0.05×10^{-7} (0.45 $\times10^{-7}$) (+0.05$\times10^{-7}$) (0.02 $\times10^{-7}$) (+0.16 $\times10^{-7}$)	94	5	6 (51.8) (21.7) (9.3) (+2)	7 (76) (70) (10) (21)

Dominant Frequency: The reduction in dominant frequency is greater than the reduction observed with previous scenarios, indicating that when material two zones have a lesser contrast in P wave velocity i.e. 1000m/s instead of 2000m/s (Table 7-2) a notable difference in dominant frequency is still observed.

Sandstone followed by the fracture zone will cause the wave to slow down quicker than the other scenarios, losing more energy thus a quicker reduction in dominant frequency is observed.

PPV: The amplitude of the PPV over the 0.2s monitoring duration at each sensor remains relatively similar, comparable to Scenario 1 (Section 7.1.1). This suggests that when the change in material properties between two zones is less pronounced PPV is not as responsive or sensitive to the change as the dominant frequency.

The PPV observed at the source is less than the PPV observed for all scenarios, indicating that when the contrast in P wave velocity is not large the material boundary causes less of the wave's energy to be reflected back towards the source.

Additional Peaks: In the power spectrum, the formation of additional peaks is not significant, therefore for the formation of significant additional peaks to be present in the spectra the contrast in material properties must be large i.e. greater than 1000m/s.

Key Observation: The dominant frequency amplitude and frequency characteristics vary differently for different material properties and when there is a material change. There is a clear difference in dominant frequency and PPV when a signal propagates from high velocity zone to a low velocity zone and from a low velocity zone to a high velocity zone.

7.1.3   **Combination of Results**

This section aims to answer the question:

Does the presence of a material property boundary affect the way that the PPV and dominant frequency of a seismic wave change over distance from the source?

Figure 7-7 (a) and (b) combine the PPV and dominant frequency data respectively from the numerical simulations in Sections 7.1.1 and 7.1.2 to determine if it is possible to detect the presence of a geological boundary or feature. Table 7-10 presents a summary of the key observations.

(a)

(b)
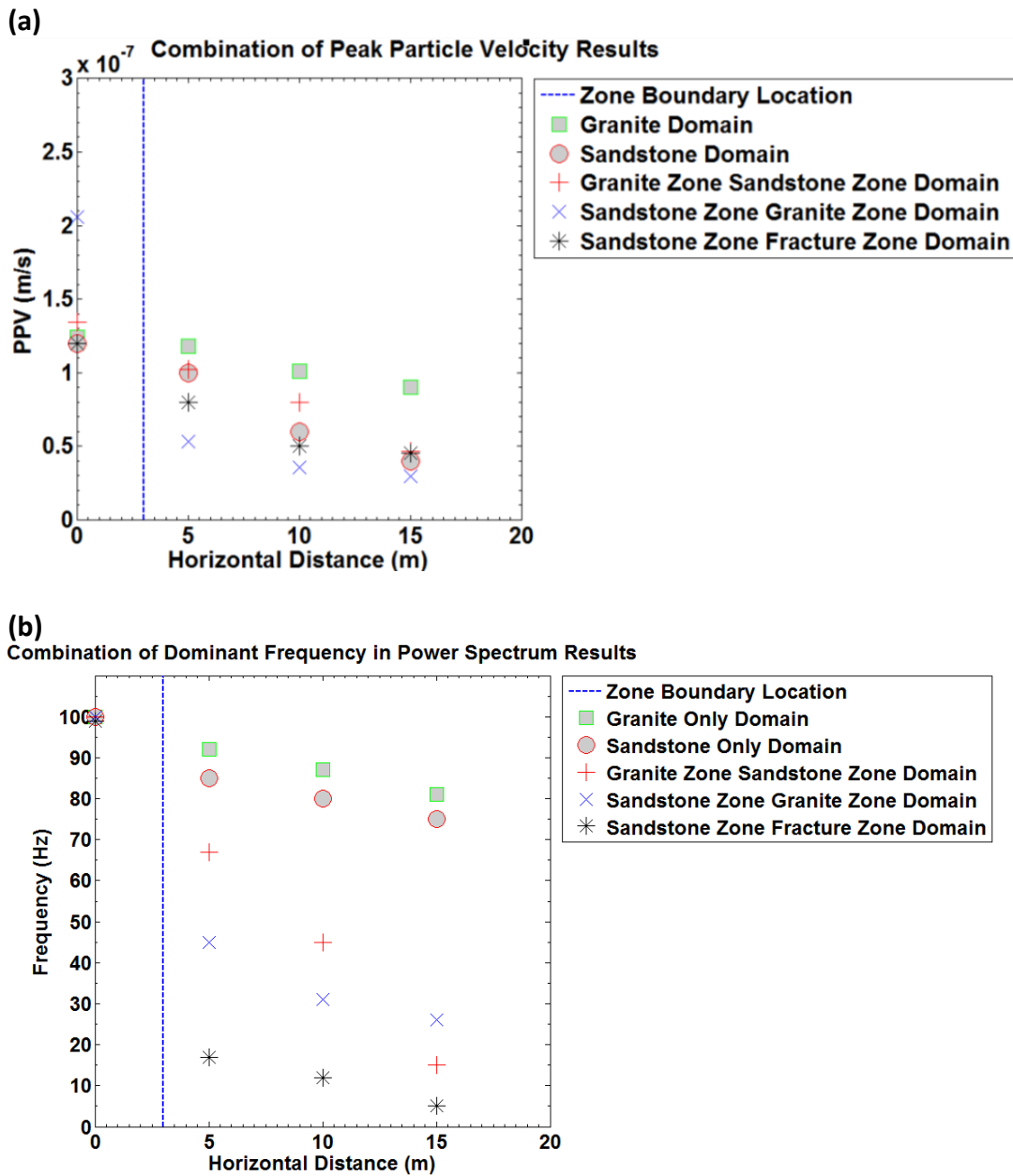
Figure 7-7: (a) PPV and (b) dominant frequency values from Section 7.1.1 and 7.1.2 as a horizontal profile along the monitoring cross section with the material boundary located at 3m from the source (dashed blue line)

PPV: There is a clear distinction between PPV values when the domain is characterised by granite (Scenario 1a: one material property).

There is potential to use the variation in PPV to detect geological feature width however, it may be more useful for detecting the location as PPV appears to vary more readily with distance.

Dominant Frequency: There is a clear distinction observed in the dominant

frequency values when the domain is characterised by one material only (Scenario 1) compared to when the domain is characterised by different material property zones (Scenario 2). There is potential to use the variation in dominant frequency to detect geological feature width due to the response when a material property boundary is present. It may be less useful for detecting the location as the dominant frequency does not vary rapidly with distance.

Table 7-10: Summary of observations obtained from simulations in this Chapter. Column 1: Scenario consdered, Column 2: Symbol Represented in Figure 7-7, Column 3: Key PPV observations, Column 4: Key dominant frequency observations. Green: Imdicates a clear dectable differnece in values is observed. Red: No clear distinction between the values is observed.

Column 1: Scenario	Column2: Figure 7-7 Symbol	Column 3: PPV	Column 4: Dominant Frequency
Scenario 1a: Granite	Green Square ▣	Clear distinction between these results and the other scenarios	Clear distinction between these results and the other scenarios Dominant frequency appears more responsive to a material change than PPV.
Scenario 1b: Sandstone	Red Circle ◯	Gradual reduction in PPV. No clear distinction between this and the other data sets where another material property zone is present.	Clear distinction between these results and the other scenarios
Scenario 2a: Granite zone followed by a sandstone zone	Red Cross ✚	Gradual reduction in PPV. No clear distinction between this and the other data sets where another material property zone is present	Clear distinction between these results and the other scenarios
Scenario 2b: Sandstone zone followed by a granite zone **Only scenario that considers a low velocity zone followed by a high velocity zone.**	Blue Cross X	Clear distinction between these results and the other scenarios	Clear distinction between these results and the other scenarios
Scenario 2c: Sandstone zone followed by a fracture zone	Black Asterisk ✳	Gradual reduction in PPV. No clear distinction in PPV. PPV detected is similar to that of Scenario 1b	Clear distinction between these results and the other scenarios

Key Observation: The presence of a material property boundary affects the way that the PPV and dominant frequency of a seismic wave change over distance from the source. Table 7-10 shows that dominant frequency offers better detectability than PPV. The dominant frequency values show a detectable distinction between all scenarios observed, for PPV this is only true when the material property contrast is sufficient.

7.2   Summary and Conclusions

In this chapter it was shown that the dominant frequency of the seismic wave is affected by the presence of a material property boundary and the P wave velocity of the medium.

A significant enough change in the dominant frequency of the seismic signal has been observed to prompt further investigation to simulate geological features that may be of interest in engineering applications. A variation in PPV was also observed particularly when there was a sufficient material property contrast. PPV may be used in conjunction with dominant frequency to determine a geological feature width and possibly used to determine geological feature location.

Previous research and this thesis have shown that the dominant frequency of the signal should be proportional to the seismic velocity as observed in Chapter 6, Figure 6-12, pg.88. The theory and these results also suggests that higher dominant frequencies are observed within rock characterised by a high P wave velocity (Tirado 2004). This can be explained by granite having greater P wave transmission than a sandstone or fracture zone, which lends support to the relationship observed and the detectability of material property change.

It was observed that the dominant frequency detected reduces as the distance from the source increases. This can be explained by the lower frequency components having travelled fewer deformation cycles, therefore have lost proportionally less energy. Higher frequencies have shorter wavelengths, therefore they require a

greater number of cycles per motion to travel the same distance as a low frequency source, thus higher frequencies are attenuated more.

8   A New Concept for a Near Surface Seismic Site Investigation Tool

Over the small distances this thesis is focusing on (no more than 10m), it has been demonstrated that the frequency of 100Hz generated by the source is not present in the frequency spectrum at the location of sensor 2 (5m from the source). This is also evidenced by the frequency convergence concept presented in Chapter 6, Section 6.2, pg.55.

In Chapter 6 it was established that the original frequency of the 100Hz signal drops to a certain value (convergence value) over distances greater than 50m. Over distances less than 50m the convergence value is not reached, although a significant reduction and change in the dominant frequency of the signal takes place.

It was observed that low frequencies (1-100Hz) converge at a faster rate, and over a shorter distance (Figure 6-9, pg.76 and Figure 6-11, pg.84) and that the dominant frequency was responsive to the presence of a material property boundary (Chapter 7, Section 7.1.2, pg.109). This could potentially be used as a concept to detect geological features.

In Chapter 7, it was established that the PPV of the signal drops as the distance from the source increases in a single material domain (Chapter 7, Section 7.1.1, pg. 105). A variation in PPV was also observed, particularly when there was a sufficient material property contrast between two material zones (Chapter 7, Section 7.1.2, pg.109). The PPV parameter could potentially be used in conjunction with the dominant frequency to determine a geological feature width and possibly be used to determine geological feature location.

This Chapter aims to further investigate whether the change in the dominant frequency and PPV observed as the seismic wave travels away from the source can be used to image geological features (i.e. identify their presence and geometrical

characteristics). Additionally, the potential of distinguishing between features or P wave velocity zones e.g. a dyke or a fracture zone is explored.

8.1   Target Geological Features

Several different geological scenarios are considered. Figure 8-1 highlights the potential scenario such as a central feature surrounded by a low velocity zone i.e. a fractured zone. Several different central feature widths were simulated for various low velocity zone widths; a schematic of the numerical set up is presented in Figure 8-2.
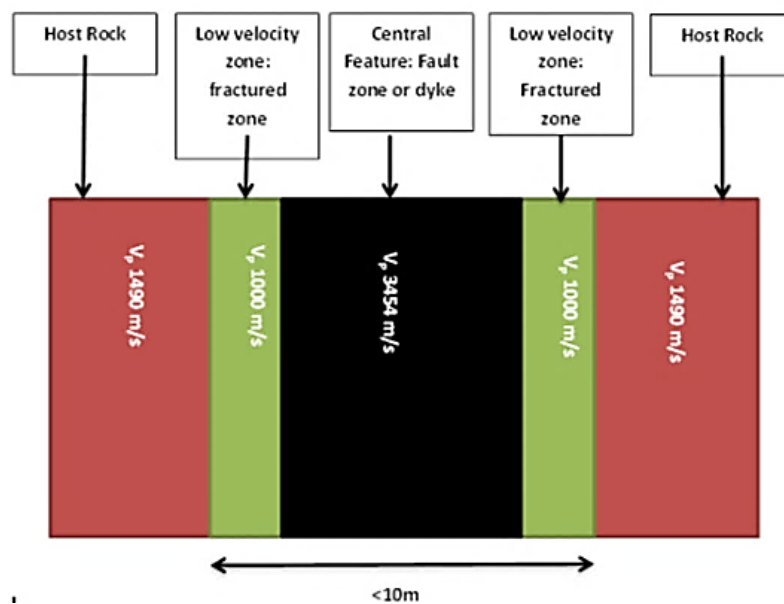
Figure 8-1: Schematic detailing the different velocity zones considered (plan view). These would be representative of a fault zone surrounded by a fractured zone or geological intrusion (dyke) that is well jointed and surrounded by a chilled and baked margin.

The simulation method used in COMSOL was the same as that applied in Chapter 7 for a 25m x 25m domain. The simulation time was 0.25s and the window analysed was 0.2s as previously demonstrated in Figure 6-2. A total of 4 low velocity zone widths were considered with various central feature widths resulting in a total of 27 simulations. The parameters used for the simulations are presented in Table 8-1, while the different model set ups are summarised in Table 8-2.

Table 8-1: Table Detailing Mechanical Properties. These values used in the simulations in line with values from Carmichael (1988).

Mechanical Property	Value
P Wave Velocity Host Rock	1490 m/s
S Wave Velocity Host Rock	985 m/s
Density Host Rock	2000 kg/m^3
P Wave Velocity Central Feature	3454 m/s
S Wave Velocity Central Feature	2100 m/s
Density Central Feature	3000 kg/m^3
P Wave Velocity Low Velocity Zone	1000 m/s
S Wave Velocity Low Velocity Zone	500 m/s
Density Host Low Velocity Zone	1000 kg/m^3

A geological feature of this nature would be representative of a dyke, fault zone or geological intrusion which could be a conduit for fluid flow. The geological feature left boundary is located 2.5m from the source in all scenarios.

For each simulation a value for the dominant frequency and for the PPV of the signal at the monitoring location 11.5m from the source (Sensor 2 in Figure 8-2), are obtained using the previously defined method. The distance between the source and the monitoring location was chosen based on the results in Chapter 7, where the largest variation in values (PPV and dominant frequency) occurred after approximately 10m from the source. In addition, the numerical setup detailed in Figure 8-2 reflects the capabilities of the seismic monitoring equipment available for potential field trials.

8.2 PPV and Power Spectrum Data

In this section the results of the numerical simulations which consider various central feature widths and low velocity zone widths are presented. The aim is to establish if there is a relationship between central feature width, the PPV and dominant frequency of the seismic signal.

Figure 8-2 presents the numerical set up used.

Key Point: The source frequency is 100Hz and the PPV used is 1.25×10^{-5} m/s. This value of PPV is different to the value previously used. This was a conscious decision to better represent the characteristics of active sources used in the field trials. Each simulation and the key findings will be presented.
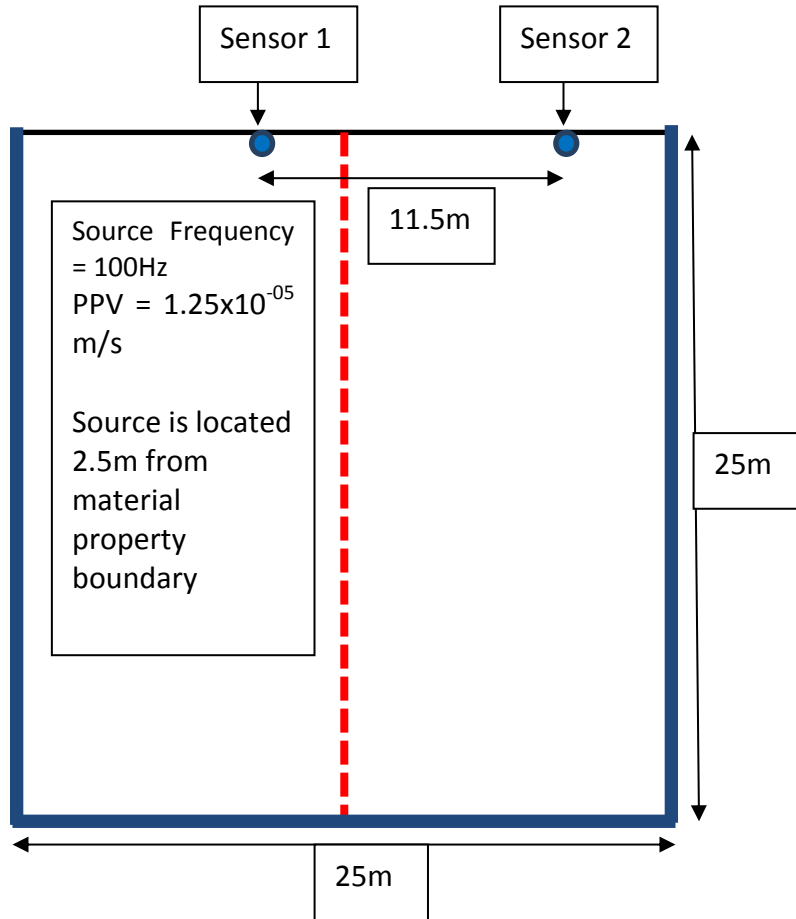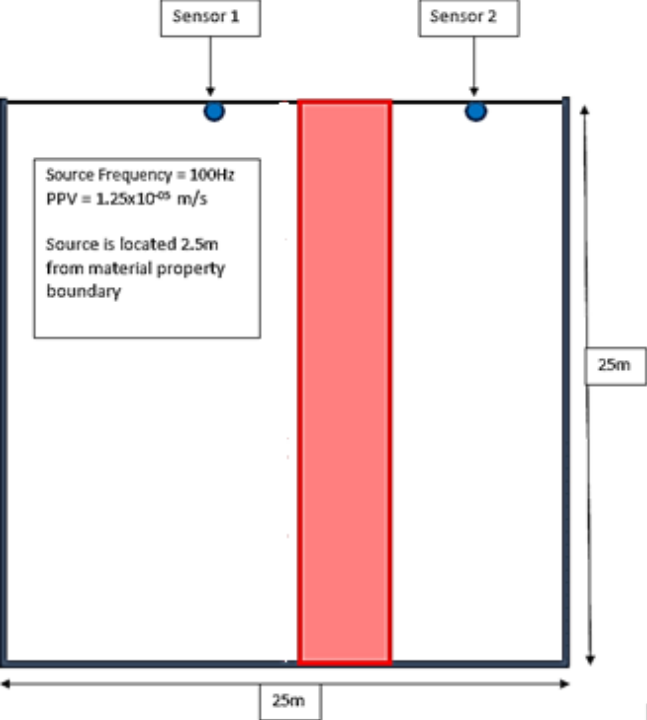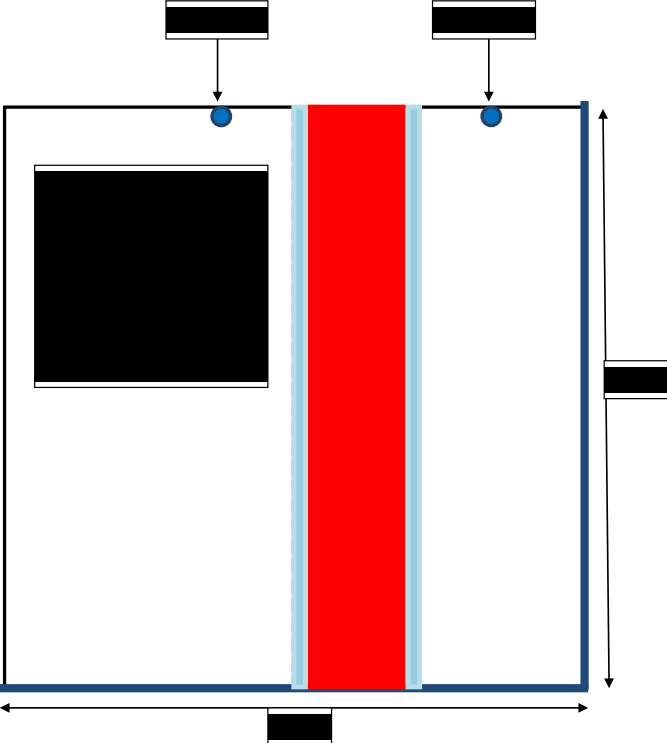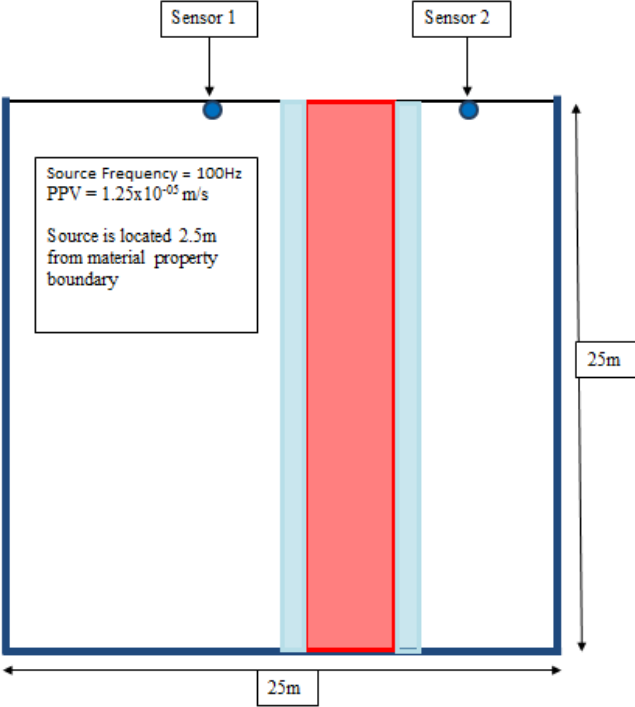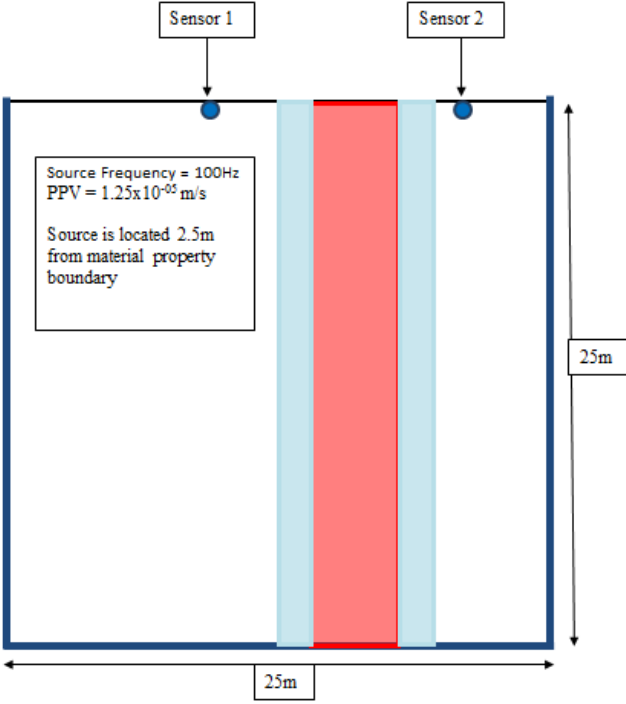
Figure 8-2: Schematic of 25m x 25m model to obtain PPV and dominant frequency values of the signal for various central feature widths and low velocity zone widths. Blue dots: Sensor 1 = source location, Sensor 2 = 11.5m from source. Low reflecting boundaries: highlighted in blue. Red dashed line: material property boundary.

Table 8-2: Table outlining the various low velocity zone widths and central feature width simulated in COMSOL Multiphysics

Scenario No.	Model Schematic Representation	Brief Description
1) No Low Velocity Zone **Central Feature Widths Considered:** • No feature • 0.5m • 1m • 2m • 3m • 4m **Red Box:** 4.0m feature **N.B.** Only one scenario is schematically represented for clarity.	Sensor 1 Sensor 2 Source Frequency = 100Hz PPV = 1.25x10⁻⁰⁵ m/s Source is located 2.5m from material property boundary 25m 25m	Modelled area is defined by three material property zones to establish the effect of a material change on the seismic signal with more than one material property boundary (central feature). **Details:** 25m x 25m model to obtain PPV and dominant frequency values of the signal highlighting the various central feature widths. **Aim:** Consider the effects of a single central feature on: 1) PPV (m/s); and 2) dominant frequency of the signal.

Scenario No.	Model Schematic Representation	Brief Description
2) 0.5m Low Velocity Zone **Central Feature Widths Considered:** • No feature • 0.5m • 1m • 1.5m • 2m • 2.5m • 3m • 4m **Light Blue Box:** 0.5m low velocity zone **Red Box:** 4.0m feature. **N.B.** Only one scenario is schematically represented for clarity.		Modelled area is defined by five material property zones to establish the effect of a material change on the seismic signal with more than one material property boundary (central feature surrounded by a 0.5m low velocity zone). **Details:** 25m x 25m model to obtain PPV and dominant frequency values of the signal highlighting the 4m central feature width surrounded by a 0.5m low velocity zone. **Aim:** Consider the effects of a central feature surrounded by a 0.5m velocity zone on: 1) PPV (m/s); and 2) dominant frequency of the signal.

Scenario No.	Model Schematic Representation	Brief Description
3) 1.0m Low Velocity Zone **Central Feature Widths Considered:** • No feature • 0.5m • 1m • 2m • 3m • 4m **Light Blue Box:** 1.0m low velocity zone **Red Box:** 4.0m feature. **N.B:** Only one scenario is schematically represented for clarity.	Sensor 1 Sensor 2 Source Frequency = 100Hz PPV = 1.25x10^{-05} m/s Source is located 2.5m from material property boundary 25m 25m	Modelled area is defined by five material property zones to establish the effect of a material change on the seismic signal with more than one material property boundary (central feature surrounded by a 1.0m low velocity zone). **Details:** 25m x 25m model to obtain PPV and dominant frequency values of the signal highlighting a 4m central feature widths surrounded by a 1.0m low velocity zone. **Aim:** Consider the effects of a central feature surrounded by a 1.0m velocity zone on: 1) PPV (m/s); and 2)dominant frequency of the signal.

Scenario No.	Model Schematic Representation	Brief Description
4) **1.5m Low Velocity Zone** **Central Feature Widths Considered:** • No feature • 0.5m • 1m • 2m • 3m • 4m **Light Blue Box:** 1.5m low velocity zone **Red Box:** 4.0m feature. **N.B:** Only one scenario is schematically represented for clarity.	Sensor 1 Sensor 2 Source Frequency = 100Hz $PPV = 1.25 \times 10^{-05}$ m/s Source is located 2.5m from material property boundary 25m 25m	Modelled area is defined by five material property zones to establish the effect of a material change on the seismic signal with more than one material property boundary (central feature surrounded by a 1.5m low velocity zone). **Details:** 25m x 25m model to obtain PPV and dominant frequency values of the signal highlighting the 4m central feature width surrounded by a 1.5m low velocity zone. **Aim:** Consider the effects of a central feature surrounded by a 1.5m velocity zone on: 1) PPV (m/s); and 2) dominant frequency of the signal.

8.2.1 Simulation Scenario 1: 0m Low velocity Zone (Central Feature)

Figure 8-3 and Table 8-3 summarise the data from simulation scenario 1, detailing the PPV and dominant frequency values obtained from the simulations for both sensor 1 and sensor 2.

Figure 8-3: Graphs presenting PPV (primary y-axis) and dominant frequency (secondary y-axis) data for (a) Sensor 1 and (b) Sensor (2) for the various central feature widths simulated (x-axis). As central feature width increases the PPV increases and there is a slight reduction in dominant frequency at Sensor 1. A gradual reduction in PPV and dominant frequency at sensor 2 is observed.

Table 8-3: Simulation Scenario 1: 0m Low Velocity Zone (Central Feature Only) Results

Simulation Scenario 1: 0m Low Velocity Zone (Central Feature Only)				
	Sensor 1		**Sensor 2**	
Central Feature Width (m)	**PPV (m/s)**	**Dominant Frequency (Hz)**	**PPV (m/s)**	**Dominant Frequency (Hz)**
No central feature	1.25×10^{-5}	99	0.99×10^{-7}	81
0.5	1.48×10^{-5}	97	0.75×10^{-7}	69
1	3.09×10^{-5}	97	0.63×10^{-7}	58
2	4.19×10^{-5}	97	0.43×10^{-7}	44
3	5.57×10^{-5}	97	0.30×10^{-7}	37
4	7.09×10^{-5}	97	0.17×10^{-7}	31

Figure 8-4 presents results where the numerical domain is characterised by a single geological feature with no low velocity zone present.

Column A: PPV Sensor	**Column B: PPV Sensor**	**Column C: Power Spectra Sensor 1**	**Column D: Power Spectra Sensor 2**	**Geological Feature Width (m)**

Figure 8-4: Results for various geological feature widths. Rows from top: 0m, 0.5m, 1.0m, 2.0m, 3.0m and 4.0m. There is no surrounding low velocity zone.
Column A: PPV over time for sensor 1. Column B: PPV over time sensor 2. Column C: Power Spectrum sensor 1. Column D: Power Spectrum sensor 2.

The key points for each simulation within this scenario are presented in Table 8-4.

Table 8-4: Scenario 1: Key Summary Points for Each Simulation

Simulation Scenario 1: 0m Low Velocity Zone (Central Feature Only)				
	Sensor 1		Sensor 2	
Central Feature Width (CFW) (m)	PPV	Power Spectra	PPV	Power Spectra
No CFW	Greater than PPV of the source.	1 peak	3 orders of magnitude less than the PPV of the source.	1 peak.
0.5	Greater than PPV of the source	1 peak Slight increase in amplitude compared to no CFW	3 orders of magnitude less than the PPV of the source.	1 peak. Reduction in amplitude, dominant frequency less than max frequency when compared to no CFW.
1	Greater than PPV of the source	3 peaks. Slight increase in amplitude compared to 0.5m CFW.	3 orders of magnitude less than the PPV of the source.	2 peaks. Reduction in amplitude, dominant frequency less than max frequency when compared to 0.5m CFW.
2	Greater than PPV of the source	4 peaks. Slight increase in amplitude compared to 1m CFW.	3 orders of magnitude less than the PPV of the source.	3 peaks. Reduction in amplitude, dominant frequency less than max frequency when compared to 1m CFW.
3	Greater than PPV of the source	5 peaks. Slight increase in amplitude compared to 2m CFW.	3 orders of magnitude less than the PPV of the source.	3 peaks. , dominant frequency less than max frequency when compared to 2m CFW.
4	Greater than PPV of the source	6 peaks. Slight increase in amplitude compared to 3m CFW.	4 orders of magnitude less than the PPV of the source.	4 peaks. , dominant frequency less than max frequency when compared to 3m CFW.

Summary: Overall, in all simulations a gradual reduction in PPV and frequency at sensor 2 is observed. There is the formation of additional peaks in the power spectrum at sensor 2. The maximum frequency value observed in the power spectrum at sensor 2 in all scenarios decreases with feature width. At Sensor 1 as feature width increases both the PPV and amplitude of the power spectra increases.

The number of frequency peaks in the power spectra also increases with feature width.

8.2.2 Simulation Scenario 2: 0.5m Low Velocity Zone

For this scenario additional feature widths are simulated. The rationale behind this was to establish if the gradual reduction in dominant frequency and PPV observed for a single geological feature (Section 8.2.1) occurred when a low velocity zone was present. The larger number of feature widths considered potentially could clarify this observation.

Figure 8-5 and Table 8-5 summarise the data from simulation scenario 2, detailing the PPV and dominant frequency values obtained from the simulations for both sensor 1 and sensor 2.
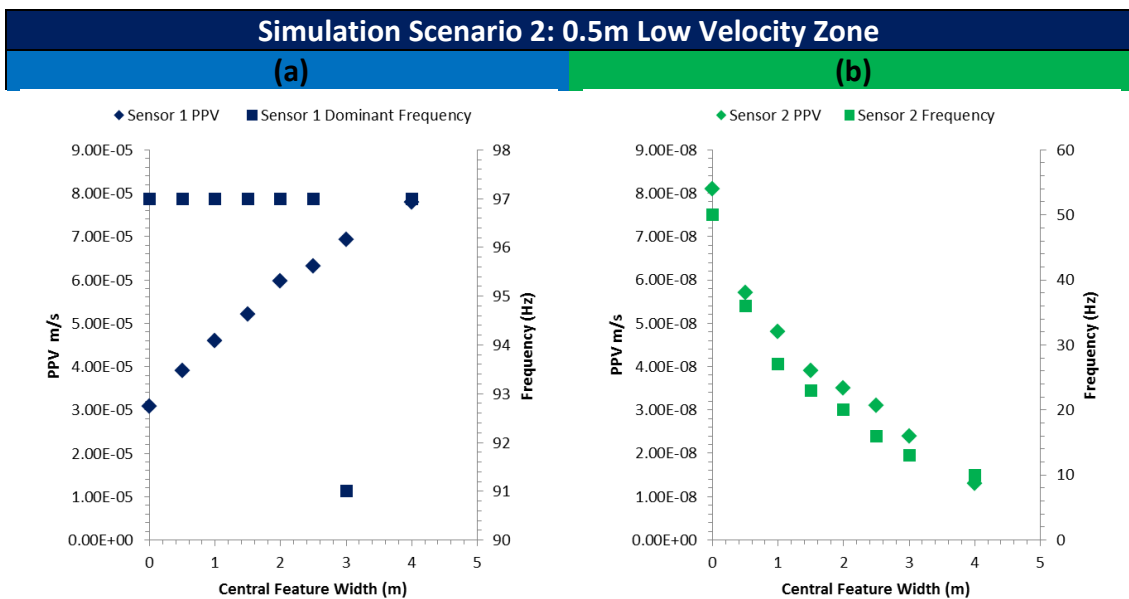
Figure 8-5: Graphs presenting PPV (primary y-axis) and dominant frequency (secondary y-axis) data for (a) Sensor 1 and (b) Sensor (2) for the various central feature widths simulated (x-axis). As central feature width increases the PPV increases and dominant frequency reamains consistent for all central feature widths except 3m where there is a 6Hz reduction at Sensor 1. A gradual reduction in PPV and dominant frequency at sensor 2 is observed.

Table 8-5: Simulation Scenario 2: 0.5m Low Velocity Zone Results

Simulation Scenario 2: 0.5m Low Velocity Zone				
	Sensor 1		Sensor 2	
Central Feature Width (m)	PPV (m/s)	Dominant Frequency (Hz)	PPV (m/s)	Dominant Frequency (Hz)
No central feature	3.09×10^{-5}	97	0.81×10^{-7}	50
0.5	3.91×10^{-5}	97	0.57×10^{-7}	36
1	4.60×10^{-5}	97	0.48×10^{-7}	27
1.5	5.21×10^{-5}	97	0.39×10^{-7}	23
2	5.97×10^{-5}	97	0.35×10^{-7}	20
2.5	6.31×10^{-5}	97	0.31×10^{-7}	16
3	6.92×10^{-5}	91	0.24×10^{-7}	13
4	7.79×10^{-5}	97	0.13×10^{-7}	10

Figure 8-6 presents results where the numerical domain is characterised by a single central feature with a 0.5m low velocity zone at either side. If additional frequency peaks are observed in the power spectra these are detailed in Figure 8-6.

Column A: PPV Sensor 1	Column B: PPV Sensor 2	Column C: Power Spectra Sensor 1	Column D: Power Spectra Sensor 2	Geological Feature Width (m)
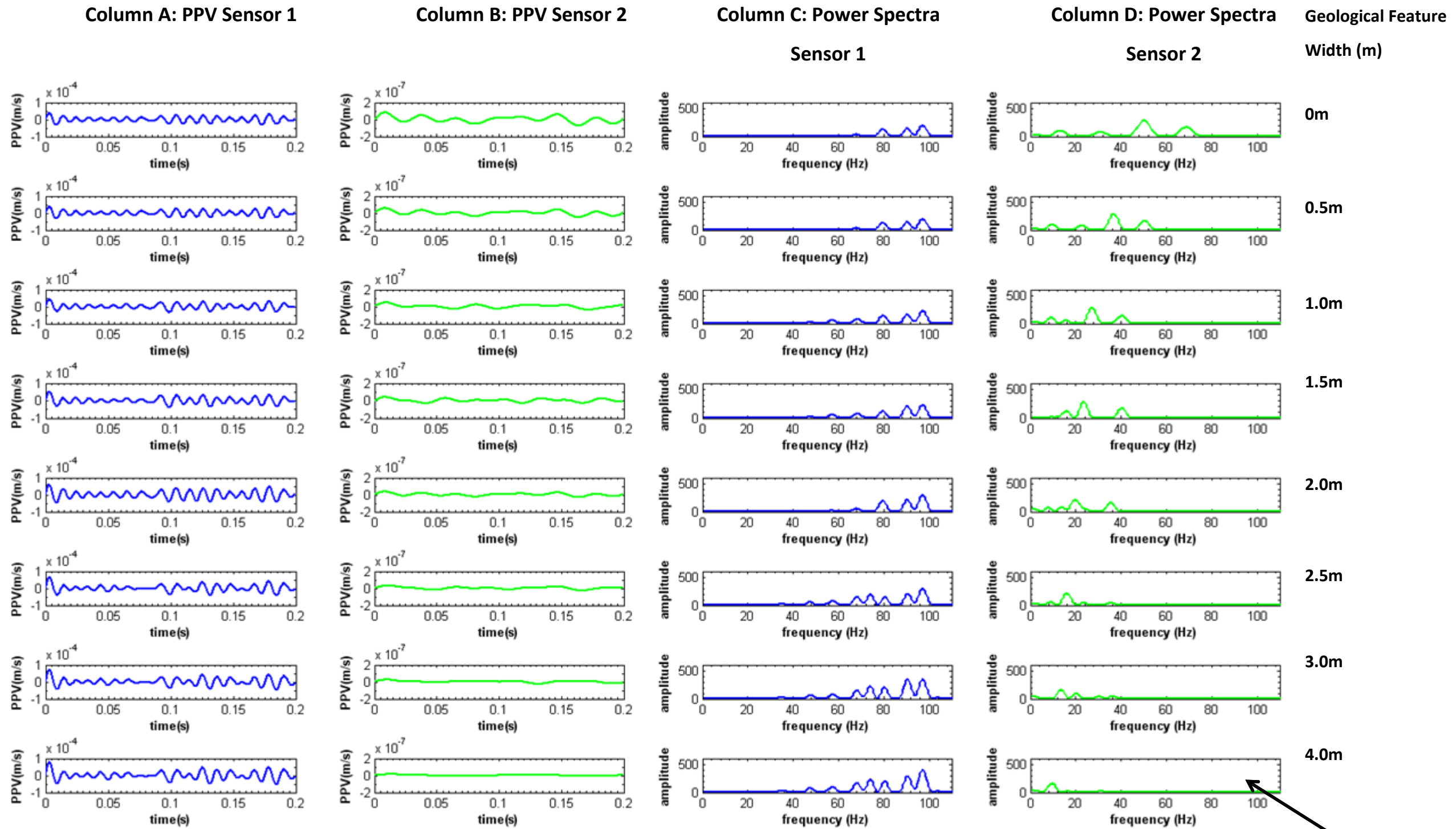
Figure 8-6: Results for various geological feature widths. Rows from top: 0m, 0.5m, 1.0m, 2.0m, 3.0m and 4.0m. There is a surrounding low velocity zone 0.5m either side of the geological feature.
Column A: PPV over time for sensor 1. Column B: PPV over time sensor 2. Column C: Power Spectrum sensor 1. Column D: Power Spectrum sensor 2. Insert: Larger power spectrum for a 4.0m central feature shown for clarity.
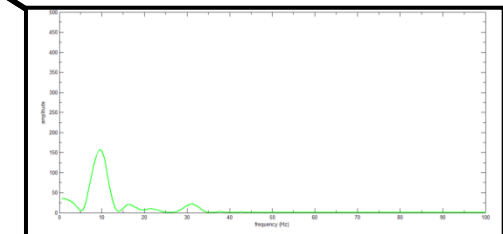
The key points for each simulation within this scenario are presented in Table 8 6.

Table 8-6: Scenario 2: Key Summary Points for Each Simulation

Simulation Scenario 2: 0.5m Low Velocity Zone				
	Sensor 1		Sensor 2	
Central Feature Width (CFW) (m)	PPV	Power Spectra	PPV	Power Spectra
No central feature	Greater than PPV of the source. Comparable to 1.0m CFW with no low velocity zone	4 peaks.	3 orders of magnitude less than PPV of the source. Less than Scenario 1	4 peaks. Dominant frequency less than Scenario 1
0.5	Greater than PPV of the source and Scenario 1	4 peaks. Slight increase in amplitude compared to 0m CFW	3 orders of magnitude less than PPV of the source. Less than Scenario 1	4 peaks. Reduction in amplitude, max frequency. Dominant frequency less than Scenario 1
1	Greater than PPV of the source and Scenario 1	6 peaks. Slight increase in amplitude compared to 0.5m CFW	3 orders of magnitude less than PPV of the source. Less than Scenario 1	4 peaks. Reduction in amplitude, max frequency. Dominant frequency less than Scenario 1
1.5	Greater than PPV of the source and Scenario 1	6 peaks. Slight increase in amplitude compared to 1m CFW	3 orders of magnitude less than PPV of the source. Less than Scenario 1	3 peaks. Reduction in amplitude, max frequency. Dominant frequency less than Scenario 1
2	Greater than PPV of the source and Scenario 1	5 peaks. Slight increase in amplitude compared to 1.5m CFW	3 orders of magnitude less than PPV of the source. Less than Scenario 1	4 peaks. Reduction in amplitude, max frequency. Dominant frequency less than Scenario 1
2.5	Greater than PPV of the source and Scenario 1	8 peaks. Slight increase in amplitude compared to 2m CFW	3 orders of magnitude less than PPV of the source. Less than Scenario 1	4 peaks. Reduction in amplitude, max frequency. Dominant frequency less than Scenario 1
3	Greater than PPV of the source and Scenario 1	8 peaks. Reduction in max frequency observed. Slight increase in amplitude when compared to 2.5m CFW	3 orders of magnitude less than PPV of the source. Less than Scenario 1	5 peaks. Reduction in amplitude. Dominant frequency less than Scenario 1

Simulation Scenario 2: 0.5m Low Velocity Zone				
	Sensor 1		Sensor 2	
4	Greater than PPV of the source and Scenario 1	8 peaks. Slight increase in amplitude. Change in dominant frequency compared to 3m CFW	3 orders of magnitude less than the PPV of the source. Less than Scenario 1	4 peaks. Reduction in amplitude, max frequency. Dominant frequency less than Scenario 1

Summary: Overall, there is a gradual reduction in PPV and dominant frequency at sensor 2 as feature width increases. There is the formation of additional peaks in the power spectrum at sensor 2. The maximum frequency value observed in the power spectrum at sensor 2 in all scenarios does not decrease as feature width increases.

At Sensor 1 as feature width increases both the PPV and amplitude of the power spectra increases. The number of frequency peaks in the power spectra also increases with feature width. There is more frequency peaks in the power spectrum and greater amplitude when compared to scenario 1. This is expected as there are a greater number of material property boundaries that the seismic signal can reflect off.

8.2.3   Simulation Scenario 3: 1.0m Low Velocity Zone

Figure 8-7 and Table 8-7 summarise the data from simulation scenario 3, detailing the PPV and dominant frequency values obtained from the simulations for both sensor 1 and sensor 2.
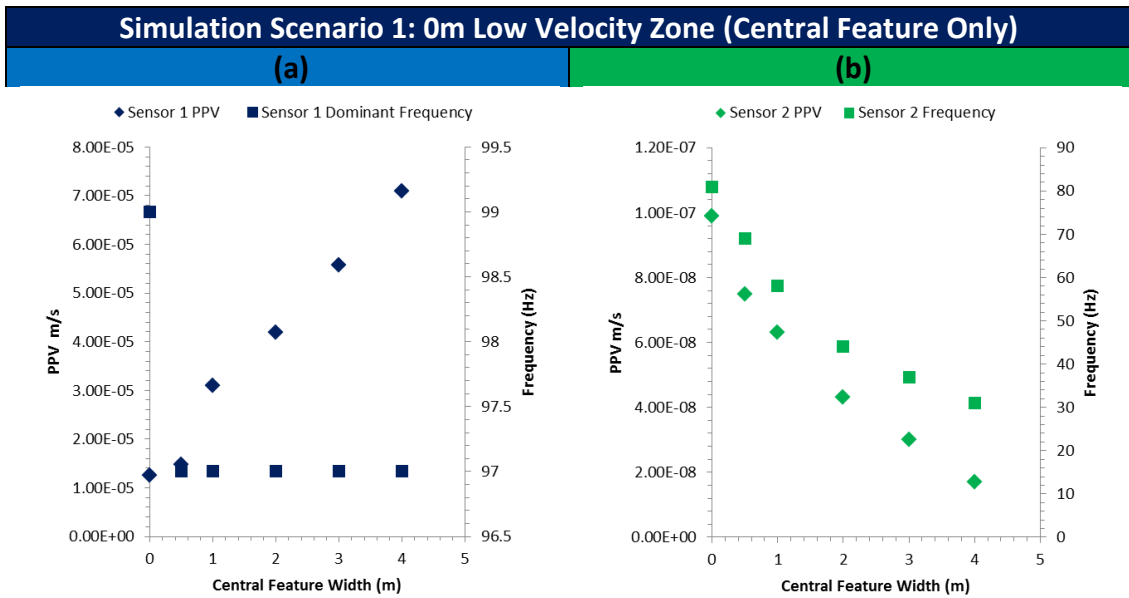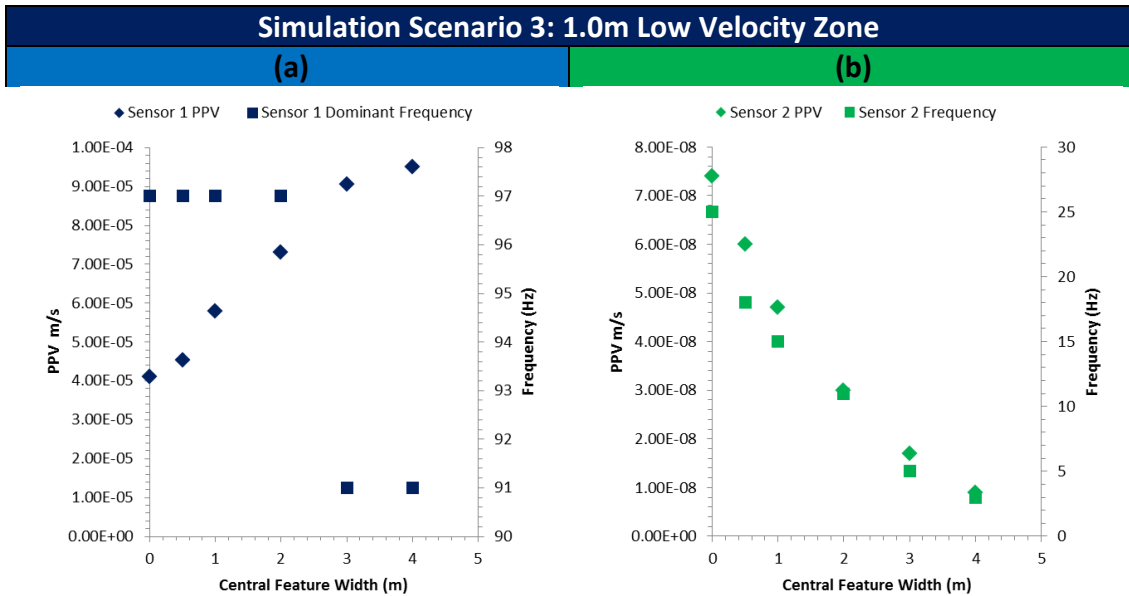

Figure 8-7: Simulation Scenario 3: 1.0m Low Velocity Zone: Graphs presenting PPV (primary y-axis) and dominant frequency (secondary y-axis) data for (a) Sensor 1 and (b) Sensor (2) for the various central feature widths simulated (x-axis). As central feature width increases the PPV increases and dominant frequency reamains consistent for all central feature widths except 3m and 4m where there is a 6Hz reduction at Sensor 1. A gradual reduction in PPV and dominant frequency at sensor 2 is observed.

Table 8-7: Simulation Scenario 3: 1.0m Low Velocity Zone Results

Simulation Scenario 3: 1.0m Low Velocity Zone				
	Sensor 1		Sensor 2	
Central Feature Width (m)	PPV (m/s)	Dominant Frequency (Hz)	PPV (m/s)	Dominant Frequency (Hz)
No central feature	4.10×10^{-5}	97	0.74×10^{-7}	25
0.5	4.54×10^{-5}	97	0.60×10^{-7}	18
1	5.79×10^{-5}	97	0.47×10^{-7}	15
2	7.31×10^{-5}	97	0.30×10^{-7}	11
3	9.06×10^{-5}	91	0.17×10^{-7}	5
4	9.51×10^{-5}	91	0.09×10^{-7}	3

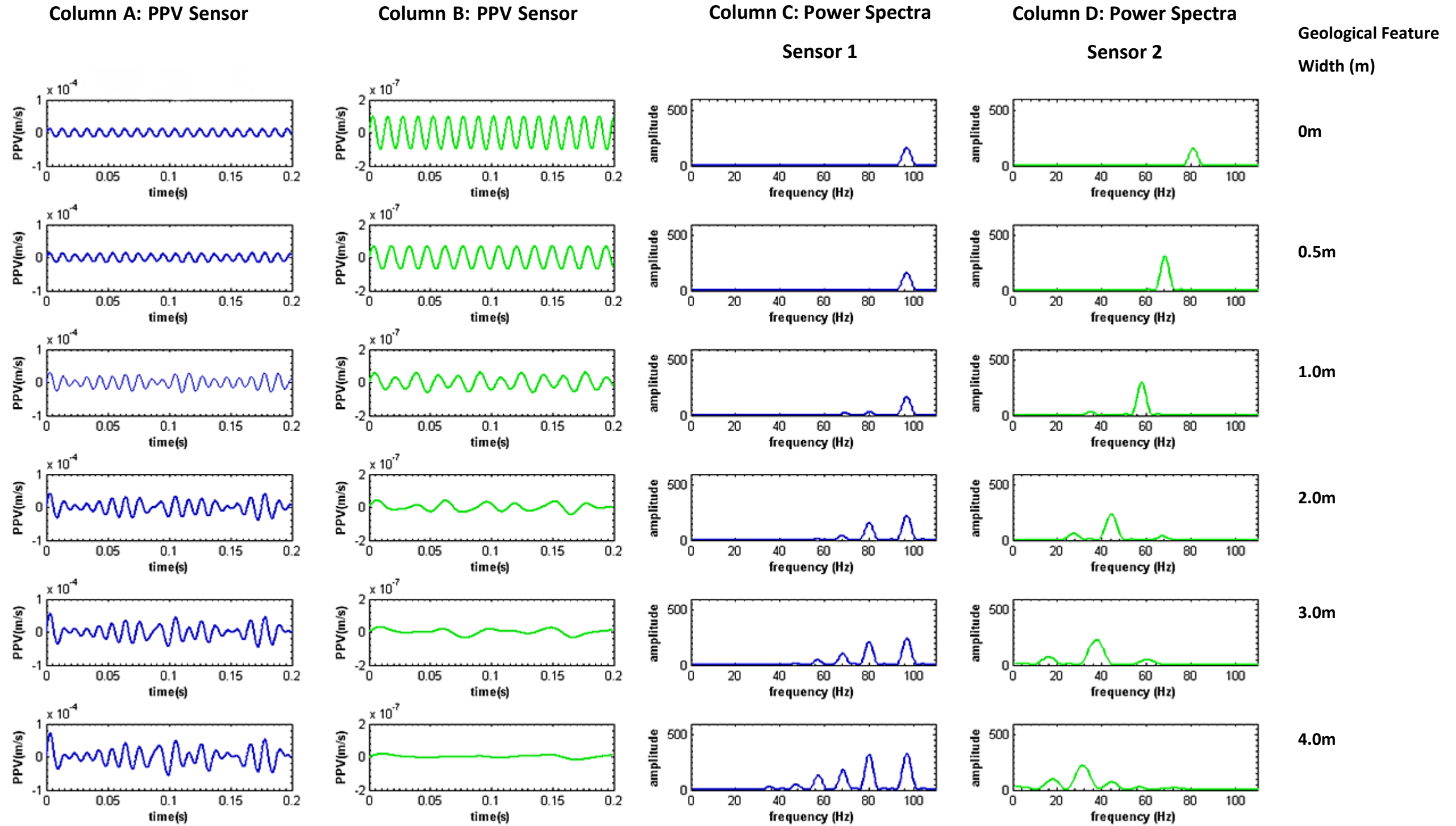Figure 8-8 presents results where the numerical domain is characterised by a single geological feature surrounded by a 1.0m low velocity zone present. If additional frequency peaks are observed in the power spectra these are presented in Figure 8-8.

| Column A: PPV Sensor 1 | Column B: PPV Sensor 2 | Column C: Power Spectra Sensor 1 | Column D: Power Spectra Sensor 2 | Geological Feature Width (m) |
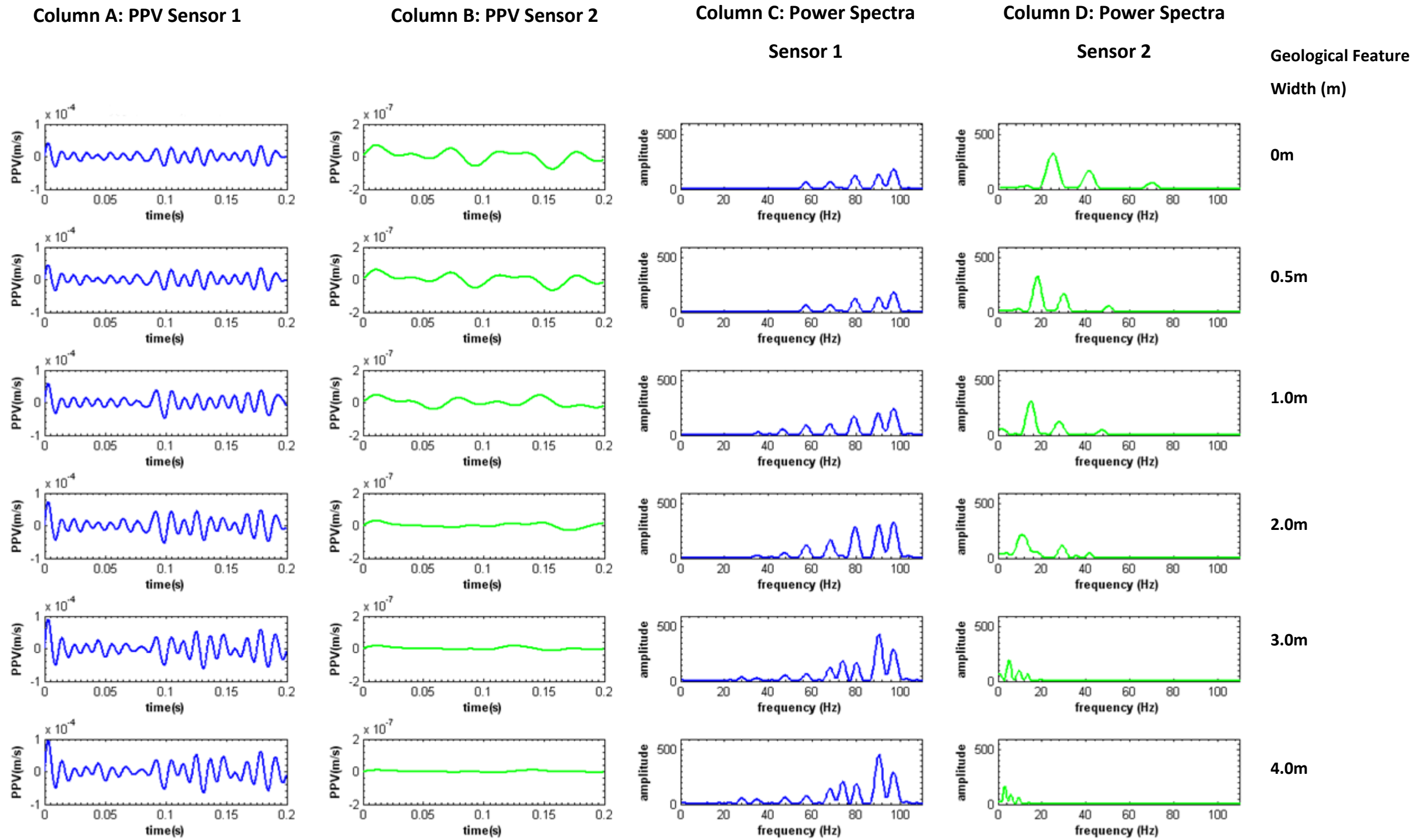
Figure 8-8: Results for various geological feature widths. Rows from top: 0m, 0.5m, 1.0m, 2.0m, 3.0m and 4.0m. There is a 1.0m surrounding low velocity/ fracture zone. Column A: PPV over time for sensor 1. Column B: PPV over time sensor 2. Column C: Power Spectrum sensor 1. Column D: Power Spectrum sensor 2.

The key points for each simulation within this scenario are presented in Table 8-8.

Table 8-8: Scenario 3: Key Summary Points for Each Simulation

Simulation Scenario 3: 1.0m Low Velocity Zone				
	Sensor 1		Sensor 2	
Central Feature Width (CFW) (m)	PPV	Power Spectra	PPV	Power Spectra
No central feature	Greater than PPV of the source. Comparable to 2.0m feature with no low velocity zone	5 peaks.	3 orders of magnitude less than the PPV of the source. Less than Scenario 1&2	3 peaks. Dominant frequency less than Scenario 1&2
0.5	Greater than PPV of the source and Scenario 1&2	5 peaks. Slight increase in amplitude compared to no CFW	3 orders of magnitude less than the PPV of the source. Less than Scenario 1&2	3 peaks. Reduction in amplitude, max frequency. Dominant frequency less than Scenario 1&2
1	Greater than PPV of the source and Scenario 1&2	7 peaks. Slight increase in amplitude compared to 0.5m CFW	3 orders of magnitude less than the PPV of the source. Less than Scenario 1&2	4 peaks. Reduction in amplitude, max frequency. Dominant frequency less than Scenario 1&2
2	Greater than PPV of the source and Scenario 1&2	7 peaks. Slight increase in amplitude compared to 1m CFW	3 orders of magnitude less than the PPV of the source. Less than Scenario 1&2	5 peaks. Reduction in amplitude, max frequency. Dominant frequency less than Scenario 1&2
3	Greater than PPV of the source and Scenario 1&2	9 peaks. Reduction in max frequency observed. Slight increase in amplitude compared to 2m CFW	3 orders of magnitude less than the PPV of the source. Less than Scenario 1&2	4 peaks. Reduction in amplitude, max frequency. Dominant frequency less than Scenario 1&2
4	Greater than PPV of the source and Scenario 1&2	9 peaks. Slight increase in amplitude compared to 3m CFW	4 orders of magnitude less than the PPV of the source. Less than Scenario 1&2	3 peaks. Reduction in amplitude, max frequency. Dominant frequency less than Scenario 1&2

Summary: A gradual reduction in PPV and dominant frequency at sensor 2 is observed for all central feature widths, this was the largest reduction for both parameters when compared to scenarios 1 and 2. There is the formation of

additional peaks in the power spectrum at sensor 2. The maximum frequency value observed in the power spectrum at sensor 2 does not decrease as feature width increases.

At sensor 1 an increase in PPV is observed as feature width increases. This implies that the reflection of the seismic signal off of the material boundary is causing amplification in the signal. There is a clear differentiation between the PPV and dominant frequency detected at sensor 2 for scenario 1, 2 and 3.

8.2.4 Simulation Scenario 4: 1.5m Low Velocity Zone

Figure 8-9 and Table 8-9 summarises the data from simulation scenario 3, detailing the PPV and dominant frequency values obtained from the simulations for both sensor 1 and sensor 2.
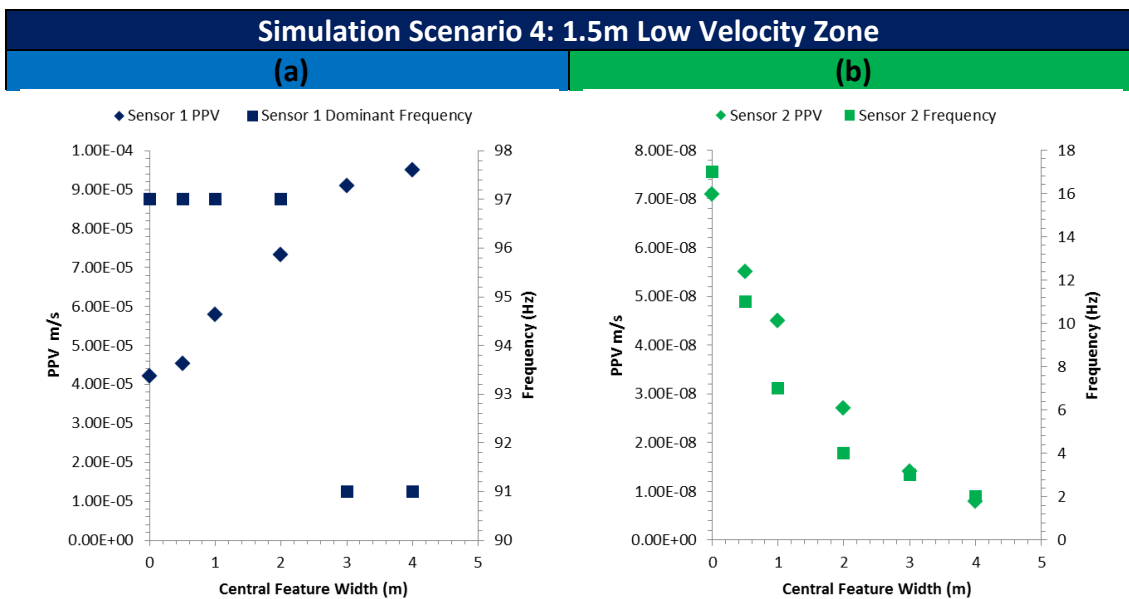
Figure 8-9: Simulation Scenario 4: 1.5m Low Velocity Zone: Graphs presenting PPV (primary y-axis) and dominant frequency (secondary y-axis) data for (a) Sensor 1 and (b) Sensor (2) for the various central feature widths simulated (x-axis). As central feature width increases the PPV increases and dominant frequency reamains consistent for all central feature widths except 3m and 4m where there is a 6Hz reduction at Sensor 1. A gradual reduction in PPV and dominant frequency at sensor 2 is observed.

Table 8-9: Simulation Scenario 4: 1.5m Low Velocity Zone Results

Simulation Scenario 4: 1.5m Low Velocity Zone				
	Sensor 1		Sensor 2	
Central Feature Width (m)	PPV (m/s)	Dominant Frequency (Hz)	PPV (m/s)	Dominant Frequency (Hz)
No central feature	4.21×10^{-5}	97	0.71×10^{-7}	17
0.5	4.53×10^{-5}	97	0.55×10^{-7}	11
1	5.79×10^{-5}	97	0.45×10^{-7}	7
2	7.32×10^{-5}	97	0.27×10^{-7}	4
3	9.10×10^{-5}	91	0.14×10^{-7}	3
4	9.51×10^{-5}	91	0.08×10^{-7}	2

Figure 8-10 presents results where the numerical domain is characterised by a single geological feature surrounded by a 1.5m low velocity zone. If additional frequency peaks are observed in the power spectra these are presented in Figure 8-10.

| Column A: PPV Sensor 1 | Column B: PPV Sensor 2 | Column C: Power Spectra Sensor 1 | Column D: Power Spectra Sensor 2 | Geological Feature Width (m) |
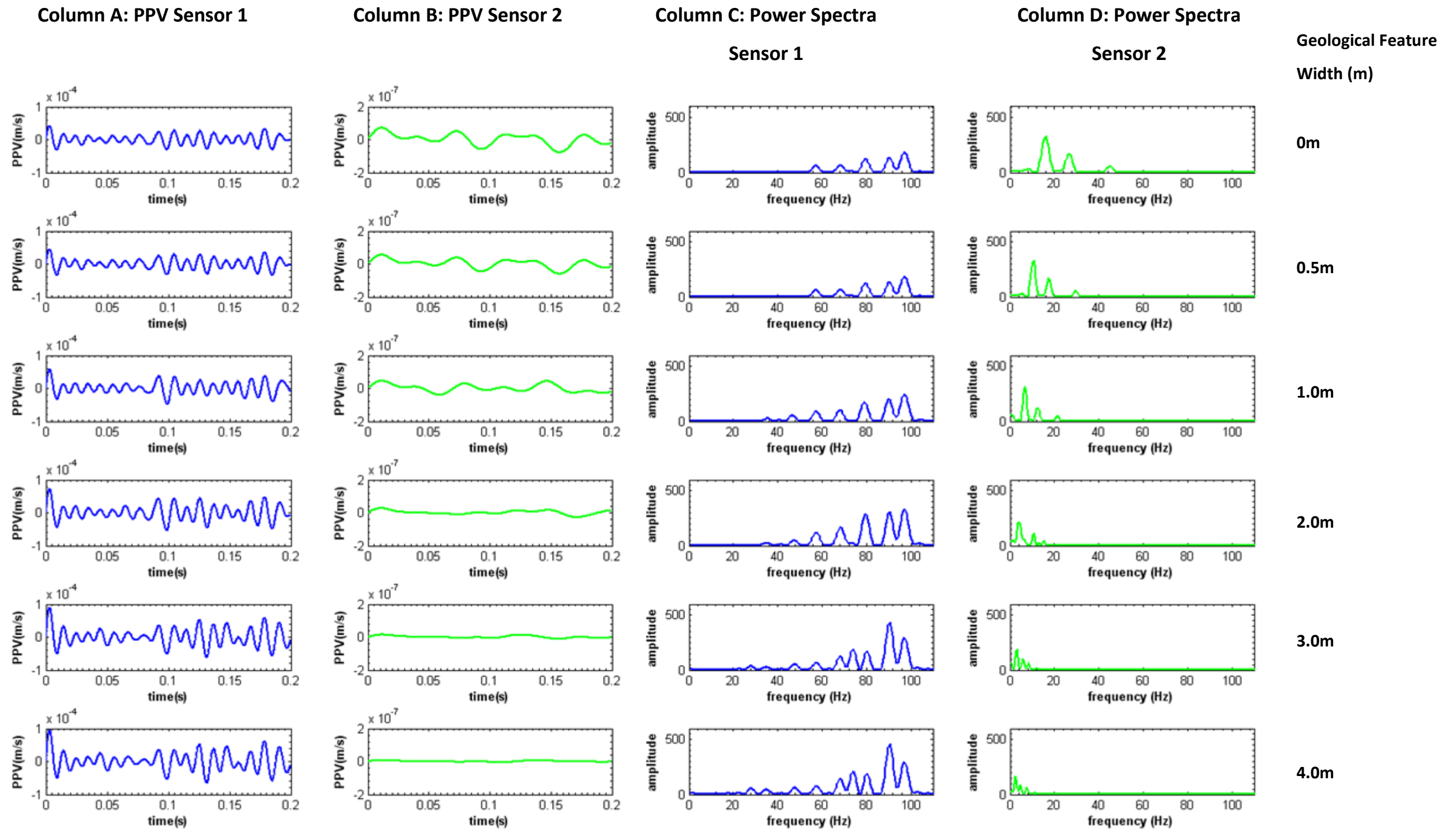
Figure 8-10: Results for various geological feature widths; Rows from top: 0m, 0.5m, 1.0m, 2.0m, 3.0m and 4.0m. There is a 1.5m surrounding low velocity/ fracture zone.
Column A: PPV over time for sensor 1. Column B: PPV over time sensor 2. Column C: Power Spectrum sensor 1. Column D: Power Spectrum sensor 2.

The key points for each simulation within this scenario are presented Table 8-10.

Table 8-10: Scenario 4: Key Summary Points for Each Simulation

Simulation Scenario 4: 1.5m Low Velocity Zone				
	Sensor 1		Sensor 2	
Central Feature Width (CFW)(m)	**PPV**	**Power Spectra**	**PPV**	**Power Spectra**
No central feature	Greater than PPV of the source and all other comparable values	5 peaks.	3 orders of magnitude less than the PPV of the source. Less than all other comparable values	3 peaks
0.5	Greater than PPV of the source and all other comparable values	5 peaks. Slight increase in the amplitude compared no CFW	3 orders of magnitude less than the PPV of the source. Less than all other comparable values	4 peaks. Reduction in amplitude, max frequency and dominant frequency
1	Greater than PPV of the source and all other comparable values	7 peaks. Slight increase in amplitude compared 0.5m CFW	3 orders of magnitude less than the PPV of the source. Less than all other comparable values	4 peaks. Reduction in amplitude, max frequency and dominant frequency
2	Greater than PPV of the source and all other comparable values	7 peaks. Slight increase in amplitude compared 1m CFW	3 orders of magnitude less than the PPV of the source. Less than all other comparable values	3 peaks. Reduction in amplitude, max frequency and dominant frequency
3	Greater than PPV of the source and all other comparable values	9 peaks. Reduction in max frequency observed. Slight increase in amplitude compared 2m CFW	3 orders of magnitude less than the PPV of the source. Less than all other comparable values	3 peaks. Reduction in amplitude, max frequency and dominant frequency
4	Greater than PPV of the source and all other comparable values	9 peaks. Slight increase in amplitude compared 3m CFW	4 orders of magnitude less than the PPV of the source. Less than all other comparable values	3 peaks. Reduction in amplitude, max frequency and dominant frequency

Summary: Gradual reduction in PPV and frequency at sensor 2 is observed. There is the formation of additional peaks in the power spectrum at sensor 2. The maximum frequency value observed in the power spectrum at sensor 2 in scenarios 1, 2, 3 and 4 decreases as feature width increases. At sensor 1 an increase in PPV as feature width increases is observed.

8.3 Relationship between Feature Width and Key Parameters

Figure 8-11 and Figure 8-12 present the PPV and dominant frequency values obtained from each of the scenarios presented in Section 8.2. This allowed a relationship between:

1) PPV and central feature width data; and

2) dominant frequency and central feature width data to be developed.

The values produced a set of curves for each low velocity zone scenario for both dominant frequency and PPV.
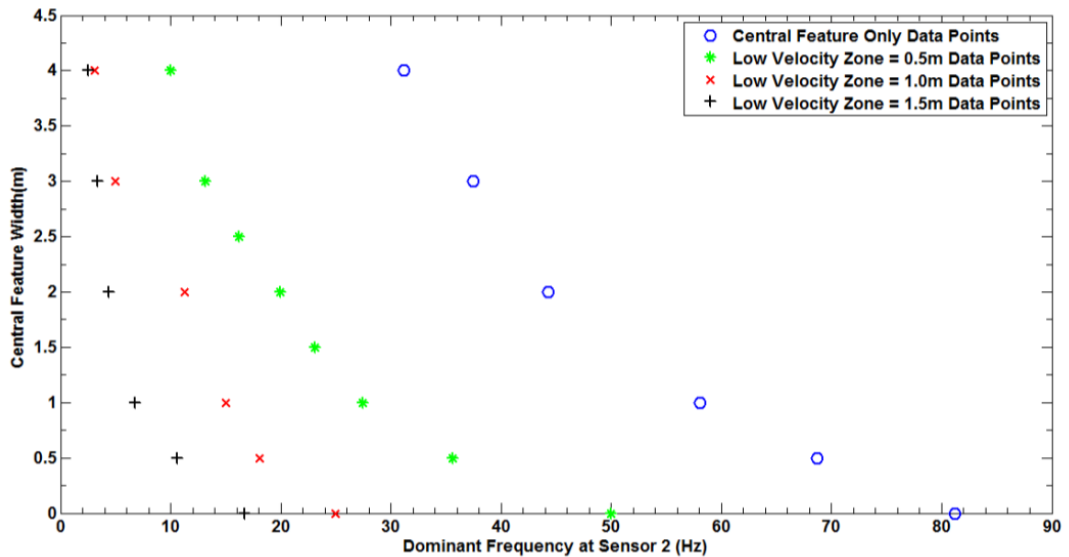
Figure 8-11: Low velocity zone widths vs dominant frequency at sensor 2. There is clear distinction between the dominant frequency observed and the various central feature widths considered.
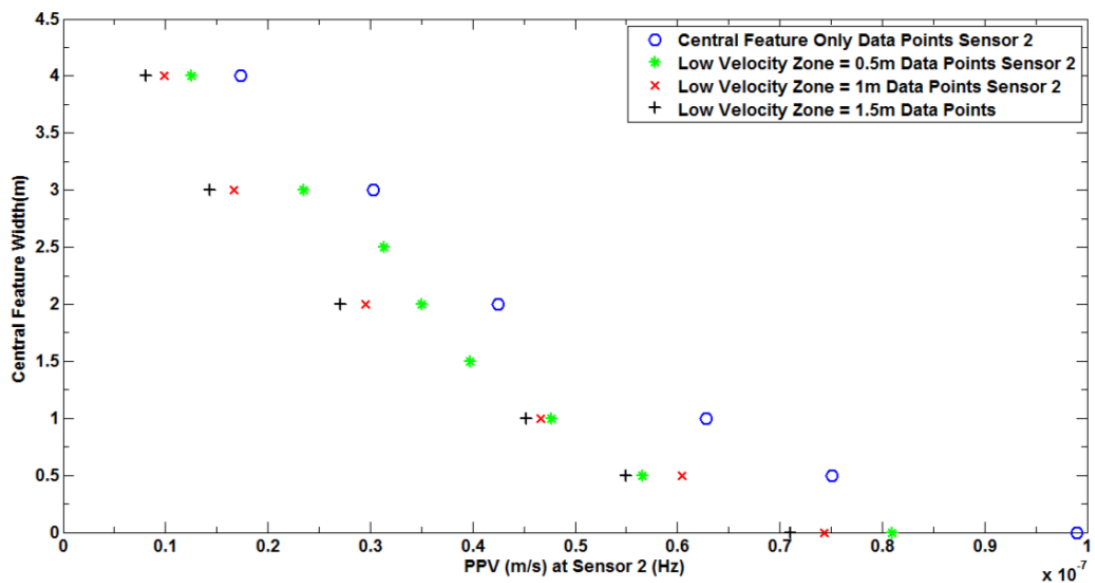
Figure 8-12: Low velocity zone widths vs PPV at the location of sensor 2. There is a distinction between the PPV observed and the various central feature widths considered, however this distinction is not as clear as that observed for the dominant frequency.

Both Figure 8-11 and Figure 8-12 demonstrate a nonlinear relationship between dominant frequency, PPV and feature width. Therefore, it was decided to explore the power law model as a potential fit for the PPV and frequency data (Section 8.2) detected at Sensor 2.

The scenario 1 (central feature only) data points (Figure 8-11) are distinctly higher in frequency than scenarios 2, 3 and 4 where there is a low velocity zone present. This indicates that the presence of an additional material property boundary causes the signal to reduce further in energy and thus the dominant frequency observed is less. There is a gradual reduction in dominant frequency in all scenarios considered that is distinguishable from one another.

The dominant frequency results reinforce the concept that the difference between the presence of a single feature and a feature surrounded by a low velocity zone is detectable. These results also suggest that the different low velocity zone widths can be detected. However, when the central feature width approaches 4.0m surrounded by a 1.5m or 1.0m low velocity zone, the difference in dominant frequency between the two scenarios becomes too small to detect (<1Hz).

The PPV data (Figure 8-14) demonstrates a gradual reduction in PPV at Sensor 2 as central feature width increases. The reduction in PPV is not quite as smooth as the dominant frequency data points further indicating that PPV might not be as good an indicator of feature width as the dominant frequency.

8.4   Model Fitting: Power Law

The rationale behind choosing to evaluate the power law detailed by Equation 8-1 (Field 2009) as a potential fit for the data, was that the data appeared to exhibit a gradual reduction in PPV and dominant frequency as central feature width and low velocity zone width increased (Figure 8-11 and Figure 8-12).

Equation 8-1

$$y = ax^b + c$$

It appears that feature width varies as a power of PPV and dominant frequency. The power law has also been used to previously describe frequency-dependent acoustic attenuation in complex media such as soft tissue, polymers (Szabo 1994, Szabo and Wu 2000, Chen and Holm 2003), the populations of cities, the intensities of

earthquakes and the sizes of power outages for example. The power law is a useful distribution to use when quantities are not well characterised by their typical or average values. Extensive discussions of this and the application of power laws can be found in reviews by Mitzenmacher (2004), Newman (2005) and Sornette (2006).

The range of values for which the law applies in this study, is the range of central feature widths. Central feature widths range from 0m to 4m and surrounding low velocity zone widths from 0m to 1.5m. The rationale behind this choice is that the resolution of most near surface geophysical techniques becomes highly varied in this range.

8.4.1   Evaluation of the model goodness of fit

After the dominant frequency and PPV characteristics are extracted from the LNP spectra and raw seismic signal respectively (Section 6.2.3, pg. 67), as presented in Figure 8-11 and Figure 8-12. Equation 8-1 was fitted to the data using Mat Lab, and the fit is presented in Figure 8-13 and Figure 8-14.
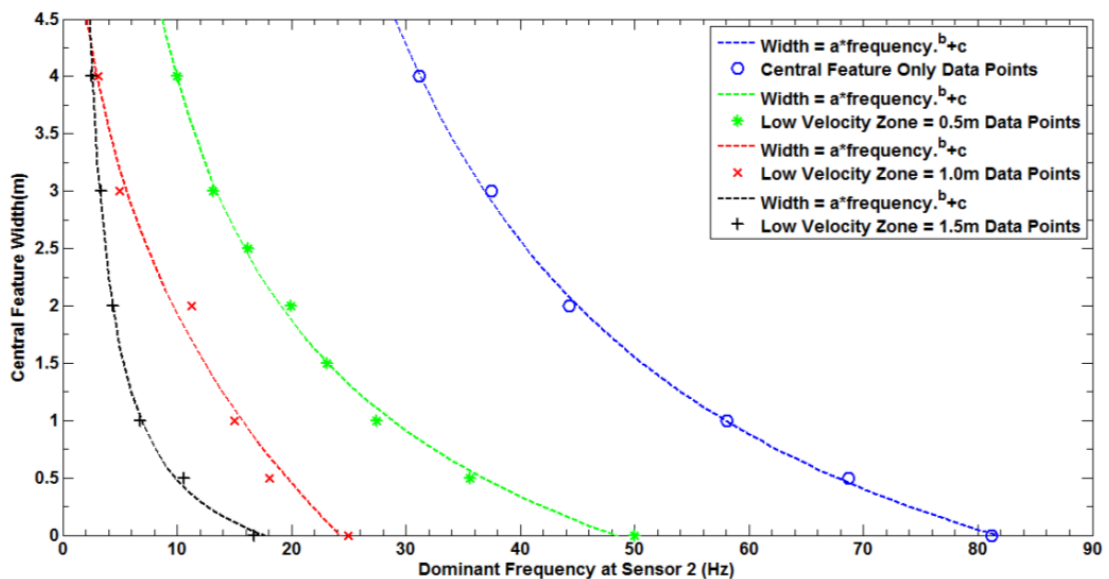
Figure 8-13: Fit of Equation 8-1 to results from numerical simulations of central feature width (m) vs dominant frequency (Hz)
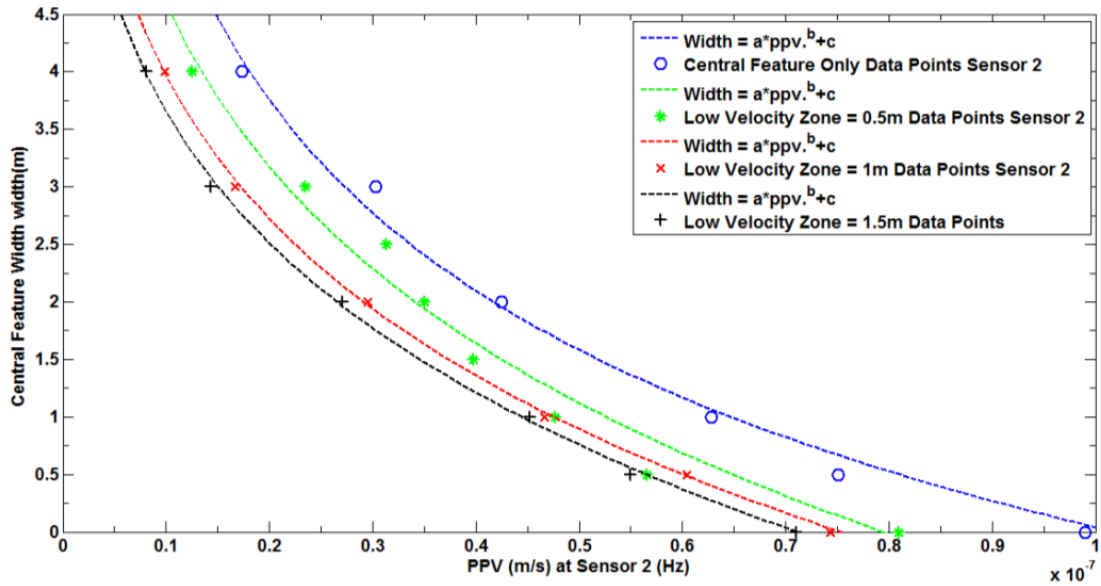
Figure 8-14: Fit of Equation 8-1 to results from numerical simulations of central feature width (m) vs PPV (m/s)

The equations corresponding to the curves for dominant frequency and PPV (Figure 8-13 and Figure 8-14) were extracted in Mat lab for each low velocity zone width and are detailed in Table 8-11.

Table 8-11: Equations corresponding to the curves for dominant frequency (Figure 8-13) and PPV (Figure 8-16)

Low Velocity Zone (m)	Dominant Frequency Equations to Calculate Central Feature Width (CFW)	PPV Equations to Calculate Central Feature Width (CFW)
0	$CFW = 231.3 * frequency^{-1.046} - 2.313$	$CFW = 7.537 * PPV^{-0.07956} - 27.13$
0.5	$CFW = 22.52 * frequency^{-0.4692} - 3.652$	$CFW = -134.2 * PPV^{0.1083} + 22.85$
1.0	$CFW = -4.753 * frequency^{0.2383} + 10.16$	$CFW = -145.7 * PPV^{0.1306} + 17.11$
1.5	$CFW = 12.22 * frequency^{-1.061} - 0.5798$	$CFW = -243.9 * PPV^{0.1822} + 12.16$

A statistical analysis was carried out using the Curve Fitting Toolbox™ Mat Lab application to evaluate the fit of the power law to the data. This application was chosen for its ease of use and efficiency.

The analysis was conducted using the following statistical parameters:

The sum of square due to error (SSE): A small SSE indicates a tight fit of the model to the data. A value closer to 0 (<0.1) indicates a fit that is useful for prediction.

R-Square: R-squared should be close to 1 for a good fit or >0.8. R-squared is a statistical measure of how close the data are to the fitted model.

Adjusted R-Square: R-squared should be close to 1 for a good fit or >0.8. Adjusted r-squared measures the proportion of the variation in the dependent variable (dominant frequency or PPV) explained by the independent variables (central feature width).

Root mean squared error (RMSE): A small RMSE indicates a tight fit of the model to the data. A value closer to 0 (<0.1) indicates a fit that is more useful for prediction.

P-Value: A small P-value (≤ 0.05) indicates that there is strong evidence that there is a relationship between PPV or dominant frequency and central feature width.

The methodology used to conduct the statistical evaluation of the fit is described in detail by Field (2009). The results for the statistical analysis are detailed in Table 8-12 and

Table 8-13.

Table 8-12: Statisical evaluation of the goodness of fit for the models presented in Figure 8-13. The goodness of fit statisitcs demonstrate that the power law fits the data for each of the low velocity widths considered well.

Statistical Parameter	Low velocity Zone Width (m)			
	0	0.5	1	1.5
SSE	0.0027	0.0001	0.0100	0.0015
R-Squared	0.9999	1.0000	0.9995	0.9999
Adjusted R-Squared	0.9987	0.9997	0.9991	0.9987
RMSE	0.0197	0.0043	0.0377	0.0147
P-Value	<0.05	<0.05	<0.05	0.0026

Table 8-13: Statisical evaluation of the goodness of fit for the models presented in Figure 8-14. The goodness of fit statisitcs demonstrate that the power law fits the data for each of the low velocity widths considered well.

Statistical Parameter	Low velocity Zone Width (m)			
	0	**0.5**	**1**	**1.5**
SSE	0.0130	0.0000	0.0004	0.0002
R-Squared	0.9994	1.0000	1.0000	1.0000
Adjusted R-Squared	0.9992	0.9999	0.9999	0.9999
RMSE	0.0430	0.0019	0.0077	0.0052
P-Value	<0.05	<0.05	<0.05	<0.05

Dominant frequency: SSE, R-Squared, Adjusted R-Squared, RMSE and P-Value are all well with the thresholds defined above demonstrating that the power law is an appropriate fit to the simulation data.

PPV: The same statistical parameters are found to be well within the thresholds, however it should be noted that not all of the data points lie directly on the line of best fit implying that the power law does not fit the PPV data as well as the dominant frequency data.

Key Finding: Both dominant frequency and PPV datasets demonstrate that the power law is a statically appropriate fit for the datasets. However, the equations presented in Table 8-11 appear to be contaminated by a covariance error. In order to overcome this, the prediction parameters were refitted with the exponent b constrained to be less than zero for all frequency curves and greater than zero for all PPV curves as presented in Section 8.5. This is discussed in more detail in Chapter 9, Section 9.1.

8.5   Interpolation between the Fitted Curves

The fit of Equation 8-1 described in the previous section, was carried out for the data referring to four distinct cases of low velocity zone width (Scenarios 1, 2, 3 and 4). In order to make it easier to find the relationship between,

- central feature width and dominant frequency; and

- central feature width and PPV,

interpolation techniques were applied. The aim was to obtain curves for low velocity zones at 0.1m intervals between 0m and 1.5m.

Interpolation between the various fitted curves for dominant frequency and PPV was completed in Mat Lab, assuming a linear change in dominant frequency and PPV between consecutive data points.

Dominant Frequency: Figure 8-15 presents the curves for the dominant frequency. A statistical analysis was conducted on each of the curves and is presented in Table 8-14 to verify that the interpolated values follow the same power law (Equation 8-1) as the computed data from the numerical models (Section 8.3).

The SSE, R-Squared, Adjusted R-Squared, RMSE and P-Value are well within the thresholds demonstrating that the power law is an appropriate model to fit to the interpolated data. Each curve is distingushable from one another indicating that the dominant frequency curves will be a good indicator and predictor of central feature width.
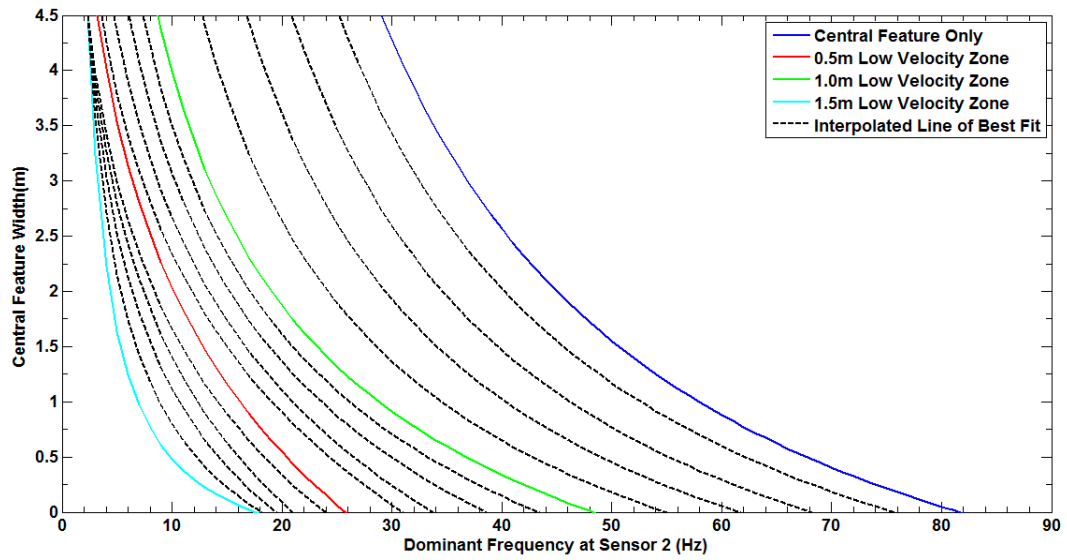
Figure 8-15: Graph presenting the curves for the various low velocity zone widths with central feature width varying with the dominant frequency observed at Sensor 2. Blue Curve: Central feature only (scenario 1) curve Green Curve: 0.5m fracture zone (scenario 2) Red Curve: 1.0m low velocity zone (scenario 3) Cyan Curve: 1.5m low velocity zone (scenario 4). All coloured curves are obtained from Figure 8-13 with the b parameter constrained to be less than zero for all curves. Black Dashed Curves: Interpolated Curves at 0.10m intervals for low velocity zone width. Each curve is distingushable from one another.

Table 8-14: Statisical evaluation of the goodness of fit for the models presented in Figure 8-15 with b constrained to be less that zero.

Best fit Data Dominant Frequency	Simulation Data	Interpolated Data				Simulation Data	Interpolated Data				Simulation Data	Interpolated Data				Simulation Data
Low Velocity Width	0	0.1	0.2	0.3	0.4	0.5	0.6	0.7	0.8	0.9	1	1.1	1.2	1.3	1.4	1.5
SSE	<0.01	0.01	<0.01	<0.01	<0.01	<0.01	0.15	0.14	0.15	0.15	0.01	0.04	0.01	0.01	0.01	<0.01
R-Squared	0.99	0.99	0.99	0.99	0.99	1.0000	0.99	0.99	0.99	0.99	0.99	0.99	0.95	0.99	0.99	0.99
Adjusted R-Squared	0.99	0.99	0.99	0.99	0.99	0.99	0.99	0.99	0.99	0.99	0.99	0.99	0.99	0.99	0.99	0.99
RMSE	0.01	0.03	0.02	0.02	0.05	0.05	0.14	0.14	0.14	0.15	0.03	0.07	0.03	0.04	0.04	0.01
P-Value	<0.05	<0.05	<0.05	<0.05	<0.05	<0.05	<0.05	<0.05	<0.05	<0.05	<0.05	<0.05	<0.05	<0.05	<0.05	<0.05

PPV: Figure 8-16 presents the curves for PPV. A statistical analysis was conducted on each of the curves and is presented in Table 8-15 to verify that the interpolated values follow the same power law (Equation 8-1) as the computed data from the numerical models (Section 8.3).

The SSE, R-Squared, Adjusted R-Squared, RMSE and P-Value are well within the thresholds demonstrating that the power law is an appropriate model to fit to the interpolated data. Each curve is not as easily distingushable from one another when compared to the dominant frequency curves. The results demonstrate a r-squared of 1 for the interpolated curves indicating a perfect fit, it is more likely that the r-squared values are a result of the PPV curves being so close together.
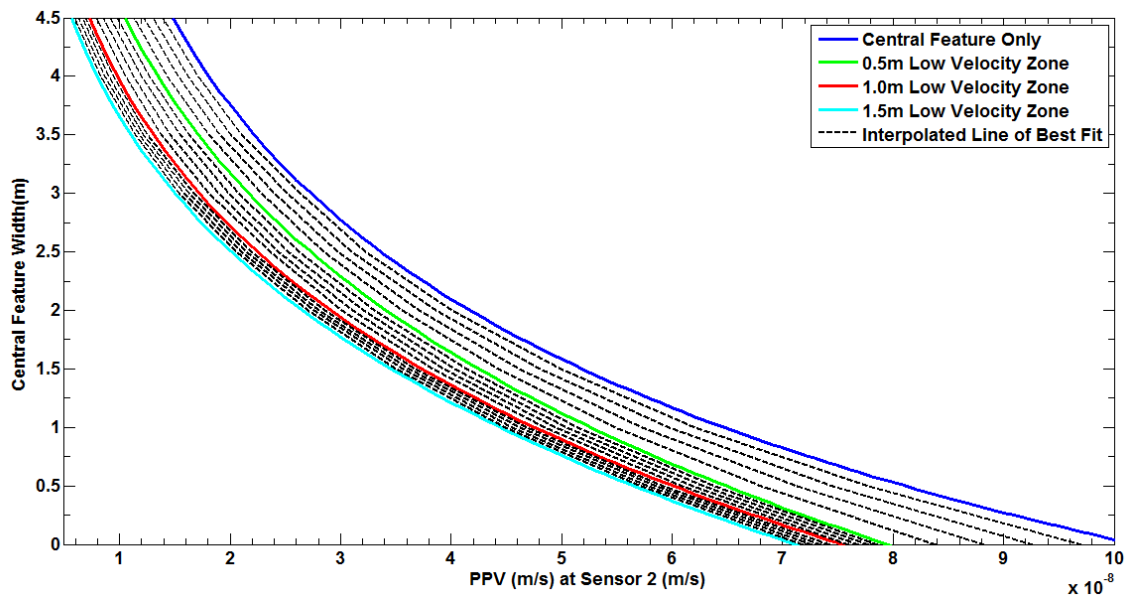
Figure 8-16: Graph presenting the curves for the various low velocity zone widths with central feature width varying with the PPV observed at Sensor 2. Blue Curve: Central feature only (scenario 1) curve Green Curve: 0.5m fracture zone (scenario 2) Red Curve: 1.0m low velocity zone (scenario 3) Cyan Curve: 1.5m low velocity zone (scenario 4). All coloured cureves are obtained from Figure 8-14 with the b parameter constrained to be greater than zero for all curves. Black Dashed Curves: Interpolated Curves at 0.10m intervals for fracture zone width. The curves are not as easily distinguishable as the dominant frequency curves.

Table 8-15: Statisical evaluation of the goodness of fit for the models presented in Figure 8-16, with b constrained to be greater than zero

Best fit Data PPV

	Simulation Data	Interpolated Data				Simulation Data	Interpolated Data				Simulation Data	Interpolated Data				Simulation Data
F-Zone Width	0	0.1	0.2	0.3	0.4	0.5	0.6	0.7	0.8	0.9	1	1.1	1.2	1.3	1.4	1.5
SSE	0.01	<0.01	<0.01	<0.01	<0.01	<0.01	<0.01	<0.01	<0.01	<0.01	<0.01	<0.01	<0.01	<0.01	<0.01	<0.01
R-Squared	0.99	1.00	1.00	1.00	1.00	1.00	1.00	1.00	1.00	1.00	1.00	1.00	1.00	1.00	1.00	1.00
Adjusted R-Squared	0.99	0.99	0.99	0.99	0.99	0.99	0.99	0.99	0.99	0.99	0.99	0.99	0.99	0.99	0.99	0.99
RMSE	0.04	<0.01	<0.01	<0.01	<0.01	<0.01	<0.01	<0.01	<0.01	<0.01	<0.01	<0.01	<0.01	<0.01	<0.01	<0.01
P-Value	<0.05	<0.05	<0.05	<0.05	<0.05	<0.05	<0.05	<0.05	<0.05	<0.05	<0.05	<0.05	<0.05	<0.05	<0.05	<0.05

8.6   Summary and Conclusions

There is a definite nonlinear relationship between the dominant frequency observed in the spectra at sensor 2, the PPV observed at sensor 2 and central feature width. A greater reduction in dominant frequency in the spectra and PPV is observed when a low velocity zone is present. There is a distinguishable difference in the results between scenarios 1, 2, 3 and 4.

Results demonstrate that there is the potential of distinguishing between features e.g. a central feature or a low velocity zone and that this can be used to develop a concept for geological feature detection establishing both the width and location of the geological feature.

Key Finding: It appears that the dominant frequency parameter will be more effective than PPV for predicting feature width. However, it is possible that the PPV curves will compliment the dominant frequency curves as a predictor variable in order to obtain accurate predictions.

There was a covariance error which contaminated the fit of the power law to the data set for both frequency and PPV. To overcome this, the b coefficient was constrained to be less than zero for all frequency curves and greater than zero for all PPV curves.

The statistical analysis was performed to ensure that the power law was a good fit for the data sets with the constrained b parameter.

9 A Feasibility Study: The Development of the Concept for a Site Investigation Tool to Determine Geological Feature Width and Location

Chapter 8 demonstrates that there is an apparent relationship between:

1. dominant frequency in the spectra and the PPV observed at a monitoring location where a geological feature exists between there and an active source; and
2. increased geological feature width.

A greater reduction in dominant frequency in the spectra and PPV is observed when a central feature is surrounded by a low velocity zone. There was a distinguishable difference in the results between scenario 1, 2, 3 and 4 in Chapter 8. This Chapter will establish if this difference can be used to develop the concept for a prediction tool.

This Chapter aims to utilise the change in the dominant frequency and PPV observed as the seismic wave travels away from the source in Chapter 8 to image geological features (i.e. identify their presence and geometrical characteristics). Additionally, the potential of distinguishing between features e.g. a central feature or a low velocity zone is explored.

9.1   Methodology: Prediction of Geological Feature Width Concept

In this Chapter, the equations derived in Chapter 8 and presented in Table 9-1 connecting central feature width, low velocity zone width, dominant frequency and PPV are used to develop a concept methodology for the prediction of a geological feature width based on the analysis of seismic data from numerical simulations.

The equations derived in Chapter 8 were contaminated by a covariance error, to overcome this the b coefficient was constrained to be less than zero for all frequency curves and greater than zero for all PPV curves as presented in Table 9-1.

Table 9-1: Coefficients corresponding to the curves for dominant frequency (Figure 8-15) and PPV (Figure 8-16). The curves have been refitted with the exponent b constrained to be less than zero for all frequency curves (Coulumn 2) and to be greater than zero for all PPV curves (Column 3).

Column 1: Low Velocity Zone (m)	Column2: Dominant Frequency Coefficients to Calculate Central feature Width (m)			Column 3: PPV Coefficients to Calculate Central feature Width (m)		
	A	B	C	A	B	C
0	231	-1.05	-2.31	-192	0.14	19.50
0.1	153	-0.96	-2.40	-128	0.1	25.35
0.2	102	-0.89	-2.43	-127	0.1	25.17
0.3	65	-0.79	-2.54	-135	0.03	87
0.4	39	-0.65	-2.82	-107	0.07	36.38
0.5	23	-0.47	-3.65	-134	0.11	22.85
0.6	20	-0.37	-4.89	-133	0.11	21.97
0.7	19	-0.25	-7.68	-134	0.11	20.9
0.8	27	-0.11	-18.16	-136	0.12	19.71
0.9	189	-0.01	-181.5	-148	0.13	17.66
1.0	265	-0.07	-259	-146	0.13	17.11
1.1	316	-0.01	-308	-159	0.14	15.91
1.2	28	-0.08	-21.94	-174	0.15	14.84
1.3	12	-2.84	-5.34	-192	0.16	13.88
1.4	10	-0.58	-1.94	-214	0.17	13.01
1.5	12	-1.06	-0.58	-244	0.18	12.16

Using the coefficient's presented in Table 9-1 the steps detailed in Figure 9-1 were applied.

Step 1
- Obtain the dominant frequency from the spectrum at sensor 2

Step 2
- Obtain the PPV value from the seismograph at sensor 2

Step 3
- Determine all possible central feature widths for each low velocity zone (Column 1, Table 9-1) using the dominant frequency coefficents (Column 2 Table 9-1)

Step 4
- Determine all possible central feature widths for each low velocity zone (Column 1, Table 9-1) using the PPV coefficients (Column 3, Table 9-1)

Step 5
- Insert all determined values into a table such as Table 9-2

Step 6
- Compare the values of central feature widths in a table such as Table 9-2 obtained using the frequency and PPV coefficients (Table 9-1).

Step 7
- Find the two values : one from the dominant frequency and one from the PPV coefficients with the smallest numerical difference between them. The corresponding low velocity zone widths must be the same for each of the selected values. Two pairs of values i.e. low velocity zone width and central feature width are determined.

Step 8
- Take the average of the two central feature widths rounded up to the nearest decimetre, as the field equipment cannot achieve a greater accuracy than this.

Figure 9-1 Steps follwed to determine low velocity zone and central feature width

Table 9-2: Table used to present calculated values of central feature width from equations in Table 9-1. The data highlighted in red correspond to values of acceptable central feature widths which have however been rejected using the concept methodology. Data highlighted in green are the paired values with the smallest numerical difference between the central feature widths calculated using the dominant frequency and PPV equations. The corresponding low velocity zone widths are the same. The predicted low velocity zone and central feature width are detailed as the bottom of the table.

Central Feature Only A					
Dominant Frequency Obtained from Sensor 2	Low Velocity Zone Width (m)	Central Feature Width (m) (Obtained from Coefficients in Column 2 Table 9-1)	PPV Obtained from Sensor 2	Low Velocity Zone Width (m)	Central Feature Width (m) (Obtained from Coefficients in Column 3 Table 9-1)
35	0	3.3	2.28E-08	0	3.4
	0.1	2.6		0.1	3.3
	0.2	2.0		0.2	3.1
	0.3	1.4		0.3	3.1
	0.4	1.0		0.4	3.0
	0.5	0.6		0.5	2.9
	0.6	0.4		0.6	2.8
	0.7	0.2		0.7	2.7
	0.8	-0.1		0.8	2.6
	0.9	-0.4		0.9	2.5
	1	-0.9		1	2.5
	1.1	-1.0		1.1	2.4
	1.2	-0.9		1.2	2.4
	1.3	-0.8		1.3	2.3
	1.4	-0.6		1.4	2.3
	1.5	-0.3		1.5	2.3

Predicted Central Feature Width=

(3.3 + 3.4)/2

Predicted Central Feature Width	3.4
Actual Central Feature Width	3.6

Predicted Fracture Zone Width	0.0
Actual Fracture Zone Width	0

9.2 Verification: Prediction of Geological Feature Width

The concept for the prediction tool methodology presented in Figure 9-1 was validated with a series of "Blind" tests.

The "Blind" tests were models set by a colleague without having knowledge of the geological setting. There was knowledge of the values for parameters that could be measured in the field or after the analysis of the recordings. More specifically the knowledge of the model was:

1) The total domain size (25m x 25m);

2) The source PPV and frequency;

3) The source location and monitoring point locations; and

4) The material properties of the host rock, central feature and low velocity zone. The presence of central feature or low velocity zone was unknown.

Six scenarios were considered to test the prediction of feature width:

1) A single geological feature (two "blind" models); and

2) A single geological feature surrounded by a low velocity zone of unknown width (four "blind" models).

There was no knowledge of the order in which the data would be received for these simulations, ensuring that the tests would be completely "blind".

9.2.1 Blind Tests Detailing Systematic (Precision) Error

Table 9-3 presents the results from the "blind" tests. As per the methodology outlined in Figure 9-1 the required observed parameters from the test model data set by a colleague were a 1) dominant frequency and PPV both obtained from sensor 2 as detailed in Column 1 of Table 9-3 .

A central feature width surrounded by a low velocity zone was predicted for each scenario i.e. Blind A – Blind F as detailed in Column 2 of Table 9-3. The actual central feature width and surrounding low velocity zone width is also presented in Column 3 of Table 9-3. The precision error is detailed in Column 4 of Table 9-3.

The maximum systematic (precision) error was obtained from Blind Test C +0.3m as highlighted in red in Table 9-3. This systematic (precision) error will be quoted in all further cases as it is recommended and deemed conservative to quote the "worst case" error (Devore and Berk 2011).

Systematic (precision) errors are reproducible inaccuracies that are consistently in the same direction. Systematic errors are often due to an error which persists throughout the entire experiment (Field 2009).

Systematic (precision) errors are difficult to detect and cannot be analysed statistically, as all the data is contaminated by an error in the same direction (i.e. either too high or too low) (Field 2009).

The calculation of the random uncertainty associated with the simulations is explained and presented in Section 9.2.2

Table 9-3: Table presenting the required and calculated parameters for the Blind Tests Column 1) required observed parameters: dominant frequency and PPV located at sensor 2 and Column 2) calculated parameters: central feature widths and corresponding low velocity zone widths generated from the equations presented in Table 9-1 with b contrained, Column 3) Actual values: central feature widths and corresponding low velocity zone obtained from blind simulations and Column 4: Precision error.

Column1: Test Data Obtained from Sensor 2	Column 2: B Constrained to be less than zero for all frequency curves and greater than zero for all PPV curves			Column 3: Actual Values			Column4: Precision Error (m)
	Predicted CFW Frequency (m)	Predicted CFW PPV (m)	Predicted CFW (m)	Predicted Low Velocity Zone Width (m)	Actual CFW (m)	Actual Low Velocity Zone Width (m)	
Blind A Dominant Frequency = 35Hz PPV= 2.28E-08 m/s	3.3	3.4	**3.4**	**0**	**3.6**	**0**	+0.2
Blind B Dominant Frequency = 53Hz PPV= 5.86E-08m/s	1.3	1.2	**1.3**	**0**	**1.3**	**0**	+0.1
Blind C Dominant Frequency = 5Hz PPV= 2.23-08 m/s	2.5	2.4	**2.5**	**1.3**	**2.8**	**1.0**	**+0.3**
Blind D Dominant Frequency = 5Hz PPV= 3.15E-08 m/s	1.7	1.7	**1.7**	**1.5**	**1.6**	**1.5**	-0.1
Blind E Dominant Frequency = 17Hz PPV= 2.99E-08 m/s	2.3	2.3	**2.3**	**0.5**	**2.2**	**0.5**	-0.1
Blind F Dominant Frequency = 5Hz PPV= 1.70E-08 m/s	3	3	**3.0**	**1.1**	**3.1**	**1**	+0.1

9.2.2   **Random Uncertainty**

All experimental uncertainty is due to either random errors or systematic (precision) errors. Random errors are statistical fluctuations (in either direction i.e. ±) in the measured data due to the precision limitations of the numerical model or seismometers. Random errors can result from the inability to take the same measurement in exactly the same way to get exact the same number (Field 2009).

Systematic (precision) error is presented in Section 9.2.1.

Note: Systematic and random errors refer to problems associated with making measurements. Mistakes made in the calculations or in reading the instrument are not considered in error analysis. It is assumed that the individual is suitability qualified and experienced.

In order to quote the parameters within their 95% confidence limits the exponent b detailed within Table 9-1 was constrained to a constant value for each scenario.

For each blind simulation parameter i.e. dominant frequency and PPV the equations were solved with the b coefficient constrained to a constant value to obtain values for low velocity zone width and central feature width as presented in Table 9-4. The b coefficients were constrained to -0.5 for all frequency curves and 0.1 for all PPV curves.

Table 9-4: b coefficients constrained to -0.5 for all frequency curves and 0.1 for all PPV curves. Column 1: Calculated low velocity zone width (m), there was no difference betweent the low velocity zone width (m) obtained from the coffecents detailed in Table 9-1. Column 2: Dominant frequency coefficients. Column 3: PPV coefficients.

	Column 1: Low Velocity Zone (m)	Column2: Dominant Frequency Coefficients to Calculate Central feature Width (m) B=-0.5			Column 3: PPV Coefficients to Calculate Central feature Width (m) B=0.1		
		A	B	C	A	B	C
Blind A	0	59	-0.5	-6.60	-192	0.1	19.50
Blind B	0	59	-0.5	-6.60	-192	0.1	19.50
Blind C	1.3	10	-0.5	-2.16	-107	0.1	20.73
Blind D	1.5	10	-0.5	-2.72	-106	0.1	20.39
Blind E	0.5	23	-0.5	-3.32	-130	0.1	25.24
Blind F	1.1	10	-0.5	-1.57	-110	0.1	21.14

These values were then compared to the low velocity zone width and central feature width parameters obtained from the values calculated using the coefficients detailed in Table 9-1, allowing the random uncertainty for the model to be obtained.

The random uncertainty was calculated using the following recommended approach for small data sets as presented in Field (2009). In order to calculate the random uncertainty in a single measurement of CFW, this uncertainty is determined by making multiple measurements i.e. comparing the calculated CFW values from:

1. B coefficient constrained to be less than zero for all frequency curves and greater than zero for all PPV curves; and

2. B coefficients were constrained to -0.5 for all frequency curves and 0.1 for all PPV curves.

Therefore it can be established from the data that CFW lies somewhere between CFW max and CFW min.

There was found to be no difference in the low velocity zone width (m) calculated using the coefficients detailed in Table 9-1, therefore the random uncertainty is related to the calculation of central feature width.

Table 9-5 presents the results from fitting the Blind Test data to the equations with b constrained to a constant value. By using these results as a benchmark this allowed the results to be quoted to their 95% confidence limit.

The 95 % confidence band was chosen as in applied practice, confidence bands are typically stated at the 95% confidence level (Field 2009).

A confidence band is used in statistical analysis to represent the uncertainty in an estimate of a curve or function based on limited data. Similarly, a prediction band is used to represent the uncertainty about the value of a new data-point on the curve, but subject to noise.

The worst case scenario was Blind Test F with a random uncertainty of ± 0.4m. This worst case uncertainty is assumed to be the random uncertainty of the prediction model and will be compared to the site investigation systematic error quoted in Chapter 10.

Table 9-5: Results obtained from B constrained to a constant value B=-0.5 for all frequency curves B=0.1 for all PPV curves. Column 1: Calculated CFW using dominant frequency coefficients. Column 2: Calculated CFW using PPV coeffcents. Column 3: Predicted CFW using the methodology presented in Figure 9-1 with B=constant. Column 4: Predicted low velcoity zone width using the methodology presented in Figure 9-1 with B=constant, there was found to be no difference it the low velocity zone width obtained. Column 5: Calculated random uncertainty.

| Test | B constrained to a constant value B=-0.5 for all frequency curves B=0.1 for all PPV curves | | | | Column 5: Random Uncertainty 95% Confidence Limits |
	Column 1: Prediction of CFW using Dominant Frequency (m)	Column 2: Prediction of CFW using PPV (m)	Column 3: Predicted CFW (m)	Column 4: Predicted Low Velocity Zone Width (m)	
Blind A	3.4	2.8	3.1	0	0.2
Blind B	1.4	1.4	1.4	0	0.1
Blind C	2.4	2.3	2.4	1.3	0.1
Blind D	2	1.6	1.8	1.5	0.1
Blind E	2.3	2.3	2.3	0.5	0
Blind F	2.7	2.7	2.7	1.1	**0.4**

9.2.3   Validation of Random Uncertainty

In order to validate the calculation of uncertainty (±0.4m) the MatLab Curve Fitting Toolbox was used as it can calculate prediction bounds for the fitted coefficients.

The prediction is based on an existing fit to the data. Additionally, the bounds measure the confidence for all predictor values at 95% based on the following equation:

Equation 9-1

$$CFW = model + random\ error$$

To exemplify this graphically the dominant frequency curve and the PPV curve for a central feature detailing the 95% prediction bounds is presented in Figure 9-2 and Figure 9-3 respectively.

The worst case random error was found to be: CFW = model ± 0.39m.

This was the maximum error obtained from all curves presented in Section 8.5. Only one curve is presented in Figure 9-2 and Figure 9-3 for clarity. Therefore in all other scenarios the random uncenrtainty will be quoted as ± 0.4m as the "worst case" to adopt a conservative approach.
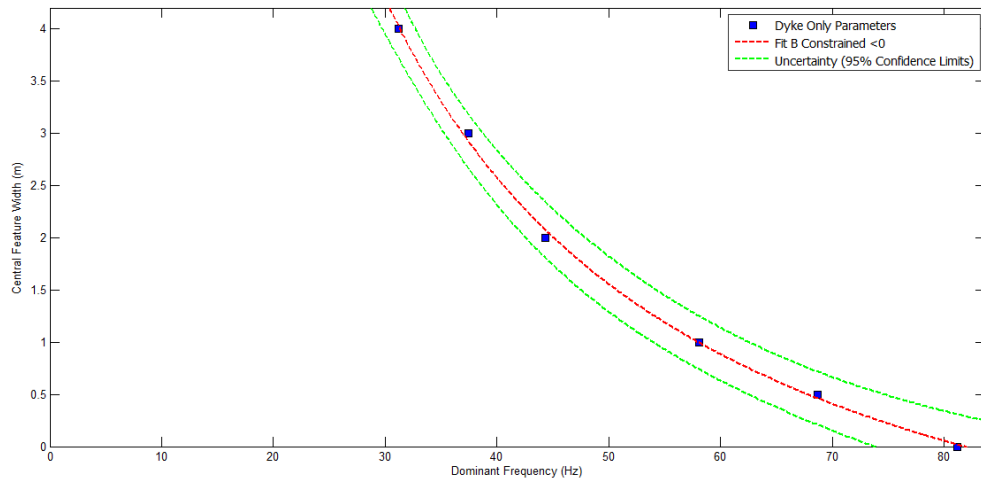
Figure 9-2: Graph detailing central feature only dominant frequency data with B constrained <0 with 95% confidence prediction bounds applied. The worst case random uncertainty was found to be ±0.37m.
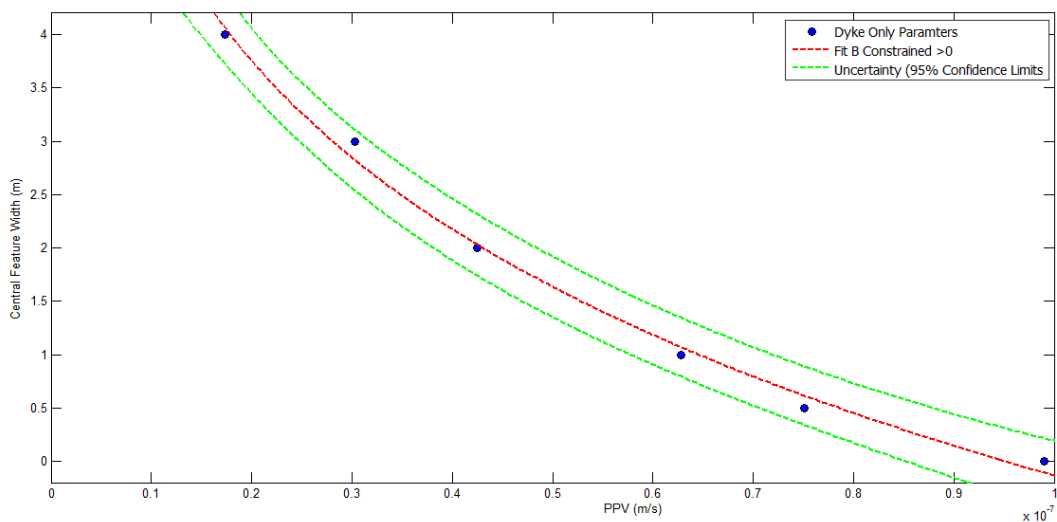
Figure 9-3: Graph detailing central feature only dominant frequency data with B constrained <0 with 95% confidence prediction bounds applied. The worst case random uncertainty was found to be ±0.37m.

9.2.4   **Summary**

From the "blind" simulations analysed using the developed concept methodology the presence of geological features and the presence of a surrounding low velocity zone can be detected with good accuracy. The values of central feature width selected using the methodology must have the same corresponding low velocity zone widths. The maximum systematic error was + 0.3m.

Using numerical simulations this Chapter successfully utilises the change in the dominant frequency and PPV observed as the seismic wave travels away from the source to image geological features, identifying their presence and geometrical characteristics with defined material properties. It has been shown that this method can distinguish between different features such as a central feature or a low velocity zone.

This methodology requires that the geological feature is between an active source and the monitoring location (sensor 2) that provides the seismic data used in the spectral analysis.

The following section will explore the location capabilities of the concept. The random uncenrtainty will be quoted as ± 0.4m as the "worst case" to adopt a conservative approach.

9.3   Methodology: Prediction of Geological Feature Location

PPV has been used as a parameter to characterize ground vibrations caused by blasts in the mining industry. Experimental models have related the PPV to the distance between the detonation source and the monitoring location as demonstrated by Arshadnejada, Yanb et al. (2013). Therefore, PPV was deemed as the optimum parameter to explore the potential of location prediction in this thesis.

To predict geological feature location it was decided to solve a numerical simulation and sample the PPV of the seismic signal every 0.5m over a 20m monitoring cross section for a 3m central feature surrounded by a 1m low velocity zone as demonstrated via the red dotted line in Figure 9-4. The rationale behind this was to establish if the PPV varies significantly enough as the signal loses energy to visualise the geological feature and its location.
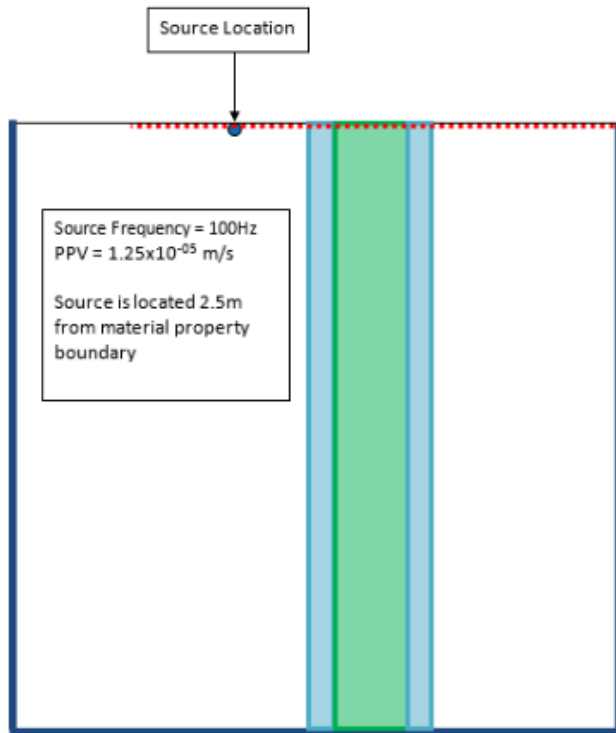
Figure 9-4: : Schematic of 25m x 25m model to obtain PPV and dominant frequency values of the signal. Green Block: 3.1m width central feature. Light Blue Blocks: 1.0m low velocity zone. Blue Circle: Source location. Red Dashed Line: Monitoring points located every 0.5m over a 20m cross section. Dark Blue Border: Low reflecting boundary condition.

To establish if the geological feature and potentially geological feature boundary locations can be visualised using PPV the steps in Figure 9-5 were followed.

Step 1
- Find the PPV from the analysis of the recordings at 0.5m intervals over the 20m monitoring cross section as demonstrated in Figure 9-2, Figure 9-4 and Table 9-9

Step 2
- Use PPV values in Table 9-9 and create a horizontal profile of PPV at 0.5m intervals over the 20m monitoring cross section as demonstrated in Figure 9-5.
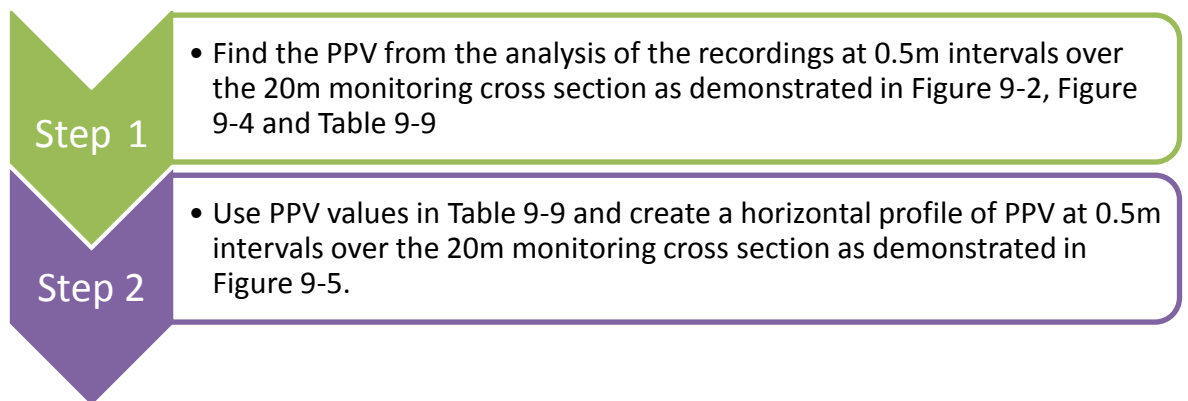
Figure 9-5: Steps follwed to visulise geological feature and potentially geological feature boundary locations using PPV
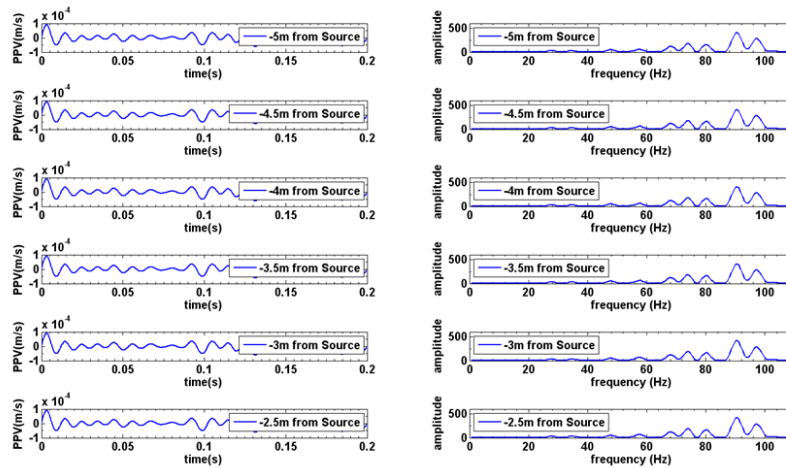
Figure 9-6: Selection of the numerical solution data obtained from the geological feature presented in Figure 9-4 Rows from top: Sensor locations: -4.5m, -4.0m, -3.5m,-3.0m, and -2.5m from the source Column A: PPV over time. Column B: Power Spectra.

Table 9-6: Table presenting the distance from the source (column 1) and PPV values (column 2) produced from the numerical simulation presented in Figure 9-4. Data corresponds to the horizontal profile presented in Figure 9-7

Column 1: Distance From Source (m)	Column 2: PPV (m/s)
-5	9.02E-05
-4.5	9.02E-05
-4	9.02E-05
-3.5	9.03E-05
-3	9.03E-05
-2.5	9.04E-05
-2	9.04E-05
-1.5	9.04E-05
-1	9.04E-05
-0.5	9.05E-05
0	9.06E-05
0.5	9.04E-05
1	9.04E-05
1.5	9.03E-05
2	9.03E-05
2.5	7.01E-05
3	6.90E-05
3.5	6.50E-05
4	7.43E-06
4.5	6.21E-06
5	5.80E-06
5.5	5.10E-06
6	4.80E-06
6.5	3.80E-06
7	2.50E-07
7.5	1.70E-07
8	1.81E-07
8.5	1.79E-08
9	1.78E-08
9.5	1.77E-08
10	1.76E-08
10.5	1.75E-08
11	1.72E-08
11.5	1.70E-08
12	1.67E-08
12.5	1.63E-08
13	1.60E-08
13.5	1.59E-08
14	1.51E-08
14.5	1.49E-08
15	1.48E-08

It has been observed that PPV varies as a result of feature presence. Each of the geological zones can clearly be visualised, in particular the low velocity zone as detailed in Figure 9-7. Figure 9-7 accurately shows that the geological feature is located 2.5m from the source.
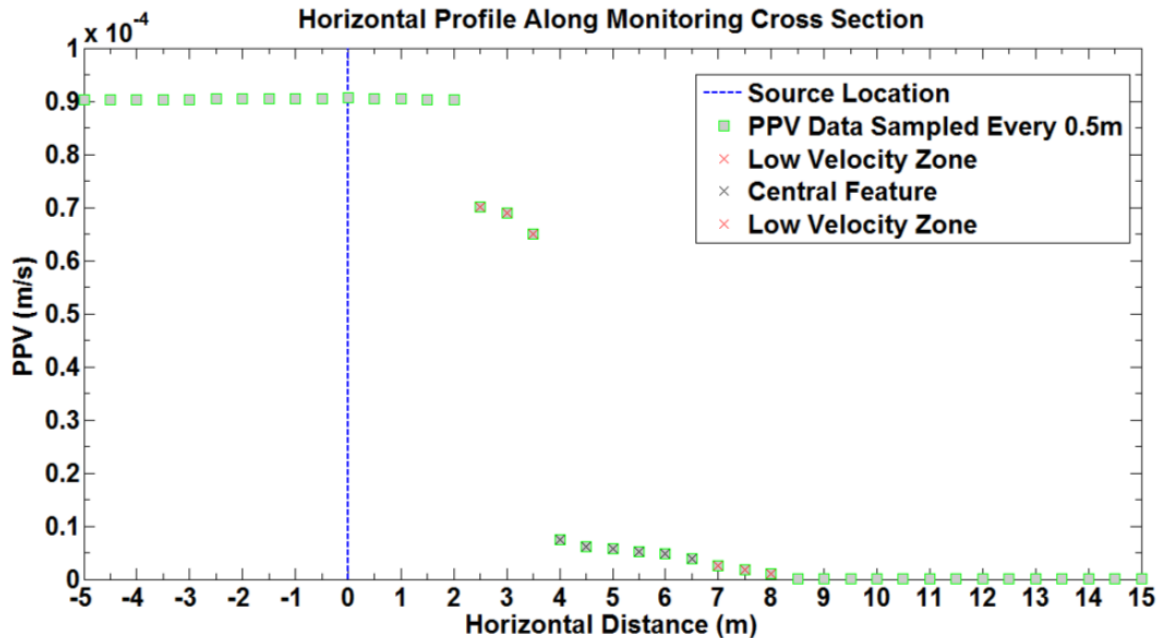
Figure 9-7: Hoizontal profile presenting the data from the numerical simulation described in Figure 9-4. Blue dashed line: source location, Green square: PPV sampled every 0.5m, Red cross: Low velocity zone and Black cross: Central feature. Each of the material zones and feature location can be clearly visualised. The geological feature is located 2.5m from the source.

Figure 9-7 demonstrates that the PPV values detected over the monitoring cross section presented as a horizontal profile highlight that the change in PPV infers the geological feature location and width. The low velocity zones and central feature can be distinguished from the surrounding host rock.

For practical applications it is unlikely that sampling this densely (every 0.5m) using microseismometers would be possible. However, it is likely that geological feature location and width can be inferred. Potentially, the utilisation of smaller accelerometers may allow increased sampling points, however this is beyond the scope of this thesis.

9.3.1   **Summary**

Plotting PPV as a horizontal profile across the monitoring cross section allowed the visualisation of the geological feature which inferred that the geological feature location can be visualised with good accuracy using PPV. However, this is dependent on the PPV being sampled densely across the monitoring area.

These results agree with the concept adopted by Marfurt and Kirlin (2001) that internal geological structures at or below the conventional seismic resolution exhibit themselves as subtle variations in PPV rather than changes in the arrival times. These variations in PPV have been used effectively in this Chapter to visualise geological feature location.

This Chapter has shown that the main factors influencing PPV of induced sources such as a generator are the:

1. vibrations transferred from the generator to the rock;
2. geological properties; and
3. distance from the source.

The vibrations transmitted from source to the rock depend on the source-rock interaction and the wave propagation and attenuation in the zone closest to the generator. There is today no prediction model that completely fulfils the criteria of the "perfect" prediction model which is reliable, yet easy to apply. However, this concept offers the potential for a solution to be developed for effectively predicting geological feature location in field applications. In the next Chapter this concept will be applied as a pilot field trial.

10 Validation: Deployment of Pilot Site Investigation Tool in the Field

10.1 Choice of Field Site for the Pilot Study

From the numerical results in Chapter 7 and 8, it was clear that when there was a significant material property contrast a notable change in the dominant frequency of the seismic signal was observed for an induced source with a frequency of 100Hz. There was also a change in PPV. Both of these parameters are investigated for potentially being able to predict a geological feature width and its location in the field. The feasibility of the concept developed in Chapter 9 demonstrated good accuracy for determining:

1. Geological feature width;
2. low velocity zone width; and
3. geological feature location inferring the geological feature boundary location.

A field site for the pilot study was chosen on the basis of:

1. the geological feature having a significant material property contrast and good exposure;
2. the site being characterised by relatively simplistic geometry i.e. clearly defined boundaries between the high and low velocity zones (simple geometry is easier to compare to the numerical simulations); and
3. material properties of the field site being comparable to those used in the numerical simulations in Chapter 8.

Ideal geological features were considered. Excellent geological feature exposure was important, primarily as the seismic sensors have a better coupling with the ground surface when placed on hard rock. Igneous intrusions such as dykes were seen to be a favourable option particularly in sandstone as there is a significant

material property contrast between the igneous rock and the sandstone host rock with the material properties being comparable to those simulated numerically i.e. going from a low velocity zone to a high velocity zone. In addition, there is an abundance of dyke formations in Scotland, particularly on the Isle of Arran allowing ease of access and minimal research costs.

The Corrie Shore area in Arran, is characterised by dyke intrusions in sandstone. A dyke formation which was approximately 2m wide and easily accessible from the road at Corrie Shore as presented in Figure 10-1, was chosen for the field validation.

Corrie Shore is in a remote location with minimal ambient noise sources i.e. from the sea waves and the occasional passing car. Ambient noise can contaminate the seismic signal and therefore was an important consideration in the choice of field site. Minimal ambient noise ensured that a good comparison between the numerical solution and field data could be made. A site with ease of access was a main characteristic in the final choice due to the extensive amount of equipment required to carry out a seismic survey.
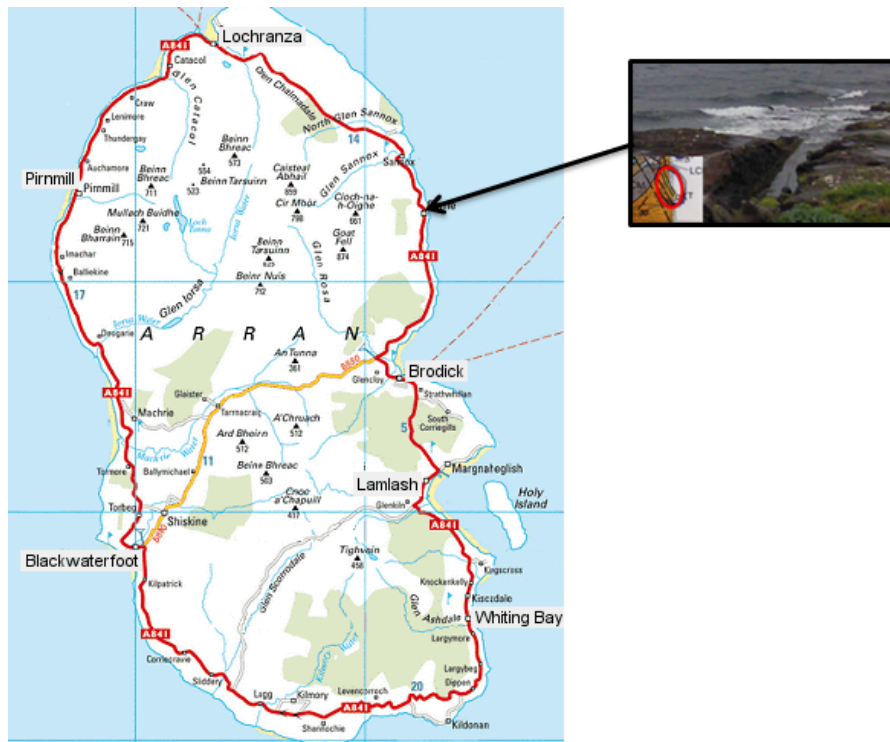
Figure 10-1: Map of Arran highlighting the location of Corrie Shore, Arran. The geological map of dyke is shown as an insert in the photograph highlighting the dolerite dyke intrusion. Insert: Geological map with dyke highlighted (red circle). The geological map details a dolerite dyke which has intruded red sandstone.

10.2 Site Reconnaissance

Initially a site reconnaissance was carried out in order to establish the viability of the site and determine the geology. A geological survey was carried out and rock samples were taken in order to give an insight into the true mechanical properties of the site. Rock samples were taken from non-intact rock to ensure that the method was entirely non-invasive as the site is contained within a Site of Special Scientific Interest (SSSI).

10.2.1 Mapping of the field site

The geological survey was a systematic investigation of the geology on Corrie Shore to create a geological map of the field site permitting the validation of the model developed in Chapter 8. The aims of the survey are presented below.

<u>**Aims**</u>

- Examine the physical characteristics and key geological features in the proposed field site; and

- identify the different rock types.

10.2.1.1 **Field Sketch**

Figure 10-2 presents a sketch of the physical features of the dyke at Corrie Shore. Once depth and height measurements were established giving the dimensions of the dyke, the sketch was drawn accurately to scale and then digitised. Observations and annotations were made:

- Obvious features and measurement of geometry;

- Structure of the dyke for example joints, baked and chilled margins; and

- Photographic evidence was used to support and reinforce sketches.

10.2.1.2 **Geology of the field site**

Figure 10-2 details the geology and the geometry of the dyke. The dyke is 2.0m wide. From the photographs and field annotations it is clear that the dyke is well jointed. This will have a direct effect on the P wave velocity of the dyke intrusion. The dyke is characterised as a dolerite dyke. Dolerite has a P wave velocity of approximately 3000-5900m/s (Carmichael 1988). As the dyke is well jointed the P wave velocity of the dolerite dyke is likely to be at the lower end of this approximation. The chilled margin which is visible extends to around 0.20m in width extending to 1.38m in length on the left hand side of the dyke and 4.52m on the right hand side of the dyke. It is possible for the chilled margin to have a comparable P wave velocity to the dolerite dyke as there is the presence of deformation bands and the chilled margin appeared to have a similar crystalline structure to the dolerite. It is also detailed in that the dyke is at an inclination of 25 degrees.

The host rock is sandstone which is characterised by deformation bands and coastal erosion. Sandstone has a P wave velocity between 1400-4000m/s (Carmichael 1988). Due to the presence of deformation bands caused by the intrusion and coastal erosion it is likely that the P wave velocity of the host rock will be at the lower end of this approximation. The sensor locations are detailed as seismometer 1 and 2.

The numerical modelling P wave velocity of 3454m/s for dolerite was appropriate due to the well jointed nature of the intrusion. A P wave velocity of 1490m/s was decided to be an appropriate value for the sandstone host rock. These values are consistent with the values used in Chapter 8. These P wave velocity approximations validate the choice of field site as an appropriate fit for the model. Due to the field site being a SSSI it was not possible to take intact rock samples, therefore the value of 1000m/s was deemed adequate for the low velocity zone and is comparable to values presented in Carmichael (1988) for a low velocity rock mass i.e. chilled/baked margin.
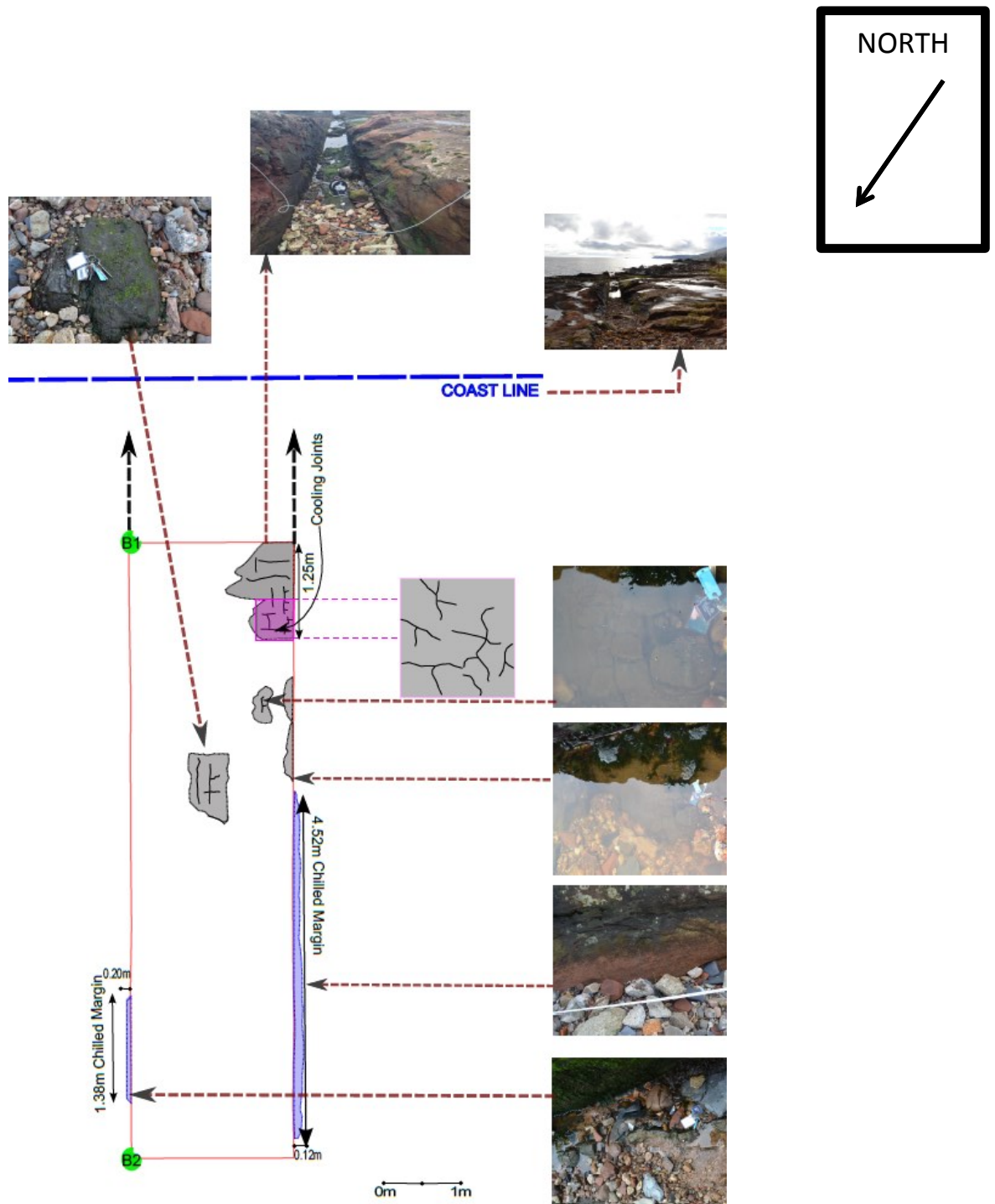
Figure 10-2: Arial view of the dolerite dyke. Digitised field sketch of the geological structure of the dolerite dyke which has intruded sandstone. The Base point is B1. The second base point is B2. The section of interest is 8m in length. There is little exposure of the dolerite. The dolerite that is exposed is heavily jointed. There is the presence of a chilled margin at either side of the dyke which are characterised by deformation bands.

10.2.2   **Field Methodology**

The equipment used for the field trial is defined in Chapter 2.2.8, Section 3.3, pg. 32:

1. seismometers (Table 3-1);
2. data logger (Figure 3-4); and
3. seismic source/generator (Figure 3-5).

In order to carry out the pilot field trial the following methodology was followed:

1. Seismometer 1 was located 2.5m from the dyke boundary (Figure 10-3 and Figure 10-4);
2. Seismometer 2 was located 10.5m from Seismometer 1 (Figure 10-3 and Figure 10-4);
3. To maintain consistency with the numerical simulations the source (generator) was placed 0.5m from the seismometer 1 (Figure 10-4);
4. The seismic array was set up and recording began 30 mins prior to the source being turned on to allow for the recording of seismic noise;
5. The generator was turned on and recording took place for 30mins;
6. The generator was turned off and recording took place for 15mins;
7. Step 8 and 9 were repeated twice giving 3 data sets. The rationale behind repeating the recording was to ensure that if any anomalies occurred they could be accounted for i.e. a person walking their dog through the site, a vehicle passing by, rainfall etc.
8. Extract the data from the data logger applying the conversion into PPV as detailed in Section 3.3 pg. 32;
9. Produce the seismograph for 100 second interval for both seismometer 1 and 2 (Figure 10-5);
10. Extract the PPV and dominant frequency values (Figure 10-5);
11. Apply the methodology detailed in Section 9.1, pg. 162 ; and

12. Obtain values for central feature width and low velocity zone width (Table 10-1.
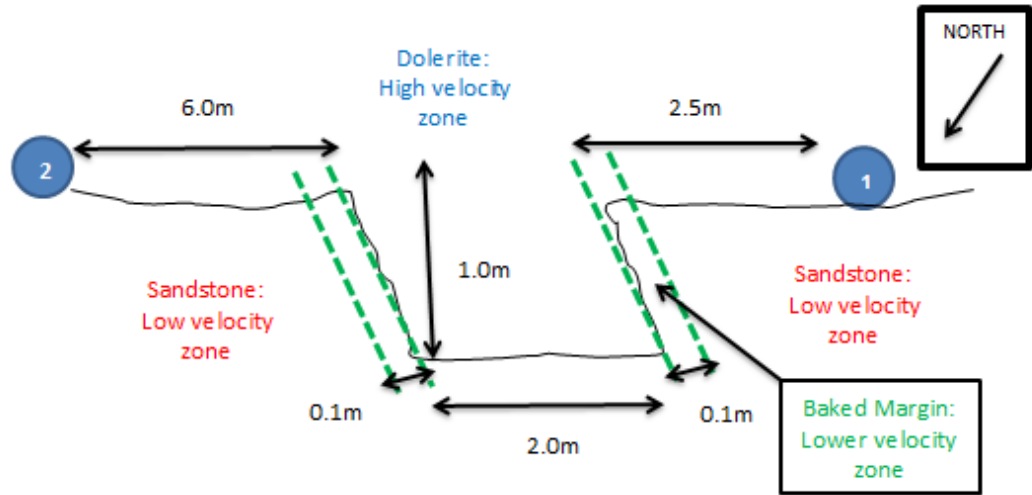
Figure 10-3: Cross-sectional view of the dyke detailing 1) seismometer 1 and 2 locations (blue circles) 2) material property zones and 3) the dimensions of the field site.
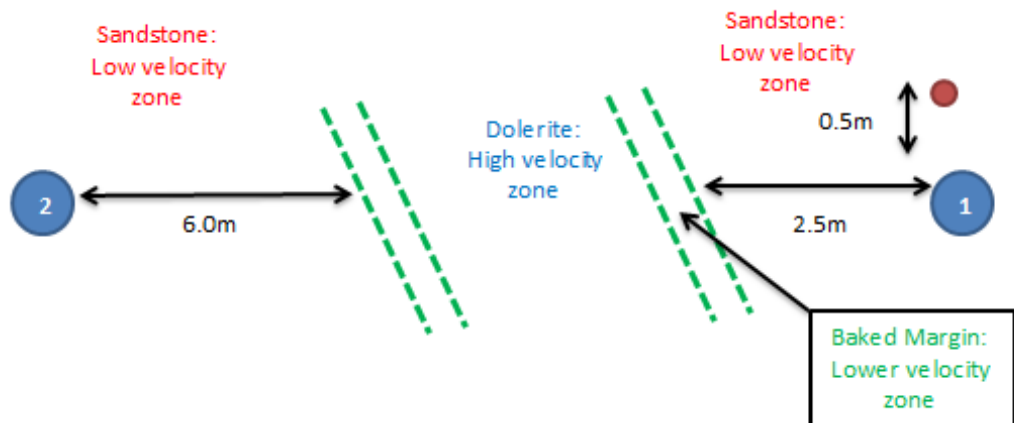
Figure 10-4: Plan view of the dyke detailing 1) seismometer 1 and 2 locations (blue dots), 2) generator location (red dot), 3) the dimensions of the field site and 4) material property zones

10.2.3   **Results**

10.2.3.1   **Pilot Study: Prediction of Geological Feature Width**

Figure 10-5 (a) and (b), present the raw seismic data obtained from seismometer 1 and 2. Both the source and the sensor locations were kept as close as possible to those used in the numerical simulations. This allows for a good comparison between the concept developed in Chapter 8 and the pilot field trial.

The details of the sample window, PPV and dominant frequency selection are outlined below:

- **Sample Window Selection:** Sample window of 100s (Figure 10-5 (a) and (b)) was selected to ensure that the PPV and dominant frequency were accurately represented in the data sample.

- **PPV:** The PPV within 100s monitoring window which has the largest value/amplitude (Figure 10-5).

- **Dominant frequency**: The frequency within the LNP spectra which has the greatest amplitude i.e. the most significant peak (Figure 10-5).

- **PPV and Dominant Frequency Selection:** The maximum values of PPV and dominant frequency were obtained using a "max" function in Mat lab. This was a conscious decision to minimise error and ensure consistency when selecting the maximum PPV and dominant frequency values for field data.

At seismometer 1 a PPV of 4.56×10^{-5} m/s is observed and a dominant frequency of 92Hz is detected. The 4.56×10^{-5} m/s is comparable to the 4.19×10^{-5} m/s PPV obtained from sensor 1 when there was a 2.0m geological feature in the numerical solution (Table 8-3, pg. 131). The 92Hz is slightly lower than 97Hz values obtained in the numerical solution (Table 8-3, pg. 131). This slight variance can be explained by the fact that the numerical model is not an exact representation of the real site conditions and also there is potential for a variation in the operating frequency of the seismic source i.e. the generator.

At seismometer 2 a PPV of 2.97×10^{-8} m/s and a dominant frequency of 45Hz was detected. The values are slightly different to those obtained from the numerical simulation at a location of 11.5m from the source (44Hz and 4.3×10^{-8} m/s.) It should be noted that the goal was not to see whether the numbers matched exactly but to test whether the concept methodology developed based on the numerical simulations can be applied to real data when these are collected in similar conditions.

N.B: The distance between sensor 1 and 2 in the comparable numerical simulation for a 2m central feature as presented in Table 8-3, pg. 131 was 11.5m. The distance between seismometer 1 and 2 in the field trial was 10.5m due to uneven surface conditions.
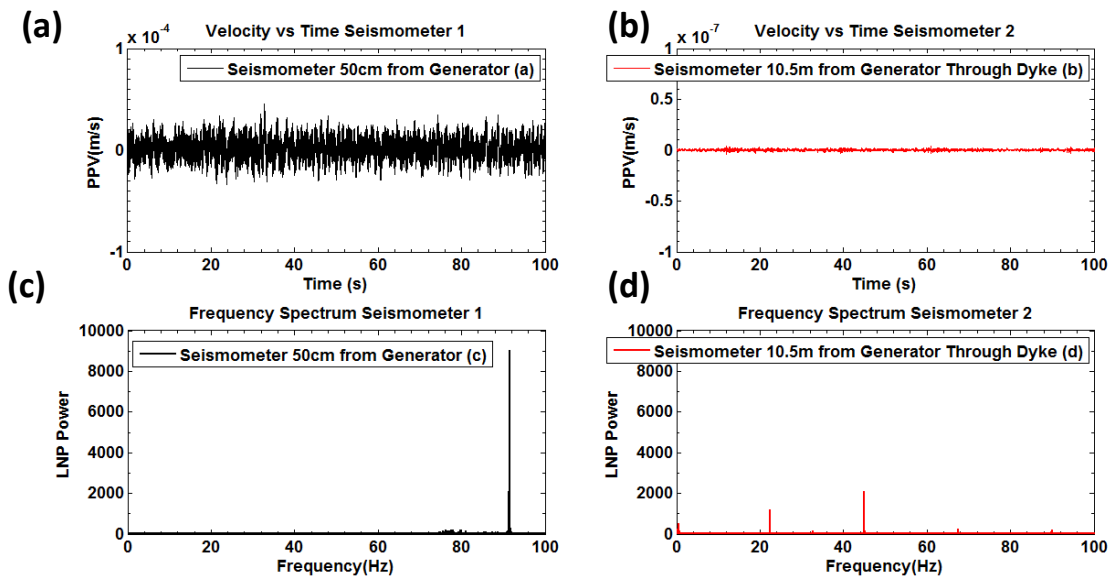
Figure 10-5: Field data . Clockwise from left (a) raw seismic vertical component data from seismometer 1 located 50cm from the generator, (b) raw seismic vertical component data from seismometer 2 located 10.5m from the generator through the dyke, (c) power spectrum created from seismogram (a) data and (d) power spectrum created from seismogram (b) data. There is a notable reduction in PPV (m/s) when comparing (a) and (b). There is a notable reduction the dominant frequency of the spectra when comparing (c) and (d). In (d) the presence of additional frequency peaks is observed. There is a notable reduction in the amplitude when comparing (c) and (d). The change in PPV (m/s) and dominant frequency are in good agreement with numerical simulations.

Table 10-1 presents the output for the PPV and dominant frequency data inserted into the system of equations derived in Chapter 9, Section 9.1. The data predicted a

central feature width of 1.6m accuracy of -0.4m. The actual feature width was 2.0m. During the geological survey there was the presence of approximately 0.1m chilled and baked margin at the dyke edges. However this was not present consistently at the dyke edges. The model predicted 0.1m low velocity zone achieving good accuracy.

Table 10-1: Table presenting the required and calculated parameters for the field data: 1) required observed parameters: dominant frequency and PPV located at seismometer 2 and 2) calculated parameters: central feature widths and corresponding low velocity zone widths generated from the equations presented in Table 9-1. Green: Paired PPV and dominant frequency results. Red: No data pair established.

Field					
Dominant Frequency Obtained from Seismometer 2	Low Velocity Zone Width (m)	Central Feature Width (m) (Obtained from Equations in Column 2 Table 9-1)	PPV Obtained from Seismometer 2	Low Velocity Zone Width (m)	Central Feature Width (m) (Obtained from Equations in Column 3 Table 9-1)
45	0	2.0	2.97E-08	0	1.8
	0.1	1.5		0.1	1.7
	0.2	1.1		0.2	1.6
	0.3	0.7		0.3	1.5
	0.4	0.4		0.4	1.4
	0.5	0.1		0.5	1.3
	0.6	-0.1		0.6	1.3
	0.7	-0.3		0.7	1.2
	0.8	-0.6		0.8	1.2
	0.9	-1.0		0.9	1.1
	1	-1.6		1	1.1
	1.1	-1.6		1.1	1.1
	1.2	-1.4		1.2	1.0
	1.3	-1.1		1.3	1.0
	1.4	-0.8		1.4	1.0
	1.5	-0.4		1.5	1.0

Predicted Central Feature Width	1.6
Actual Central Feature Width	2

Predicted Fracture Zone Width	0.1
Actual Fracture Zone Width	0.1

Key Point: A numerical solution is not an exact representation of the field site i.e. it is not exactly the same therefore a precision of -0.4m is not unreasonable for central feature width. In addition, the low velocity zone (chilled baked margin) did not have consistent exposure at the field site therefore the detection of a 0.1m low velocity zone is a positive result.

Comparison to Random Uncertainty: The precision error of -0.4 in consistent with the "worst case" random uncertainty of ± 0.4m calculated in Section 9.2.2.

10.2.3.2   **Pilot Study: Prediction of Geological Feature Location**

In order evaluate the potential to detect the location of seismometer 1 and 2 and the potential to infer the location of the dyke, the PPV data from a previous simulation which modelled a 2.0m central feature with no low velocity zone was used (Chapter 8, Section 8.2.1, Table 8-3, pg. 131). The monitoring points were located every 0.5m as presented in Chapter 9, Section 9.3.

Table 10-2 presents the PPV data obtained from the numerical simulation.

Table 10-2: Table presenting the numerical simulation data Column 1: distance from source (m) and Column 2: the corresponding PPV values generated from the monitoring points located every 0.5m.

Column 1: Distance From Source (m)	Column 2: PPV (m/s)
-5	4.10E-05
-4.5	4.10E-05
-4	4.10E-05
-3.5	4.10E-05
-3	4.10E-05
-2.5	4.10E-05
-2	4.10E-05
-1.5	4.10E-05
-1	4.10E-05
-0.5	4.10E-05
0	4.19E-05
0.5	4.09E-05
1	4.09E-05
1.5	4.05E-05
2	4.05E-05
2.5	3.21E-06
3	1.57E-06
3.5	5.20E-07
4	1.72E-07
4.5	1.54E-07
5	9.50E-08
5.5	9.10E-08
6	8.90E-08
6.5	8.20E-08
7	7.50E-08
7.5	6.30E-08
8	5.80E-08
8.5	5.10E-08
9	4.99E-08
9.5	4.84E-08
10	4.66E-08
10.5	4.50E-08
11	4.42E-08
11.5	4.30E-08
12	3.82E-08
12.5	3.74E-08
13	2.95E-08
13.5	2.45E-08
14	2.37E-08
14.5	2.24E-08
15	2.15E-08

The PPV data in Table 10-2 was plotted as a horizontal profile across the monitoring cross section as presented in Figure 10-6. The aim was to establish if the PPV obtained from seismometer 1 and 2 (Figure 10-5) can be aligned with PPV values obtained from the numerical model. This would allow a feature location and width to be inferred using numerical simulations as a forward model.
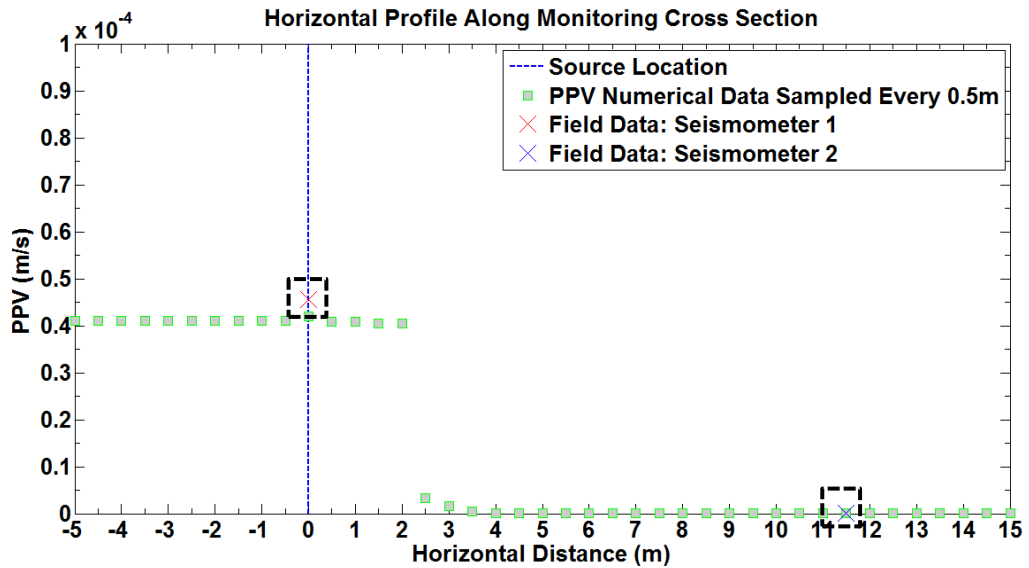
Figure 10-6: Hoizontal profile presenting (1) the data from the numerical simulation for 2m central feature (grey square with green outline) detailing seismic source location (blue dashed line), (2) Seismometer 1 field data (red cross), (3) Seismometer 2 field data (blue cross). The field data (surrounded by black dashed boxes) algins well with the numerical simulation.

Seismometer 1: The PPV of 4.56 x10^{-5} m/s (seismometer 1) at the source is slightly higher than the 4.19 x10^{-5} m/s corresponding numerical value (Table 10-2).

Seismometer 2: The PPV 4.28 x10^{-8} m/s (seismometer 2) obtained 10.5m from the source is lower than the 4.50 x10^{-8} m/s corresponding numerical value (Table 10-2). When pairing the data values the seismometer 2 PPV corresponds to a location of approximately 11.5m from the source in the numerical data which is a good accuracy of ± 1.0m.

Key Point: The presence of the chilled and baked margins, deformation bands and coastal erosion could have resulted in additional reflections of the seismic signal causing amplification in the PPV. In other words, the numerical simulation is not an exact representation of the field site. The aim here was not to establish whether the PPV values match exactly but to test whether utilising numerical models as a forward modelling tool can be applied to real data when collected in similar conditions, to infer geological feature location and width.

Amplification in PPV was visible in previous simulations when a material property boundary was present. The greater the number of material property boundaries the greater the amplification in PPV. If this pilot study was to be conducted again the addition of more seismometers or accelerometers would allow for a better comparison between numerical and field data i.e. sample more densely.

10.3   Summary

The pilot field study has demonstrated positive results demonstrating that numerically a good representation of a field site geometry and geology can be achieved. There are some errors in the concept which can be explained by operational, systematic and numerical errors or that the field site is not exactly the same as the numerical simulation.

Feature Width: The systematic error of -0.4 in consistent with the "worst case" random uncertainty of ±0.4m calculated in the numerical model presented in Section 9.2.2.

Feature Location: PPV plotted as a horizontal profile across the monitoring cross section can visually infer geological feature presence as well as location using numerical simulations combined with field data. The ability to use field data is dependent on the number of seismometers available.

Combined with other geophysical methods such as GPR, the concept developed in this thesis could be particularly valuable, complimenting results and further evidencing geological feature detection.

11 Effect of Noise

The effect of noise is important in terms of resolution and the applicability of the method defined in Chapter 9 and presented in the field study in Chapter 10. Noise will be considered in addition to the sensitivity analysis presented in Chapter 9.

11.1   Ambient noise

In seismic and acoustical engineering, background noise or ambient noise is any sound other than the signal being monitored (i.e. primary signal). Background noise is a form of noise interference. Background noise is an important concept in understanding single processing (Miller, Bradford et al. 2010).

Examples of background noises are environmental noises such as waves, traffic noise, alarms, people talking, bioacoustic noise from animals or birds and mechanical noise from devices such as refrigerators or air conditioning, power supplies or motors (Shearer 1999).

11.1.1   The effect of ambient noise on field data

The effect of ambient noise on the recorded field data was considered. Figure 11-1 highlights that the field site chosen for the field study is characterised as a very low ambient noise environment. It is likely that the ambient noise recorded was from the sea and perhaps a passing car. This was particularly infrequent and can be assumed to have a minimal effect on the recorded signal.

For example as presented by Urick (1986) the sea, rain drops impacting the earth and the implosion of air bubbles caused by rain are generally in the range of frequency = 1kHz-100 kHz. This out with the frequency range (1-100Hz) of this study and can be considered to have no effect.
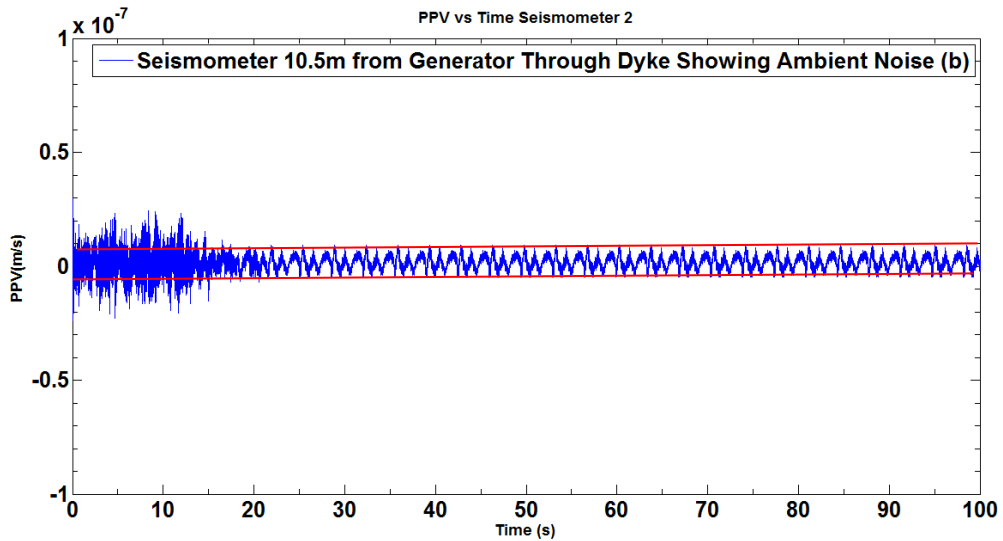
Figure 11-1: Field data highlighting ambient noise recorded when the generator is turned off. The ambient noise recored is 3 times less than the maximum PPV of $2.97x10^{-8}$ m/s observed at Seismometer 2 located 10.5m from the generator.

In the field trial the maximum PPV value obtained while the generator was turned off was $9.10x10^{-9}$m/s, 3 times less than the maximum PPV of $2.97x10^{-8}$ m/s observed at Seismometer 2 located 10.5m from the generator. It can therefore be concluded that the negative effects of ambient noise at the field site were negligible. This is also reinforced by the lack of ambient noise detected in the power spectrum (Figure 10-5).

However, this research intentionally selected a field site that was characterised by a low ambient noise environment i.e. the PPV measured as a result of ambient noise is at least 3 times less than the smallest PPV detected 10.5m from the seismic source. In addition, this removed the requirement to utilise signal processing filtration methods as the impact from ambient noise was deemed insignificant. Consideration will now be given to sites that may be characterised by ambient noise that is greater than the maximum PPV produced by the seismic source.

11.2   High ambient noise environments

In order to investigate the deployment of this method in a high noise environment, to quantify the precision and to investigate how this changes as the ambient noise is increased the White Gaussian Noise function in MatLab was applied to the data set. The White Gaussian Noise function was chosen as it allowed the amount of noise added to the signal to be accurately quantified (Butt 2009). The additive white Gaussian noise (AWGN) function in MatLab is a basic noise model used to mimic the frequencies of many random processes that occur in nature. The maximum amplitude (PPV) of the added noise is defined allowing the noise added to the signal to be quantified. .

The data set chosen was the central feature only simulations presented in Figure 8-13. As ambient noise is generally present at frequency ranges >50Hz (Urick 1986), this data set would be more susceptible to a negative impact on precision due to the effects of ambient noise.

11.2.1   Method

Two different levels of ambient noise were added to the model:

- 1.25 times the source PPV ($1.5 \times 1.25 \times 10^{-5}$ m/s); and
- 2 times the source PPV ($2 \times 1.25 \times 10^{-5}$ m/s).

The following methodology was used:

1. White Gaussian noise added to signal for each of the central feature width scenarios to allow model curves to be produced which take into consideration noise;

2. Establish the central feature width using the Blind Test A and B dominant frequency and PPV data (see Section 9.2.1);

3. Quantify the random uncertainty using the noise model to a 95% confidence limit by constraining the b coefficient to a constant value;

4. Compare the random uncertainty to the systematic error quoted in the field study.

11.2.2   **Results**

Figure 11-2 and Table 11-1 summarise the data from the ambient noise simulations, detailing the PPV and dominant frequency values obtained when noise was added to the signal.

Figure 11-2: Graphs presenting PPV and Dominant Frequency curves with b coefficient constrained to be less than zero for all frequency curves and greater than zero for all PPV curves for the paramters measured as sensor 2. (a) PPV curves with 1) CFW only data points 2) Noise 1.5 times the source PPV (1.5 x 1.25x10-5 m/s); and 2 times the source PPV (2 x 1.25x10-5 m/s). (b) Dominant Freuquency curves with 1) CFW only data points 2) Noise 1.5 times the source PPV (1.5 x 1.25x10-5 m/s); and 2 times the source PPV (2 x 1.25x10-5 m/s). A gradual reduction is PPV and dominant frequency is observed as CFW is increased which aligns with previous simulations. The PPV paramter exhibts a greater variation as noise is increased.

Table 11-1: Ambient noise central feature only results. PPV exhibits are greater over all variation when noise is increased. The variation decreases as central feature width is increased. Dominant frequency only exhibits a variation when the central feature width is greater than 1m.

Ambient Noise: Central Feature Only						
	Zero Noise		2 times the source PPV (2 x 1.25x10^{-5} m/s).		1.5 times the source PPV (1.5 x 1.25x10^{-5} m/	
Central Feature Width (m)	PPV (m/s)	Dominant Frequency (Hz)	PPV (m/s)	Dominant Frequency (Hz)	PPV (m/s)	Dominant Frequency (Hz)
0	0.99x10^{-7}	81	2.76x10^{-7} (+1.77 x10^{-7})	81 (0)	2.20x10^{-7} (+1.21x10^{-7})	81 (0)
0.5	0.75x10^{-7}	69	1.85x10^{-7} (+1.10 x10^{-7})	69 (0)	1.31x10^{-7} (+0.56x10^{-7})	69 (0)
1	0.63x10^{-7}	58	1.36x10^{-7} (+0.73 x10^{-7})	58 (0)	1.10x10^{-7} (+0.47x10^{-7})	58 (0)
2	0.43x10^{-7}	44	0.74x10^{-7} (+0.44 x10^{-7})	35 (-9)	0.69x10^{-7} (+0.26x10^{-7})	41 (-3)
3	0.30x10^{-7}	37	0.58x10^{-7} (+0.28 x10^{-7})	22 (-15)	0.42x10^{-7} (+0.12x10^{-7})	31 (-6)
4	0.17x10^{-7}	31	0.33x10^{-7} (+0.16 x10^{-7})	16 (-15)	0.27x10^{-7} (+0.1 x10^{-7})	25 (-6)

Figure 11-3 and Figure 11-4 present the results when the numerical domain is characterised by a single geological feature with no low velocity zone present when noise 2 times the source PPV and 1.25 times the source PPV is added to the signal respectively.
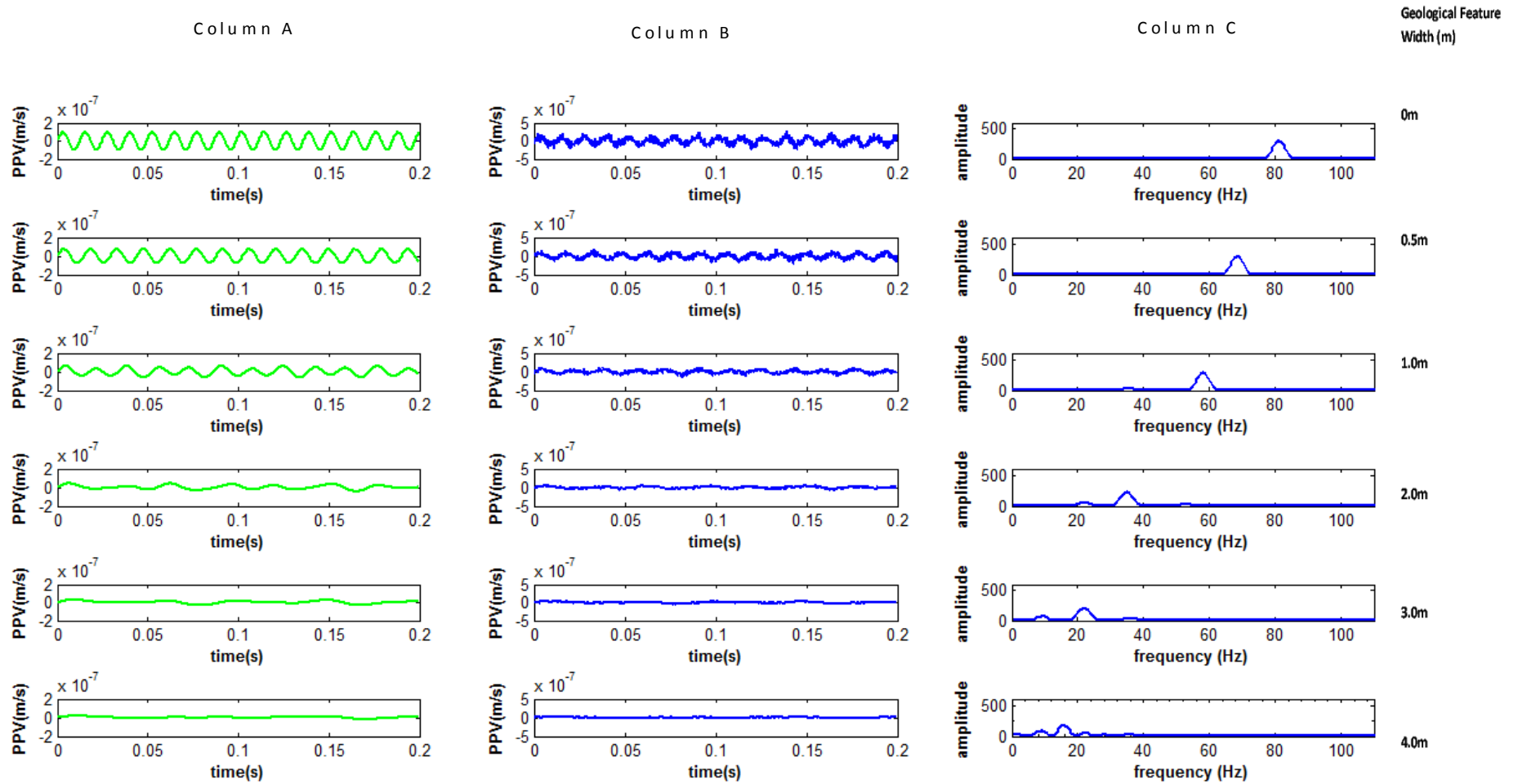
Figure 11-3: Results for the various geological feature widths. Rows from top: 0m, 0.5m, 1.0m, 2.0m, 3.0m and 4.0m. There is no surrounding low velocity zone. Column A: PPV over time for sensor 2. Column B: PPV over time for sensor 2 with noise added 2 times the source PPV. Column C: Power spectrum sensor 2 with noise added 2 times the source PPV
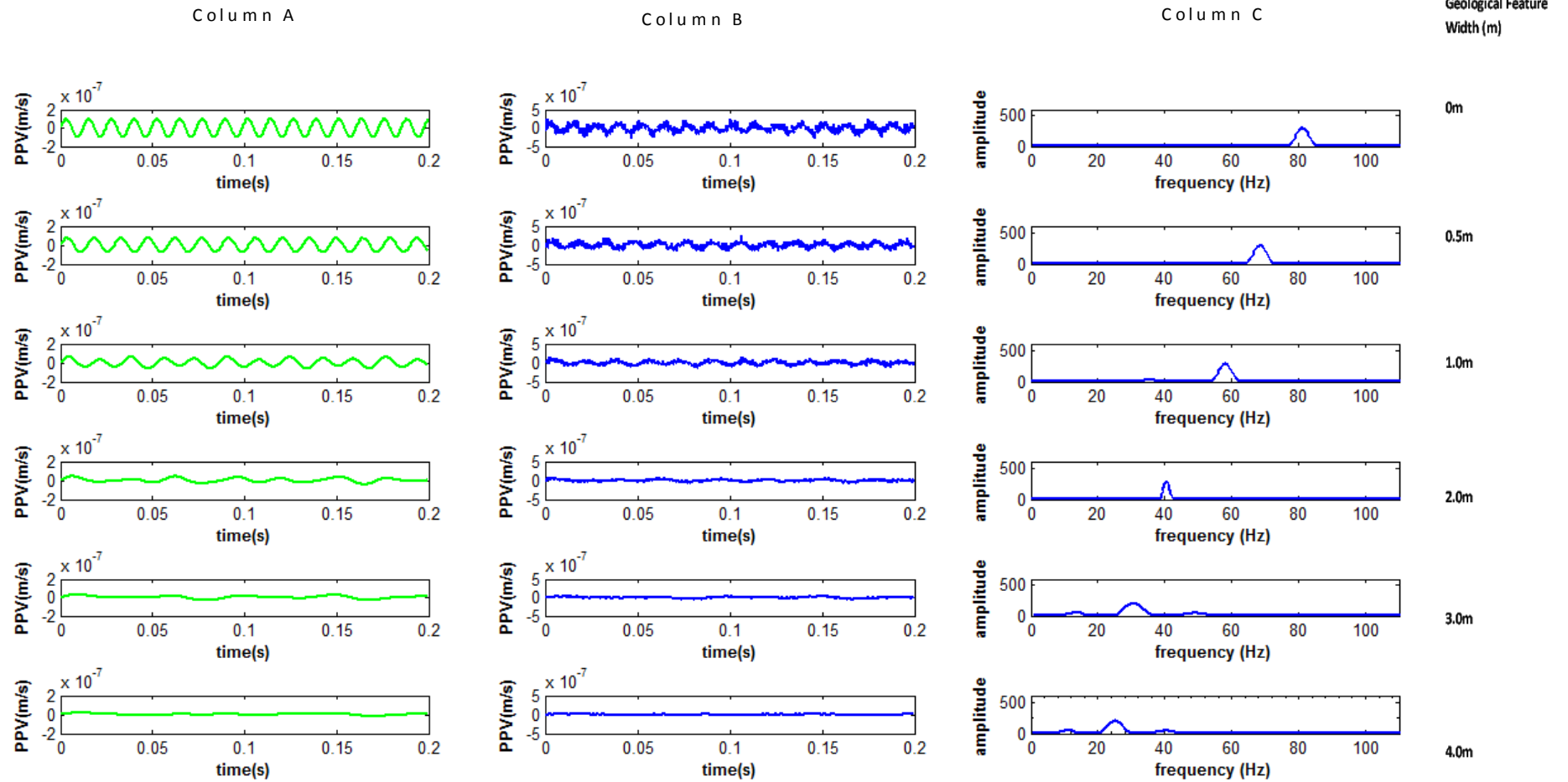
Figure 11-4: Results for the various geological feature widths. Rows from top: 0m, 0.5m, 1.0m, 2.0m, 3.0m and 4.0m. There is no surrounding low velocity zone. Column A: PPV over time for sensor 2. Column B: PPV over time for sensor 2 with noise added 1.25 times the source PPV. Column C: Power spectrum sensor 2 with noise added 2 times the source PPV

11.2.3 Comparison to Random Uncertainty and Systematic Error

In order to quantify the random uncertainty and compare the results the systematic error in the field trial the coefficients were obtained for both the PPV and dominant frequency curves:
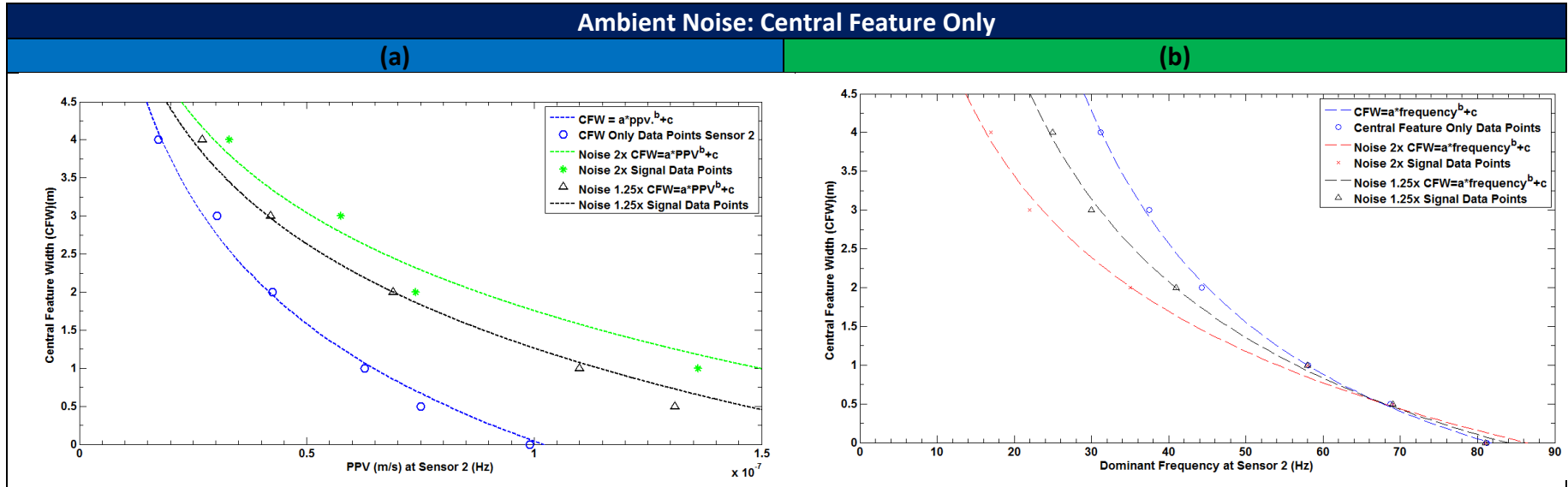
1. The b coefficient was constrained to be less than zero for all frequency curves and greater than zero for all PPV curves as presented in Table 11-2; and

2. The b coefficients were constrained to -0.5 for all frequency curves and 0.1 for all PPV curves as presented in Table 11-3.

This is consistent with the approach used in Chapter 9.

In order to quantify the effect of noise the central feature width for Blind Test Scenario A and B were recalculated using the coefficients for the two increased noise scenarios (Table 11-4).

Table 11-2: Equations corresponding to the curves for dominant frequency and PPV (Figure 11-2). The curves have been fitted with the exponent b constrained to be less than zero for all frequency curves (Coulumn 2) and to be greater than zero for all PPV curves (Column 3).

Ambient Noise Central Feature Only						
Column1: Noise Added to Source PPV	Column2: Dominant Frequency Coefficients to Calculate Central feature Width (m)			Column 3: PPV Coefficients to Calculate Central feature Width (m)		
	A	B	C	A	B	C
0	231	-1.05	-2.31	-192	0.14	19.50
Noise 1.25x	50	-0.56	-4.04	-137	0.02	100.8
Noise 2x	25	-0.19	-10.86	-112	0.02	80

Table 11-3: B coefficients constrained to -0.5 for all frequency curves and 0.1 for all PPV curves (Figure 11-2). Column 1: Noise added to source PPV. Column 2: Low velocity zone width. Column 3: Dominant frequency coefficients. Column 4: PPV coefficients.

Ambient Noise Central Feature Only							
Column1: Noise Added to Source PPV	Column 2: Low Velocity Zone (m)	Column3: Dominant Frequency Coefficients to Calculate Central feature Width (m) B=-0.5			Column 4: PPV Coefficients to Calculate Central feature Width (m) B=0.1		
		A	B	C	A	B	C
0	0	59	-0.5	-6.60	-192	0.1	19.50
Noise1.25	0	44	-0.5	-4.61	-102	0.1	21.6
Noise 2x	0	29	-0.5	-2.96	-96	0.1	21.05

Table 11-4 Results obtained from calculations considering noise. Column1: Blind Test Scenario. Column 2: Actual CFW. Column 3: CFW calculated using curves with zero added noise. Column 4: CFW calculated using curves with 1.25 x source PPV noise added, detailing B = variable and B = constant and random uncertainty. Column 5: CFW calculated using curves with 2 x source PPV noise added, detailing B = variable and B = constant and random uncertainty. The "worst case" random uncetainty as a result of added noise was ± 1.6m.

*Note B = variable: b coefficient were constrained to be less than zero for all frequency curves and greater than zero for all PPV curves
B = Constant: b coefficients were constrained to -0.5 for all frequency curves and 0.1 for all PPV curves..
Numbers highlighted in red referred to systematic (precision) error quoted against Actual CFW

Column 1: Blind Test	Column 2: Actual CFW	Column 3: CFW width Zero Noise	Column 4: CFW with 1.25 x Noise			Column 5: CFW with 2 x Noise		
			B=Variable	B=Constant	Random Uncertainty	B=Variable	B=Constant	Random Uncertainty
A	3.6	3.4 (-0.2)	3.6 (0)	3.4	0.2	1.6 (-2)	3.2	**1.6**
B	1.2	1.3 (+0.1)	1.8 (+0.6)	1.9	0.1	1.9 (+0.7)	1.8	0.1

Key Point: The "worst case" systematic error when noise was 1.25 x source PPV was +0.6m and the random uncertainty was ± 0.2m. Both the systematic error and the random uncertainty is less than the -0.4m systematic error observed in the field trial presented in Chapter 10. When noise was increased to 2 x source PPV the "worst case" systematic error was -2m and the random uncertainty was ± 1.6m. Both of which are greater than systematic error observed in the field trial. It would appear that the detection of larger geological features is more likely to be negatively affected by the presence of noise.

11.3   Summary

In conclusion the effect of ambient noise on the field trial observation was deemed to be negligible due to the field site being characterised by a low ambient noise environment.

However, in order to investigate the deployment of this concept method in a high noise environment, in order to quantify the precision and to investigate how this changes as the ambient noise is increased the White Gaussian Noise function in MatLab was applied to the data set at 1.25 and 2 times the source PPV respectively.

When noise was increased to 2 x source PPV the "worst case" systematic error was - 2m and the random uncertainty was ± 1.6m. Both of which are greater than systematic error observed in the field trial.

In high noise environments it would be advantageous prior to the experiment to establish the PPV of the ambient noise and establish if the PPV of the seismic source is powerful enough to overcome the effect of ambient noise i.e. at least 3 times greater as presented Section 11.1.1. If this is not the case consideration will have to be given to either changing the seismic source to a source with an greater energy i.e. can produce a greater PPV or consider applying filtration techniques to reduce the effects. Additionally, future work could develop curves specifically tailored for geological feature detection in high noise environments to overcome this constraint.

12 Future Applications

The potential future applications of this geophysical site investigation tool concept will be discussed in distinct categories related to natural geological and hydrogeological features (Section 12.1).

Preliminary simulations in Section 12.2 related to real world problems in the UK specifically, near surface disused mine workings, coal seams and sink holes will then be presented.

12.1   Potential Geological Applications

12.1.1   Fault Zones and Fractured Zones

This concept for a site investigation tool could be applied to obtain information on the location and characterisation of existing joints, fractured zones and faults. These features can vary from individual joints and fracture zones to much larger features such as faults. It is important to highlight the joints, fractures and fault zones may be dry, fluid filled or sealed with clay or weathered rock. The sensitivity of this concept to detect features of this type increases with feature size and with the presence of highly contrasting material properties.

12.1.2   Rock Layers

This concept for a site investigation tool can be used to determine if there is an interface i.e. different rock layers using the change in dominant frequency and PPV of the seismic signal. Good examples of these interfaces in practical scenarios are: limestone sitting on top of a granite or sandstone sitting on top of shale and discontinuous bedding planes. The ability of this concept to effectively resolve the rock layers is dependent on the mechanical properties, depth and thickness of the rock layers and will require further development.

12.1.3   **Depth to Bedrock**

This concept for a site investigation tool, if further developed could be applied to establish the depth to bedrock that is overlain by unconsolidated overburden. In order for the concept developed in this thesis to be successful there must be a significant contrast in material properties between the bedrock and the overlying layers.

12.1.4   **Voids and Sinkholes**

Voids and sink holes are also known as karst features. Karst features can be weathered depressions in the rock, open, gravel or water filled sinkholes, cavities and subsurface cave networks. When investigating sinkholes the site investigation problems can be beyond the resolution capacity of many geophysical methods. Deep cavities or voids can be detected or shows signs of their presence in the near surface and in the interpretation of near surface data. The ability to detect cavities decreases with depth. The preliminary simulations presented in Section 12.2 will explore the potential application of the concept developed in this thesis at high level.

12.2   **Supporting Simulations**

In order provide an indication on whether this concept for a site investigation tool can be applied to potentially detect voids such as sink holes, coal seams and disused mine workings the change in the characteristic of the dominant frequency and PPV parameters will be obtained from numerical simulations.   The aim of these preliminary simulations is:

1. Establish if a significant change in the dominant frequency and PPV of the seismic signal; and
2. Establish if several peaks are observed within the power spectra which imply from previous simulations that there is a geological boundary or feature present.

These supporting simulations will not establish the dimensions and location of the scenarios considered, they will only infer if there is a potential to further develop the concept developed in this thesis as a site investigation tool.

12.2.1   **Disused Mine Workings in Glasgow**

Disused mine workings are a costly hazard for Glasgow City Council particularly in the Jordanhill area of the city where there are many near surface mine workings, pits and shafts. With the average house prices between £450,000 and £600,000 this is also a hazardous concern for homeowners. One of the main hazards is a lack of knowledge surrounding the location of abandoned mine workings (Figure 12-1). It was not until 1872 that the law required mine owners to record their workings in what were known as "abandonment plans" but the records were often poor and inaccurate. In 1912 the law made it a requirement that all mineral workings must be recorded by qualified surveyors.
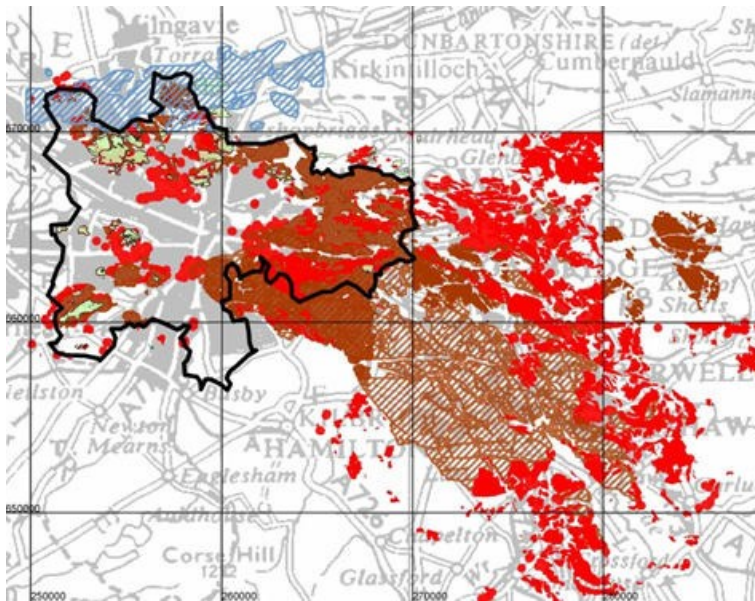
Figure 12-1 Mining locations in the Glasgow area .Brown areas indicate where mining is known to have taken place. Red areas show where mining is likely to have been at shallow depths (Ranalli and Murphy 1987)

For the purpose of this preliminary assessment there are four scenarios considered:

1. A coal seam after exploitation (long cross section) modelled as a material property boundary;

2. A coal seam after exploitation (small cross section) modelled as a material property boundary;

3. A coal seam after exploitation (small cross section) modelled as a free surface; and

4. A coal seam after exploitation (small cross section) modelled as a free surface with sensor locations moved.
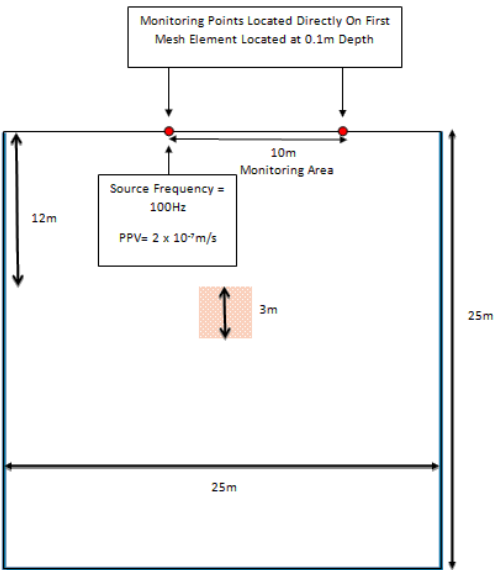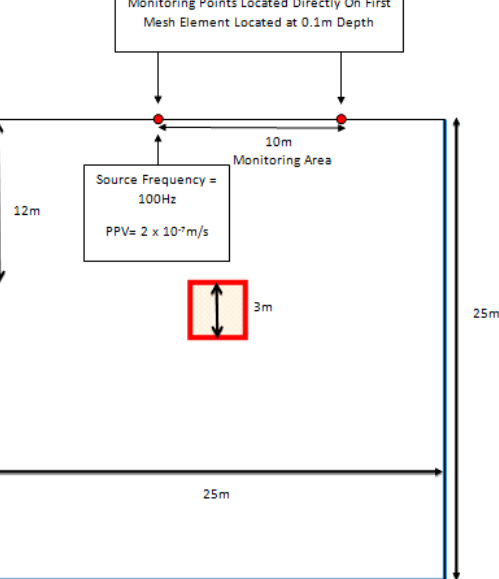
These scenarios are presented in detail in Table 12-1.

The coal seam is located at 12m depth and characterised by a height of 3m. The material properties of the host rock were defined as clay the same as those used in Section 6.2.6: P wave velocity, S wave velocity and Poisson Ratio of 500m/s, 400m/s and 0.2, respectively.

The material properties of the void which represents the coal seam after exploitation were representative of air with a P wave velocity of 320 m/s and an S wave velocity of 0 m/s.

Table 12-1: Summary of scenarios considered, detailing 1) Scenario, 2) Schematic representation and 3) Brief Description

Scenario	Model Schematic Representation	Brief Description
Number 1 Coal Seam After Exploitation (Long Cross Section)		Horizontal layer, representative of a coal seam after exploitation. This was modelled as a material property boundary. 25m x 3m coal seam located at 12m depth. Blue outline: Low reflecting boundary condition. Light red strip: Coal seam. Red dots: Monitoring points

Scenario	Model Schematic Representation	Brief Description
Number 2 Coal Pit After Exploitation (Small Cross Section)		3m x 3m block, representative of a coal pit after exploitation. This was modelled as a material property boundary 3m x 3m coal pit located at 12m depth. Blue outline: Low reflecting boundary condition. Light red square: Pit. Red dots: Monitoring points
Number 3 Coal Seam After Exploitation modelled as a free surface (Small Cross Section)		3m x 3m block, representative of a coal seam prior to exploitation. This was modelled as a free surface to see if this improves the representation 3m x 3m coal pit located at 12m depth. Blue outline: Low reflecting boundary condition. Light red square: Pit. Red dots: Monitoring points. Red outline: Free Surface Boundary Condition

Scenario	Model Schematic Representation	Brief Description
Number 4 Coal Seam After Exploitation modelled as a free surface (Small Cross Section)	Monitoring Points Located Directly On First Mesh Element Located at 0.1m Depth 5m 10m 5m Monitoring Area Source Frequency = 100Hz PPV= 2 x 10⁻⁷m/s 12m 3m 25m 25m	3m x 3m block, representative of a coal seam prior to exploitation. This was modelled as a free surface with sensor locations moved. 3m x 3m coal pit located at 12m depth. Blue outline: Low reflecting boundary condition. Light red square: Pit. Red circled dots: Monitoring points Red outline: Free Surface Boundary Condition
Expected Observations: A greater effect on the PPV detected is expected. The dominant frequency detected is also expected to change based on previous work.		

12.2.2   Scenario 1: Coal Seam After Exploitation Long Cross section

Table 12-1 presents the numerical set up used to simulate the coal seam.

Figure 12-2 presents the results from the simulation. A notable difference in the PPV at Sensor 1 when compared with Sensor 2 and the formation of additional peaks in the power spectrum are observed.
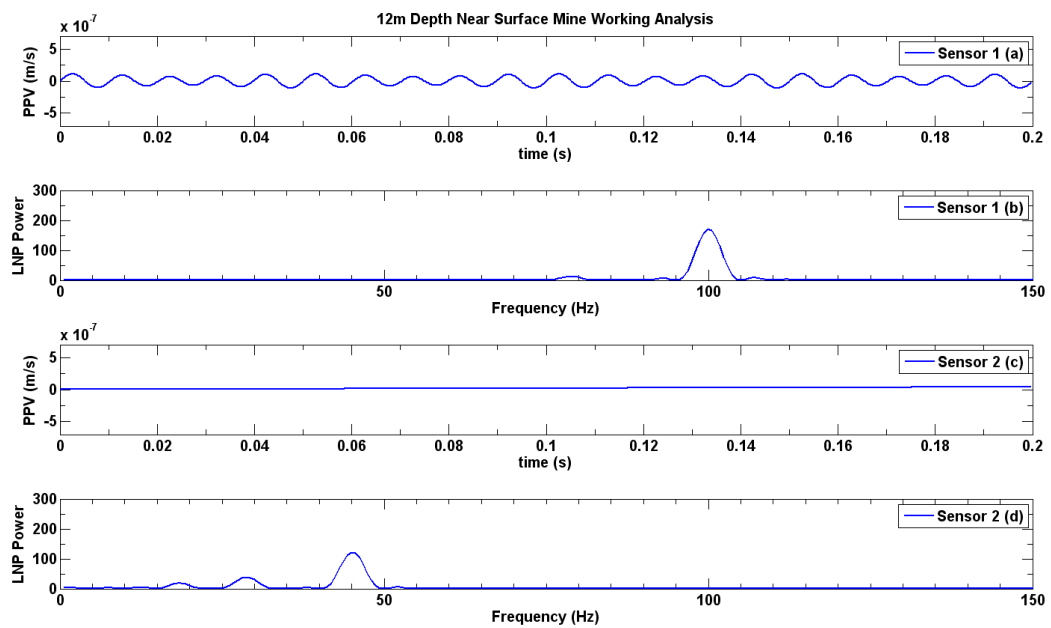
Figure 12-2: Results from numerical simulation of a coal seam at depth, (a) PPV results from Sensor 1 (b) power spectrum produced from Sensor 1, (c) PPV results from Sensor 2, (d) power spectrum produced from Sensor 2. PPV of Sensor 2 is less than Sensor 1. Frequency spectra are notably different: with Sensor 1 having a dominant frequency of 100Hz and a second peak at 79Hz. Sensor 2 has dominant frequency peak at 45Hz, a second peak at 29Hz and a third peak at 19Hz. There is the formation of additional frequency peaks and a reduction in PPV.

The PPV at Sensor 1 and Sensor 2 was 1.1×10^{-7} m/s and 4×10^{-8} m/s. The dominant frequency and amplitude detected at Sensor 1 and Sensor 2 was 100Hz and 170 and 45Hz and 122 respectively. The reduction in dominant frequency and amplitude is probably due to the attenuation effects of the seismic signal travelling through the clay layer. This agrees with the previous simulations that when there is a significant

material property contrast additional frequency peaks form in the power spectra due to the reflection off of the material property boundary.

Key Finding: The preliminary results imply that changes in the dominant frequency and power spectra can potentially be used to infer the presence of a material property boundary at depth with a horizontal orientation.

12.2.3 Scenario 2: Coal Seam after Exploitation Small Cross Section

Table 12-1 presents the numerical set up used to simulate the coal pit. This simulation is representative of a tunnel or pit cross section. Here the pit is modelled as a material property boundary. Figure 12-3 presents the results from the simulation.
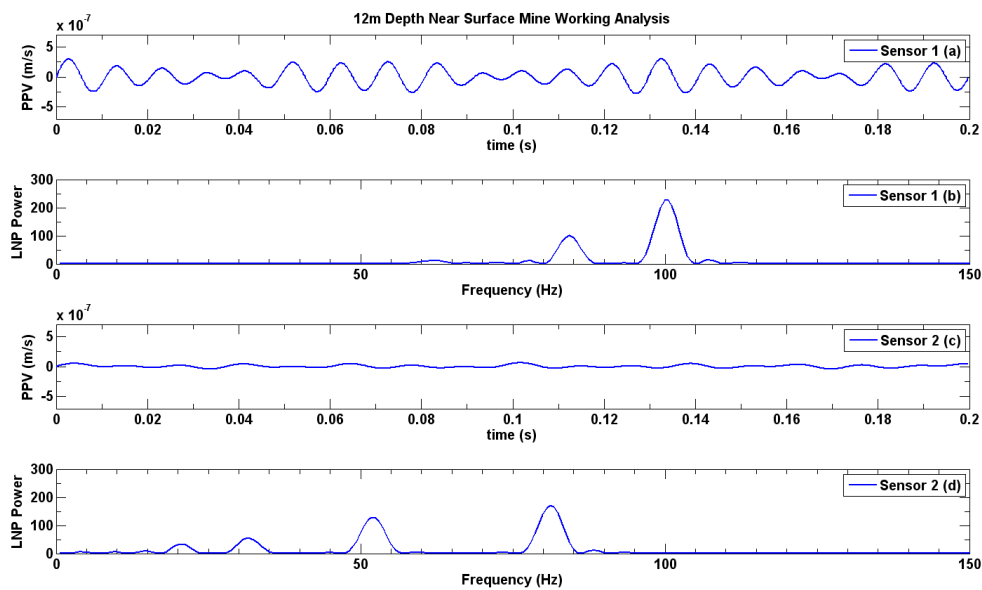
Figure 12-3: Results from numerical simulation of a coal pit at depth, (a) PPV results from Sensor 1 (b) power spectrum produced from Sensor 1, (c) PPV results from Sensor 2, (d) power spectrum produced from Sensor 2. PPV of Sensor 2 is less than Sensor 1. Frequency spectra are notably different: with Sensor 1 having a dominant frequency of 100Hz, a second peak at 84Hz and a third peak at 62Hz. Sensor 2 has dominant frequency peak at 81Hz, a second peak at 52Hz, a third peak at 32Hz and fourth peak at 20Hz. There is the formation of additional frequency peaks and a reduction in PPV. There are a greater number of peaks in the spectra than Scenario 1. The PPV and amplitude of the frequency spectra is greater than Scenario 1.

There is a notable difference in the PPV observed at Sensor 1 when compared with Sensor 2. The formation of additional peaks in the power spectra is observed. More peaks are observed in scenario 2 than scenario 1 (Section 12.2.2).

The PPV at Sensor 1 and Sensor 2 was 3.0 x10^{-7} m/s and 6 x 10^{-8} m/s. The dominant frequency and amplitude detected at Sensor 1 and Sensor 2 was 100Hz and 228 and 81Hz and 172 respectively. This agrees with the previous simulations i.e. when there is a significant material property contrast additional frequency peaks form in the power spectra and a reduction in dominant frequency are observed.

In this scenario, as the pit is simulated as a square block there are a greater number of material property boundaries that the seismic signal can reflect off of potentially explaining the formation of the additional peaks in the spectra and the increase in amplitude.

The PPV is higher for both sensors when compared to Scenario 1 which suggests that this signal has lost less energy. This is expected as there is a lower volume of low velocity material present in the domain. Materials with a low P wave velocity filter out higher frequencies and attenuate a seismic signal faster.

Kind Findings: The preliminary results imply that changes in the dominant frequency and power spectra can be used to infer the presence of a material property boundary at depth which is representative of a tunnel or pit. This scenario infers that this implied change in PPV and dominant frequency can be used to establish the dimensions and location of the coal seam. However, this is out with the scope of this thesis.

12.2.4   Scenario 3: Coal Seam After Exploitation Small Cross Section - Pit Modelled as a Free Surface

In this scenario the void was modelled as a free surface to ensure that no seismic waves passed through the void. A limitation of the model may be that Comsol

permits the propagation of seismic waves through an air domain. In reality this would not happen or if it did it would be very difficult to detect.

Table 12-1 presents the numerical set up used to simulate the coal pit. This simulation is representative of a tunnel or pit cross section as a void. Figure 12-4 presents the results from the simulation.
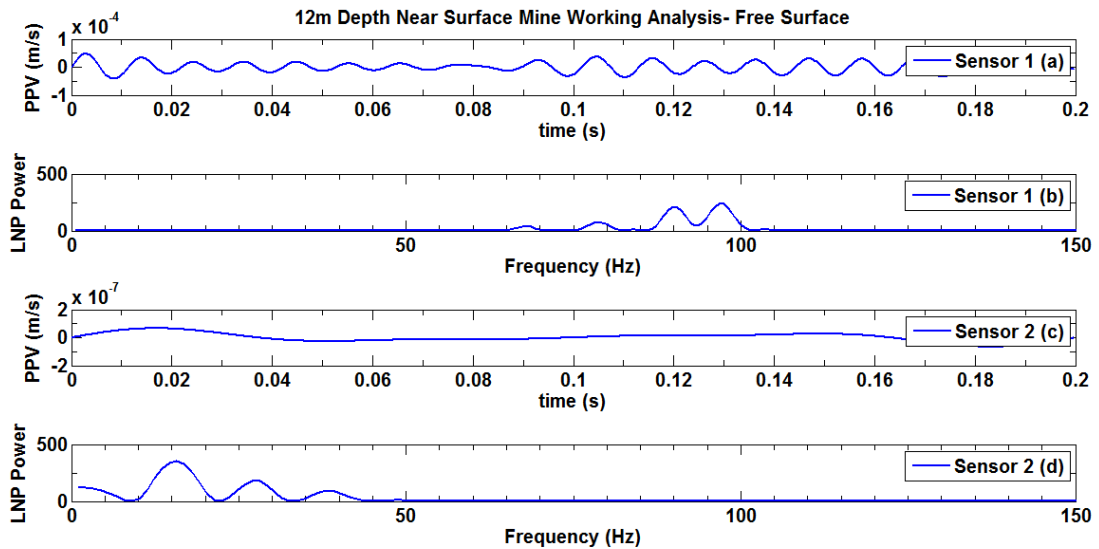
Figure 12-4 Results from numerical simulation of a coal pit modelled a free surface at depth , (a) PPV results from Sensor 1 (b) power spectrum produced from Sensor 1, (c) PPV results from Sensor 2, (d) power spectrum produced from Sensor 2. PPV of Sensor 2 is less than Sensor 1. Frequency spectra are notably different: with Sensor 1 having a dominant frequency of 97Hz, a second peak at 90Hz, a third peak at 77Hz and a fourth peak at 68Hz. Sensor 2 has dominant frequency peak at 16Hz, a second peak at 38Hz, a third peak at 28Hz and fourth peak at 3Hz. There is the formation of additional frequency peaks and a reduction in PPV. There are a greater number of peaks in the spectra than Scenario 1 and 2.

A notable difference in the PPV is observed at Sensor 1 when compared with Sensor 2. The formation of additional peaks in the power spectrum is also observed. There is an increased number of peaks in the spectra when compared to scenario 1 (Section 12.2.2) and 2 (Section 12.2.3). At Sensor 2 the maximum detectable frequency is much lower than when the void is modelled as a material property boundary.

The PPV at Sensor 1 and Sensor 2 was 4.7 x10^{-5} m/s and 6.6 x 10^{-8} m/s. The PPV of Sensor 1 is two orders of magnitude greater than the other two scenarios. This

implies that modelling the void as a free surface causes an amplification of the signal as the seismic wave and thus energy cannot pass into the domain.

The dominant frequency and amplitude detected at Sensor 1 and Sensor 2 was 97Hz and 240 and 16Hz and 354 respectively. This agrees with the previous simulations that when there is a significant material property contrast additional frequency peaks form in the power spectra. In this scenario as the pit is simulated as a square there are a greater number of material property boundaries that the seismic signal can reflect off potentially explaining the formation of the additional peaks in the spectra and the increase in amplitude. As the void is modelled as a free surface this could also potentially cause a greater reflection as the wave cannot propagate through the void.

The PPV is higher for both sensors when compared to Scenario 1 and 2 which suggests that this signal has lost less energy. This is expected as there is no low velocity material present in the domain. When the void is modelled as a free surface a lower dominant frequency value at Sensor 2 is observed. This implies that modelling a void as a free surface increases the sensitivity of the frequency of a seismic signal allowing effective detection of a void.

Key Findings: Preliminary results imply that changes in the dominant frequency and PPV can be used to infer the presence of a material property boundary at depth which is representative of a tunnel or pit. It can be concluded that numerically simulating the void as a free surface is a better representation, particularly as the frequency characteristics appear to have an increased response to the presence of a void. This scenario infers that this implied change in PPV and dominant frequency can be used to establish the dimensions and location of the coal seam. However, this is out with the scope of this thesis.

12.2.5 Scenario 4: Coal Seam After Exploitation Small Cross section - Pit Modelled as a Free Surface (Sensor Locations Moved)

The sensor locations were moved 5m either side, Table 12-1 presents the numerical set up used to simulate the coal pit as a free surface.

The rationale behind moving the sensor locations was to establish the effect that this would have. Based on previous simulations I would expect minimal change in the frequency spectra and reduction in the amplitude of the frequency values detected. I would expect a reduction also in PPV.

Figure 12-5 presents the results from the simulation. A notable difference in the PPV at Sensor 1 when compared with Sensor 2 and the formation of additional peaks in the power spectrum is observed. At Sensor 2 the maximum detectable frequency is much lower than when the void is modelled as a material property boundary in scenario 1 (Section 12.2.2) and 2 (Section 12.2.3).
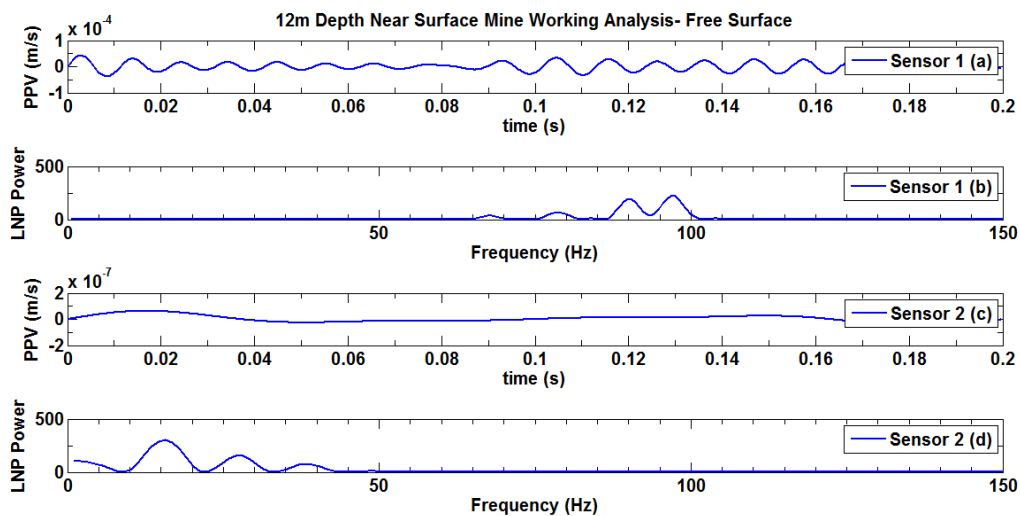
Figure 12-5: Results from numerical simulation of a coal pit modelled a free surface at depth with sensor locations moved , (a) PPV results from Sensor 1 (b) power spectrum produced from Sensor 1, (c) PPV results from Sensor 2, (d) power spectrum produced from Sensor 2. PPV of Sensor 2 is less than Sensor 1. Frequency spectra are notably different: with Sensor 1 having a dominant frequency of 97Hz, a second peak at 90Hz, a third peak at 77Hz and a fourth peak at 68Hz. Sensor 2 has dominant frequency peak at 16Hz, a second peak at 38Hz, a third peak at 28Hz and fourth peak at 3Hz. There is the formation of additional frequency peaks and a reduction in PPV. There are the same frequency peaks when compared to Scenario 3, there is a reduction in amplitude and PPV for both Sensors.

The PPV at Sensor 1 and Sensor 2 was 4.2 x10^{-5} m/s and 6.3 x 10^{-8} m/s. The PPV of Sensor 1 is two orders of magnitude greater than the other two scenarios as in Scenario 3. This again implies that modelling the void as a free surface causes an amplification of the signal.

Comparison to Scenario 3: There is reduction in the PPV values detected at both Sensor 1 and Sensor 2 when compared to Scenario 3 as expected as they are both located further away from the source (Figure 12-6). However this change is very small and further investigation would be required to establish if it is significant.
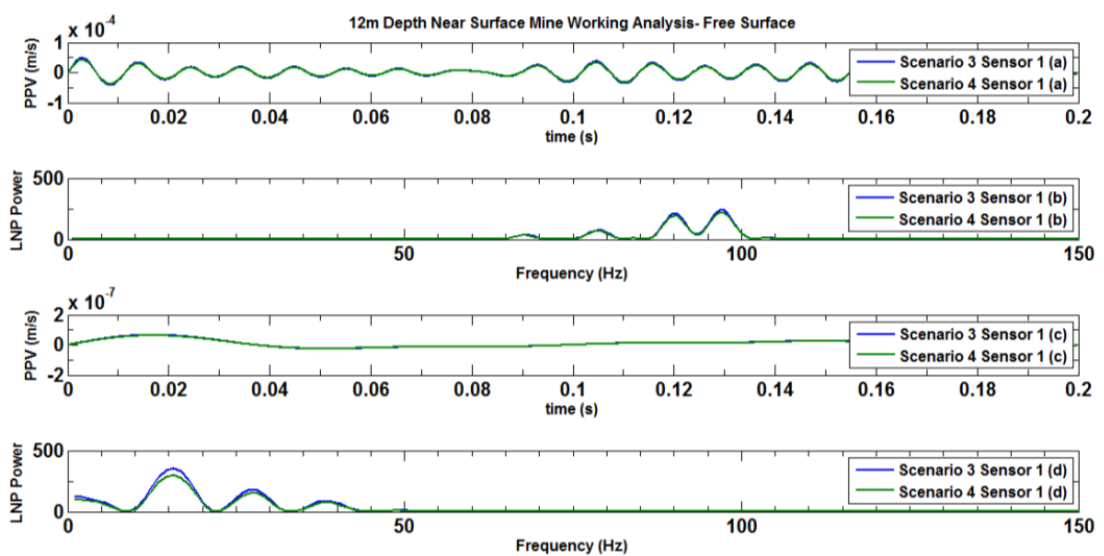
Figure 12-6: Results from numerical simulation of a coal pit modelled a free surface at depth with sensor locations moved compared to Scenario 3 results. There is not a significant change in either dominant frequency or PPV. There is a slight variation in the amplitude of the dominant frequency in (d).

The dominant frequency and amplitude detected at Sensor 1 and Sensor 2 was 97Hz and 217 and 16Hz and 300 respectively. This agrees with the previous simulations that when there is a significant material property contrast additional frequency peaks form in the power spectra. In this scenario as the pit is simulated as a square there are a greater number of material property boundaries that the seismic signal can reflect off potentially explaining the formation of the additional peaks in the spectra and the increase in amplitude. There is a reduction in

amplitude as expected when compared with Scenario 3. As the signal has travelled a further distance it would be expected to lose more energy.

Key Findings: Preliminary results imply that changes in the dominant frequency and power spectra can be used to infer the presence of a material property boundary at depth which is representative of a tunnel or pit. This scenario implies that further research will be required to establish if the location capabilities are significant or not due to the similarity in results between scenario 3 and 4.

12.3   Summary

The results from this Chapter imply that there is potential to utilise the changes in the dominant frequency and PPV to locate voids and other geological features at depth. In particular when modelling voids numerically as a free surface. However, the results do imply that there may be some limitations with respect to location detection.

These preliminary results suggest that there is potential of utilising engineering equipment as a seismic source to detect voids and features in the near surface. The results further evidence utilising low frequency source and mapping the changes in PPV as an effective concept for seismic imaging. The simulations further the work carried out by Marfurt and Kirlin (2001) who adopt the concept that internal geological structures at or below the conventional seismic resolution exhibit themselves as subtle variations in PPV and dominant frequency rather than changes in the seismic wave arrival times.

13 Discussion and Conclusions

13.1 Introduction

This thesis set out to explore the feasibility of creating a concept for a new geophysical tool to detect the presence, width and location of near surface geological features, voids and near surface subsurface infrastructure such as:

- small fault zones;

- geological intrusions;

- mine workings;

- sink holes;

- voids; and

- fractures.

This thesis focuses on the development of a novel approach to image the near surface based on finite element analysis and verifying the results with a pilot field trial. The motivation for this thesis is that in the last 25-30 years, near surface geophysics and the demand for geophysical tools has grown rapidly, calling for novel geophysical tools and concepts to be developed.

The current geophysical technologies used in near surface site investigations have their own specific limitations. This thesis sought to answer the main question:

Can we use seismic wave characteristics i.e. PPV and frequency, to effectively map and locate near surface geological and manmade structures?

Specifically the objectives investigated were:

1. Considering the effect of medium properties, is there a significant effect on seismic wave characteristics such as PPV and frequency when utilising low frequency seismic sources?

2. Considering the presence of a material property boundary, is there a significant effect on seismic wave characteristics and subsequently can that effect potentially be used to detect the presence and location of a subsurface feature?

3. Can the presence of a subsurface feature surrounded by a low velocity zone be detected numerically at metre scale accuracy and if so, can this concept be validated in pilot field trials?

13.2   Key Findings

This thesis presents a proof of concept for a near surface seismic investigation tool. The potential of utilising microseismic monitoring to image the near surface was explored by examining the changes in the dominant frequency and PPV of a seismic signal as it propagates through near surface features characterised by different central feature widths and low velocity zones.

Seismic waves were generated by a low frequency (100Hz) seismic source located on the ground surface. Using finite element analysis the propagation of a wave emitted by the seismic source was simulated. After model refinement techniques were applied, a 25m by 25m domain with low reflecting external boundaries and a free surface boundary at the surface was used. The dominant frequency and PPV were observed at monitoring points located on the free surface over a distance of 15m.

Numerical models were developed for a number of scenarios taking into account different media, the presence of material boundaries, the presence of geological features of varying geometrical characteristics and their combinations.

When considering domains of a single material, numerical results show that the dominant frequency of the seismic wave reduces significantly as the distance of the monitoring point (microseismic sensor location) from the seismic source increases. The reduction depends on the medium properties, with a less dense material (low P wave velocity) resulting in a higher reduction rate (attenuation). This also depends

on the wavenumber k which is related to the p wave velocity of the domain and is calculated using the dispersion coefficient automatically applied in COMSOL, to ensure that the modelled wave exhibit behaviour that is representative of that observed in the field. The effect of the medium properties on the PPV was found to be less significant.

Media consisting of more than one material, i.e. with a material property boundary being present, resulted in changes in both the PPV and dominant frequency. The analysis has shown that it is possible to use these changes to determine the width of a geological feature and surrounded by low velocity zone (e.g. a dyke surrounded by a chilled/baked margin or a fault zone surrounded by a fracture zone) at sub-meter accuracy.

The effect of noise is important in terms of resolution and applicability of the method, and was investigated by adding noise to the sensitivity analysis. This research intentionally selected a field site that was characterised by a low ambient noise environment i.e. the PPV measured as a result of ambient noise is at least 3 times less than the smallest PPV detected. This removed the requirement to utilise signal processing filtration methods as the impact from ambient noise was deemed insignificant.

Consideration was given to sites that may be characterised by ambient noise that is greater than the maximum PPV produced by the seismic source. When noise was increased to 2 x source PPV the "worst case" systematic error was -2m and the random uncertainty was ± 1.6m. Both of which are greater than systematic error observed in the field trial.

In high noise environment it would be advantageous prior to the experiment to establish the PPV of the ambient noise and establish if the PPV of the seismic source is powerful enough to overcome the effect of ambient noise i.e. at least 3 times greater. If this is not the case consideration will have to be given to either changing

the seismic source to a source with an greater energy i.e. can produce a greater PPV or consider applying filtration techniques to reduce the effects of noise.

A concept has been developed to define the geometrical characteristics of a geological feature based on the plots of frequency and PPV over central feature width for varying low velocity zone widths as obtained from the numerical modelling. Plots of PPV as a horizontal profile over the monitoring cross section have inferred geological feature presence, location and width. This feasibility of this concept was successfully validated using "blind" numerical tests and a pilot field trial with a systematic error of +0.4m and a random uncertainty of ±0.39m.

13.3 Theoretical Implications

Currently, one of the most significant limitations in near surface site investigations is accurately predicting geological feature width by non-invasive methods.

This thesis addressed the following gaps in theoretical knowledge as to my knowledge there is:

- No study to demonstrate if the relationship between dominant frequency and geological feature thickness is observed in the near surface (i.e. depths less than 100m) at metre scale accuracy (i.e. <10m);

- No study has used micro seismometers to apply this technique for near surface applications; and

- No study which has considered if the dominant frequency and PPV characteristics can be used to develop a concept for a near surface site investigation tool deployed in the near surface.

The findings of this thesis align with Marfurt and Kirlin (2001) who adopt the concept that internal geological structures at or below the conventional seismic resolution exhibit themselves as subtle variations in amplitude (PPV) and dominant frequency rather than changes in the arrival times. The prediction tool concept developed in this thesis agrees with and contributes to this concept. The originality

is that the concept has been applied in a near surface context and has been used to form the basis for a novel near surface site investigation tool.

Conventionally, in seismology $\lambda/4$ (approximately 8.75m for this thesis) has been assumed to be the resolution limit for determining the thickness of geological features according to the Rayleigh criteria (Chopra, Castagna et al. 2006). Where, λ is the wavelength (m) of the seismic wave. The Rayleigh criterion derived from optics theory states that the resolution threshold of a reflected seismic wave is $\lambda/4$. A detailed explanation of this method can be found in the literature e.g. Bleistein, Cohen et al. (2001). Widess furthered the threshold to $\lambda/8$ (Widess 1973), this paper concluded that for thin geological features below $\lambda/8$ (approximately 4.4m for this thesis) the seismic wave characteristics of PPV and dominant frequency do not change appreciably with thickness and that the PPV varies nearly linearly with thickness. The geophysical prediction tool concept developed in this thesis and the research conducted by Marfurt and Kirlin (2001) have shown that the boundaries of this limitation can be pushed when the geological characteristics of the site are favourable i.e. low ambient noise environment, well defined geological features with clear material boundaries, good material property contrasts between material zones.

Widess (1973), stated that below $\lambda/8$ the only seismic characteristic that changes appreciably with thickness is PPV there is no way to separate changes in reflections from changes in geological feature thickness. He also considered the change in dominant frequency of the seismic signal. This thesis has shown that a key factor that determines the resolution of seismic imaging is dominant frequency combined with PPV. The main parameter in determining the resolution is dependent on the P wave velocity of the rock and the frequency of the seismic source. The P wave velocity of the rock cannot be influenced; therefore the key factor that establishes resolution according to the Widess model is frequency.

The threshold of λ/8 is considered by many conventional exploration geophysicists to be the fundamental threshold for seismic resolution. It has been demonstrated by several authors including Chopra, Castagna et al. (2006) that the threshold limit of seismic resolution are found to be much smaller than the Widess model suggests. The weakness of the Widess criteria is that it is based on models and the application is restricted to situations that approximate the models developed (Knapp 1990).

Tirado (2004), presented the variation of the dominant frequency as a function of the geological feature thickness. As the thickness increases there is a decrease in the dominant frequency, as observed in this thesis. However, Tirado (2004) also demonstrated that below a certain geological feature thickness the dominant frequency shows little variation from the dominant frequency of the source.

Detection limitations were also observed in this thesis, for example there was a small variation in dominant frequency (<1Hz) when the central feature width became significantly greater than the surrounding low velocity zone width i.e. it became difficult to detect the width of the low velocity zone.

Chopra, Castagna et al. (2006), show that noise will control the fundamental limit of the seismic resolution and that contrary to the Widess model, below the conventional threshold there is a strong dependency of dominant frequency on geological feature thickness, which aligns with this thesis, implying that the seismic response to geological feature width is more sensitive than previously thought.

This thesis shows that the behaviour predicted by Widess becomes more uncharacteristic as the feature width becomes smaller and that PPV and dominant frequency vary far below the conventional view of the limit of seismic resolution.

The conventional limit of seismic resolution for this thesis is approximately 8.75m. The results in this thesis have shown via a pilot field study that the seismic resolution is in the region of 2m ± 0.4m for a geological feature and accurate prediction of the surrounding low velocity zone width.

Further research will be required to fully develop the feasibility of the concept developed in this thesis.

13.4   Industrial Implications

The problem focal to this thesis focuses on exposed rock therefore, the sensors couple well with the surface. In rock, the attenuation of the seismic signal is small, and hence, the seismometers can be deployed at the surface. There is not a requirement to deploy the sensors in boreholes or bury them, which can be costly and invasive.

The concept developed in this thesis works well in a low noise, hard rock environment, where there is a sufficient material property contrast between the near surface feature and the surrounding rock. The generator used as the seismic source for this thesis was small and portable for practical reasons i.e. ease of transportation. Due to the favourable site conditions, the seismic signal produced by the small generator had sufficient amplitude to be detected in a low noise rock environment.

However, if the concept developed in this thesis was applied to a site characterised by soil or glacial drift, deploying the sensors in boreholes may be required to allow a better coupling between the surface and the sensor to allow the seismic signal to be detected. As sites characterised by soil or drift tend to have a low P wave velocity the signal produced by the seismic source will attenuate more therefore, it may be more appropriate to use a larger generator with the capabilities of generating a seismic signal with a greater amplitude i.e. causes a greater particle displacement.

This concept does not require costly site preparation and the resolution is not negatively affected by noise, due to the favourable site conditions. The acquisition time and survey area of the concept developed in this thesis is short and the resolution of this concept increases with material property contrast. However, the resolution of the method developed in this thesis is likely to be relative to the depth and dimensions of the subsurface feature. This concept is not intended to replace

other geophysical methods but rather compliment and used in combination with other site investigation techniques.

13.5   Requirement for Future Research

In order to further develop the concept presented in this thesis, further inversion software will have to be created allowing the potential for the application of a surface scanning tool. For limited geometries it has been shown that this concept can predict subsurface feature presence and width with sub metre scale accuracy. For other geometries the initial simulations show that the concept can detect subsurface feature presence. Further work will have to be carried out in order to fully develop the method.

The preliminary results considering future applications imply that there is potential to utilise the changes in the dominant frequency and PPV to locate voids and other geological features at depth. In particular when modelling voids numerically as a free surface. Further work is required to determine whether such subsurface feature can be accurately located.

14 References

Abdellah, W., H. S. Mitri, D. Thibodeau and L. Moreau-Verlaan (2014). "Geotechnical risk assessment of mine development intersections with respect to mining sequence." Geotechnical and Geological Engineering **32**(3): 657-671.

Alterman, Z. and F. Karal (1968). "Propagation of elastic waves in layered media by finite difference methods." Bulletin of the Seismological Society of America **58**(1): 367-398.

Arshadnejada, S., W. Yanb, L. Thamc and J. Zhoud (2013). AN EMPIRICAL APPROACH TO INTRODUCE THE RELATIONSHIP BETWEEN BLAST-INDUCED VIBRATION AND ROCK MASS CONDITION IN TUNNELING. Proceedings of the 18th Southeast Asian Geotechnical Conference cum Inaugural AGSSEA Conference, Research Publishing Service.

ASTRON (2015). "Seismic Interferometry " Netherlands Institute for Radio Astronomy **Seismic Interferometry**

Barrows, L. and J. E. Rocchio (1990). "Magnetic surveying for buried metallic objects." Groundwater Monitoring & Remediation **10**(3): 204-211.

Benson, A. K. (1995). "Applications of ground penetrating radar in assessing some geological hazards: examples of groundwater contamination, faults, cavities." Journal of Applied Geophysics **33**(1): 177-193.

Benson, R., R. A. Glaccum and M. R. Noel (1984). Geophysical techniques for sensing buried wastes and waste migration. Geophysical techniques for sensing buried wastes and waste migration, EPA.

Blakely, R. J. (1996). Potential theory in gravity and magnetic applications, Cambridge University Press.

Bleistein, N., J. K. Cohen and J. W. J. Stockwell (2001). Mathematics of Multidimensional Seismic Imaging, Migration, and Inversion, Springer.

Bolt, B. A. and W. D. Smith (1976). "Finite-element computation of seismic anomalies for bodies of arbitrary shape." Geophysics **41**(1): 145-150.

Bradford, J., M. Ramaswami and C. Peddy (1996). Imaging PVC gas pipes using 3-D GPR. SAGEEP.

Buckingham, M. J. (1997). "Theory of acoustic attenuation, dispersion, and pulse propagation in unconsolidated granular materials including marine sediments." The Journal of the Acoustical Society of America **102**(5): 2579-2596.

Burger, H. R. (1992). "Exploration geophysics of the shallow subsurface."

Butler, D. K. (1984). "Interval gravity-gradient determination concepts." Geophysics **49**(6): 828-832.

Butt, R. (2009). Introduction to Numerical Analysis Using MATLAB®, Jones & Bartlett Learning.

Carmichael, R. S. (1988). Practical Handbook of Physical Properties of Rocks & Minerals, Taylor & Francis.

Carmichael, R. S. and G. Henry Jr (1977). "Gravity exploration for groundwater and bedrock topography in glaciated areas." Geophysics **42**(4): 850-859.

Carnevale M, Young G, Hager J and C. M.C. (2000). Monitoring of TBM-induced ground vibrations. "The Revolution Continues": Proceedings of the NAT 2000, Boston, MA, 6-11 June 2000 A. U.-C. Association. Balkema, Rotterdam, CRC Press; Cdr edition (1 Jan. 2000)

Carpenter, P. J., S. F. Calkin and R. S. Kaufmann (1991). "Assessing a fractured landfill cover using electrical resistivity and seismic refraction techniques." Geophysics **56**(11): 1896-1904.

Cassidy, N. J. (2007). "Evaluating LNAPL contamination using GPR signal attenuation analysis and dielectric property measurements: Practical implications for hydrological studies." Journal of Contaminant Hydrology **94**(1–2): 49-75.

Chen, W. and S. Holm (2003). "Modified Szabo's wave equation models for lossy media obeying frequency power law." J. Acoustic. Soc. Am **114**(5): 2570-2574.

Chopra, S., J. Castagna and O. Portniaguine (2006). "Seismic resolution and thin-bed reflectivity inversion." CSEG recorder **31**(1): 19-25.

Cohen and a. Jennings (1983). Silent Boundary Methods for Transient Analysis,Computational methods for transient analysis.

COMSOLMultiphysics (2013). "Structural Mechanics Module User Guide." **VERSION 4.3b**.

Courant, R., K. Friedrichs and H. Lewy (1928). "Über die partiellen Differenzengleichungen der mathematischen Physik." Mathematische Annalen **100**(1): 32-74.

Desai, Y. M. (2011). Finite Element Method with Applications in Engineering, Dorling Kindersley.

Devore, J. L. and K. N. Berk (2011). Modern Mathematical Statistics with Applications, Springer.

Dilay, A. and J. Eastwood (1995). "Spectral analysis applied to seismic monitoring of thermal recovery." The Leading Edge **14**(11): 1117-1122.

Dobrin, M. B. and C. H. Savit (1960). Introduction to geophysical prospecting, McGraw-Hill New York.

Dupuis, J. C., K. E. Butler and A. W. Kepic (2007). "Seismoelectric imaging of the vadose zone of a sand aquifer." Geophysics **72**(6): A81-A85.

Ebrom, D. (2004). "The low-frequency gas shadow on seismic sections." The Leading Edge **23**(8): 772-772.

Ellis, D. V. and J. M. Singer (2007). Well logging for earth scientists, Springer Science & Business Media.

Elmo, D. and D. Stead (2010). "An Integrated Numerical Modelling–Discrete Fracture Network Approach Applied to the Characterisation of Rock Mass Strength of Naturally Fractured Pillars." Rock Mechanics and Rock Engineering **43**(1): 3-19.

Ewing, M., G. P. Woollard and A. C. Vine (1939). "Geophysical investigations in the emerged and submerged Atlantic Coastal Plain PART III: BARNEGAT BAY, NEW JERSEY, SECTION." Geological Society of America Bulletin **50**(2): 257-296.

Field, A. P. (2009). "Discovering statistics using SPSS." <u>Sage, London</u>: 539-585.

FlowScience (2015). Implicit Vs. Explicit Numerical Methods. <u>Flow Science Partners </u>S. o. E. a. U. o. N. Mexico.

Frey, W. (2013). Solutions to Linear Systems of Equations: Direct and Iterative Solvers. <u>COMSOL Blog</u>.

Gautschi, A. (2001). "Hydrogeology of a fractured shale (Opalinus Clay): Implications for deep geological disposal of radioactive wastes." <u>Hydrogeology Journal</u> **9**(1): 97-107.

Grandjean, G., J. C. Gourry and A. Bitri (2000). "Evaluation of GPR techniques for civil-engineering applications: study on a test site." <u>Journal of Applied Geophysics</u> **45**(3): 141-156.

Griffiths, D. H. and R. F. King (1981). <u>Applied geophysics for geologists and engineers: the elements of geophysical prospecting</u>, Oxford.

Grotzinger, J., T. H. Jordan, F. Press and R. Siever (2009). <u>Understanding earth</u>, WH Freeman.

Günther, T., C. Rücker and K. Spitzer (2006). "Three-dimensional modelling and inversion of DC resistivity data incorporating topography—II. Inversion." <u>Geophysical Journal International</u> **166**(2): 506-517.

Hakso, A., M. D. Zoback and J. Du (2015). <u>Utilization of Microseismic Multiplets to Detect Velocity Changes During Multi-Stage Hydraulic Fracturing in the Barnett Shale</u>. 2015 SEG Annual Meeting, Society of Exploration Geophysicists.

Harari, I. and T. J. Hughes (1992). "Galerkin/least-squares finite element methods for the reduced wave equation with non-reflecting boundary conditions in unbounded domains." <u>Computer Methods in Applied Mechanics and Engineering</u> **98**(3): 411-454.

Hardy, H. R. (2005). <u>Acoustic Emission/Microseismic Activity: Volume 1: Principles, Techniques and Geotechnical Applications</u>, CRC Press.

Hinze, W. J., R. R. B. von Frese, R. Von Frese and A. H. Saad (2013). <u>Gravity and Magnetic Exploration: Principles, Practices, and Applications</u>, Cambridge University Press.

Honda (2002). Honda EU10i User Manual. http://campaigns.hondampe.com.au/Power%20Equipment/ownersmanuals/generator/eu10iown01.pdf.

Hustedt, B., S. Operto and J. Virieux (2004). "Mixed-grid and staggered-grid finite-difference methods for frequency-domain acoustic wave modelling." <u>Geophysical Journal International</u> **157**(3): 1269-1296.

IRIS and PASSCAL. (2013). "Working with Responses to Get Units of Ground Motion." Retrieved 08/11/13, 2013, from http://www.passcal.nmt.edu/content/instrumentation/field-procedures/working-responses-get-units-displacement.

Jaeger, J. C. and N. G. W. Cook (1976). Fundamentals of rock mechanics.

Jeanne, P., J. Rutqvist, C. Hartline, J. Garcia, P. F. Dobson and M. Walters (2014). "Reservoir structure and properties from geomechanical modeling and microseismicity analyses associated with an enhanced geothermal system at The Geysers, California." <u>Geothermics</u> **51**: 460-469.

Jo, C.-H., C. Shin and J. H. Suh (1996). "An optimal 9-point, finite-difference, frequency-space, 2-D scalar wave extrapolator." Geophysics **61**(2): 529-537.

Johnson, T. C., J. D. Halfman, B. R. Rosendahl and G. S. Lister (1987). "Climatic and tectonic effects on sedimentation in a rift-valley lake: Evidence from high-resolution seismic profiles, Lake Turkana, Kenya." Geological Society of America Bulletin **98**(4): 439-447.

Johnston, D. H., M. Toksöz and A. Timur (1979). "Attenuation of seismic waves in dry and saturated rocks: II. Mechanisms." Geophysics **44**(4): 691-711.

Joswig, M. (2008). "Nanoseismic monitoring fills the gap between microseismic networks and passive seismic." First Break **26**: 121-128.

Kamei, R., N. Nakata and D. Lumley (2015). "Introduction to microseismic source mechanisms." The Leading Edge **34**(8): 876-880.

Kane, M., D. Harwood and N. Hatch (1971). "Continuous magnetic profiles near ground level as a means of discriminating and correlating rock units." Geological Society of America Bulletin **82**(9): 2449-2456.

Kaven, J., S. Hickman, A. McGarr and W. Ellsworth (2015). "Surface Monitoring of Microseismicity at the Decatur, Illinois, CO_2 Sequestration Demonstration Site." Seismological Research Letters **86**(4): 1096-1101.

Kelly, K., R. Ward, S. Treitel and R. Alford (1976). "Synthetic seismograms: a finite-difference approach." Geophysics **41**(1): 2-27.

Knapp, R. W. (1990). "Vertical resolution of thick beds, thin beds, and thin-bed cyclothems." Geophysics **55**(9): 1183-1190.

Knight, R. (2008). Physics for Scientists and Engineers: A Strategic Approach

Knox, W., A. Musgrave, R. Bratton and H. Mendenhall (1967). "Seismic refraction prospecting."

Koppe, V., F. Gambin, J. L. Costa, J. Koppe, G. Fallon and N. Davies (2005). Incorporating Uncertainty in Coal Seam Depth Determination via Seismic Reflection and Geostatistics. Geostatistics Banff 2004. O. Leuangthong and C. Deutsch, Springer Netherlands. **14:** 537-542.

Kühn, D., J. Albaric, D. Harris, V. Oye, G. Hillers, F. Brenguier, M. Ohrnberger, A. Braathen and S. Olaussen (2014). Microseismic monitoring of a future CO_2 storage site in the Arctic (Svalbard)-Suppression and utilization of seismic noise. EGU General Assembly Conference Abstracts.

Kumar, C. (2015). "Impact of climate change on groundwater resources." Handbook of Research on Climate Change Impact on Health and Environmental Sustainability: 196.

Lennartz_Electronic (2015). Seismometer Quotation. 82189. **Lennartz electronic GmbH**.

Leroy, P., A. Revil, S. Altmann and C. Tournassat (2007). "Modeling the composition of the pore water in a clay-rock geological formation (Callovo-Oxfordian, France)." Geochimica et Cosmochimica Acta **71**(5): 1087-1097.

Lomb, N. R. (1976). "Least-squares frequency analysis of unequally spaced data." Astrophysics and space science **39**(2): 447-462.

Lowrie, W. and Z. Swiss Federal Institute of Technology (2007). <u>Fundamentals of Geophysics</u>, Cambridge University Press.

Lowrie, W. and S. F. I. o. Technology (2007). <u>Fundamentals of Geophysics</u>, Cambridge University Press.

Marchetti, M., M. Chiappini and A. Meloni (1998). "A test site for the magnetic detection of buried steel drums."

Marfurt, K. and R. Kirlin (2001). "Narrow-band spectral analysis and thin-bed tuning." <u>Geophysics</u> **66**(4): 1274-1283.

Marfurt, K. J. (1984). "Accuracy of finite-difference and finite-element modeling of the scalar and elastic wave equations." <u>Geophysics</u> **49**(5): 533-549.

McLaskey, G. and S. Glaser (2009). "Nanoseismic measurement of the localized initiation of sliding friction." <u>Proceedings of Batsheva de Rothschild Seminar on shear physics and the Mezzo-Scale in earthquake and landslide mechanics</u>

Miller, R. D., J. H. Bradford, K. Holliger and R. B. Latimer (2010). <u>Advances in Near-surface Seismology and Ground-penetrating Radar</u>, Wiley.

Miller, R. D. and D. W. Steeples (1991). "Detecting voids in a 0.6 m coal seam, 7 m deep, using seismic reflection." <u>Geoexploration</u> **28**(2): 109-119.

Mitchell, J. T., N. Derzhi and E. Lickman (1997). <u>Low frequency shadows: The rule, or the exception</u>. 67th Annual International Meeting, SEG, Expanded Abstracts.

Mitzenmacher, M. (2004). "A brief history of generative models for power law and lognormal distributions." <u>Internet mathematics</u> **1**(2): 226-251.

Muchan, K., M. Lewis, J. Hannaford and S. Parry (2015). "The winter storms of 2013/2014 in the UK: hydrological responses and impacts." <u>Weather</u> **70**(2): 55-61.

Multiphysics, C. (2012). "COMSOL 4.3 Release Highlights." from http://www.uk.comsol.com/products/4.3/.

Multiphysics, C. (2014) "Resolving time-dependent waves." <u>knowledgebase 1118</u> **1118**.

Munkholm, M. S. and E. Auken (1996). "Electromagnetic noise contamination on transient electromagnetic soundings in culturally disturbed environments." <u>Journal of Environmental and Engineering Geophysics</u> **1**(2): 119-127.

Musset, A. and M. Khan (2007). <u>Looking into the Earth: An Introducion to Geological Geophysics</u>, Cambridge University Press.

Nekut, A. and B. R. Spies (1989). "Petroleum exploration using controlled-source electromagnetic methods." <u>Proceedings of the IEEE</u> **77**(2): 338-362.

Nettleton, L. L. (1971). <u>Elementary gravity and magnetics for geologists and seismologists</u>, SEG Books.

Newman, M. E. (2005). "Power laws, Pareto distributions and Zipf's law." <u>Contemporary physics</u> **46**(5): 323-351.

Nicolson, H., A. Curtis, B. Baptie and E. Galetti (2012). "Seismic interferometry and ambient noise tomography in the British Isles." <u>Proceedings of the Geologists' Association</u> **123**(1): 74-86.

Nye, J. F. (1985). Physical Properties of Crystals. Their representation by tensors and matrixes., Oxford University Press.

Oldenburg, D. W. and D. A. Pratt (2007). "Geophysical Inversion for Mineral Exploration:

a Decade of Progress in Theory and Practice." The Leading Edge **Proceedings of Exploration 07: Fifth Decennial International Conference on Mineral Exploration"**: 61-95.

Olhoeft. (1999). "Ground Penetrating Radar."   Retrieved December 2014, 2014, from http://inside.mines.edu/~golhoeft/research/gpr.html.

Operto, S., J. Virieux, P. Amestoy, J.-Y. L'Excellent, L. Giraud and H. B. H. Ali (2007). "3D finite-difference frequency-domain modeling of visco-acoustic wave propagation using a massively parallel direct solver: A feasibility study." Geophysics **72**(5): SM195-SM211.

Pine, R. J., J. S. Coggan, Z. N. Flynn and D. Elmo (2006). "The Development of a new Numerical Modelling Approach for Naturally Fractured Rock Masses." Rock Mechanics and Rock Engineering **39**(5): 395-419.

Polívka, J. (2008). MATHEMATICAL AND NUMERICAL MODELING OF THE TRANSIENT ANALYSIS

IN ACOUSTICS PhD, West Bohemian University.

Press, W. H., B. P. Flannery, S. A. Teukolsky and W. T. Vetterling (1986). Numerical recipes, Cambridge Univ Press.

Pyrak-Nolte, L. J., L. R. Myer and N. G. W. Cook (1990). "Transmission of Seismic Waves Across Single Natural Fractures." J. Geophys. Res. **95**(B6): 8617-8638.

Pytharouli, S., R. Lunn, Z. Shipton, J. Kirkpatrick and A. do Nascimento (2011). "Microseismicity illuminates open fractures in the shallow crust." Geophysical Research Letters **38**(Article).

Pytharouli, S. I. and S. C. Stiros (2008). "Spectral analysis of unevenly spaced or discontinuous data using the "normperiod" code." Computers & Structures **86**(1–2): 190-196.

Raleigh, L. and J. Strutt (1885). "On waves propagating along the plane surfaces of an elastic solid." Proc. London Math. Soc **17**: 4-11.

Ranalli, G. and D. Murphy (1987). "Rheological stratification of the lithosphere." Tectonophysics **132**(4): 281-295.

Ren, J., L. Zhang, S. Ren, J. Lin, S. Meng, G. Ren and T. Gentzis (2014). "Multi-branched horizontal wells for coalbed methane production: Field performance and well structure analysis." International Journal of Coal Geology **131**: 52-64.

Reynolds, J. M. (2011). An Introduction to Applied and Environmental Geophysics, Wiley.

Rezos, M. M., J. J. Schultz, R. A. Murdock and S. A. Smith (2011). "Utilizing a Magnetic Locator to Search for Buried Firearms and Miscellaneous Weapons at a Controlled Research Site*,†." Journal of forensic sciences **56**(5): 1289-1295.

Roberts, R., W. Hinze and D. Leap (1990). "Application of the gravity method to investigation of a landfill in the glaciated midcontinent, USA." Geotechnical and environmental geophysics **2**: 253-260.

Romanelli, F. (2004). <u>Surface Waves and Dispersion</u>. University of Trieste University of Trieste

Romig, P. (2000). "Seeing into the Earth: Noninvasive characterization of the shallow subsurface for environmental and engineering application." <u>Natl. Acad. Press, Washington, DC</u>.

SANDBERG_GPR (2014). Quotation for Ground Penetrating Radar Surveys. <u>Head Office 40 Grosvenor Gardens London SW1W 0EB</u>.

Scargle, J. D. (1982). "Studies in astronomical time series analysis. II-Statistical aspects of spectral analysis of unevenly spaced data." <u>The Astrophysical Journal</u> **263**: 835-853.

Schürch, M. and D. Buckley (2002). "Integrating geophysical and hydrochemical borehole-log measurements to characterize the Chalk aquifer, Berkshire, United Kingdom." <u>Hydrogeology Journal</u> **10**(6): 610-627.

Schuster, G. T. (2008). <u>Seismic interferometry</u>, Cambridge University Press Cambridge.

Shearer, P. M. (1999). <u>Introduction to seismology</u>, Cambridge Univ Pr.

Shuting, W., X. Zhaofeng, L. Yonggang, H. Zili and L. Heming (2003). <u>Analysis of generator vibration characteristic on rotor winding interturn short circuit fault</u>. Electrical Machines and Systems, 2003. ICEMS 2003. Sixth International Conference on, IEEE.

Sinha, S., P. S. Routh, P. D. Anno and J. P. Castagna (2005). "Spectral decomposition of seismic data with continuous-wavelet transform." <u>Geophysics</u> **70**(6): P19-P25.

Sornette, D. (2006). <u>Critical phenomena in natural sciences: chaos, fractals, selforganization and disorder: concepts and tools</u>, Springer Science & Business.

Stager, J. and T. Johnson (2008). "The late Pleistocene desiccation of Lake Victoria and the origin of its endemic biota." <u>Hydrobiologia</u> **596**(1): 5-16.

Stein, S. and M. Wysession (2009). <u>An introduction to seismology, earthquakes, and earth structure</u>, Wiley-Blackwell.

Stein., S. and M. Wysession (2003). <u>An Introduction to Seismology, Earthquakes, and Earth Structure</u>, Blackwell Plublishing.

Suharsono, S. (2014). "AN ALTERNATIVE ANALYSIS OF SURFACE WAVES DATA FOR SITE CHARACTERIZATION." <u>MTG</u> **1**(2).

Szabo (1994). "Time domain wave equations for lossy media obeying a frequency power law." <u>J. Acoustic. Soc. Am</u> **96**(1): 491-500.

Szabo, T. and J. Wu (2000). "A model for longitudinal and shear wave propagation in viscoelastic media." <u>J. Acoust. Soc. Am</u> **107**(5): 2437-2446.

Takeshita, Y., H. Kobayashi, T. Kazunori and I. Kaihotsu (2004). <u>Measurement of groundwater behavior in sandy soils using surface ground penetrating radar</u>. Ground Penetrating Radar, 2004. GPR 2004. Proceedings of the Tenth International Conference on.

Tandon, N., B. C. Nakra, D. R. Ubhe and N. K. Killa (1998). "Noise control of engine driven portable generator set." <u>Applied Acoustics</u> **55**(4): 307-328.

Telford, W. M. and R. E. Sheriff (1990). <u>Applied geophysics</u>, Cambridge university press.

Tirado, S. K. (2004). <u>Sand Thickness Estimation Using Spectral Decomposition</u>, University of Oklahoma.

Urick, R. J. (1986). <u>Ambient noise in the sea</u>, Peninsula Pub.

Wapenaar, C. P. A., D. Draganov and J. O. A. Robertsson (2008). <u>Seismic Interferometry: History and Present Status</u>, Society of Exploration Geophysicists.

Warpinski, N., S. Wolhart and C. Wright (2001). <u>Analysis and prediction of microseismicity induced by hydraulic fracturing</u>. SPE Annual Technical Conference and Exhibition, Society of Petroleum Engineers.

Watanabe, T., T. Matsuoka and Y. Ashida (1999). "Seismic traveltime tomography using Fresnel volume approach." <u>69th Proceedings Society Exploration Geophysics, Houston, USA, SPRO12</u> **5**.

Widess, M. (1973). "How thin is a thin bed?" <u>Geophysics</u> **38**(6): 1176-1180.

Wightman, W., F. Jalinoos, P. Sirles and K. Hanna (2004). Application of geophysical methods to highway related problems.

Wust-Bloch, H. (2010). "Characterizing and Locating Very Weak (-2.2 C ML C -3.4) Induced Seismicity

in Unstable Sandstone Cliffs by Nanoseismic Monitoring." <u>Pure and Applied Geophysics</u> **167**(1): 153-167.

Yin, H. (2011). <u>Application of Resistivity-Tool-Response Modeling For Formation Evaluation: AAPG Archie Series, No. 2</u>, American Association of Petroleum Geologists.

Zoback, M. D., A. Kohli, I. Das and M. W. Mcclure (2012). <u>The importance of slow slip on faults during hydraulic fracturing stimulation of shale gas reservoirs</u>. SPE Americas Unconventional Resources Conference, Society of Petroleum Engineers.